

Dissertation zur Erlangung des Doktorgrades
der Fakultät für Chemie und Pharmazie
der Ludwig-Maximilians-Universität München

Development of Functional Covalent Organic Frameworks for Optoelectronics

Mona Julia Calik

aus

Starnberg, Deutschland

2016

Erklärung

Diese Dissertation wurde im Sinne von § 7 der Promotionsordnung vom 28. November 2011 von Herrn Prof. Dr. Thomas Bein betreut.

Eidesstattliche Versicherung

Diese Dissertation wurde eigenständig und ohne unerlaubte Hilfe bearbeitet.

München, den 15.06.16

Mona Calik

Dissertation eingereicht am: 16.06.2016

Erstgutachter: Prof. Dr. Thomas Bein

Zweitgutachter: Dr. Dina Fattakhova-Rohlfing

Mündliche Prüfung am: 18.07.2016

Danksagung

An erster Stelle möchte ich ganz herzlich meinem Doktorvater Prof. Dr. Thomas Bein für die freundliche Aufnahme in seine Gruppe danken. Sein großes Vertrauen, die Freiheit eigenverantwortlich Forschung zu betreiben und die vielen richtungsweisenden Ratschläge haben mir sehr in meiner Entwicklung geholfen. Dank seiner Unterstützung konnte ich an vielen Konferenzen teilnehmen um meine Ergebnisse einem nationalen und internationalen Publikum vorzustellen. Er ermöglichte durch seine großzügige Unterstützung auch Veranstaltungen wie Hütten-workshops oder Skitage was sehr zu dem guten Arbeitsklima beigetragen hat. Neben der Freiheit und der Selbstständigkeit wurde es einem nicht zuletzt durch die hervorragende Ausstattung seiner Arbeitsgruppe ermöglicht verschiedene Projekte erfolgreich abzuschließen.

Dr. Dina Fattakhova-Rohlfing möchte ich sehr herzlich für die Bereitschaft danken, das Zweitgutachten für diese Arbeit zu erstellen.

Während der Entstehung dieser Doktorarbeit hatte ich die Gelegenheit zu erfolgreichen Kooperationen mit anderen Arbeitsgruppen der LMU.

Prof. Dr. Achim Hartschuh, Dr. Matthias Handloser, Kathrin Handloser, Irene Grill und Harald Budde möchte ich für Photoinduced Absorption und Fluoreszenz Messungen danken, welche einen sehr großen Beitrag zu den Projekten geleistet haben.

Prof. Dr. Dirk Trauner, Dr. Laura Salonen und Florian Löbermann möchte ich für die erfolgreiche Zusammenarbeit im Bereich der Porphyrine und Phthalocyanine danken. Durch ihr Engagement und Einsatz ermöglichten sie einen stetigen Nachschub an Molekülen ohne die das Projekt nicht möglich gewesen wäre.

Prof. Dr. Paul Knochel und Dr. Simon Herbert möchte ich für die schöne und produktive Zusammenarbeit bei der Linker-entwicklung danken.

Dr. Florian Auras möchte ich für die vielen erfolgreichen gruppeninternen Kooperationen und die großartige Zusammenarbeit danken. Ohne seine Hilfe und Unterstützung und sein großes Wissen im Bereich der Solarzellenanalytik wären unsere Veröffentlichungen so nicht möglich gewesen.

Ich danke auch sehr Dr. Mirjam Dogru, die mir den Weg bereitet hat und mich in das Thema der kovalent organischen Netzwerke eingelernt und die Leidenschaft dafür vermittelt hat. Ihre vielen Tips und Tricks im Umgang mit Lösemitteln und Linkern haben mir sehr geholfen ein besseres Verständnis für COFs und deren Synthese zu bekommen. Vielen Dank auch an Dr. Dana Medina für ihre Unterstützung und Hilfe bei den Projekten.

Natürlich Danke ich auch der gesamten MOF/COF Subgroup die über die Jahre sehr gewachsen ist, Dr. Dana Medina, Laura Ascherl, Maria Lohse, Erika Mühlbauer, Stefan Reuther, Patrick Hirschle, Dr. Stefan Wuttke, Dr. Florian Auras, Torben Sick, Niklas Keller, Julian Rotter, Sabrina Rager und Andreas Zimpel für die vielen wissenschaftlichen als auch privaten Diskussionen.

Einen wichtigen Beitrag zu dieser Arbeit haben auch meine Bachelor- und Masterstudenten und meine Praktikantin geleistet. Vielen Dank an Carolin Rehermann, Niklas Keller und Sabine Hübner.

Das großartige Arbeitsklima im AK Bein ist natürlich den netten Arbeitskollegen geschuldet, mit denen man auch seine Freizeit gerne verbringt. Vielen Dank an Dr. Hans Feckl, Dr. Norma Minar, Dr. Fabian Hanusch, Andreas Zimpel, Julian Rotter, Sabrina Rager, Andreas Binek, Florian Auras, Constantin von Schirnding, Stefan Datz, Bastian Rühle und Ilina Kondofersky, dafür das ihr nicht nur Arbeitskollegen sondern über die Jahre auch Freunde geworden seid und die Zeit sehr kurzweilig gemacht habt. Natürlich auch einen großen Dank an den gesamten AK Bein, für die vielen netten Kaffeepausen,

Grillfeste und großartigen Konferenzen.

Vielen Dank an Tina Reuther für die zahllosen Messungen und die stets gut gefüllten Chemikalien und Labormaterialien und Dr. Markus Döblinger für die vielen wunderschönen TEM Bilder, gezaubert aus nur mäßig kristallinen Proben.

Besonderer Dank gilt Regina Huber, für ihre Fürsorge in allen organisatorischen als auch motivatorischen Angelegenheiten, und dafür immer da zu sein um sich all unsere Probleme als auch Freuden anzuhören.

Der größte Dank gilt meiner Familie, meinen Eltern und Schwestern für ihre unerschöpfliche Unterstützung bei all meinen Vorhaben nicht nur während des Studiums und der Doktorarbeit. Ohne euch wär all das so nicht möglich gewesen!

Abstract

Covalent organic frameworks (COFs) represent an emerging class of crystalline, porous materials exhibiting unique structural and functional diversity. By connecting multidentate building blocks via covalent bonds, two- or three-dimensional frameworks with defined pore size and high specific surface area in conjunction with appreciable thermal and chemical stability can be constructed. Crystallinity and porosity are of central importance for many properties of COFs including adsorption, diffusion, and electronic transport. In this work, a new method was developed for strongly enhancing both of these aspects through the introduction of a modulating agent in the synthesis. This modulator competes with one of the building blocks during the solvothermal COF growth, resulting in highly crystalline frameworks with greatly increased domain sizes reaching several hundreds of nanometers. Using functionalized modulators, this synthetic approach also provides a new and facile method for the external surface functionalization of COF domains, providing accessible sites for post-synthetic modification reactions.

The unique structural order of COFs offers a strategy to position molecular semiconductors within a rigid network in a highly controlled and predictable manner. The π -stacked columns of layered two-dimensional COFs enable electronic interactions between the COF sheets, thereby providing a path for exciton and charge carrier migration. Frameworks comprising two electronically separated subunits can form highly defined interdigitated donor–acceptor heterojunctions, which can drive the photogeneration of free charge carriers. As a first example of a photovoltaic device that utilizes exclusively a crystalline organic framework with an inherent type II heterojunction as the active layer, a new triphenylene–porphyrin COF was developed. This COF was found to efficiently generate and separate charges upon illumination to be

collected within a solar cell device.

In a newly developed thienothiophene-porphyrin COF, evidence for a stacking order with a slight offset between successive layers in a preferred direction was found. This caused a loss in symmetry of the unit cell, which can be seen by the splitting of reflections in the X-ray diffraction pattern. Furthermore, the influence of the linear linker molecule within porphyrin COFs on the photo-luminescent decay lifetime was investigated. The lifetime can thereby be increased by pairing electron rich with deficient molecules, allowing for internal charge transfer from the porphyrin unit to the linear linker molecule.

To integrate linker molecules with extended π -systems, a new strategy was developed by constructing asymmetric building blocks. The installation of solubilizing groups in an asymmetric fashion allows the linker molecule to alternate within the COF structure and hence reduce steric strain. As an example a new Pyr-4T COF was synthesized, consisting of four armed pyrene building blocks and linear tetra thiophenes, equipped with solubilizing groups, that form square planar sheets which stack in the third dimension with a high degree of crystalline order.

An established strategy for extending the light harvesting capabilities of polymer solar cell devices is the design of materials with alternating electron-rich and electron-deficient subunits, enabling intramolecular charge transfer upon photon excitation at photon energies considerably lower than required for $\pi - \pi^*$ transitions. Selection of the subunits also enables one to modulate the energy levels of the highest occupied molecular orbital (HOMO) and the lowest unoccupied molecular orbital (LUMO) in such a way to proper match the energy levels of a fullerene derivative used as acceptor phase. To realize this concept, a new push-pull linker was developed that comprises electron rich and deficient areas within its structure. Integrated within a COF structure, it was

found to increase the absorption spectrum such that light can be harvested efficiently throughout almost the entire visible region. The energy levels of the push-pull linker were finely tuned to align with those of a fullerene acceptor to eventually, when integrated within a COF structure, function as donor material in an ordered bulk heterojunction solar cell device.

Table of contents

1.	Introduction.....	1
1.1	Organic Polymer Solar Cell Devices.....	2
1.2	Covalent Organic Frameworks- A New Class of Materials.....	6
1.3	COFs as Electroactive Materials.....	10
1.4	References.....	15
2.	Characterization.....	18
2.1	X-Ray Diffraction.....	18
2.2	Nitrogen Physisorption.....	21
2.3	Specific Surface Area.....	25
2.4	Pore Size Calculation.....	26
2.5	Thermogravimetric Analysis.....	27
2.6	Infrared Spectroscopy.....	28
2.7	Nuclear Magnetic Resonance.....	29
2.8	UV-Vis Absorption Spectroscopy.....	30
2.9	Fluorescence Spectroscopy.....	32
2.10	Time Correlated Single Photon Counting (TCSPC).....	34
2.11	Current-Voltage Measurements.....	36
2.12	External Quantum Efficiency.....	38
2.13	Scanning Electron Microscopy (SEM).....	39
2.14	Transmission Electron Microscopy.....	41
2.15	References.....	43
3.	From Highly Crystalline to Outer Surface-Functionalized Covalent Organic Frameworks – A Modulation Approach.....	45
3.1	Introduction.....	46
3.2	Results and Discussion.....	48
3.3	Conclusion.....	58
3.4	Experimental.....	59
3.5	References.....	79
4.	Extraction of Photogenerated Electrons and Holes from a COF Integrated Heterojunction.....	82
4.1	Introduction.....	83
4.2	Results and Discussion.....	85

4.3	Conclusion	93
4.4	Experimental	94
4.5	References	116
5.	Tuning Photoluminescent Lifetimes within Metal-Free Porphyrin Covalent Organic Frameworks	119
5.1	Introduction	120
5.2	Results and Discussion	122
5.3	Conclusion	127
5.4	Experimental	129
5.5	References	137
6.	Development of an Asymmetric Linker as Key for the Construction of Extended Covalent Organic Frameworks.....	139
6.1	Introduction	141
6.2	Results and Discussion	142
6.3	Conclusion	147
6.4	Experimental	148
6.5	References	159
7.	Hand-Tailoring the Properties of a Covalent Organic Framework by the Integration of a Push-Pull Building Block.....	161
7.1	Introduction	162
7.2	Results and Discussion	164
7.3	Conclusion	168
7.4	Experimental	169
7.5	References	180
8.	Conclusion.....	182

1. Introduction

Global environmental concerns and the world's rapidly growing demand for energy require alternative zero-carbon energy solutions. The sunlight hitting the earth on one day would be sufficient to cover the energy needs of mankind for one year if harvested and stored in an efficient and cost-effective way.¹ 1.74×10^{17} W solar energy continuously reaches the earth, more than 10,000 times the world's energy demand.

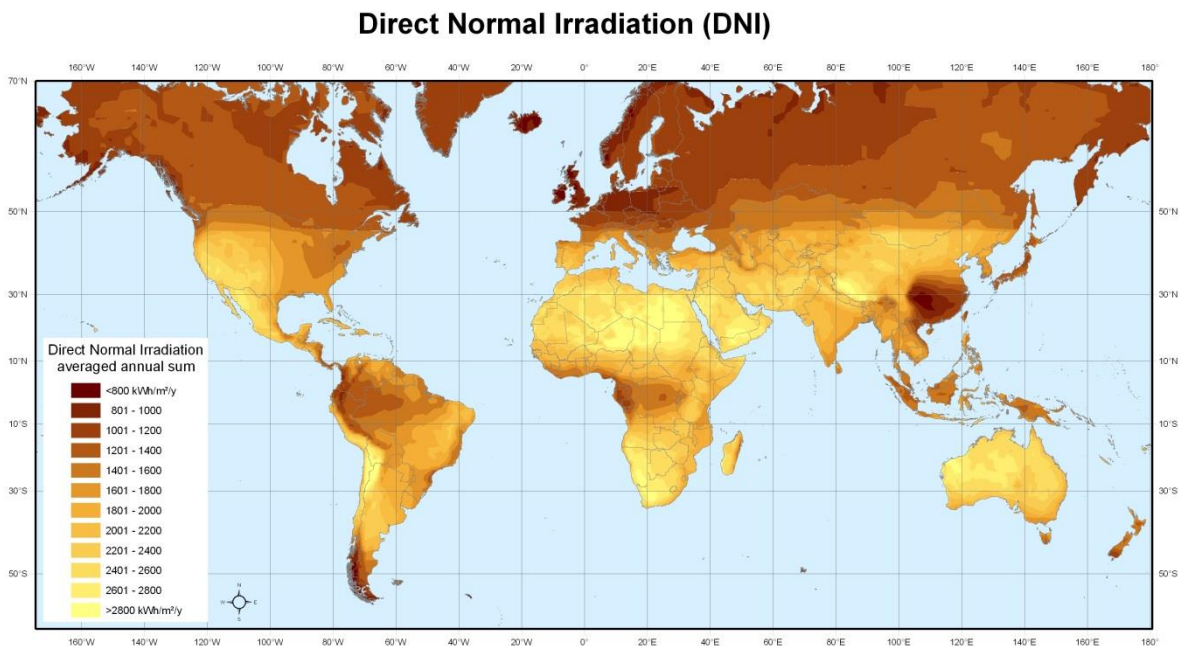


Figure 1.1. World solar energy map depicting the direct normal irradiation averaged annual sum showing regions from under 800 kWh/m²/y (brown) to over 2800 kWh/m²/y (bright yellow).²

To utilize this free and inexhaustible resource and convert its energy to electricity, many different strategies were developed with the goal of maximum power at minimum cost, initiated by Alexandre-Edmund Becquerel in 1839.³

Silicon wafer based photovoltaic (PV) technology is most commonly used, constituting about 92 % of the market, as the solar cells exhibit good power conversion efficiencies

1.1 Organic Polymer Solar Cell Devices

and long lifetimes.⁴ Their production is however, slow and requires a supply of highly pure chemicals, which makes the electricity they produce still more expensive compared to non-renewable utility-supplied electricity. The way towards a sustainable energy future therefore would benefit from an efficient and low-cost alternative to already existing PV technologies, while retaining the required stability. Organic compounds acting as active materials in solar cell devices can be fabricated on flexible substrates by fast and facile deposition processes and could therefore be a solution for the current limitations.⁵

1.1 Organic Polymer Solar Cell Devices

Organic photovoltaics have been in the focus of international research as they offer the potential of roll-to-roll processing on low-cost substrates.⁶ Thin films of organic semiconductors, typically in the range of 100 nm thickness, can be processed with printing and coating techniques on flexible substrates.

The working principle of organic PV is often based on an intermixed phase of electron donor and acceptor materials, in which the donor is usually excited upon light illumination, causing an electron to be transferred to the acceptor phase. The holes and electrons created in this process are then transported to opposite electrodes to be utilized before recombination.⁷

In 1986, Tang *et al.* reported a 1 % PCE for a donor-acceptor heterojunction, which helps to dissociate strongly bound excitons.⁸ The introduction of a bulk heterojunction (BHJ), which decreases the diffusion length of excitons from their generation to dissociation sites through an interpenetrated network of donor and acceptor phases (Figure 1.2)

1.1 Organic Polymer Solar Cell Devices

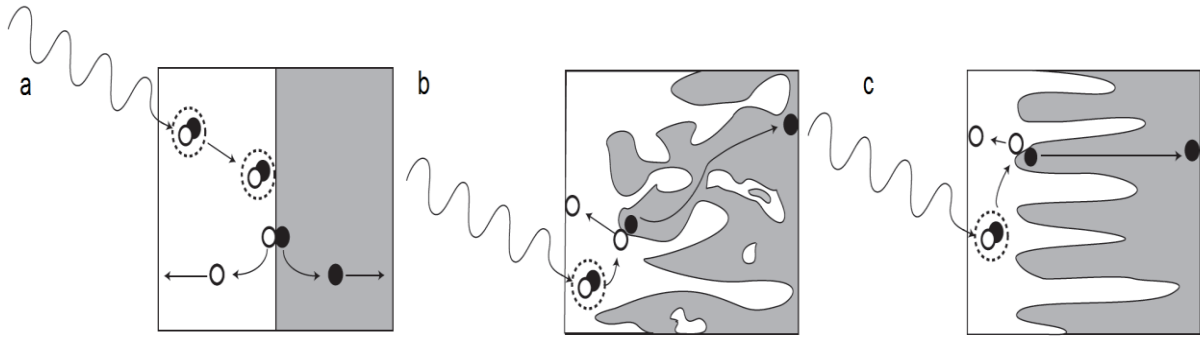


Figure 1.2. Schematic diagram of the different types of organic donor-acceptor heterojunctions and the structure of a controlled bulk heterojunction (BHJ) device. (a) Planar heterojunction. (b) Thermodynamically driven BHJ formed by phase segregation. The carrier-conducting pathways contain bottlenecks and cul-de-sacs. (c) BHJ with a large donor-acceptor interface area and continuous carrier-conducting pathways to the opposing electrodes formed by a controlled growth. Electrons are indicated by closed circles, holes by open circles, and excitons by pairs enclosed in dashed circles.⁹

triggered further improvements in efficiency.⁹⁻¹² The donor-acceptor heterojunction is used to generate charge carriers at the interface by dissociating excitons through an energy offset in LUMO levels between donor and acceptor materials that is sufficient to break the Coulomb attraction.¹³⁻¹⁴ To be converted to charge carriers before relaxing to the ground state, excitons need to diffuse into the interface between donor and acceptor material. The diffusion length is thereby depending on the exciton lifetime which is typically around 1 ns, limiting the diffusion length to less than 20 nm. As a result, only a fraction of excitons can diffuse to the interface in planar heterojunctions (Figure 1.2a).¹³ Hence, optimizing the nature and structure of the interface could potentially lead to higher device efficiencies.

A thermodynamically driven distribution of donor and acceptor phase can, however lead to bottlenecks and cul-de-sacs, which can cause a loss or recombination of the generated charges (Figure 1.2b). A controlled formation of the BHJ, resulting in an ordered, yet maximized interface area is favored (Figure 1.2c). This can be achieved by organic vapor phase deposition (OVPD) and can lead to an increase of efficiency from 1.4 to 2.7 %, compared to disordered interfaces.^{9, 15} The development of new donor-acceptor

1.1 Organic Polymer Solar Cell Devices

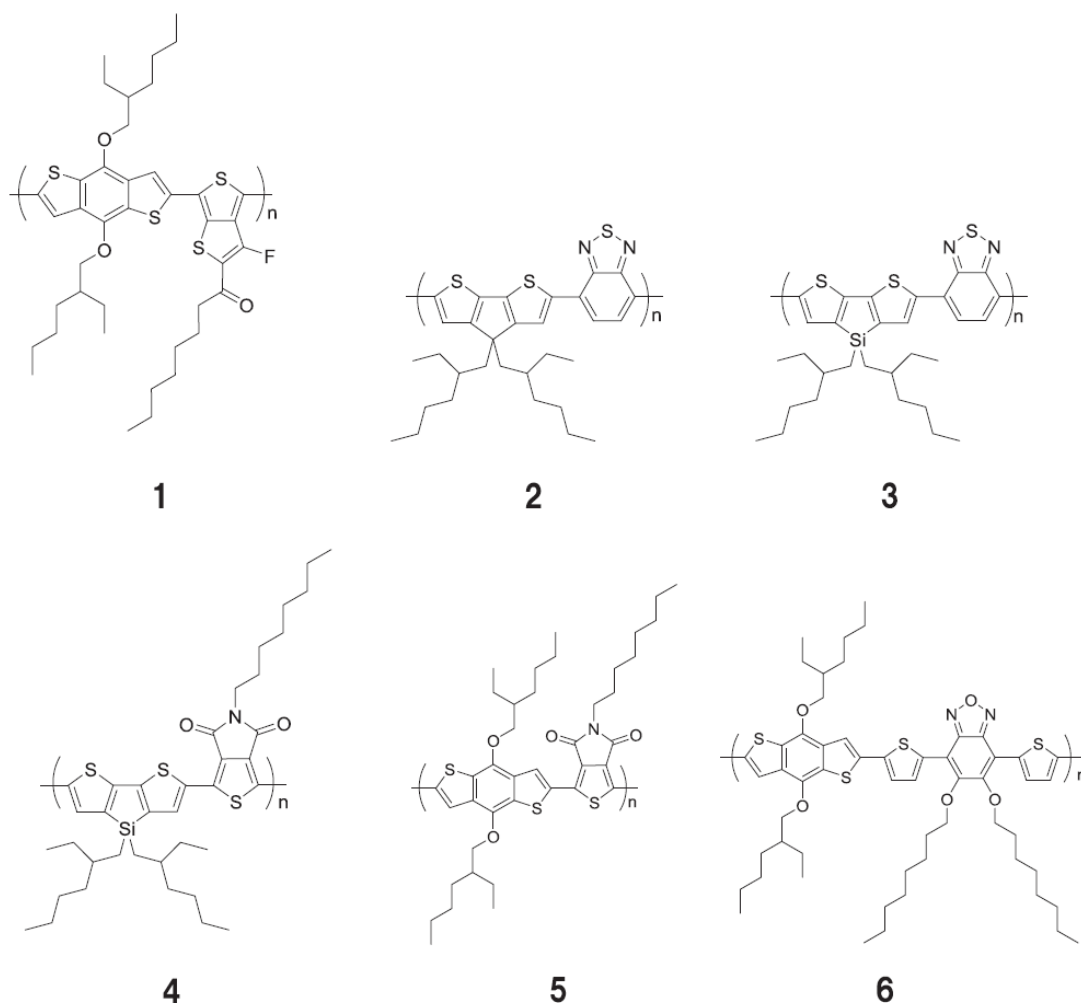


Figure 1.3. Long wavelength absorbing polymers with donor and acceptor units.¹⁶

materials and new device concepts contributed to the rapid progress in efficiency, achieving maximum values of over 10 %.¹⁷

A commonly used p-type semiconducting polymer is P3HT with an absorption spectrum reaching 650 nm. As incident light with longer wavelengths is not used effectively by this polymer, new materials with alternating donor-acceptor units in polymer chains were designed to widen the absorption spectrum, caused by intramolecular charge transfer (Figure 1.3).¹⁶

An alternative to donor-acceptor polymers to achieve high PCE are polymers constructed to achieve high fill factors (*FF*). The *FF* is dependent on the shape of the

1.1 Organic Polymer Solar Cell Devices

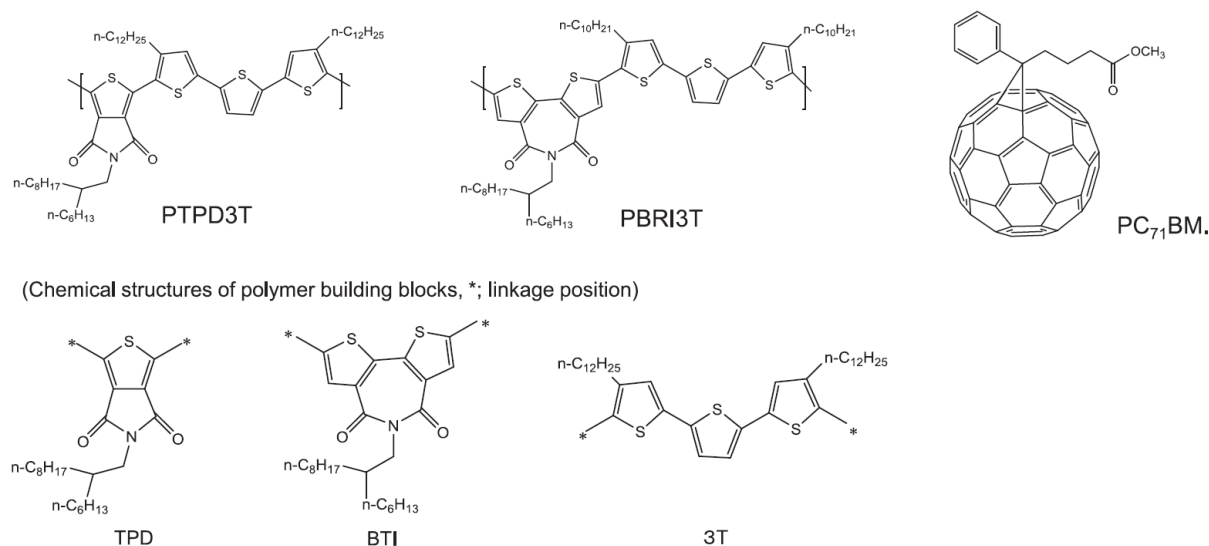


Figure 1.4. Chemical structures of polymer donors (PTPD3T, PBTI3T) and fullerene acceptor (PC₇₁BM).^{16, 18}

current-voltage (J - V) curve (Chapter 2.11) and exhibits ideally a rectangular shape. Enhanced charge mobility in the active layer can improve the transport efficiency and lower space charge build-up at near short-circuit conditions. Close to the open circuit-voltage, the lifetimes of the charge carriers determine the charge extraction efficiency and thereby the shape of the J - V curve.¹⁶ Consequently, in order to increase the FF , both aspects, lifetime and carrier mobility have to be enhanced. It is believed that π - π interactions of highly ordered polymers could increase the mobility and thereby enhance the FF .¹⁹ Examples for polymers that achieve a high FF in combination with [6,6]-phenyl-C₇₁-butyric acid methyl ester (PC₇₁BM) as electron acceptor can be seen in Figure 1.4.

The device performance, influenced by the photogeneration and separation of charges is thereby strongly dependent on the morphology of the donor and acceptor phase. A technique to fully control and design the interface of organic bulk heterojunctions would therefore be highly beneficial.

1.2 Covalent Organic Frameworks- A New Class of Materials

1.2 Covalent Organic Frameworks- A New Class of Materials

In 2005, Côté *et al.* were the first to develop covalent organic frameworks (COFs), a new class of crystalline materials, constituted solely of light-weight elements like carbon, hydrogen, nitrogen, oxygen, and boron.²⁰ COFs are crystalline polymers, constructed from organic linker molecules by forming covalent bonds. This new material class allows for the integration of organic building blocks into an ordered structure with atomic precision. The first two examples of COFs were COF-1, formed by the self-condensation reaction of 1,4-benzenediboronic acid (BDDBA) and COF-5, a combination of BDDBA and 2,3,6,7,10,11-hexahydroxytriphenylene (HHTP) (Figure 1.5).

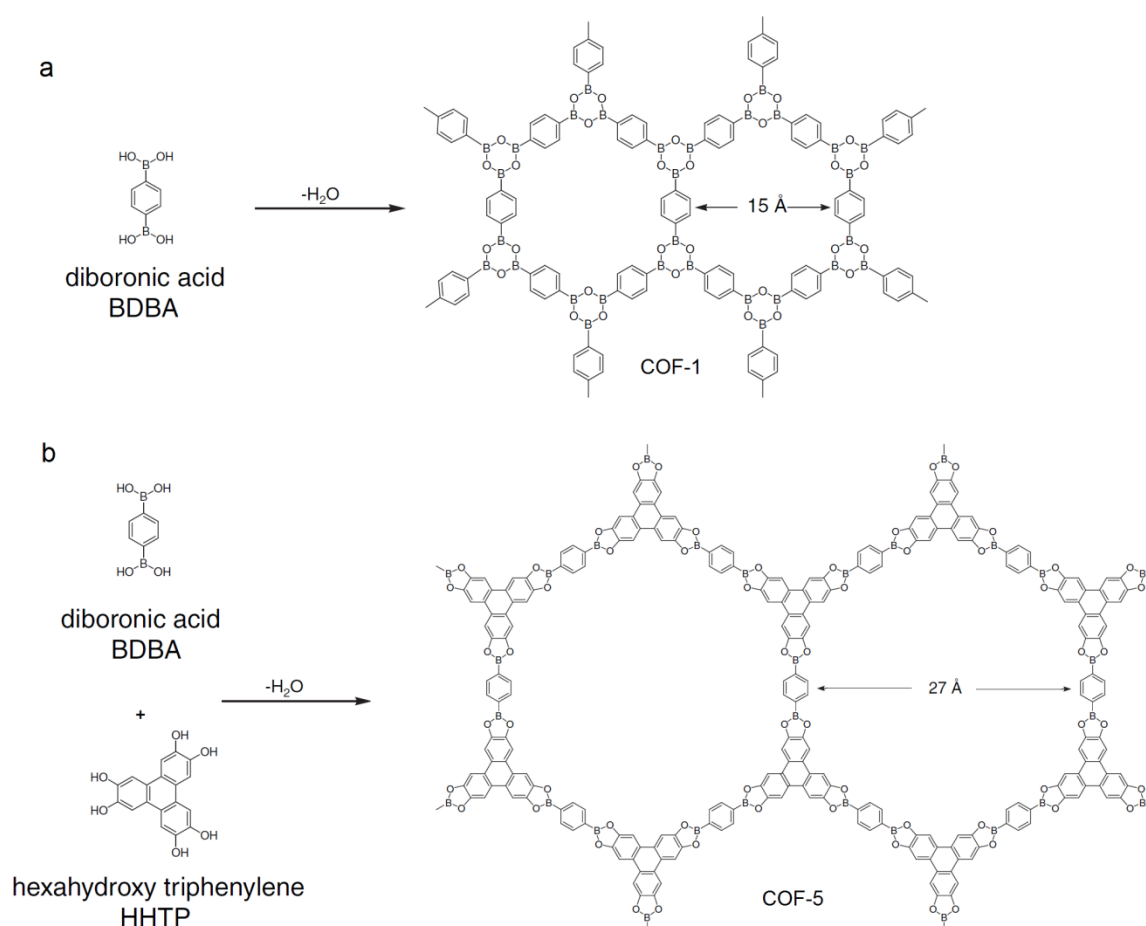


Figure 1.5. (a) self-condensation reaction of BDDBA to form the extended network COF-1 and (b) co-condensation reaction of BDDBA and HHTP to form COF-5.²⁰

1.2 Covalent Organic Frameworks- A New Class of Materials

The combination of light-weight units linked by strong covalent bonds to form defined structures gives this new material a low mass density, high thermal stability and permanent porosity with exceptionally high specific surface areas.

Based on the geometry of the linker molecules, the geometry of the resulting network can be tuned, leading to tetragonal, hexagonal or three-dimensional (3D) frameworks (Figure 1.6).²¹

1.2 Covalent Organic Frameworks- A New Class of Materials

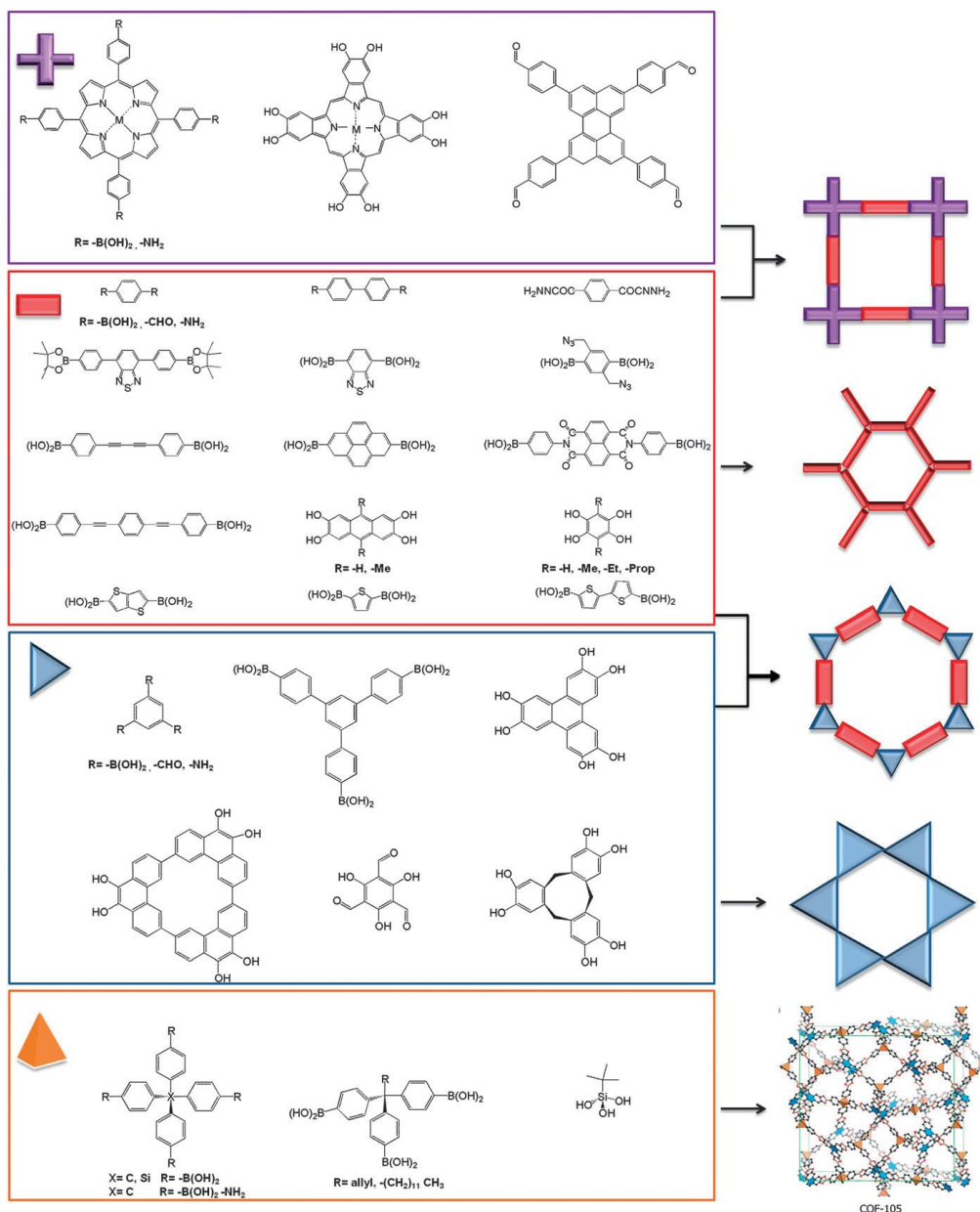


Figure 1.6. Examples of different building blocks used for the synthesis of COFs with tetragonal, hexagonal or 3D geometry.²¹

In 2D COFs, the linker molecules form 2D sheets that are stacking via π - π interactions to form aligned columnar structures. These ordered structures are uniquely constructed π -systems, which would be difficult to create by conventional covalent or non-covalent approaches.²²

In contrast to kinetically controlled polymer synthesis with irreversible covalent bond formation, COFs can only form in slightly reversible reactions.²³ In order to yield a

1.2 Covalent Organic Frameworks- A New Class of Materials

crystalline material, the bond formation needs to be reversible so that covalent bonds can be formed, broken and reformed to provide the system with a “self-healing” feedback. This feedback reduces the probability of defects, allowing an ordered system with high thermodynamic stability to be formed.

Several different linkage motifs have been established for the construction of COFs. The first examples of COFs were based on boronic acids, as they are able to either self-condense by forming six-membered boroxine rings, or co-condense with di-alcohols to obtain boronic ester linkages (Figure 1.5). Yaghi and coworkers introduced in 2009 a new linkage motif, by reacting amines and aldehydes in the presence of an acid to obtain imine bonds between the organic linker molecules (Schiff base reaction).²⁴ Further linking motifs comprise imide bonds²⁵ and hydrazone²⁶, triazine²⁷, and borazine²⁸ formation.

The unique structure of the 2D COF materials, coupled with the extended π -system formed by the interlayer interactions, could lead to the development of new photoactive materials for optoelectronics. Thus, COFs represent a new platform to molecularly design semi- and photoconducting materials.

1.3 COFs as Electroactive Materials

1.3 COFs as Electroactive Materials

The ordered, conjugated π -system of COFs renders these materials promising candidates for electroactive materials in optoelectronics. COFs allow for tailoring the optical and electroactive properties by choosing the building units accordingly. Electron rich and/or photoluminescent linkers can be integrated into the COF walls, changing the properties of the resulting network accordingly.

The feasibility of this material as photoactive material thereby strongly depends on the interlayer interactions, caused by the stacking mechanism of the 2D sheets. DFT calculations carried out by Spitler *et al.* showed that perfectly eclipsed layers with an AA-stacking behavior are un-favored. The layers rather appear to adopt a slight offset between one another of about 1.7 – 1.8 Å to exhibit a minimum in energy (Figure 1.7a).²⁹ The offset will happen in all symmetry-equivalent directions with the same probability and therefore cannot easily be monitored via X-ray diffraction. Calculations performed by Patwardhan *et al.* gave new insights into the delocalization of electrons in triphenylene based COFs. Up to distances of 3.6 Å, electrons were calculated to be completely delocalized over all triphenylenes in a stack (Figure 1.7b).³⁰

In 2008, Jiang and coworkers reported the first COF with high luminescent efficiencies and a broad absorption spectrum. The hexagonal TP-COF, formed by the co-condensation of HHTP and pyrene-2,7-diboronic acid (PDBA) shows electronic conductivity which is attributed to the eclipsed stacking of the layers (Figure 1.8).³¹

Owing to their large π -systems, a variety of phthalocyanine (Pc) containing COFs were developed to investigate their electronic properties.³²⁻³⁷

1.3 COFs as Electroactive Materials

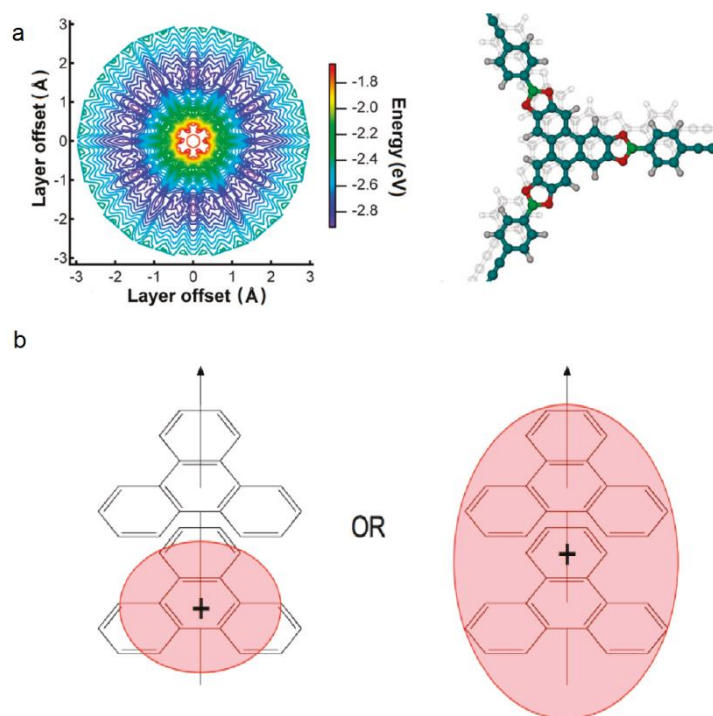


Figure 1.7. (a) Potential energy surface generated with density functional theory calculations and atomic representation of the two-layer eclipsed structure.²⁹ (b) Nature of charge carriers: localized or delocalized.³⁰

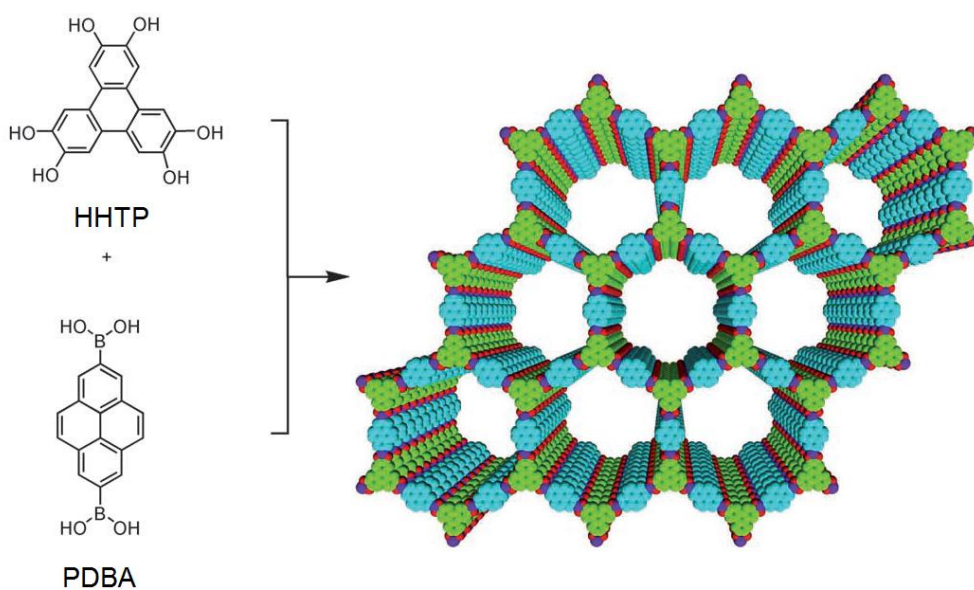


Figure 1.8. Synthesis of TP-COF from the co-condensation of HHTP and PDBA to form a hexagonal structure.³¹

1.3 COFs as Electroactive Materials

Ding *et al.* were able to control the π -electronic structure of Pc macrocycles within the COF structure to extend the absorbance to 1200 nm, ease the carrier transport, and tune the photocurrent gain by changing the central metal.³⁸

Charge carrier dynamics were also studied in a donor-acceptor COF consisting of Zn phthalocyanine electron-donor units and naphthalene diimide acting as electron accepting units. The COF promoted charge dissociation upon illumination with a prolonged lifetime of the charges, caused by suppressed recombination through delocalization within the π -stacked columns (Figure 1.9).³⁷

Moreover, chromophores like porphyrins, which exhibit extended π -electronic systems, were used to construct electroactive COFs.³⁹⁻⁴⁴ Feng *et al.* measured the influence of the central metal of a porphyrin macrocycle on the conductivity of the resulting networks. They could show that depending on the integrated metal, the porphyrin COF exhibited hole, ambipolar or electron conductivity (Figure 1.10).⁴⁰

To further tune the electronic properties of COFs, thiophene linker molecules were used to construct frameworks.⁴⁵ Thiophene-based polymers possess an inherent electrical conductivity and are known components in organic photovoltaics.⁴⁶ The first reported COF solar cell device was developed by Dogru *et al.* in 2013.⁴⁷ Thin films of a thienothiophene-HHTP COF were grown on conductive substrates and infiltrated with the fullerene derivative PCBM as acceptor (Figure 1.11a and b). These films, covered with aluminum as top electrode, promote charge transfer from the electron donating TT-COF framework to the PCBM acceptor within the pores indicated by a complete quenching of photoluminescence (Figure 1.11c). This is the first example of a COF bulk heterojunction solar cell device with a unique order of the donor and acceptor phases with a power conversion efficiency reaching 0.053 % (Figure 1.11d).

1.3 COFs as Electroactive Materials

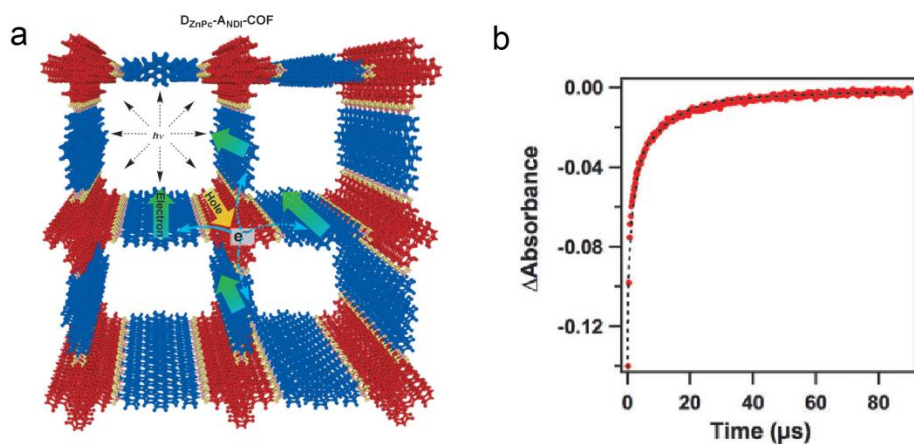


Figure 1.9. (a) Illustration of a 2x2 cell of the donor-acceptor COF ($D_{ZnPC}-A_{NDI}-COF$). Donor and acceptor units are shown in red and blue, respectively. (b) The time profile of the nanosecond transient absorption band at 480 nm of a benzonitrile-dispersed COF suspension at 298 K (red dot). The lifetime of the charge-separated state was estimated to be 10 μs using curve fitting (dotted black curve).³⁷

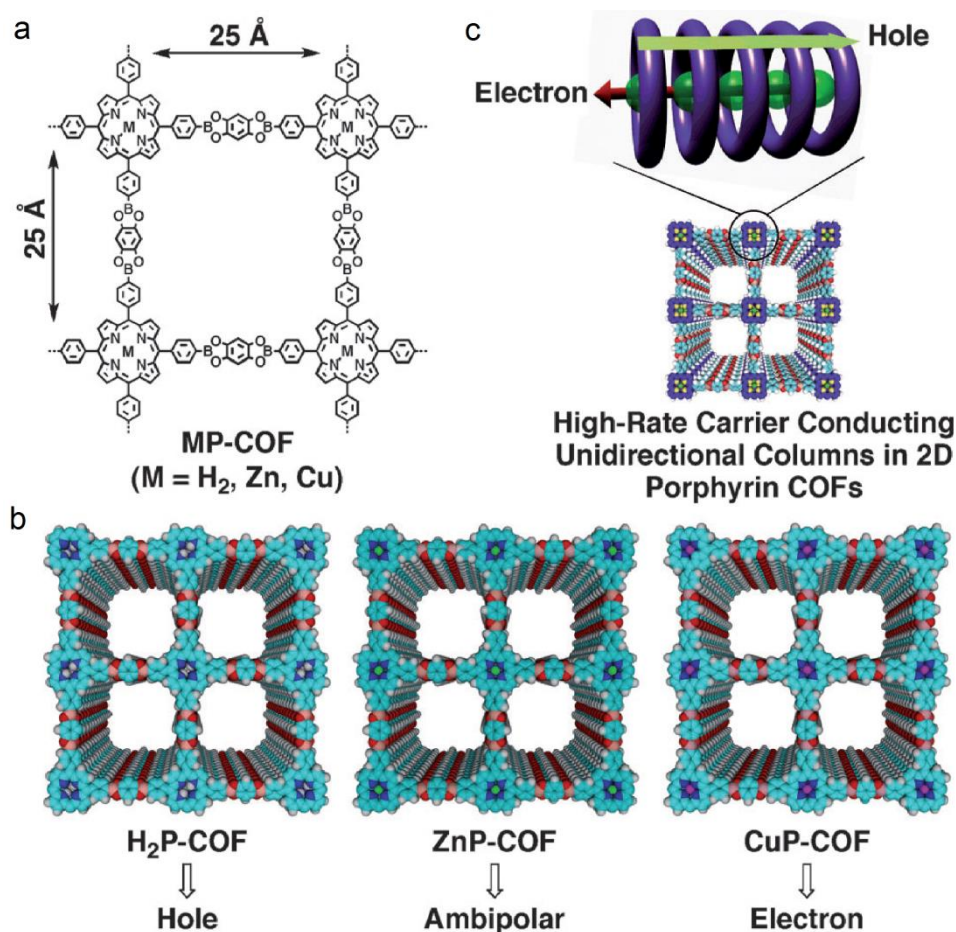


Figure 1.10. (a) Schematic representation of MP-COFs ($M=H_2, Zn, \text{ and } Cu$). (b) Schematic graphs of a 2x2 grid of MP-COFs with AA stacking 2D sheets (C: light blue; N: deep blue; H: white; O: red; B: pink; Zn: green; Cu: violet). (c) Graphical representation of metal-on-metal and macrocycle-on-macrocycle channels for respective electron and hole transport in stacked porphyrin column of 2D porphyrin COFs.⁴⁰

1.3 COFs as Electroactive Materials

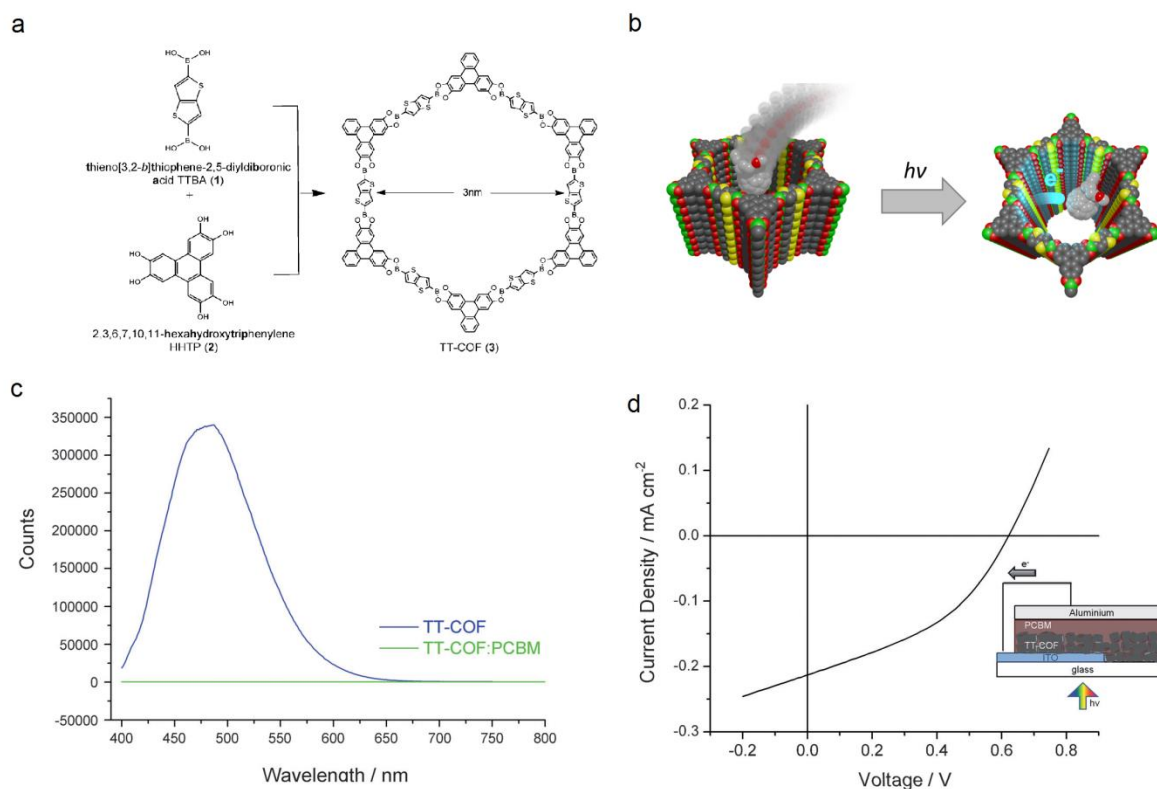


Figure 1.11. (a) Co-condensation reaction of TT (1) and HHTP (2) to form the TT-COF. (b) Illustration of the infiltration of the hexagonal TT-COF pores with PCBM and the charge transfer from the COF to the PCBM electron acceptor within the pores upon irradiation with light. (c) Photoluminescence spectrum of TT-COF (blue) and TT-COF:PCBM showing a complete quenching of photoluminescence indicating the successful charge transfer. (d) Current-voltage characteristics of the TT-COF:PCBM device measured under simulated solar light and illustration of the device fabrication.⁴⁸

As illustrated above, COFs have emerged as a new class of materials, combining light weight with robustness given by the strong covalent bonds. They are structures with designable geometry, pore size and optical properties. The well-defined crystalline structure together with the large accessible surface area that can be filled with functional molecules makes this class of materials an excellent candidate to investigate electronic processes in donor-acceptor systems at the nanoscale.

1.4 References

1. D. L. Chandler, Vast amounts of solar energy radiate to the Earth, but tapping it cost-effectively remains a challenge. *phys.org* **2011**.
2. http://www.dlr.de/tt/desktopdefault.aspx/tabid-2885/4422_read-16596/.
3. A.-E. Becquerel, Mémoire sur les effets électriques produits sous l'influence des rayons solaires. *Comptes Rendus* **1839**, 9 (567), 1839.
4. F. ISE *PHOTOVOLTAICS REPORT*; Fraunhofer ISE: 2016.
5. B. Ecker, Flexibel, leicht und durchsichtig. *Physik in unserer Zeit* **2013**, 44 (2), 84-91.
6. C. J. Brabec, Organic photovoltaics: technology and market. *Solar energy materials and solar cells* **2004**, 83 (2), 273-292.
7. L. El Chaar; N. El Zein, Review of photovoltaic technologies. *Renewable and Sustainable Energy Reviews* **2011**, 15 (5), 2165-2175.
8. C. W. Tang, Two-layer organic photovoltaic cell. *Appl. Phys. Lett. b* **1986**, 48 (2), 183-185.
9. K. M. Coakley; Y. Liu; C. Goh; M. D. McGehee, Ordered organic-inorganic bulk heterojunction photovoltaic cells. *Mater. Res. Bull.* **2005**, 30 (01), 37-40.
10. K. Yoshino; S. Morita; T. Kawai; H. Araki; X. H. Yin; A. A. Zakhidov, Characteristics of buckminsterfullerene doped conducting polymer. *Synth. Met.* **1993**, 56 (2), 2991-2996.
11. M. Hiramoto; H. Fujiwara; M. Yokoyama, Three-layered organic solar cell with a photoactive interlayer of codeposited pigments. *Appl. Phys. Lett.* **1991**, 58 (10), 1062-1064.
12. G. Yu; J. Gao; J. C. Hummelen; F. Wudl; A. J. Heeger, Polymer photovoltaic cells: Enhanced efficiencies via a network of internal donor-acceptor heterojunctions. *Science* **1995**, 270 (5243), 1789.
13. Y. Tamai; H. Ohkita; H. Benten; S. Ito, Exciton diffusion in conjugated polymers: From fundamental understanding to improvement in photovoltaic conversion efficiency. *J. Phys. Chem. Lett.* **2015**, 6 (17), 3417-3428.
14. C. Deibel; V. Dyakonov, Polymer? fullerene bulk heterojunction solar cells. *Reports on Progress in Physics* **2010**, 73 (9), 096401.
15. P. Peumans; S. Uchida; S. R. Forrest, Efficient bulk heterojunction photovoltaic cells using small-molecular-weight organic thin films. *Nature* **2003**, 425 (6954), 158-162.
16. C. Sekine; Y. Tsubata; T. Yamada; M. Kitano; S. Doi, Recent progress of high performance polymer OLED and OPV materials for organic printed electronics. *Science and Technology of Advanced Materials* **2016**.
17. <http://www.nrel.gov/ncpv/>.
18. X. Guo; N. Zhou; S. J. Luo; J. Smith; D. B. Tice; J. W. Hennek; R. P. Ortiz; J. T. L. Navarrete; S. Li; J. Strzalka; L. X. Chen; R. P. H. Chang; A. Facchetti; T. J. Marks, Polymer solar cells with enhanced fill factors. *Nat. Photon.* **2013**, 7, 825-833.
19. X. Guo; N. Zhou; S. J. Lou; J. Smith; D. B. Tice; J. W. Hennek; R. P. Ortiz; J. T. L. Navarrete; S. Li; J. Strzalka, Polymer solar cells with enhanced fill factors. *Nat. Photon.* **2013**, 7 (10), 825-833.
20. A. P. Côte; A. I. Benin; N. W. Ockwig; M. O'Keeffe; A. J. Matzger; O. M. Yaghi, Porous, Crystalline, Covalent Organic Frameworks. *Science* **2005**, 310, 1166-1170.
21. M. Dogru; T. Bein, On the road towards electroactive covalent organic frameworks. *Chem. Commun.* **2014**, 50 (42), 5531-5546.

1.4 References

22. X. Feng; X. Ding; D. Jiang, Covalent organic frameworks. *Chemical Society Reviews* **2012**, *41* (18), 6010-6022.
23. S. J. Rowan; S. J. Cantrill; G. R. Cousins; J. K. Sanders; J. F. Stoddart, Dynamic covalent chemistry. *Angew. Chem. Int. Ed.* **2002**, *41* (6), 898-952.
24. F. J. Uribe-Romo; J. R. Hunt; H. Furukawa; C. Klöck; M. O’Keeffe; O. M. Yaghi, A crystalline imine-linked 3-D porous covalent organic framework. *J. Am. Chem. Soc.* **2009**, *131* (13), 4570-4571.
25. Q. Fang; Z. Zhuang; S. Gu; R. B. Kaspar; J. Zheng; J. Wang; S. Qiu; Y. Yan, Designed synthesis of large-pore crystalline polyimide covalent organic frameworks. *Nat. Comm.* **2014**, *5*.
26. F. J. Uribe-Romo; C. J. Doonan; H. Furukawa; K. Oisaki; O. M. Yaghi, Crystalline covalent organic frameworks with hydrazone linkages. *J. Am. Chem. Soc.* **2011**, *133* (30), 11478-11481.
27. P. Kuhn; M. Antonietti; A. Thomas, Porous, Covalent Triazine-Based Frameworks Prepared by Ionothermal Synthesis. *Angew. Chem. Int. Ed.* **2008**, *47* (18), 3450-3453.
28. K. T. Jackson; T. E. Reich; H. M. El-Kaderi, Targeted synthesis of a porous borazine-linked covalent organic framework. *Chem. Commun.* **2012**, *48* (70), 8823-8825.
29. E. L. Spitler; B. T. Koo; J. L. Novotney; J. W. Colson; F. J. Uribe-Romo; G. D. Gutierrez; P. Clancy; W. R. Dichtel, A 2D covalent organic framework with 4.7-nm pores and insight into its interlayer stacking. *J. Am. Chem. Soc.* **2011**, *133* (48), 19416-19421.
30. S. Patwardhan; A. A. Kocherzhenko; F. C. Grozema; L. D. Siebbeles, Delocalization and mobility of charge carriers in covalent organic frameworks. *J. Phys. Chem. C* **2011**, *115* (23), 11768-11772.
31. S. Wan; J. Guo; J. Kim; H. Ihee; D. Jiang, A Belt-Shaped, Blue Luminescent, and Semiconducting Covalent Organic Framework. *Angew. Chem. Int. Ed.* **2008**, *120* (46), 8958-8962.
32. E. L. Spitler; W. R. Dichtel, Lewis acid-catalysed formation of two-dimensional phthalocyanine covalent organic frameworks. *Nat. Chem.* **2010**, *2* (8), 672-677.
33. V. S. P. K. Neti; X. Wu; M. Hosseini; R. A. Bernal; S. Deng; L. Echegoyen, Synthesis of a phthalocyanine 2D covalent organic framework. *CrystEngComm* **2013**, *15* (36), 7157-7160.
34. V. S. P. K. Neti; X. Wu; S. Deng; L. Echegoyen, Synthesis of a phthalocyanine and porphyrin 2D covalent organic framework. *CrystEngComm* **2013**, *15* (35), 6892-6895.
35. J.-H. Guo; H. Zhang; Z.-P. Liu; X.-L. Cheng, Multiscale study of hydrogen adsorption, diffusion, and desorption on Li-doped phthalocyanine covalent organic frameworks. *J. Phys. Chem. C* **2012**, *116* (30), 15908-15917.
36. X. Ding; J. Guo; X. Feng; Y. Honsho; J. Guo; S. Seki; P. Maitarad; A. Saeki; S. Nagase; D. Jiang, Synthesis of metallophthalocyanine covalent organic frameworks that exhibit high carrier mobility and photoconductivity. *Angew. Chem. Int. Ed.* **2011**, *50* (6), 1289-1293.
37. S. Jin; X. Ding; X. Feng; M. Supur; K. Furukawa; S. Takahashi; M. Addicoat; M. E. El-Khouly; T. Nakamura; S. Irle, Charge dynamics in a donor-acceptor covalent organic framework with periodically ordered bicontinuous heterojunctions. *Angew. Chem. Int. Ed.* **2013**, *52* (7), 2017-2021.
38. X. Ding; X. Feng; A. Saeki; S. Seki; A. Nagai; D. Jiang, Conducting metallophthalocyanine 2D covalent organic frameworks: The role of central metals in controlling π -electronic functions. *Chem. Commun.* **2012**, *48* (71), 8952-8954.
39. S. Wan; F. Gándara; A. Asano; H. Furukawa; A. Saeki; S. K. Dey; L. Liao; M. W. Ambrogio; Y. Y. Botros; X. Duan, Covalent organic frameworks with high charge carrier mobility. *Chem. Mater.* **2011**, *23* (18), 4094-4097.

1.4 References

40. X. Feng; L. Liu; Y. Honsho; A. Saeki; S. Seki; S. Irle; Y. Dong; A. Nagai; D. Jiang, High-Rate Charge-Carrier Transport in Porphyrin Covalent Organic Frameworks: Switching from Hole to Electron to Ambipolar Conduction. *Angew. Chem. Int. Ed.* **2012**, *124* (11), 2672-2676.
41. W. Ma; P. Yu; T. Ohsaka; L. Mao, An efficient electrocatalyst for oxygen reduction reaction derived from a Co-porphyrin-based covalent organic framework. *Electrochem. Commun.* **2015**, *52*, 53-57.
42. N. Huang; R. Krishna; D. Jiang, Tailor-made pore surface engineering in covalent organic frameworks: systematic functionalization for performance screening. *J. Am. Chem. Soc.* **2015**, *137* (22), 7079-7082.
43. X. Chen; M. Addicoat; E. Jin; L. Zhai; H. Xu; N. Huang; Z. Guo; L. Liu; S. Irle; D. Jiang, Locking Covalent Organic Frameworks with Hydrogen Bonds: General and Remarkable Effects on Crystalline Structure, Physical Properties, and Photochemical Activity *J. Am. Chem. Soc.* **2015**, *137* (9), 3241-3247.
44. H. Liao; H. Wang; H. Ding; X. Meng; H. Xu; B. Wang; X. Ai; C. Wang, A 2D porous porphyrin-based covalent organic framework for sulfur storage in lithium-sulfur batteries. *J. Mater. Chem. A* **2016**, *4* (19), 7416-7421.
45. D. D. Medina; V. Werner; F. Auras; R. Tautz; M. Dogru; J. Schuster; S. Linke; M. Döblinger; J. Feldmann; P. Knochel; T. Bein, Oriented Thin Films of a Benzodithiophene Covalent Organic Framework. *ACS Nano* **2014**, *8* (4), 4042-4052.
46. A. Facchetti, π -conjugated polymers for organic electronics and photovoltaic cell applications†. *Chem. Mater.* **2010**, *23* (3), 733-758.
47. M. Dogru; M. Handloser; F. Auras; T. Kunz; D. Medina; A. Hartschuh; P. Knochel; T. Bein, A Photoconductive Thienothiophene-Based Covalent Organic Framework Showing Charge Transfer Towards Included Fullerene *Angew. Chem. Int. Ed.* **2013**, *125* (10), 2992-2996.
48. M. Dogru; M. Handloser; F. Auras; T. Kunz; D. Medina; A. Hartschuh; P. Knochel; T. Bein, A Photoconductive Thienothiophene-Based Covalent Organic Framework Showing Charge Transfer Towards Included Fullerene. *Angew. Chem. Int. Ed.* **2013**, *52*, 2920-2924.

2. Characterization

2.1 X-Ray Diffraction

X-ray diffraction (XRD) is an analytical technique to determine the atomic structure of crystalline materials and to identify the composition of phase mixtures. X-rays were first observed by Wilhelm Conrad Röntgen in 1895. They are a form of electromagnetic radiation with typical wavelengths between 0.01 and 10 nm. X-rays are generated by bombarding cold metal targets with accelerated, focused electrons. The collision of the electrons with a specimen causes the emission of Bremsstrahlung, a continuous spectrum of X-rays. Furthermore, X-rays can arise from fluorescence. Impinging electrons create holes in the inner atomic shells, which are thereupon filled by electrons from outer shells. The energy difference between those two states is emitted as X-ray photon. By choosing different metal targets, the wavelength of the fluorescent X-rays can be varied. The correlation between the atomic number Z and the wavelength λ of the emitted characteristic radiation is described by Moseley's Law:

$$\frac{1}{\lambda} = \frac{K}{(Z - \sigma)^2} \quad (2.1)$$

where K and σ are constant for a given spectral line.

1912, Max von Laue discovered the interference of X-rays passing through crystals, acting as three-dimensional diffraction gratings.¹ The scattering of electromagnetic waves in the Ångström range (X-rays) on structures that have about the same characteristic dimensions (Figure 2.1) allows for structure determination by monitoring the diffraction maxima caused by constructive interference of the scattered X-rays.

2.1 X-Ray Diffraction

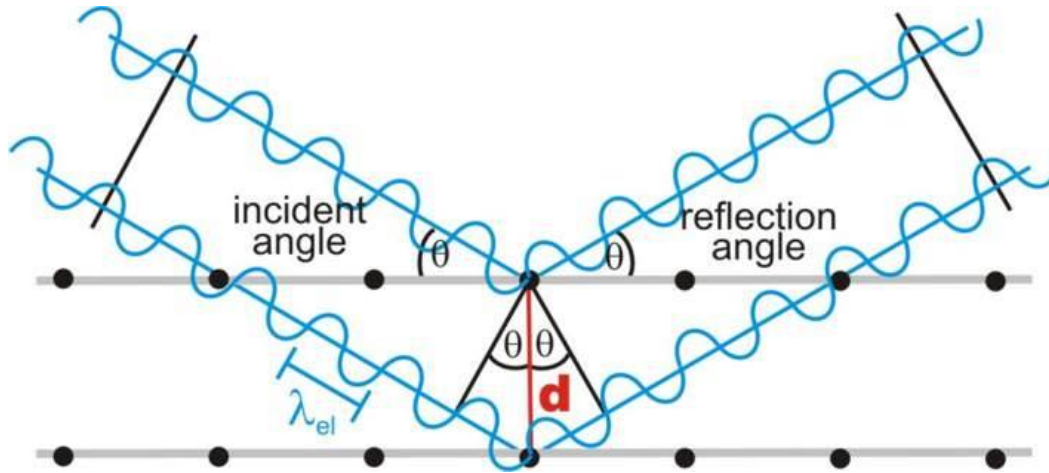


Figure 2.1: Schematic representation of the constructive interference of reflected waves during the XRD measurement.²

For constructive interference to occur, the lattices of matter have to be periodic and the path difference an integral number of wavelengths. This correlation is described by Bragg's Law:

$$n\lambda = 2d \sin(\theta) \quad (2.2)$$

λ : X-ray wavelength

n : order of interference

d : lattice plane distance

θ : angle of incidence

Powder X-ray diffraction is used to study crystalline, finely ground powders, showing statistical distributions of all possible diffractions projected onto one dimension. By applying the Scherrer equation the average crystalline domain size can be determined:

$$D = \frac{K \lambda}{\beta \sin\theta} \quad (2.3)$$

D : crystalline domain size

2.1 X-Ray Diffraction

K: Scherrer constant, in general set to 0.9

λ : wavelength

β : full width at half maximum in radians

θ : angle of incidence

2.2 Nitrogen Physisorption

2.2 Nitrogen Physisorption

Sorption measurements are an important technique to characterize porous materials regarding their pore size distribution, pore volume, and surface area.³ Nitrogen sorption can be classified as physisorption, where only weak interactions, like van-der-Waals forces occur between the material and gas molecules.

During physisorption, the amount of adsorbed nitrogen is measured at different relative pressures p/p_0 (with p being the absolute pressure and p_0 being the saturation vapor pressure) with constant temperature (77 K) to obtain sorption isotherms (Figure 2.2).

Six different isotherm types are classified by IUPAC; these can be assigned to different pore structures and sizes, and surface interactions between adsorbed nitrogen and adsorbent.⁴

Type I describes microporous materials, with steep increase of adsorbed volume at small relative pressures, reaching a nearly constant value after pore filling.

Type II shows the typical isotherm for macro, or non-porous materials. It shows a monolayer adsorption followed by unrestricted multilayer condensation.

Type III occurs, when only weak interactions between adsorptive and adsorbent are present.

2.2 Nitrogen Physisorption

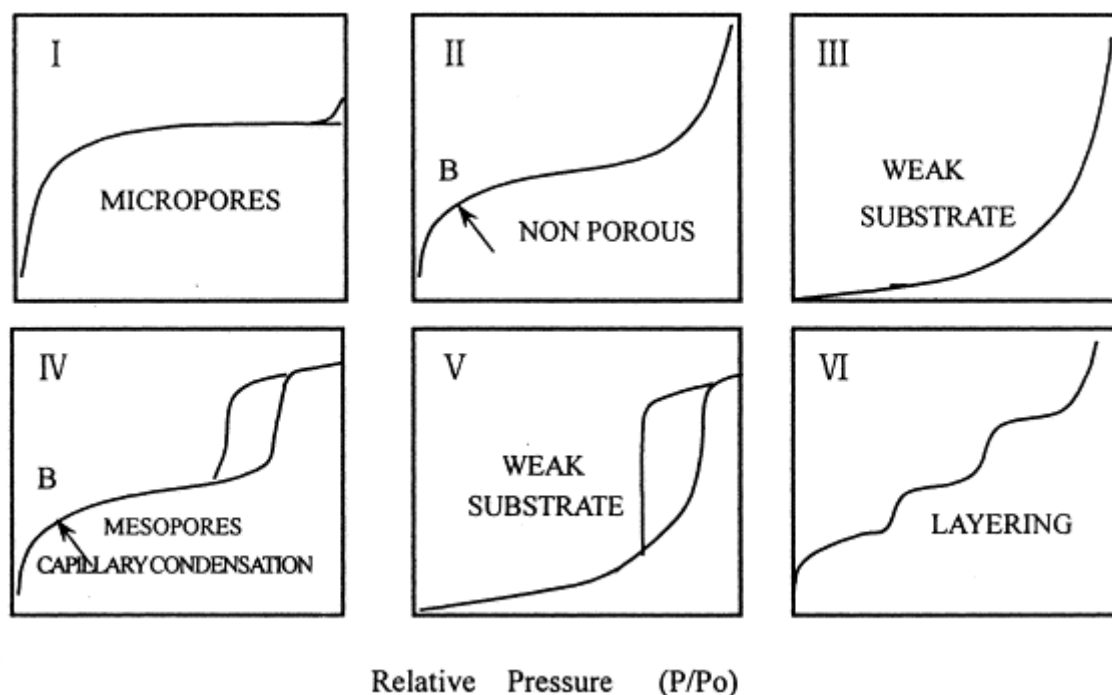


Figure 2.2. IUPAC classification of six different sorption isotherms.⁵

Type IV describes mesoporous materials. The hysteresis loop is caused by capillary condensation within the mesopores.

Type V describes materials similar to type III materials with weak adsorbate-adsorbent interactions, but also shows a hysteresis loop.

Type VI can be observed for non-porous materials with stepwise multilayer adsorption.

Covalent organic frameworks can have pore sizes between about 2 and 5 nm and therefore exhibit a type IV isotherm. Typical for this isotherm is the occurrence of a hysteresis loop. During the adsorption process, multilayers are formed which condense at a certain relative pressure inside the pores. This process is enthalpically favored. After complete pore filling, the isotherm reaches a constant value. When reducing the relative pressure to desorb the adsorbens, more energy has to be applied to overcome the van-der-Waals forces, resulting in a hysteresis loop (Figure 2.3). Specifically, it is

2.2 Nitrogen Physisorption

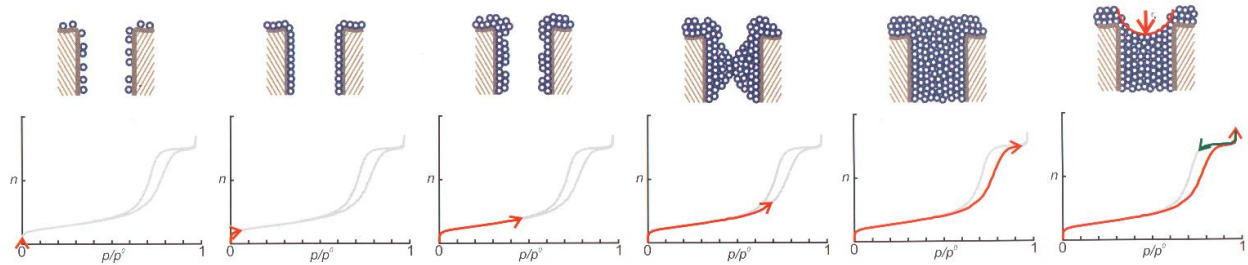


Figure 2.3. Adsorption and desorption process on a mesoporous material, depicting the capillary condensation and the cause of the hysteresis loop.⁶

proposed that hysteresis is related to the different geometry of the liquid-gas interface during adsorption (cylindrically concave) and desorption (semi-spherically concave). The shape of the hysteresis thereby bears information about the pore shape. Four different types are classified by IUPAC (Figure 2.4).⁵ H1 occurs for cylindrical/slit-like pores, the delayed condensation is due to metastable pore fluid where the desorption branch reflects the equilibrium of transition. H2, H3, H4 hysteresis can describe pore networks and ink-bottle pores, where a delay in evaporation occurs in addition to the delayed condensation, potentially due to pore blocking, cavitation or percolation phenomena.

2.2 Nitrogen Physisorption

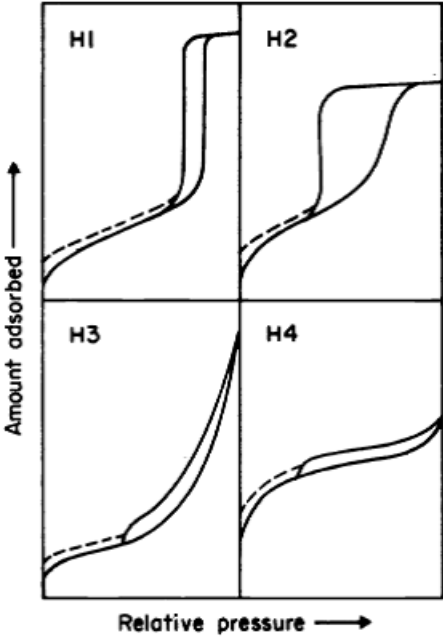


Figure 2.4: Different types of hysteresis loops. ⁵

2.3 Specific Surface Area

2.3 Specific Surface Area

There are different methods to describe isotherms mathematically. The simplest model, developed and named after Langmuir, assumes (a) that the adsorption is limited to monolayer formation, (b) the surface of the material is homogeneous, (c) all binding sites are equal, and (d) there are no interactions between adsorbed molecules. The Langmuir model is described in equation (2.4):

$$\frac{n}{n_m} = \frac{K \cdot p}{1 + K \cdot p} \quad (2.4)$$

n : amount of adsorbate, n_m : capacity of one monolayer, p : pressure, $K = k_{ad}/k_{des}$

This model was extended by Brunauer, Emmett and Teller (BET) to also include the formation of multilayers.⁷ The BET model can be expressed as the following equation (2.5).

$$\frac{n}{n_m} = \frac{C \cdot \frac{p}{p_0}}{\left(1 - \frac{p}{p_0}\right) \left(1 + C - \frac{p}{p_0}\right)} \quad (2.5)$$

n : amount of adsorbate, n_m : capacity of one monolayer, C : BET constant, p : equilibrium pressure, p_0 : saturation vapor pressure of adsorbate

To calculate the BET surface area, the linear region, typically between 0.05 and 0.3 p/p_0 is plotted with a linear regression.

2.4 Pore Size Calculation

2.4 Pore Size Calculation

The isotherm can be further analyzed to determine the pore size distribution and pore volume of the material. This method implies the change of properties of adsorbed gas molecules within porous channels. The Kelvin equation describes the thermodynamic relation between the reduced pore radius r_k and the relative vapor pressure p/p_0 :

$$r_k = \frac{-2\gamma V_L}{RT \cdot \ln\left(\frac{p}{p_0}\right)} \quad (2.6)$$

with r_k being the reduced radius, γ the surface tension of the adsorbate, V_L the molar volume, R the gas constant, T the temperature, p the equilibrium pressure and p_0 the saturation vapor pressure of the adsorbate.

This equation often leads to smaller calculated pore diameters, compared to the actual size. An extension of the Kelvin equation by Barrett-Joyner-Halenda (BJH) includes the thickness t of the monolayer to r_k .⁸ However, this model is also limited as it does not consider inhomogeneities on surfaces, assuming only perfectly ordered layers and is therefore only applicable for cylindrical pores. Density functional theory based calculations, which also include grand canonical Monte Carlo (GCMC) simulations, are able to overcome these limitations. These simulations contain terms describing attractive and repulsive interactions in the solid-fluid and fluid-fluid states. For silica materials and ordered homogeneous carbon materials, a non-local density functional theory (NLDFT) method was deployed which allows, in combination with Monte Carlo simulations, an exact description of the local fluid structure at curved solid wall interfaces.⁹ NLDFT is, however, limited to silica materials or homogeneous carbon materials. To analyze heterogeneous carbon materials a new method was developed, named the quenched solid density functional theory (QSDFT).¹⁰ This method allows for a reliable pore size analysis in the pore width range from 0.35 nm to ca. 40 nm. It was therefore used in this work.

2.5 Thermogravimetric Analysis

2.5 Thermogravimetric Analysis

Thermogravimetric analysis (TGA) allows for the compositional analysis of materials with combustible components.¹¹ TGA monitors the mass loss of the sample with increasing temperature. This method reveals the stability and purity of the material. A temperature program heats the sample in an oven with a constant heating rate up to 900 °C. The heating procedure can be either under synthetic air or inert gas atmosphere. A sensitive thermobalance measures the weight loss as function of temperature.

2.6 Infrared Spectroscopy

2.6 Infrared Spectroscopy

Infrared (IR) spectroscopy can be used to obtain information about the presence of functional groups or to confirm the formation of chemical bonds by exciting vibrational transitions.¹²⁻¹⁴ The energy difference between excited and ground state is often characteristic for specific bond types or functional groups. For IR spectroscopy, typically radiation in the mid infrared region ($200 - 4000 \text{ cm}^{-1}$) is used. Modern IR instruments use Fourier transformed infrared spectroscopy (FTIR) which uses polychromatic light to pass first through a Michelson interferometer before exciting the sample. Performing a background subtraction and Fourier transformation on the data allows for calculating the spectrum from the recorded interferogram. This technique yields data fast with a better signal-to-noise ratio (SNR) and higher accuracy. In order to be able to analyze a vibrational transition via FTIR spectroscopy, the dipole moment of the molecule has to change.

2.7 Nuclear Magnetic Resonance

2.7 Nuclear Magnetic Resonance

Nuclear magnetic resonance (NMR) spectroscopy is a powerful tool to determine the electronic environment of atoms, the interactions with their neighboring atoms or to give information about the composition of compounds.¹²⁻¹³ It is based on the change of the magnetic moment of nuclei by interacting with an electromagnetic field within strong magnetic fields. In order to investigate elements, their nuclear spin has to be non-zero, which applies for ^1H , ^{13}C , ^{19}F , ^{29}Si and ^{31}P , amongst others.

Electromagnetic waves in the radio frequency range can induce transitions between different energetic states if resonance conditions apply. The difference between the local magnetic field and the applied external field bears information about the electronic and chemical environment of the nuclei. The external magnetic field influences the magnetic energy level to differentiate to $(2J+1)$ distinct energy states (J represents nuclear spin).

2.8 UV-Vis Absorption Spectroscopy

2.8 UV-Vis Absorption Spectroscopy

UV-Vis spectroscopy enables insights into the electronical structure of materials by monitoring the optical transition from the ground state to excited states. It is thereby possible to analyze solutions, bulk material or thin films on transparent substrates.

For a solution, the Lambert Beer law defines the absorbance A at a certain wavelength with the intensity I and the intensity of the incident beam I_0 :

$$A(\lambda) = -\log \frac{I(\lambda)}{I_0(\lambda)} = \varepsilon(\lambda) c L \quad (2.7)$$

A : absorbance,

λ : wavelength

ε : specific absorption coefficient,

c : concentration

L : optical path length.

For not fully transparent samples, scattering particles can make the determination of absorbed light difficult. An integrating sphere that collects scattered light at almost all angles can eliminate this problem with the choice of a suitable reference.¹⁵

The sample is irradiated by electromagnetic light spanning from the ultraviolet (180-400 nm) to the visible (400-750nm) and to the IR (>3000 nm) region. When absorbing the light, electrons from the highest occupied molecular orbital (HOMO) will be excited to the lowest unoccupied molecular orbital (LUMO). For semiconducting materials with a direct band gap, the energy of the difference can be estimated via UV-Vis spectroscopy.

2.8 UV-Vis Absorption Spectroscopy

With the Tauc equation, the band gap of semiconductors can be estimated:

$$\alpha h\nu = C(h\nu - E_g)^n \quad (2.8)$$

with α = absorption coefficient, $h\nu$ = photon energy, E_g = band gap energy, $n = 1/2$ (for direct band gap).¹⁶

To estimate the optical band gap, $(\alpha h\nu)^2$ is plotted against $h\nu$ for direct transitions. The linear regime of the absorption spectrum is extrapolated and the intersection with the abscissa yields the value for E_g (Figure 2.5).

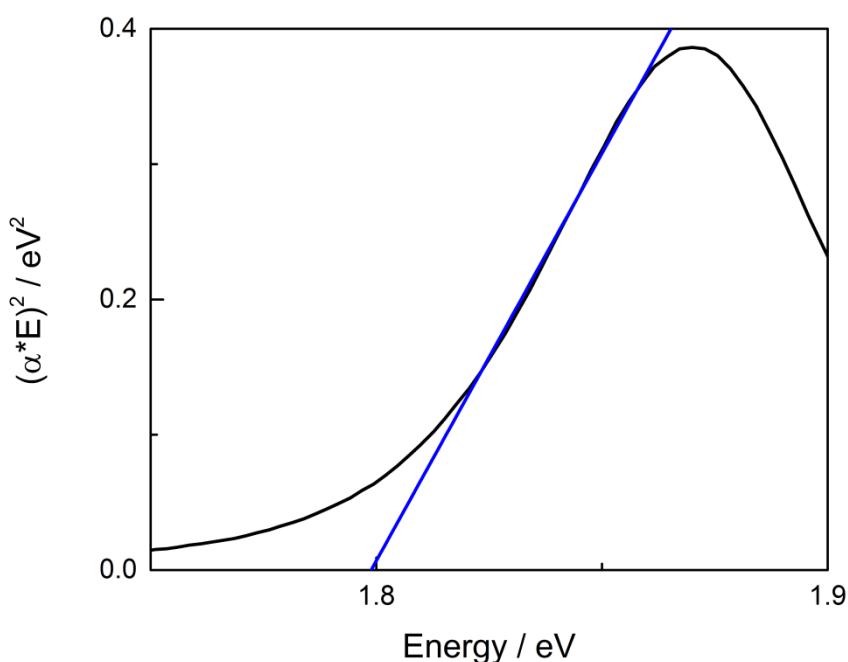


Figure 2.5. Tauc Plot applied to an absorption spectrum of a material with a direct transition. The intersection with the abscissa of the linear fit gives the value of the optical band gap energy E_g .

For small molecules the maximum in the absorption spectrum is defined as the maximum of lowest-energy band in the vibrational multiplet of the $S_0 \rightarrow S_1$ transition and is determined most accurately from a multippeak fit.

2.9 Fluorescence Spectroscopy

2.9 Fluorescence Spectroscopy

Fluorescence describes a physical process in which a material absorbs photons and subsequently emits photons of lower energy. Thereby, the fluorescence is the result of a three-stage process in the electron shells: Absorption of the light, resulting in an excited state, non-radiative transitions which occur within 10^{-12} s or less by thermalization to the lowest-energy S_1 state, resulting in a loss of energy, followed by the emission of the photon, which can be observed as fluorescence. The Jablonski diagram depicts these processes in a simplified scheme (Figure 2.6).

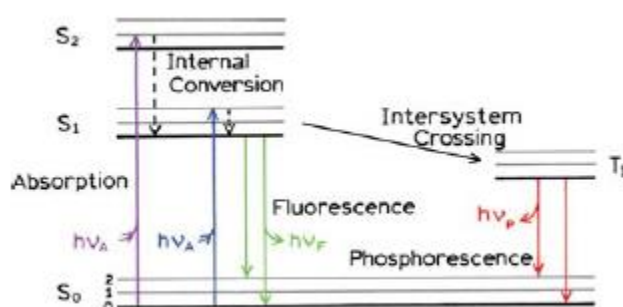


Figure 2.6: Jablonski diagram of fluorescence.¹⁷

When the fluorophore is excited with the energy $h\nu_{ex}$ provided by an external source (lamp or laser), an electron is excited from the ground state S_0 to the excited state S_1 . The absorption process occurs in the femtosecond range. This process is followed by a non-radiative relaxation from the excited state S_1 to the relaxed excited state S_1 , which is caused by conformational changes within the fluorophore.

In the last step, the electrons reach the ground state by emitting photons with the energy $h\nu_{em}$ of lower energy compared to $h\nu_{ex}$. This usually takes 1 – 10 ns to occur. This loss in energy explains the red shift of fluorescence spectra compared to the

2.9 Fluorescence Spectroscopy

corresponding absorption spectra and is called Stokes shift.¹⁸⁻¹⁹

Besides fluorescence, also other processes can take place, leading to a return of the excited electrons to the ground state, namely quenching, intersystem crossing (phosphorescence) or fluorescence energy transfer (FRET).

2.10 Time Correlated Single Photon Counting (TCSPC)

2.10 Time Correlated Single Photon Counting (TCSPC)

Time correlated single photon counting measurements offer the possibility to record time resolved kinetics of the band gap photoemission.

Repetitive excitation of the sample with a pulsed laser source is followed by the detection of a photon. The time between excitation and detection is monitored using an electronic “stopwatch”. Figure 2.7 shows that the start-stop-time is not constant, but differs for every excitation cycle. Quantum mechanics predict that it is not possible to determine the exact time of the relaxation process. Only the statistical expectation value over time of the excited species can be predicted.

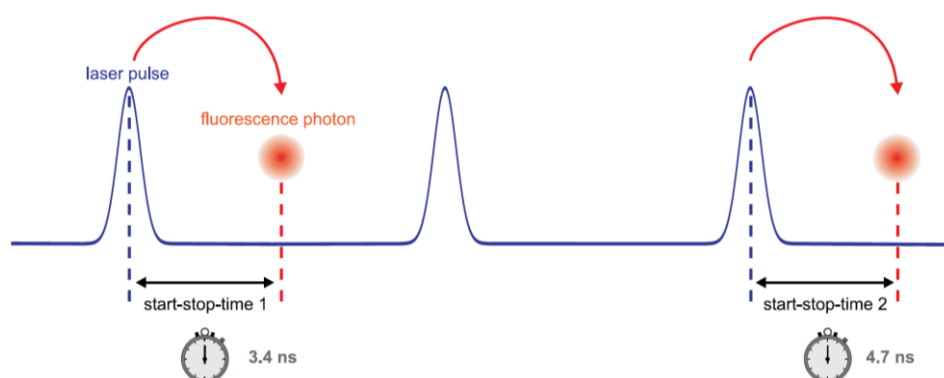


Figure 2.7: Measurement of start-stop times in a time-resolved fluorescence measurement with TCSPC.²⁰

To get the statistical expectation values, TCSPC usually uses lasers, pulsed at frequencies between 100 kHz and 80 MHz. This allows for the collection of a multitude of single photon measurement to assemble an average lifetime. Therefore, the exciting laser source needs to be weak enough to ensure a maximum of one photoemission event per laser pulse cycle. The collected individual data are sorted into a histogram, consisting of a range of time bins (Figure 2.8). This histogram typically shows an exponential decay over time, which can be fitted with one or more functions to extract the half-lifetime of the excited species.

2.10 Time Correlated Single Photon Counting (TCSPC)

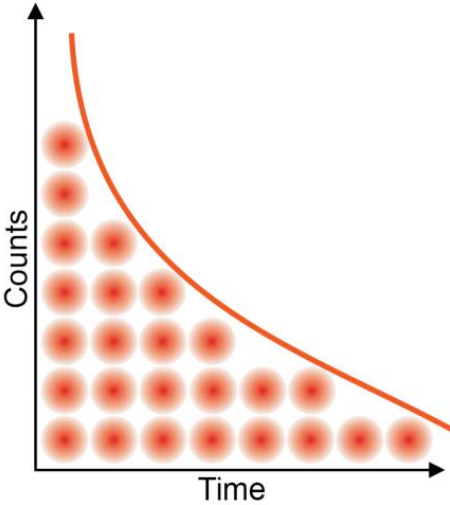


Figure 2.8: Histogram of start-stop times in a time-resolved fluorescence measurement with TCSPC.²⁰

2.11 Current-Voltage Measurements

2.11 Current-Voltage Measurements

To evaluate the quality of a solar cell device, their power conversion efficiency (PCE, η) is determined under well-defined conditions. The current standard is the ASTM G173-3 air mass 1.5 global (AM1.5G) spectrum at a total light intensity of 100 mW cm^{-2} which is defined as 1 sun.²¹ This spectrum includes absorption and scattering of the atmosphere and hemispheric illumination by diffuse light to mimic the real spectrum of the sun. Typically, laboratory solar simulators are equipped with a xenon lamp and appropriate filters to simulate this spectrum.

The efficiency of a device can be obtained by performing a current-voltage (J - V) measurement under 1 sun illumination. A typical J - V curve for a bulk heterojunction in an inverted cell device assembly is shown in Figure 2.9.

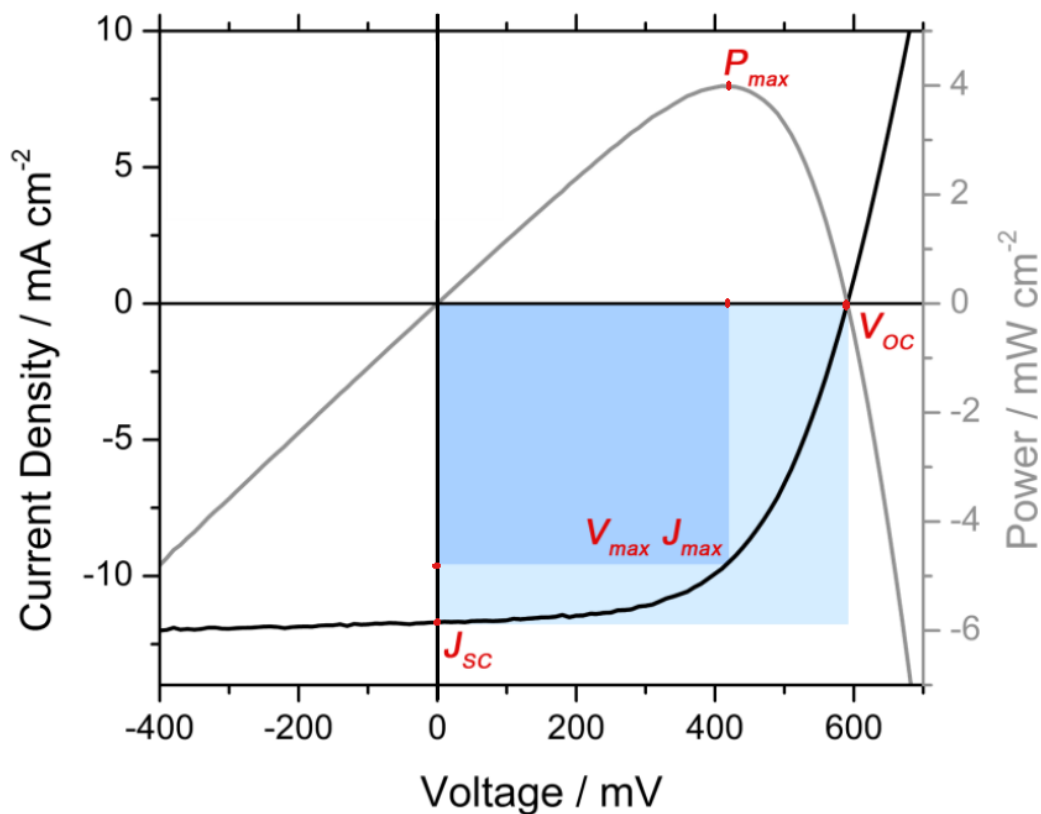


Figure 2.9: Typical J - V and power curve for a bulk heterojunction inverted solar cell.

2.11 Current-Voltage Measurements

The basic parameters of the solar cell can be extracted from this curve. The open-circuit voltage (V_{oc}) is the voltage that has to be applied to neutralize the internal electrical field of the solar cell. V_{oc} is influenced by the quasi-Fermi levels of the donor and acceptor phases. The short circuit current (J_{sc}) displays the current running through the cell without any applied bias. J_{sc} mainly depends on the optical absorption properties of the active material, the ability of creating free charge carriers from absorbed photons and the transport of the carriers to the electrodes.

P_{max} is defined as the point where the maximum of the power curve is reached and indicates the necessary voltage for the cell to perform most efficiently. The corresponding V_{max} and J_{max} define the PCE of the cell via the relation:

$$PCE = \frac{P_{MAX}}{P_{in}} = \frac{V_{MAX} \cdot J_{MAX}}{P_{in}} \quad (2.9)$$

with P_{in} being the power of the incident light.

The fill factor (FF) defines thereby the quality of the device and follows the correlation:

$$FF = \frac{V_{MAX} \cdot J_{MAX}}{V_{oc} \cdot J_{sc}} = \frac{P_{MAX}}{V_{oc} \cdot J_{sc}} \quad (2.10)$$

This equation describes the ratio between the light blue and dark blue rectangles in Figure 2.9.

2.12 External Quantum Efficiency

2.12 External Quantum Efficiency

External quantum efficiency measurements (EQE) allow one to complement the information of the device performance gained under white light illumination, by giving insights about the spectral response of the device. To this end, the current response of the device is measured spectrally resolved. The EQE is defined as the number of collected charges per incident photon of a certain wavelength given by the following equation:

$$EQE(\lambda) = \frac{n_e(\lambda)}{n_{ph}(\lambda)} = \eta_{abs}(\lambda) \cdot \eta_{ex} \cdot \eta_{ED} \cdot \eta_{PD}(V) \cdot \eta_{coll}(n_e n_h) \cdot \eta_{CT} \quad (2.11)$$

where η_{abs} is the photon absorption efficiency in the active layer, η_{ex} is the exciton generation efficiency, η_{ED} the efficiency for exciton diffusion and dissociation which is independent of the applied field as excitons are neutral quasi-particles, η_{PD} the polaron dissociation efficiency, and η_{coll} the collection efficiency which is contingent on the number of charge carriers in the active layer. η_{CT} is the charge transport efficiency and depends on the built-in and the external field.

To measure the EQE, an incident beam of monochromatic light, derived from a xenon lamp coupled to a monochromator with order sorting filters, is directed onto the sample and the current response at the respective wavelength is measured in relation to the response of a calibrated reference diode. To receive a better signal to noise ratio, the incident beam is chopped and the signal is detected by a lock-in amplifier, which is locked to the chopping frequency.

EQE allows for identifying the photoactive species within a device, as the spectrum strongly correlates with the absorption spectrum of the active species.

2.13 Scanning Electron Microscopy (SEM)

2.13 Scanning Electron Microscopy (SEM)

Scanning electron microscopy (SEM) is a technique to visualize surfaces and morphologies at the nanoscale. A scheme of the set-up is depicted in Figure 2.10.

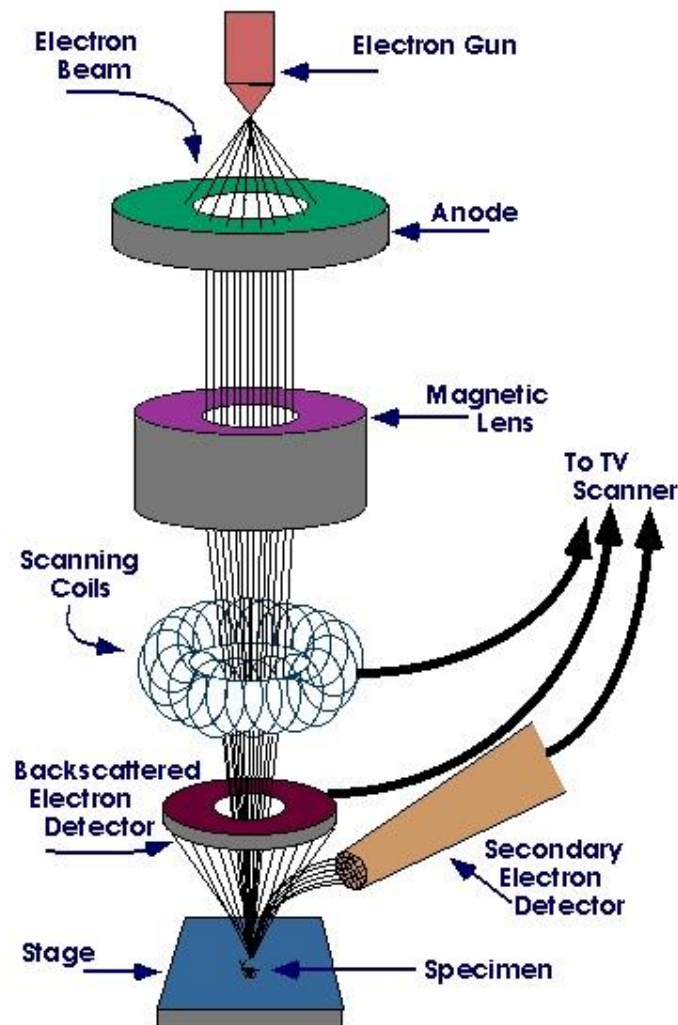


Figure 2.10: Scheme of a scanning electron microscope (SEM) set-up.²²

Heating a tungsten filament with voltages between 3 and 30 kV creates highly energetic electrons. An aperture like anode accelerates the electrons, which are then focused by various condenser lenses. Hitting the specimen, the primary electrons (PE) can produce several different signals that hold information about the morphology, shape and

2.13 Scanning Electron Microscopy (SEM)

composition of the analyzed material: Transmittance of the electron beam through the sample, allowing for phase and diffraction information (TEM) or backscattered electrons, which are almost constant in energy (BSE). If absorbed by the sample, these electrons can relax within the sample, accompanied by a loss of energy and emitted again as so-called secondary electrons (SE). A secondary electron detector, placed at a specific angle to the sample holder, detects these SE.²³ The electron beam interaction diagram is depicted in Figure 2.11.

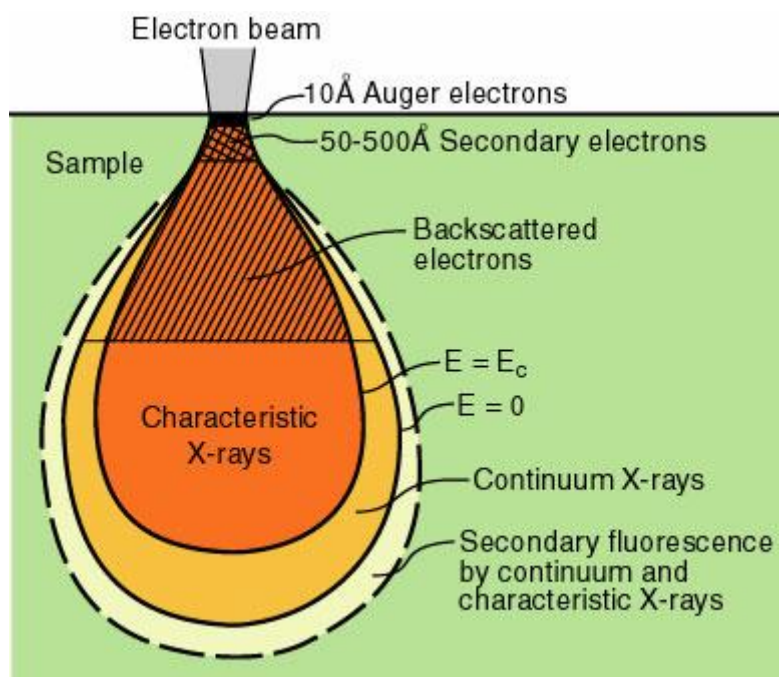


Figure 2.11. Interaction of electrons with matter.²⁴

In this work, SEM was used to take cross section images of COF based solar cell devices to determine thickness and morphology of the COF films.

2.14 Transmission Electron Microscopy

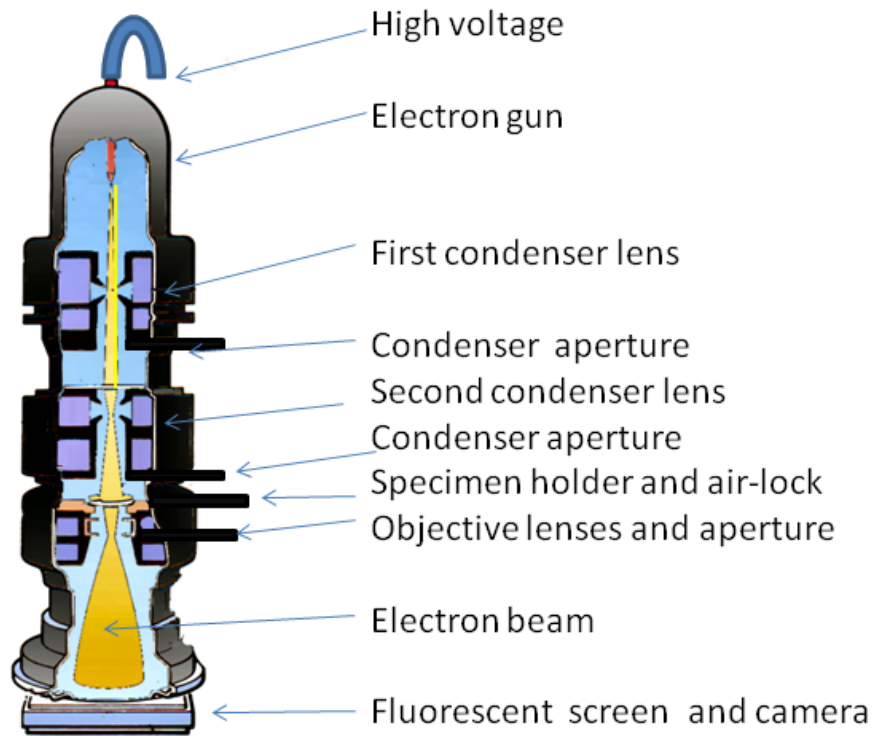
2.14 Transmission Electron Microscopy

Transmission electron microscopy (TEM) is a powerful technique to observe structures at the atomic length scale due to spatial resolution down to 0.1 nm.²⁵

For imaging, an electron beam is generated by heating a pin-shaped tungsten filament (cathode) with a negative potential, which is focused by electromagnetic lenses. In order to generate the highest possible resolution, TEM requires ultrahigh vacuum, as strong interactions between electron beam and matter can occur. Limiting factors for the highest resolution are spherical aberrations, chromatic aberrations, and astigmatism.²⁶

When the electron beam hits the target, multiple processes can occur, generating X-rays, SE, BSE or Auger electrons. These electrons can be detected and used to image the material. Additionally, a certain percentage of electrons are transmitted through the sample without any loss in energy or directional change. These transmitted electrons are detected by a fluorescent screen or a CCD camera, which allows for a characterization of the internal structure of a specimen. A scheme of a TEM is depicted in Figure 2.12.

2.14 Transmission Electron Microscopy



Transmission Electron Microscope

Figure 2.12: Schematic representation of a transmission electron microscope. The pathway of the electron beam is presented in yellow.²⁹

TEM was used to investigate and characterize the morphology and crystallinity of COFs, especially their domain size and the geometry of the crystallites.

2.15 References

2.15 References

1. M. Laue, Zur Theorie des Versuches von Trouton und Noble. *Annalen der Physik* **1912**, 343 (7), 370-384.
2. E. Zürich Bragg's Law of Diffraction. <http://www.microscopy.ethz.ch/bragg.htm>.
3. S. Lowell; J. E. Shields; M. A. Thomas; M. Thommes, *Characterization of porous solids and powders: surface area, pore size and density*. Springer Science & Business Media: 2012; Vol. 16.
4. K. S. Sing, Reporting physisorption data for gas/solid systems with special reference to the determination of surface area and porosity (Recommendations 1984). *Pure and applied chemistry* **1985**, 57 (4), 603-619.
5. Z. Ryu; J. Zheng; M. Wang; B. Zhang, Characterization of pore size distributions on carbonaceous adsorbents by DFT. *Carbon* **1999**, 37 (8), 1257-1264.
6. M. Fröba <https://www.chemie.uni-hamburg.de/ac/froeba/Gasadsorption08.pdf>.
7. S. Brunauer; P. H. Emmett; E. Teller, Adsorption of gases in multimolecular layers. *J. Am. Chem. Soc.* **1938**, 60 (2), 309-319.
8. E. P. Barrett; L. G. Joyner; P. P. Halenda, The determination of pore volume and area distributions in porous substances. I. Computations from nitrogen isotherms. *J. Am. Chem. Soc.* **1951**, 73 (1), 373-380.
9. P. Ravikovitch; S. Ó. Domhnaill; A. Neimark; F. Schüth; K. Unger, Capillary hysteresis in nanopores: theoretical and experimental studies of nitrogen adsorption on MCM-41. *Langmuir* **1995**, 11 (12), 4765-4772.
10. P. I. Ravikovitch; A. V. Neimark, Density functional theory model of adsorption on amorphous and microporous silica materials. *Langmuir* **2006**, 22 (26), 11171-11179.
11. L. S. Pang; J. D. Saxby; S. P. Chatfield, Thermogravimetric analysis of carbon nanotubes and nanoparticles. *J. Phys. Chem.* **1993**, 97 (27), 6941-6942.
12. M. Hesse; H. Meier; B. Zeeh; H. Meier, *Spektroskopische Methoden in der organischen Chemie*. Georg Thieme Verlag: 1979; Vol. 4.
13. C. R. Brundle; C. A. Evans; S. Wilson, *Encyclopedia of materials characterization: surfaces, interfaces, thin films*. Gulf Professional Publishing: 1992.
14. J. M. Hollas, *Modern spectroscopy*. John Wiley & Sons: 2004.
15. H. J. Snaith; C. Ducati, SnO₂-Based Dye-Sensitized Hybrid Solar Cells Exhibiting Near Unity Absorbed Photon-to-Electron Conversion Efficiency. *Nano Lett.* **2010**, 10 (4), 1259-1265.
16. J. Tauc; R. Grigorovici; A. Vancu, Optical properties and electronic structure of amorphous germanium. *physica status solidi (b)* **1966**, 15 (2), 627-637.
17. J. R. Lakowicz, *Principles of Fluorescence Spectroscopy*. Springer: 2008.
18. P. Atkins, *Physikalische Chemie*; 3. korr. Auflage. Wiley-VCH Verlag, Weinheim: 2001.
19. J. R. Lakowicz, *Topics in Fluorescence Spectroscopy: Volume 4: Probe Design and Chemical Sensing*. Springer Science & Business Media: 1994; Vol. 4.
20. M. Wahl, Technical Note: Time-Correlated Single Photon Counting (TCSPC). 2014.
21. http://www.dlr.de/tt/desktopdefault.aspx/tabid-2885/4422_read-16596/.
22. I. Encyclopædia Britannica Scanning electron microscope. <http://www.britannica.com/technology/scanning-electron-microscope/images-videos/Scanning-electron-microscope/110970>.
23. M. von Ardenne, Das Elektronen-Rastermikroskop. *Z. Physik* **1938**, 109 (9-10), 553-572.

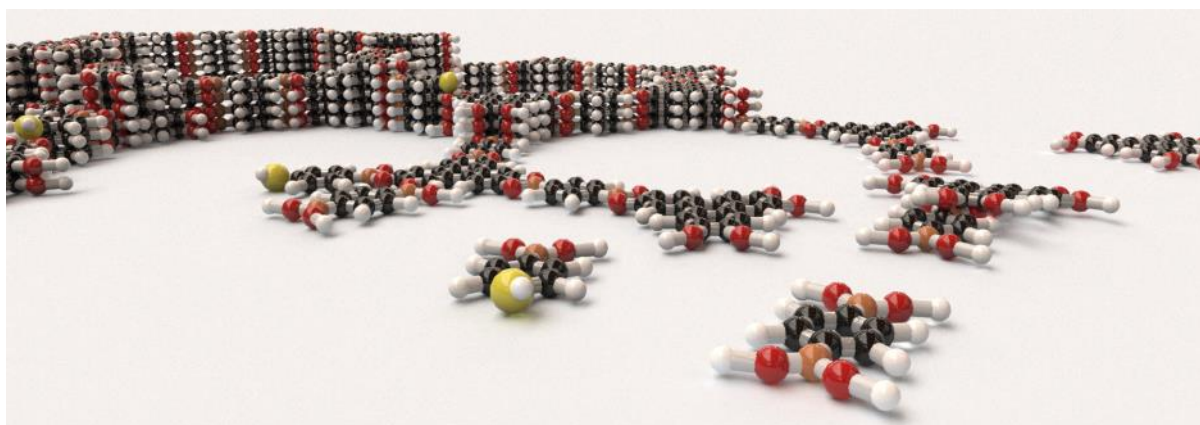
2.15 References

24. F. M. Q. Xie, Nanotechnology Engineering. U. o. Waterloo, Ed. 2007; pp 61 - 67.
25. D. B. Williams; C. B. Carter, *The transmission electron microscope*. Springer: 1996.
26. B. Fultz; J. M. Howe, *Transmission electron microscopy and diffractometry of materials*. Springer Science & Business Media: 2012.

3. From Highly Crystalline to Outer Surface-Functionalized Covalent Organic Frameworks – A Modulation Approach

This chapter is based on the following publication:

Calik, M.; Sick, T.; Dogru, M.; Döblinger, M.; Datz, S.; Budde, H.; Hartschuh, A.; Auras, F.; Bein, T. *J. Am. Chem. Soc.* **2015**, DOI 10.1021/jacs.5b10708.



Abstract

Crystallinity and porosity are of central importance for many properties of covalent organic frameworks (COFs) including adsorption, diffusion, and electronic transport. We have developed a new method for strongly enhancing both aspects through the introduction of a modulating agent in the synthesis. This modulator competes with one of the building blocks during the solvothermal COF growth, resulting in highly crystalline frameworks with greatly increased domain sizes reaching several hundreds of nanometers. The obtained materials feature fully accessible pores with an internal surface area of over 2000 m² g⁻¹. Compositional analysis via NMR spectroscopy revealed that the COF-5 structure can form over a wide range of boronic acid to catechol ratios, spanning from highly boronic acid-deficient frameworks to networks with catechol voids. Visualization of an -SH functionalized modulating agent via iridium staining

3.1 Introduction

revealed that the COF domains are terminated by the modulator. Using functionalized modulators, this synthetic approach thus also provides a new and facile method for the external surface functionalization of COF domains, providing accessible sites for post-synthetic modification reactions. We demonstrate the feasibility of this concept by covalently attaching fluorescent dyes and hydrophilic polymers to the COF surface. We anticipate that the realization of highly crystalline COFs with the option of additional surface functionality will render the modulation concept beneficial for a range of applications including gas separations, catalysis, and optoelectronics.

3.1 Introduction

Covalent organic frameworks (COFs) represent an emerging class of crystalline, porous materials exhibiting unique structural and functional diversity. By combining multidentate building blocks via covalent bonds, two- or three-dimensional frameworks with defined pore size and high specific surface area in conjunction with appreciable thermal and chemical stability can be constructed.¹⁻² Depending on their topology and functionality, these reticular materials are promising candidates for various applications, such as gas adsorption³⁻⁴, separation⁵⁻⁶, catalysis⁷⁻⁸, proton conduction⁹, energy storage¹⁰ and optoelectronics.¹¹⁻¹⁵

In the context of the latter applications COFs consisting of two-dimensional layers (2D-COFs) are of particular interest. These frameworks are realized by combining virtually planar building units into extended two-dimensional sheets, which assemble via dispersive forces (π -stacking) into highly anisotropic porous, crystalline materials. While the topology of a COF can be pre-designed via the geometry of its building blocks, the actual formation of a long-range ordered network relies on the reversibility of the covalent bond formation. Only if the reaction conditions are chosen such that the

3.1 Introduction

covalent bonds can be formed, broken and reformed at a sufficiently high rate, thus providing a functional 'self-healing' mechanism, will crystalline frameworks be obtained. COF syntheses have predominantly been realized through reversible condensation reactions, including the formation of B-O bonds (boroxines, boronate esters¹⁶⁻¹⁸ and borosilicates¹⁹), imines²⁰⁻²¹, imides²²⁻²³ and others²⁴⁻²⁶.

While the optimization of the COF growth conditions can produce fairly crystalline frameworks, the realization of particularly well-ordered COFs with large domain sizes requires an even higher degree of synthetic control.

The effects of ligands on the nucleation, growth, and properties of materials have been studied extensively for metal²⁷ and inorganic semiconductor nanocrystals²⁸⁻²⁹. Also, nanoparticles of coordination polymers have been modified by the addition of surfactants and capping agents.³⁰ In the field of metal-organic frameworks (MOFs) modulation concepts, which utilize the competition between the bridging ligands and a mono-functionalized terminating ligand, have proven very successful. Enabling the adjustment of growth kinetics and energies of specific crystal facets via selection of the modulator, this approach has been demonstrated to allow for the growth of highly crystalline MOFs with tailored morphology and domain sizes.³¹⁻³⁴

Dichtels's group recently demonstrated that 3D COFs can be functionalized internally by adding truncated building blocks bearing functional groups to the synthesis mixture.³⁵⁻³⁷

Growth rates of 2D COFs have been studied depending on the monomer reactivity and solvent mixtures.³⁸⁻⁴⁰

In this work, we transfer the modulation concept to the synthesis of a 2D COF. Applying monoboronic acids as a modulator in the solvothermal synthesis of the archetypical COF-5 we are able to influence and optimize the crystallinity, domain size, and porosity of the resulting framework. Moreover, the addition of phenylboronic acids bearing a

3.2 Results and Discussion

functional group opens up a novel, convenient way for the surface functionalization of COF crystallites, which can be used for subsequent modifications, such as the attachment of dyes or polymers.

3.2 Results and Discussion

The hexagonal COF-5 was synthesized via a microwave-assisted co-condensation of 2,3,6,7,10,11 hexahydroxytriphenylene (HHTP) with 1.5 equivalents of benzene-1,4-diboronic acid (BDBA) in a 1:1 solvent mixture of mesitylene and 1,4-dioxane (Figure 3.1). When a modulating agent was used in the synthesis, 2 equivalents of the modulator (denoted as COF-5-x, where x is expressed in %) were substituted for a fraction x of BDBA, thus keeping the amount of boronic acid groups in the reaction mixture constant. In our study the degree of substitution was systematically varied from 0 to 70 %. As a first example for a modulating agent we chose 4-mercaptophenylboronic acid (MPBA), as its size, shape and solubility are similar to BDBA. Additionally, its thiol group provides a way of detecting the incorporated modulator (see below).

The influence of the modulator on the COF-5 crystallinity was monitored by powder X-ray diffraction (PXRD) analysis (Figure 3.2a). Successful formation of the COF-5 framework was observed up to $x = 60$. We found that the introduction of small amounts of the modulating agent led to an enhanced crystallinity of the resulting COF, as evidenced by a sharpening of the reflections. The COF-5-5 and COF-5-10 samples exhibit a series of particularly sharp reflections and a number of higher-order reflections,

3.2 Results and Discussion

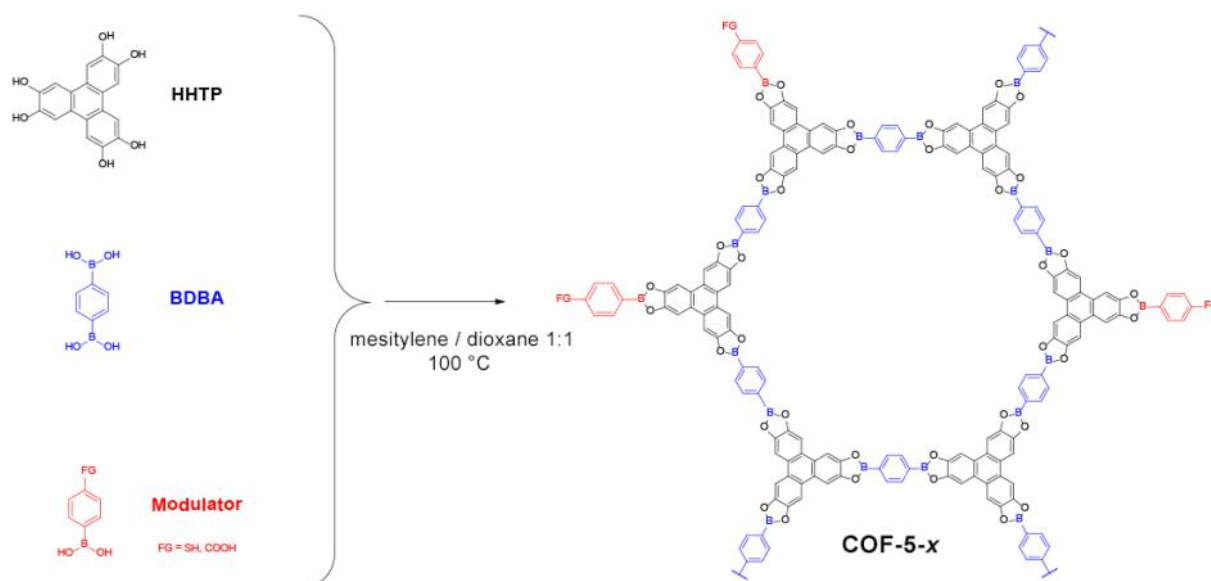


Figure 3.1. Synthesis of COF-5-x via a co-condensation reaction of benzene-1,4-diboronic acid (blue) and 2,3,6,7,10,11-hexahydroxytriphenylene (black) in the presence of a modulating agent (red) bearing a functional group.

indicating the presence of large crystalline domains with a very low concentration of defects (Figure 3.9). The XRD patterns can be indexed assuming a hexagonal $P6/mmm$ -symmetry (Figure 3.2b and Figure 3.7a). Small deviations from this idealized model, i.e. a tilt of the bridging phenyl groups (P-3, Figure 3.7b) or a serrated rather than a fully eclipsed layer arrangement ($Cmcm$, Figure 3.7c) would produce nearly identical patterns and thus cannot be identified based on the experimental data (Figure 3.7). Pawley refinement of the experimental data applying the $P6/mmm$ -symmetric model produced lattice parameters of $a = b = 2.98 \pm 0.02$ nm and $c = 0.35 \pm 0.01$ nm.

COF-5 has been reported to be highly porous with a Brunauer–Emmett–Teller (BET) surface area of up to $1590 \text{ m}^2 \text{ g}^{-1}$ and a pore volume of $0.998 \text{ cm}^3 \text{ g}^{-1}$ (Figure 3.2c). Nitrogen sorption experiments carried out for the COF-5-x series reveal a close correlation of the surface area and pore volume with the crystallinity of the frameworks (Figure 3.2d and 2.2e).

3.2 Results and Discussion

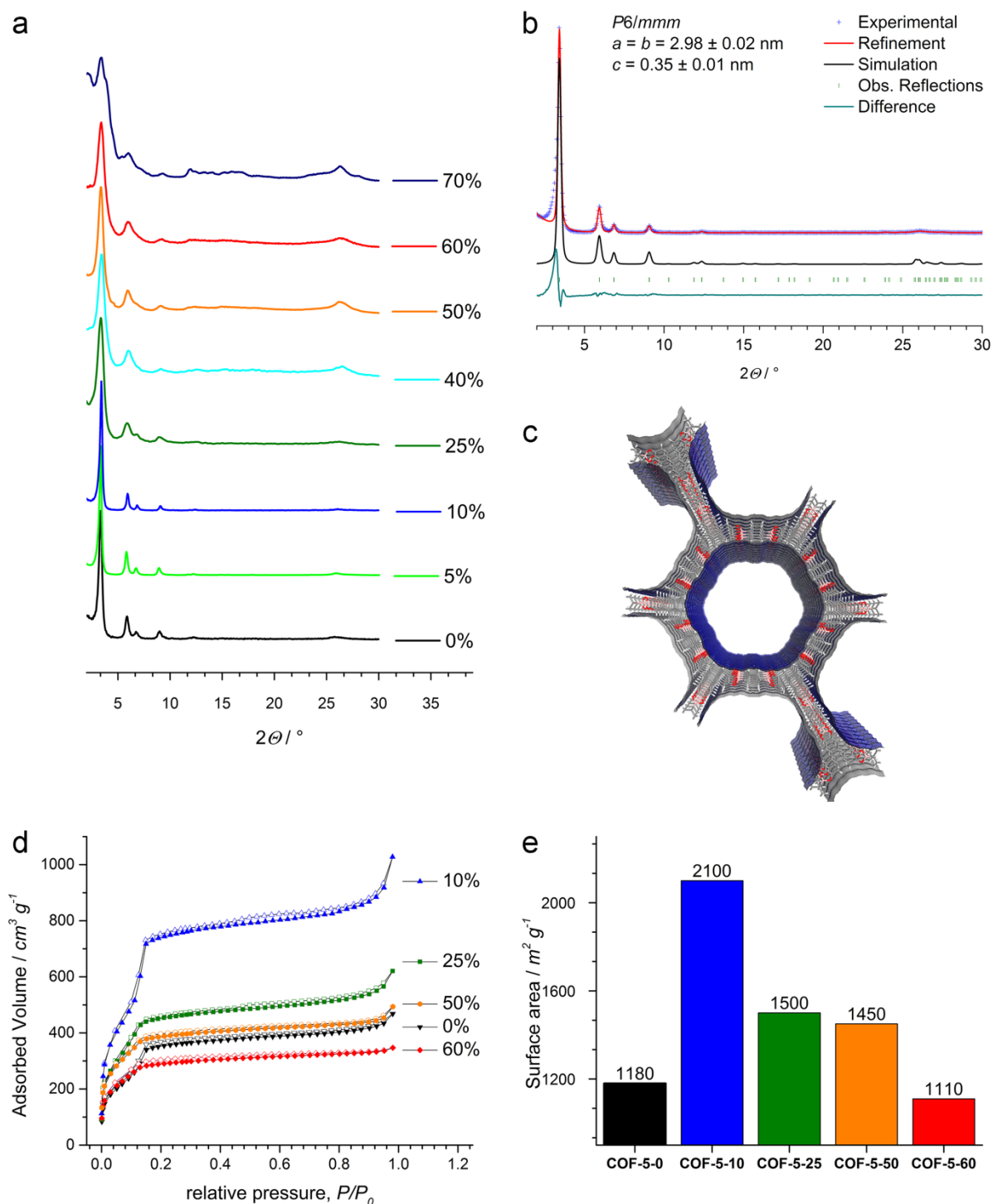


Figure 3.2. (a) Comparison of the PXRD patterns of the COF-5-x series. (b) Pawley refinement assuming $P6/mmm$ symmetry (red) of the COF-5-10 PXRD pattern (blue), simulated pattern (black), reflection positions (green) and difference plot (dark green). (c) Illustration of COF-5 showing the hexagonal pores and the Connolly surface (blue). (d) Nitrogen sorption isotherms of the COF-5-x series recorded at 77 K. (e) BET surface areas obtained from the nitrogen sorption experiments.

While in our hands the modulator-free synthesis produced frameworks with a surface

3.2 Results and Discussion

area of $1200 \text{ m}^2 \text{ g}^{-1}$ and a pore volume of $0.64 \text{ cm}^3 \text{ g}^{-1}$, the substitution of the modulator for 10 % of the BDBA increased the surface area to $2100 \text{ m}^2 \text{ g}^{-1}$ at a pore volume of $1.14 \text{ cm}^3 \text{ g}^{-1}$. This represents an increase of 32 % in surface area when compared to literature values and 75 % when compared to our own data for the modulator-free COF-5-0. Moreover, these values are close to the theoretical Connolly surface area and pore volume ($2130 \text{ m}^2 \text{ g}^{-1}$ and $1.21 \text{ cm}^3 \text{ g}^{-1}$, respectively), indicating the realization of a highly crystalline network with fully open and accessible pores. Furthermore, the distinct step in the sorption isotherms at $p/p_0 = 0.1$ underlines the very well-defined porosity of this material.⁴¹⁻⁴³ A further increase of the modulator content above $x = 10$ led to a gradual decrease in surface area and pore volume.

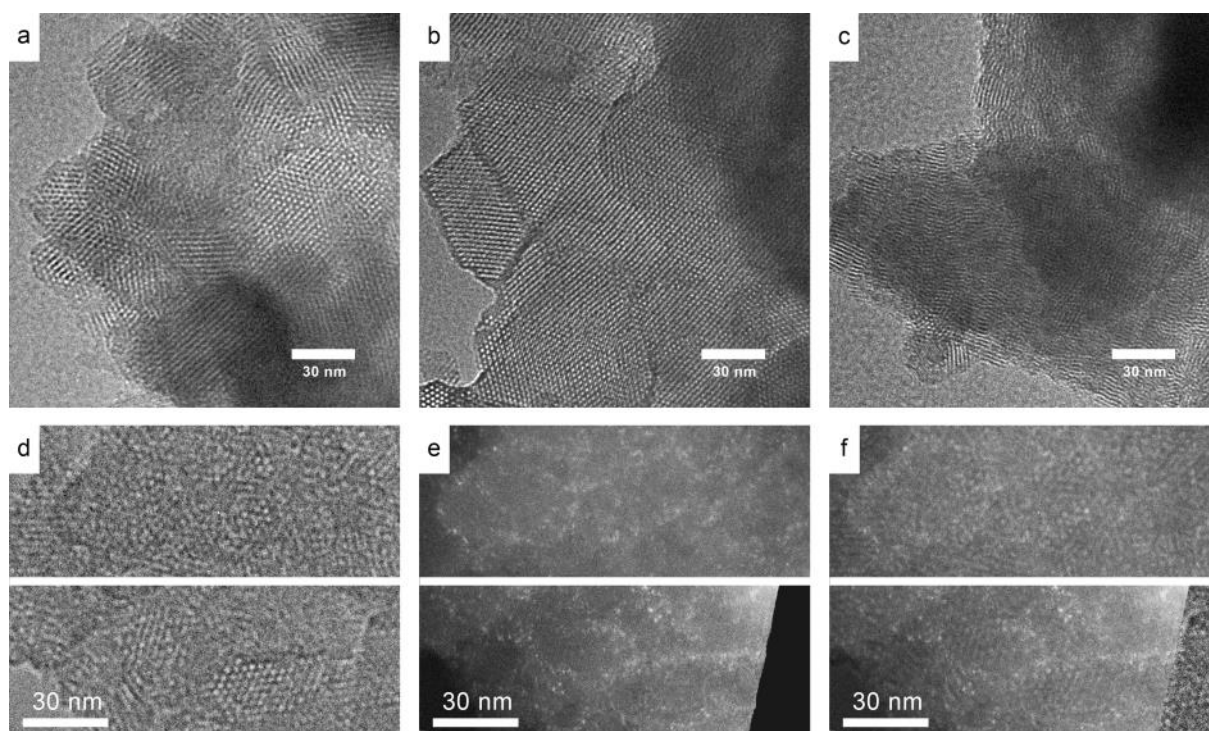


Figure 3.3. TEM micrographs of (a) COF-5-0, (b) COF-5-10 and (c) COF-5-25. (d) TEM micrographs of COF-5-10 stained with iridium at two different sample positions. (e) Corresponding scanning transmission electron microscopy (STEM) micrographs of the same sample positions (f) Overlay of TEM and STEM micrographs of COF-5-10 showing the increased Ir occurrence at the grain boundaries of the crystallite domains.

The shape of the obtained isotherms also changes upon the substitution. COF-5-0 and

3.2 Results and Discussion

the COF-5-10 exhibit the typical sharp increase at $p/p_0 = 0.1$ that is caused by the simultaneous pore condensation in the uniformly sized pores. The samples grown at a higher modulator concentration, COF-5-25, COF-5-50 and COF-5-60, however, display an increasingly broadened slope, suggesting less uniform pores and an increasing contribution of textural porosity. This trend is also reflected in the corresponding pore size distributions determined by quenched solid density functional theory (QSDFT) calculations (Figure 3.14).

Transmission electron microscopy (TEM) images of the COF grown at several modulator contents underline the influence of the MPBA on the resulting material. While COF-5-0 is composed of intergrown domains that are 30-50 nm in size (Figure 3.3a), the domains of COF-5-10 can extend to hundreds of nanometers (Figure 3.3b). Depending on the orientation of a domain, either the hexagonal arrangement of the pores or straight porous channels are visible. Increased content of the modulator results in an apparent deterioration of the structural quality and a decrease of the domain size to only 15-20 nm for COF-5-25, which we attribute primarily to the depletion of the bridging diboronic acid in the reaction mixture (Figure 3.3c).

Based on these experimental findings we propose the following mechanism for the modulator-assisted COF growth:

The modulator acts as a capping agent for the developing COF, terminating the 2D sheets during lateral growth. By repetitive attachment and detachment, the modulator slows the COF formation. The COF crystals thus experience an increased number of precipitation and dissolution steps, thus facilitating the healing of defects and bringing the system closer to thermodynamic equilibrium. Moreover, the modulator can saturate point or line defects, such as partially unreacted building blocks and dislocations, thus reducing strain in the crystal and allowing for a more stable overall crystal

3.2 Results and Discussion

conformation. Consequently, adding small amounts of the modulator enables the formation of very large and highly crystalline COF domains.

In order to gain further insights into the formation mechanism, we compared the growth kinetics of unmodulated and modulated COF-5 (Figure 3.12). In absence of a modulator, the first reflections of the COF appear already after 0.5 h. After 4 h all of the starting material has been consumed and the crystallinity increases only moderately over the next 92 h (Figure 3.12a). If 10 % MPBA is used in the synthesis, the COF formation is slowed down appreciably, while the reflections of the starting material disappear faster (Figure 3.12b). First very weak reflections appear after 1 h, but remain considerably weaker than the corresponding ones of the unmodulated sample for the next hours. Only after 16 h the same reflection intensity is reached and the crystallinity of the modulated sample outperforms the unmodulated sample thereafter. The same trend was also observed for CPBA as modulator (Figure 3.12c).

As the COF formation is thermodynamically favored over the precipitation of oligomers that might block the porous channels, we expect the modulator-assisted synthesis to produce COFs with very high porosity. Indeed, the surface area and pore volume are the highest for the modulator contents that yield the most crystalline COFs. Also, porosity values that are close to the theoretical maximum were achieved without an activation procedure, during which precipitated reactants and oligomers are digested and washed away.

From the above considerations, some of the modulator is expected to incorporate into the crystal structure at high modulator concentration. For a quantitative compositional analysis the COF-5 samples grown at different modulator concentrations were dissolved by adding pinacol in deuterated DMSO. The proton NMR signals of HHTP, pinacol-terminated BDBA and the pinacol-terminated modulators (MPBA or CPBA) were found

3.2 Results and Discussion

to be sufficiently separated to allow for a quantification of the COF constituents.

For the highly ordered COF-5- x samples ($x \leq 10$) no modulator was detected (Figure 3.4 - Figure 3.6). As the surface to volume ratio is very small for the relatively large domains of COF-5-5 and COF-5-10, the amount of modulator that could be attached to the outer surface would be below the detection limit of this method. Starting from $x = 25$ we observe an advancing incorporation of the modulator into the structure, reaching a BDBA:MPBA ratio of 1:1 for $x = 60$ (Table 3.4).

The HHTP:BDBA ratio reveals striking deviations from the expected 2:3 molecular composition of the idealized COF-5 structure. In the absence of the modulator, we observe a 6:4.3 ratio of the aryl proton integrals, corresponding to a 1:1.1 molar ratio of the two building blocks. This BDBA deficiency requires a significant amount of voids to be incorporated into the COF structure. Indeed, the pore size distribution of COF-5-0 features an additional contribution of smaller pores around 20 Å (Figure 3.14).

The composition of COF-5-10, which exhibits the highest degree of order, was found to be very close to the theoretical HHTP:BDBA molar ratio. In line with this observation, this material does not possess any porosity in addition to the hexagonal porous channels.

Increasing the modulator content in the reaction mixture leads to a gradual decrease of the incorporated BDBA, which is, however, fully balanced by the increasing incorporation of the modulator. The overall HHTP:boronic acid group ratio remains constant at 1:3, indicating that all OH groups were saturated in the framework (Table 3.4). As the space occupied by the diboronic acid in the framework is too small to accommodate two molecules of the modulator, the observed amount of modulator can only be incorporated alongside with HHTP voids (Figure 3.15). This would cause additional small pores inside the COF walls, which are indeed observed in the pore size

3.2 Results and Discussion

distributions of COF-5-25, -50, and -60 (Figure 3.14).

In addition to the non-specific incorporation at high modulator concentration in the synthesis mixture, we expect the modulator, acting as capping agent for the growing crystal domains, to accumulate at grain boundaries. Due to the instability of the framework at large TEM probe currents, a direct determination of the -SH distribution inside the framework via energy-dispersive X-ray (EDX) analysis was not possible. Therefore an indirect method was chosen, where the -SH groups that are pointing into free space were stained with iridium clusters (Figure 3.13a) and visualized by scanning TEM in high angle annular dark field mode (STEM-HAADF) imaging. (for further information see chapter 3.4).⁴⁴ In STEM-HAADF images, the intensity distribution is approximately proportional to the square of the atomic number. By overlaying the STEM-HAADF images and TEM images, recorded at the same sample positions, an accumulation of Ir-clusters at grain boundaries, with respect to the crystal domains, was observable as white dots (Figure 3.3d-f). A COF-5-0 sample that does not feature the -SH functionalization did not show any preferred localization of the iridium clusters but a random distribution within the network (Figure 3.20).

Having studied the effect of substituting an -SH functionalized modulator for a fraction of the diboronic acid, we asked whether a similar effect on the COF crystallization was also achievable with phenylboronic acids bearing other functional groups. Introducing carboxyphenyl boronic acid (CPBA) as modulating agent resulted in the same increase in domain size up to $x = 10$ followed by a gradual decrease as the modulator content was increased beyond 10 % (Figure 3.10). The application of the non-functionalized phenylboronic acid as modulator, however, did not produce crystalline COFs, possibly due to a different solubility and polarity.

The above substitution approach proved to be very sensitive to the modulator

3.2 Results and Discussion

concentration and led to small domains for $x > 10$, which we attribute primarily to an increasingly unfavorable ratio between the bridging diboronic acid and the terminating monoboronic acid. In order to allow for high modulator contents, thus ensuring optimal reaction control, but at the same time provide enough diboronic acid to form extended networks, we tested the addition of variable amounts of the modulating agent to a stoichiometric reaction mixture of HHTP and BDBA. The addition of CPBA to a 2:3 mixture of HHTP and BDBA resulted in improved crystallinity with the optimal modulator:BDBA ratio being at 3:10 (Figure 3.11). Optimal crystallinity of the COF was achieved at slightly higher modulator:BDBA ratio than for the substitution approach (i.e. 2:9 corresponding to 10 % substitution), while the resulting domain sizes and the general trends were very similar.

Post-functionalization of framework materials typically includes the risk of sample decomposition or the loss of crystallinity. In the case of 2D COFs, the delamination of the π -stacked, and thus comparably weakly interacting layers can be an issue of particular importance. Moreover, sterically demanding functional groups might prove very difficult to incorporate into close-packed 2D COFs and to convert in post-modification reactions. In cases where a modification on the outer surface of a COF domain is sufficient, the use of functionalized modulators during the COF synthesis can provide a convenient and versatile alternative. As discussed above the modulator is expressed at the outer surface of individual COF crystallites. Thus, the functional group of a para-substituted modulator, such as MPBA or CPBA, will be pointing away from the COF, rendering it easily accessible for subsequent reactions.

As a first example for illustrating this concept we chose the attachment of a fluorescent dye to the carboxylic acid functionalized CPBA-modulated COF-5-10 surface. The *N*-ethyl-*N'*-(3-dimethylaminopropyl)carbodiimide hydrochloride (EDC) activated -COOH

3.2 Results and Discussion

groups were found to react readily at room temperature with the amino functionalized ATTO 633 dye. Any unreacted, not covalently bound dye was removed by extensive washing prior to the measurements. PXRD measurements confirmed that the crystallinity had been fully retained during this process (Figure 3.13b). The newly formed amide bond was identified via IR spectroscopy (Figure 3.16a). Moreover, the presence of the dye was confirmed via UV-VIS diffuse reflectance measurements (Figure 3.18). While the COF-5-COOH absorbs strongly at wavelengths below 400 nm, its absorption in the visible range is very low and free of spectral features. The attachment of the dye gives rise to an increased absorption between 400 and 600 nm with a distinct absorption feature at 643 nm. The successful attachment of the dye was further confirmed via photoluminescence measurements (Figure 3.19). Upon excitation with a HeNe laser at 633 nm the ATTO 633 modified COF exhibits a broad emission centered at 766 nm. As expected for a dye that is immobilized at a surface both the absorption and emission spectra are broadened and red-shifted versus the respective spectra of the dye in solution.⁴⁵

This strategy can also be used to coat the COF crystallites with a shell of a different material, thus altering properties like stability, dispersibility, or bio-compatibility. Methoxypolyethylene glycol maleimide (PEG-maleimide) was successfully attached to MPBA-modified COF-5-10 via a Michael-type addition (Figure 3.16b).⁴⁶ While the bare COF-5-x is not stable towards alcohols, the PEG-modified material was found to retain its crystallinity upon soaking in ethanol. The corresponding PXRD pattern does not show any loss in crystallinity, whereas the non-functionalized COF-5-10 sample degrades rapidly (Figure 3.13c).

3.3 Conclusion

We have developed a modulation strategy for the growth of highly crystalline COFs with large domains and very high porosity. The competition between the bridging COF building block and the terminating modulation agent was found to influence the dynamic equilibrium during framework formation, slowing down the COF growth and supporting the self-healing of crystal defects. Under optimized conditions, the crystal domains of the boronate ester-linked COF-5 reached several hundreds of nanometers. The pores of the framework were found to be open and fully accessible even without any activation procedure, which is reflected by a surface area close to the theoretical maximum and a very narrow pore size distribution.

Compositional analysis via NMR revealed that the COF-5 structure forms over a wide range of molecular compositions, from highly diboronic acid-deficient frameworks to networks comprising an excess of the linear building block.

The use of functionalized modulating agents furthermore provides a new strategy for functionalizing the outer surface of COF crystallites. These functional groups were found to be accessible for the subsequent covalent attachment of molecules or polymers, allowing for further modification of the chemical, physical, or electronic properties of the COF.

The combination of an enhanced degree of crystallinity and the option for an outer surface post-modification of COF domains might prove beneficial for a range of applications, such as gas separation, catalysis, super resolution imaging, and optoelectronics.

3.4 Experimental

3.4 Experimental

Materials and Methods

All reagents and solvents were obtained from commercial suppliers and used as received.

Benzene-1,4-diboronic acid (BDBA, $\geq 95\%$, Sigma-Aldrich), 4-carboxyphenylboronic acid (CPBA, Sigma-Aldrich), 2,3,6,7,10,11-hexahydroxytriphenylene hydrate (HHTP, $>95\%$, TCI) and 4-mercaptophenylboronic acid (MPBA, 90% , Sigma-Aldrich) were used without further purification.

Nuclear magnetic resonance (NMR) spectra were recorded on Bruker AV 400 and AV 400 TR spectrometers. Proton chemical shifts are expressed in parts per million (δ scale) and are calibrated using residual undeuterated solvent peaks as an internal reference (DMSO- d_6 : 2.50).

Infrared (IR) spectra were recorded on a Perkin Elmer Spectrum BX II FT-IR system and a Thermo Scientific Nicolet™ 6700 FT-IR spectrometer in transmission mode. IR data are reported in wavenumbers (cm^{-1}).

UV-Vis spectra were recorded using a Perkin-Elmer Lambda 1050 spectrometer equipped with a 150 mm integrating sphere. Diffuse reflection measurements of COF powders were performed with a Harrick Praying Mantis accessory and referenced to BaSO_4 .

For the **photoluminescence measurements** the COF powder was deposited on a glass slide. A 60x oil immersion objective with high numerical aperture ($NA=1.49$) was used in backscattering geometry to focus the laser beam onto the sample and to collect the emitted light. The samples were excited using a linearly polarized HeNe laser ($\lambda_{exc} =$

3.4 Experimental

632.8 nm). Photoluminescence spectra were recorded using a multichannel spectrometer equipped with a 633 nm longpass filter.

Thermogravimetric analysis (TGA) measurements were performed on a Netzsch Jupiter ST 449 C instrument equipped with a Netsch TASC 414/4 controller. The samples were heated from room temperature to 900 °C under a synthetic air atmosphere at a heating rate of 1 K/min.

Nitrogen sorption isotherms were recorded on a Quantachrome Autosorb 1 at 77 K within a pressure range from $p/p_0 = 0.001$ to 0.98. Prior to the measurement of the sorption isotherms the samples were heated for 24 h at 120°C under turbo-pumped vacuum. For the evaluation of the surface area the BET model was applied between 0.05 and 0.2 p/p_0 . Pore size distributions were calculated using the QSDFT equilibrium model with a carbon kernel for cylindrical pores.

X-ray diffraction (XRD) measurements were performed using a Bruker D8 Discover with Ni-filtered Cu K_α radiation and a LynxEye position-sensitive detector.

Transmission electron microscopy (TEM) and **scanning transmission electron microscopy (STEM)** were performed on a Titan Themis at 300 kV. For STEM-HAADF, a camera length of 130 mm and a semi-convergence angle of 16.6 mrad were chosen.

Syntheses

COF-5 Modulation with MPBA - COF-5-x (SH)

A 10 mL microwave glass tube was equipped with BDBA, HHTP and MPBA according to Table 3.1. The reagents were suspended in 4 mL of a mixture of 1,4-dioxane and mesitylene (2 mL : 2 mL). The reaction mixture was sonicated for 5 min. Afterwards, the sealed flask was placed in a microwave apparatus and heated for 1 h at 100 °C with

3.4 Experimental

300 W. The gray solid product was isolated by filtration, washed with acetone and dried under vacuum. For the gas sorption measurement the product was heated to 120°C for 1 d under dynamic vacuum.

3.4 Experimental

Table 3.1. Applied initial weights for the syntheses of COF-5-x with MPBA as modulator.

x [%]	molar ratios (BDBA:HHTP:MPBA)	BDBA [mg]	BDBA [mmol]	HHTP [mg]	HHTP [mmol]	MPBA [mg]	MPBA [mmol]
0	3.00 : 2 : 0.0	18.7	0.113	24.3	0.075	0.0	0.000
5	2.85 : 2 : 0.3	17.7	0.107	24.3	0.075	1.7	0.011
10	2.70 : 2 : 0.6	16.8	0.101	24.3	0.075	3.5	0.023
25	2.25 : 2 : 1.5	14.0	0.084	24.3	0.075	6.9	0.056
40	1.80 : 2 : 2.4	13.1	0.068	24.3	0.075	10.4	0.090
50	1.50 : 2 : 3.0	9.30	0.056	24.3	0.075	17.3	0.112
60	1.20 : 2 : 3.6	7.5	0.045	24.3	0.075	20.8	0.135
70	0.90 : 2 : 4.2	5.6	0.034	24.3	0.075	24.3	0.158

COF-5 Modulation with CPBA - COF-5-x (COOH)

The synthesis of COF-5-x in the presence of CPBA as modulating agent was carried out following the procedure described above. BDBA, HHTP and CPBA were added to the reaction tube according to Table 3.2. The gray products were isolated by filtration and after washing with acetone dried under vacuum.

Table 3.2. Applied initial weights for the syntheses of COF-5-x with CPBA as modulator.

x [%]	molar ratios (BDBA:HHTP:CPBA)	BDBA [mg]	BDBA [mmol]	HHTP [mg]	HHTP [mmol]	CPBA [mg]	CPBA [mmol]
0	3.00 : 2 : 0.0	18.7	0.113	24.3	0.075	0.0	0.000
5	2.85 : 2 : 0.3	17.7	0.107	24.3	0.075	1.9	0.011
10	2.70 : 2 : 0.6	16.8	0.101	24.3	0.075	3.7	0.023
15	2.55 : 2 : 0.9	15.9	0.096	24.3	0.075	5.6	0.034
20	2.40 : 2 : 1.2	14.9	0.090	24.3	0.075	7.5	0.045
30	2.10 : 2 : 1.8	13.1	0.079	24.3	0.075	11.2	0.068
40	1.80 : 2 : 2.4	11.2	0.068	24.3	0.075	14.9	0.090
50	1.50 : 2 : 3.0	9.3	0.056	24.3	0.075	18.7	0.113
60	1.20 : 2 : 3.6	7.5	0.045	24.3	0.075	22.4	0.135

3.4 Experimental

Modulation synthesis of COF-5 by the addition of CPBA

The synthesis of COF-5-x in the presence of CPBA was carried out with addition of CPBA to a constant amount of BDBA instead of substituting BDBA, according to Table 3.3.

Table 3.3. Applied initial weights for the synthesis of COF-5 with the addition of CPBA as modulator.

BDBA : CPBA ratio	molar ratios (BDBA:HHTP:CPBA)	BDBA [mg]	BDBA [mmol]	HHTP [mg]	HHTP [mmol]	CPBA [mg]	CPBA [mmol]
1 : 0	3.00 : 2 : 0.00	18.7	0.113	24.3	0.075	0.0	0.0
1 : 0.05	3.00 : 2 : 0.15	18.7	0.113	24.3	0.075	0.93	0.007
1 : 0.1	3.00 : 2 : 0.30	18.7	0.113	24.3	0.075	1.85	0.011
1 : 0.2	3.00 : 2 : 0.60	18.7	0.113	24.3	0.075	3.71	0.023
1 : 0.3	3.00 : 2 : 0.90	18.7	0.113	24.3	0.075	5.56	0.034
1 : 0.4	3.00 : 2 : 1.20	18.7	0.113	24.3	0.075	7.42	0.045
1 : 0.5	3.00 : 2 : 1.50	18.7	0.113	24.3	0.075	9.27	0.056
1 : 0.6	3.00 : 2 : 1.80	18.7	0.113	24.3	0.075	11.13	0.068

Post-modification of COF-5-10 (SH)

To a suspension of 1 mg thiol-functionalized COF-5-10 material in 1 mL 1,4-dioxane, 1 μ L of methoxypolyethylene glycol maleimide (0.5 mg/mL in DMF) was added and reacted for 1 h. After several washing steps with 1,4-dioxane, the obtained solid was collected by centrifugation (4 min, 16873 rcf).

Staining of COF-5-10 (SH) / COF-5-0 with IrCl₃

To a suspension of 1 mg COF (COF-5-10 (SH) or COF-5-0) in 1 mL 1,4-dioxane, 100 μ L of a 0.1 M ethanolic solution of IrCl₃ was added and reacted for 3 h. The solid was collected after several washing steps with 1,4-dioxane by centrifugation (4 min, 16900 rcf).

3.4 Experimental

Post-modification of COF-5-10 (COOH)

1 mg as-synthesized COOH-functionalized COF-5-10 material was mixed with 3 μL 1-ethyl-3-(3-dimethylaminopropyl)carbodiimide (EDC) in 1 mL 1,4-dioxane. After 1 h, 1 μL ATTO 633-NH₂ (0.5 mg/mL in DMF) was added. The material was collected after centrifugation (4 min, 16900 rcf) and washed several times with 1,4-dioxane until no dye could be detected in the supernatant. The modification led to a slightly blue solid.

Compositional Analysis by NMR

For the compositional analysis by NMR the COFs were digested by the addition of a stoichiometric amount of pinacol in deuterated DMSO.

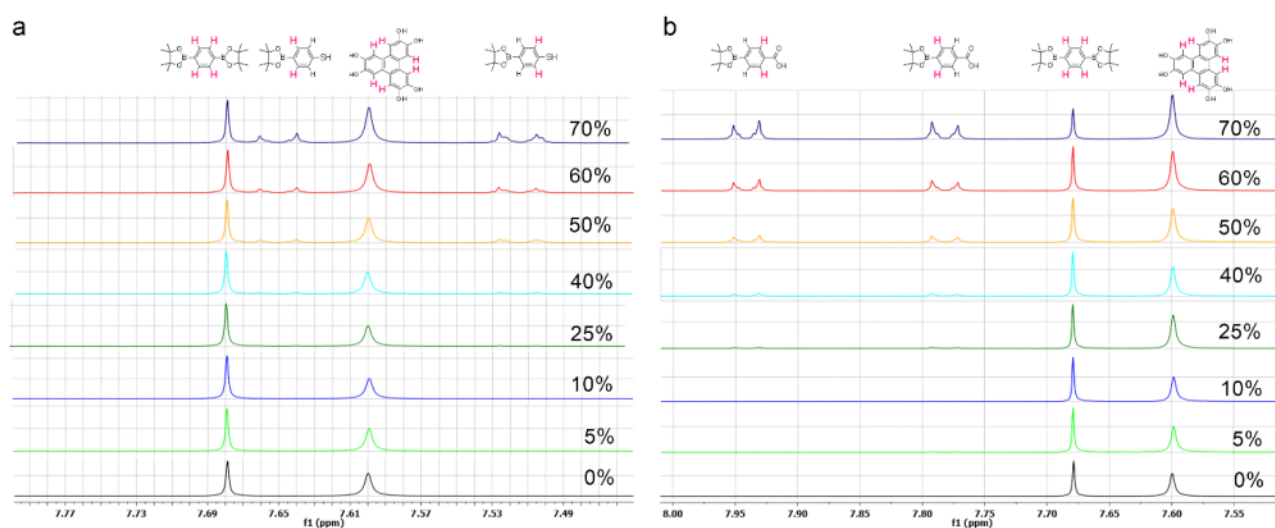


Figure 3.4. Overview of the NMR spectra of a) COF-5-x (SH) and b) COF-5-x (COOH) showing the additional signals arising from the incorporation of the modulator at higher degrees of substitution. Up to a modulator content of 10 % in the reaction mixture, the amount of incorporated modulator is below the detection limit.

3.4 Experimental

Table 3.4. Molecular composition of the MPBA-modulated COF-5 samples analyzed by NMR.

Modulator in reaction mixture [%]	HHTP aryl protons integral	BDBA protons integral	MPBA protons integral*	HHTP molar ratio	BDBA molar ratio	MPBA molar ratio	Total boronic acid groups
0	6	4.25	0	1	1.06	0	2.12
5	6	4.95	0	1	1.24	0	2.48
10	6	5.82	0	1	1.46	0	2.92
25	6	5.40	0.24	1	1.35	0.12	2.82
40	6	5.00	0.77	1	1.25	0.39	2.89
50	6	4.41	1.50	1	1.10	0.75	2.95
60	6	3.81	1.82	1	0.95	0.91	2.81
70	6	3.13	3.01	1	0.78	1.51	3.06

* The doublet at 7.52 ppm was used for the analysis.

Table 3.5. Molecular composition of the CPBA-modulated COF-5 samples analyzed by NMR.

Modulator in reaction mixture [%]	HHTP aryl protons integral	BDBA protons integral	CPBA protons integral*	HHTP molar ratio	BDBA molar ratio	CPBA molar ratio	Total boronic acid groups
0	6	4.22	0	1	1.06	0	2.11
5	6	4.48	0	1	1.12	0	2.24
10	6	4.74	0.11	1	1.19	0.06	2.43
25	6	3.46	0.38	1	0.87	0.19	1.92
40	6	3.90	0.91	1	0.98	0.46	2.41
50	6	3.74	1.62	1	0.94	0.81	2.68
60	6	2.06	2.95	1	0.52	1.48	2.51
70	6	1.83	3.09	1	0.46	1.55	2.47

* The doublet at 7.78 ppm was used for the analysis.

3.4 Experimental

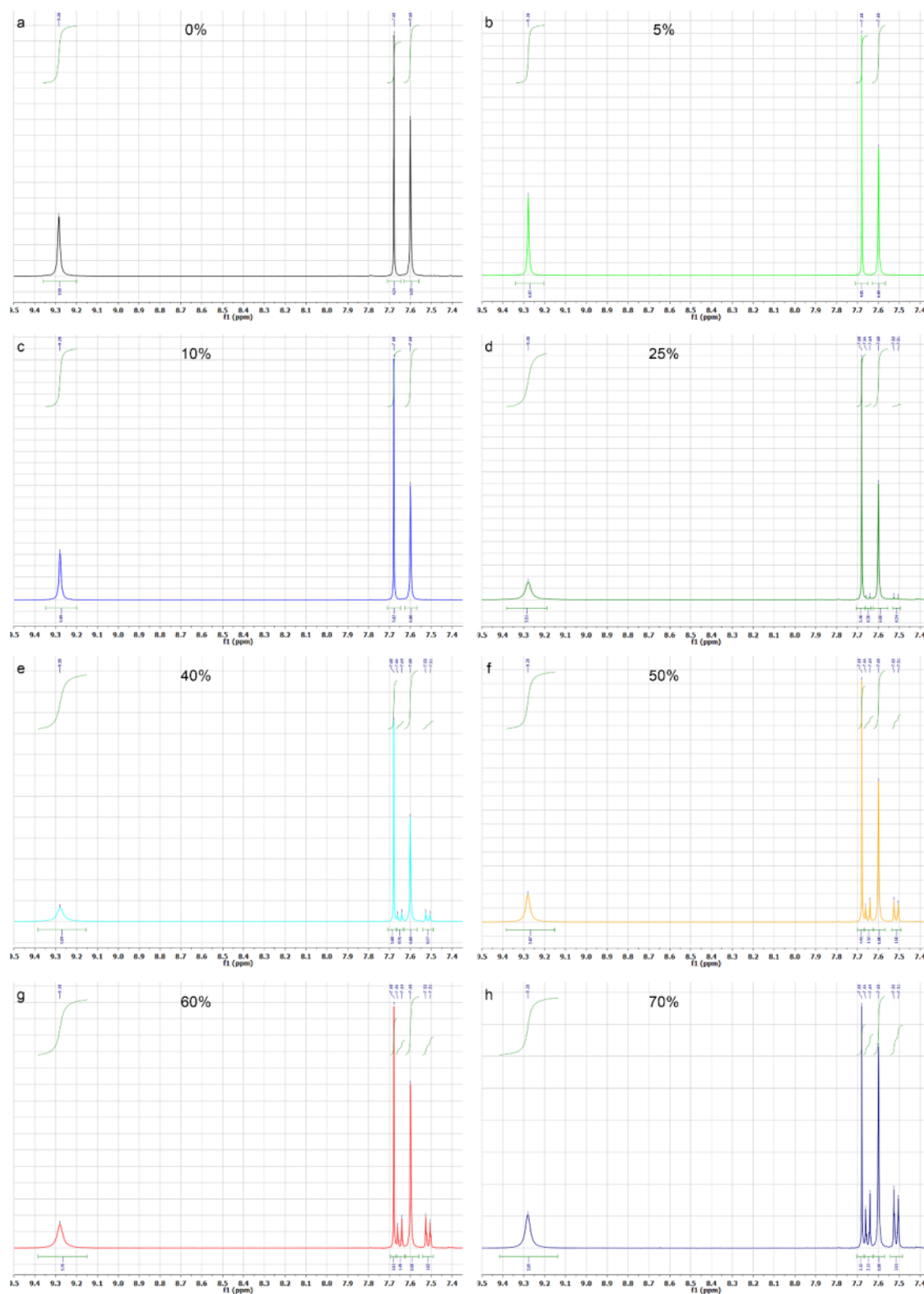


Figure 3.5. NMR spectra of COF-5-x (SH) grown with different modulator contents. The integrals were referenced to the signal at 7.6 ppm arising from the HHTP protons. As expected for fully hydrolyzed HHTP, the ratio between the aryl and the -OH protons at 9.28 ppm is constant at 1:1 in all samples. The ratio between the HHTP and BDBA protons, however, deviates considerably from the theoretical ratio depending on the modulator content in the reaction mixture. Only at a modulator content of 10 %, the ratio between the trigonal and the linear building blocks reaches the expected theoretical ratio, i.e. 2:3, corresponding to a 1:1 proton ratio.

3.4 Experimental

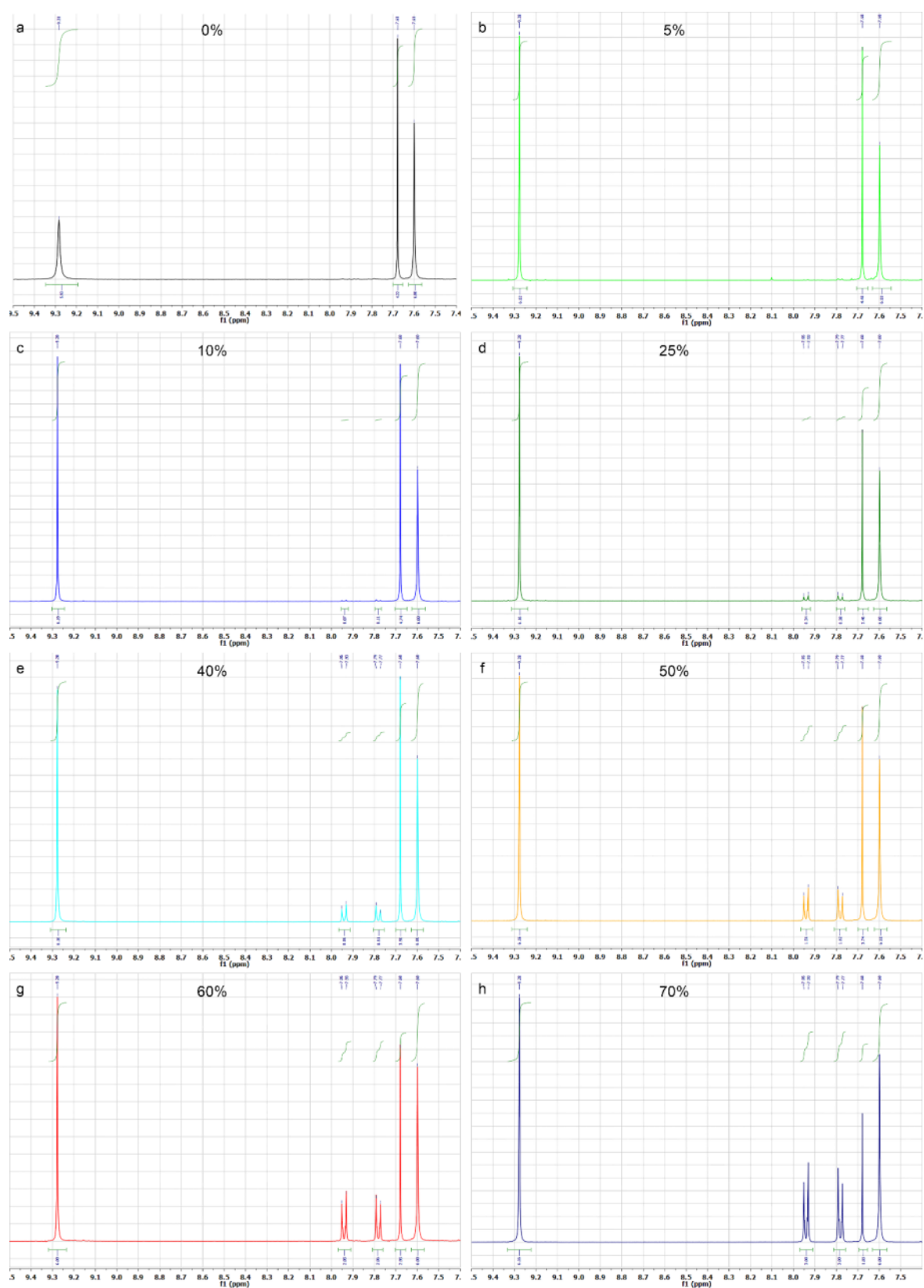


Figure 3.6. NMR spectra of COF-5-x (COOH) grown with different modulator contents. The integrals were referenced to the signal at 7.6 ppm arising from the HHTTP protons. Similar to the -SH modulated COF-5, the ratio between the HHTTP and BDBA protons deviates considerably from the theoretical ratio depending on the modulator content in the reaction mixture. At a modulator content of 5-10 %, the ratio between the trigonal and the linear building blocks is closest to the expected theoretical ratio, i.e. 2:3, corresponding to a 1:1 proton ratio.

3.4 Experimental

Simulation of the COF-5 Crystal Structures

Structure simulations were carried out using force-field methods with the Accelrys Materials Studio software package.

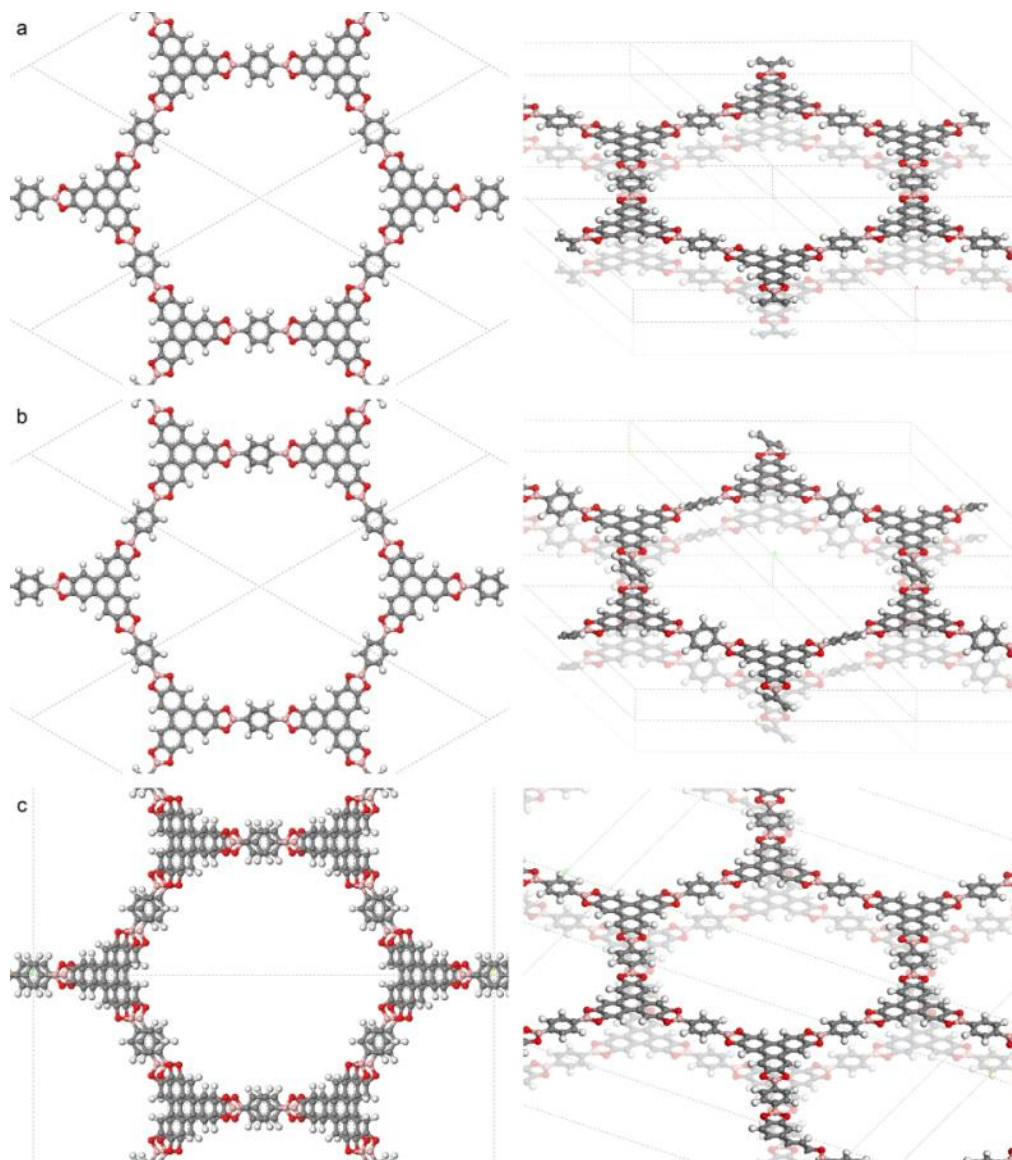


Figure 3.7. Simulation of the COF-5 structure assuming (a) P6/mmm, (b) P-3, and (c) Cmcm symmetry.

3.4 Experimental

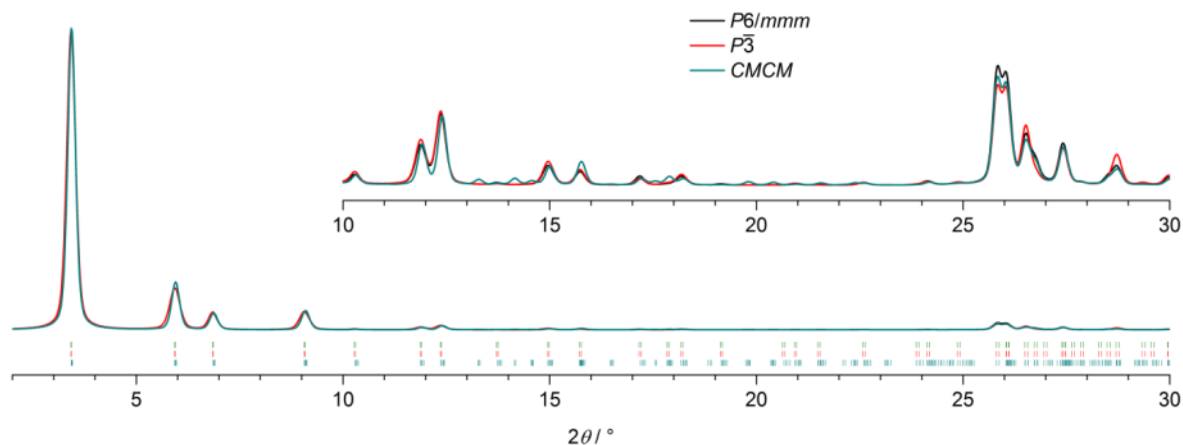


Figure 3.8. Simulated PXRD patterns (lines) and Bragg positions (symbols) using the structures displayed in Figure 2.7. Inset: Enlarged plot of the 10-30 ° 2θ range.

X-Ray Diffraction Analysis of Modulated COF-5-x

COF-5 Modulation with MPBA - COF-5-x (SH)

For XRD analysis in reflection mode a small amount of powder was flattened on top of a glass substrate. Domain sizes were estimated from the broadening of the *100* reflection using the Scherrer formula

$$FWHM(2\theta) = \frac{K \lambda}{L \cos(\theta)}$$

with $K = 0.9$ (assuming spherical particles), $\lambda = 0.15418$ nm, θ being the diffraction angle, and L being the domain size. The observed FWHM was corrected for the instrument broadening of 0.11° .

3.4 Experimental

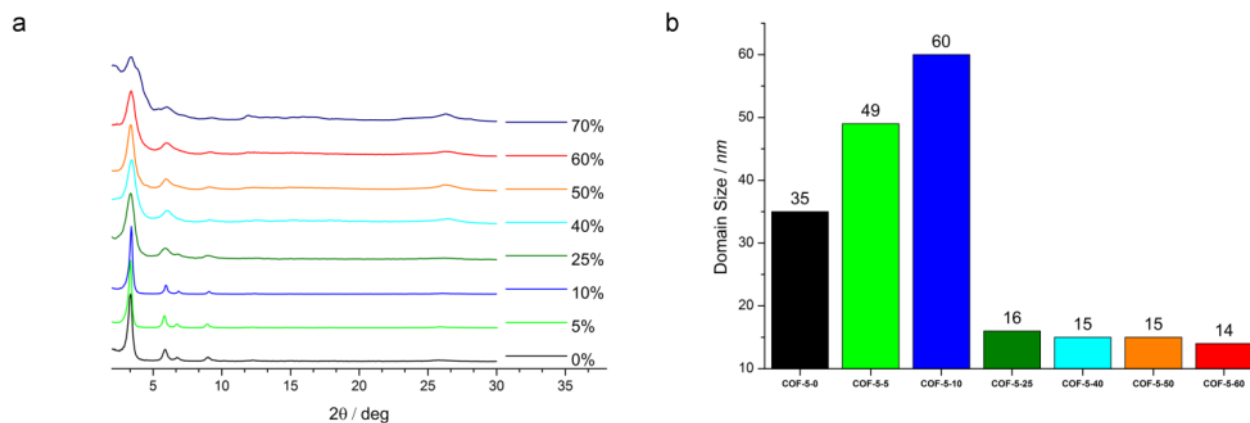


Figure 3.9. a) Comparison of XRD pattern of COF-5-x modulated by substituting BDBA with MPBA (with $x = 0, 5, 10, 25, 40, 50, 60$ and 70%). b) Calculated domain sizes of COF-5-x using the FWHM of the 100 reflection at $3.4^\circ 2\theta$.

COF-5 Modulation with CPBA - COF-5-x (COOH)

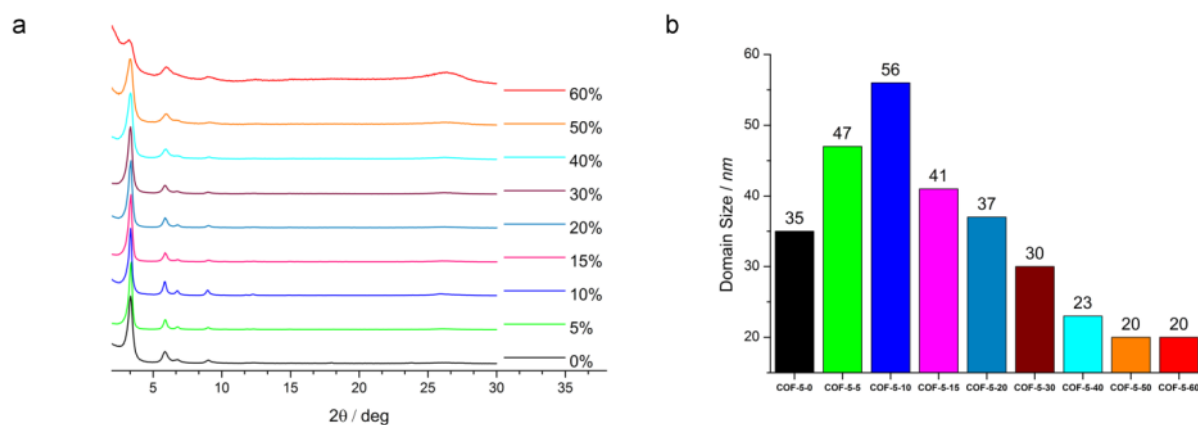


Figure 3.10. a) Comparison of XRD patterns of COF-5-x modulated by substituting BDBA with CPBA (with $x = 0, 5, 10, 15, 20, 30, 40, 50$ and 60%). b) Calculated domain sizes of COF-5-x using the FWHM of the 100 reflection at $3.4^\circ 2\theta$.

3.4 Experimental

Modulation synthesis of COF-5 by the addition of CPBA

In a different approach neither of the starting materials were substituted, but the modulating agent CPBA was added to the reaction mixture. Upon addition an increase in crystallinity and domain size could be observed. This technique was found to be less sensitive concerning the used modulator amount (compare to Figure 3.10).

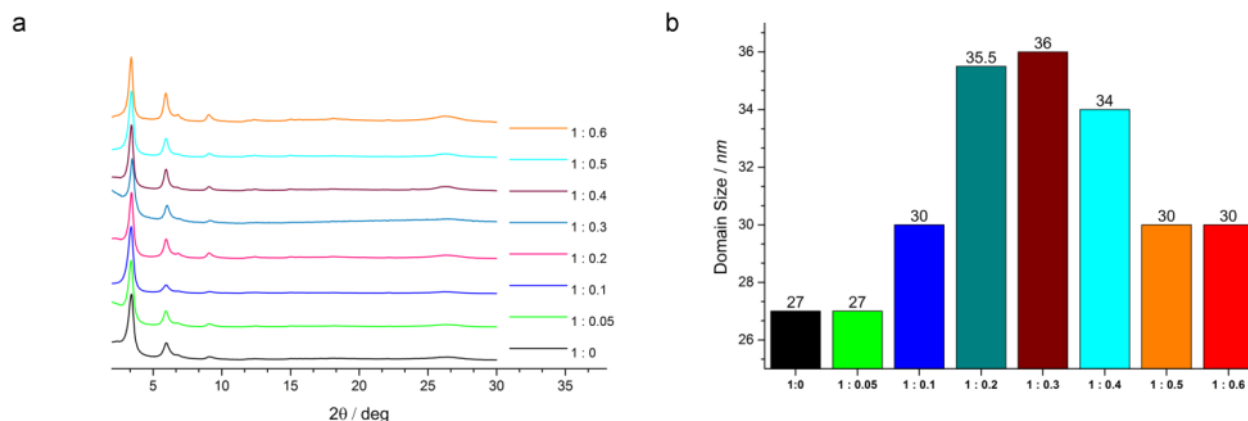


Figure 3.11. **a)** XRD pattern for COF-5 modulated by adding CPBA to the reaction mixture. BDBA to CPBA ratios were varied from 1:0 up to 1:0.6. **b)** Calculated domain sizes of COF-5-x using the FWHM of the 100 reflection at $3.4^\circ 2\theta$.

Growth kinetics

For studying the COF growth kinetics, the samples were prepared and handled as described in the synthesis section, except that the reactions were carried out by heating at 100°C in a conventional oven. This way, the reaction was sufficiently slow to be able to monitor the framework formation. In all cases, the final products after 96 h were comparable to the products from the microwave-assisted syntheses. All samples were measured with identical instrument and scan settings.

3.4 Experimental

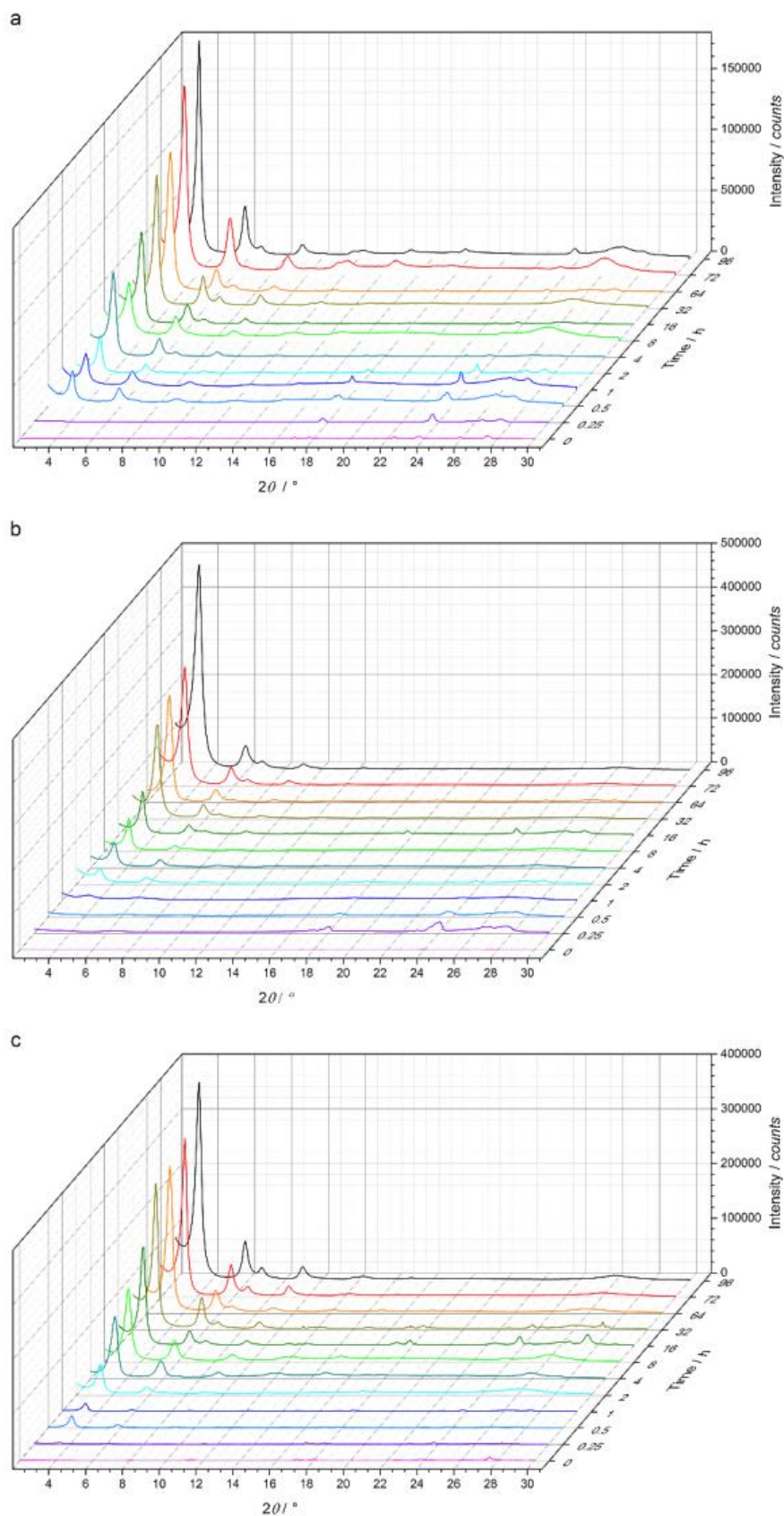


Figure 3.12. Time evolution of the COF formation. a) in absence of a modulator, b) with 10 % MPBA and c) 10 % CPBA. At identical scan settings, the peak intensities are more than doubled for the samples grown in the presence of a modulator.

Post-modification of COF-5-10

3.4 Experimental

Regardless of the modulating agent, COF-5-10 samples showed the highest crystallinity with the largest domain sizes. Therefore, these samples were used for post-modifications. COF-5-10 (SH) was treated with an IrCl_3 solution to promote the formation of Ir-S-clusters. The comparison of the PXRD data of the treated and untreated sample confirms that the crystallinity is retained (Figure 3.13a).

Furthermore, COOH functionalized COF-5-10 was post-modified by the attachment of an ATTO 633 dye. The PXRD pattern of COF-5-10-ATTO reveals the intact crystallinity of the framework (Figure 3.13b).

To a thiol-functionalized COF-5-10 sample maleimide-bearing polyethyleneglycol was added. The attachment of these PEG-groups was found to stabilize COF-5 toward EtOH. After dispersing COF-5-PEG (SH) in ethanol for 3 h the PXRD pattern confirms the completely maintained crystallinity of the framework (Figure 3.13c).

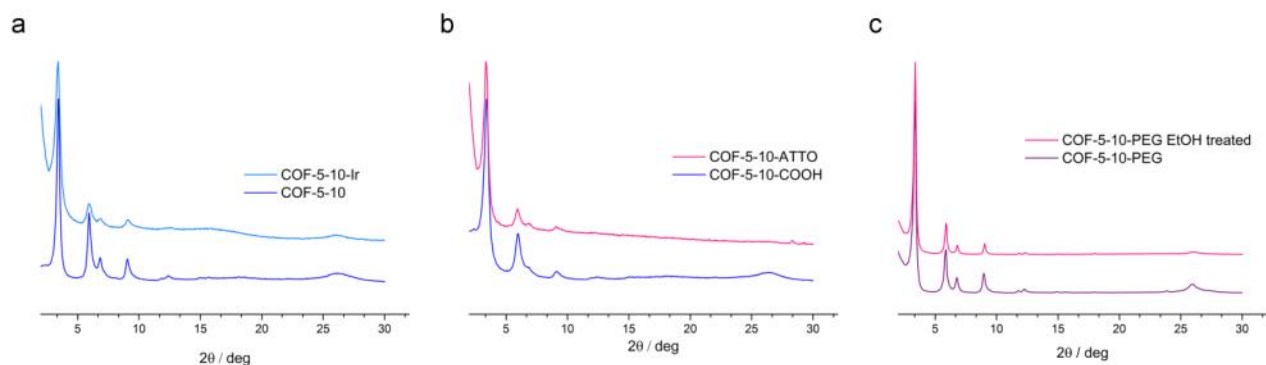


Figure 3.13. Comparison of COF-5-10 before and after post-modifications. a) COF-5-10 (SH) and COF-5-10-Ir showing the retained crystallinity of the framework after the addition of IrCl_3 . b) COF-5-10 (COOH) and ATTO 633 labeled COF-5-10 (COF-5-10-ATTO) and c) COF-5-10-PEG (SH) and COF-5-10-PEG (SH) after dispersing the sample in EtOH for 3 h.

3.4 Experimental

Pore Size Distribution Analysis

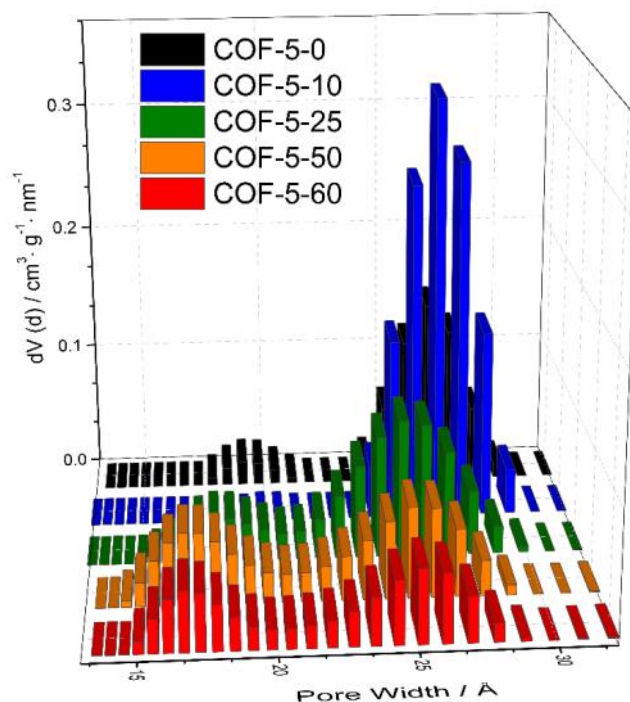


Figure 3.14. Bar chart of pore size distributions calculated for COF-5-x (SH) (with $x = 0, 10, 25, 50$ and 60) samples using a QSDFT equilibrium model with a carbon kernel for cylindrical pores. The pore size distribution for COF-5-10 shows the highest intensity with the narrowest distribution of all compared samples. The unmodulated sample as well as the COF-5-x samples with $x \geq 25$ feature additional pores of smaller diameter.

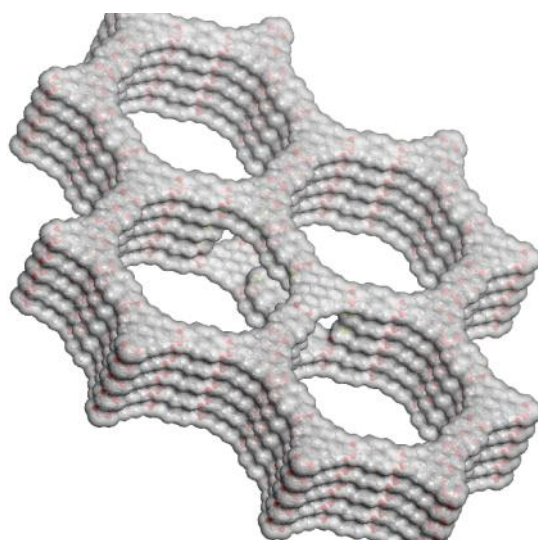


Figure 3.15. Illustration of the additional porosity arising from the incorporation of the modulator into the COF that is accompanied by HHTP voids.

IR spectroscopy

3.4 Experimental

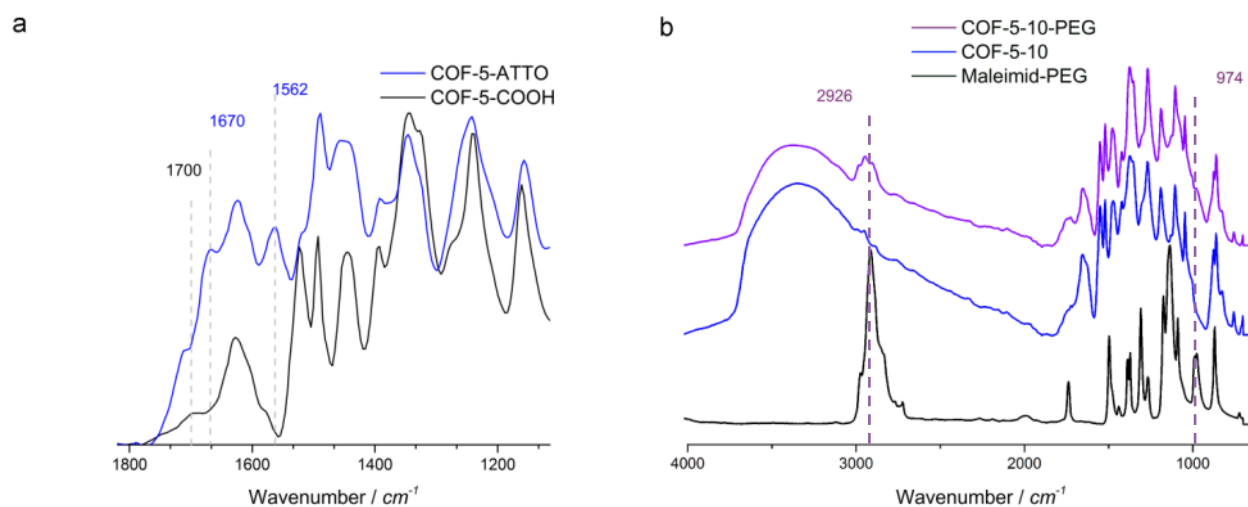


Figure 3.16. IR spectra of a) COF-5-10 (COOH) powder and ATTO 633 labeled COF-5-10 (COOH) (COF-5-ATTO) showing the characteristic signals of the C=O stretching vibration at 1700 cm^{-1} of the carboxylic acid, the amide I C=O stretching vibration at 1670 cm^{-1} and amide II N-H deformation vibration at 1562 cm^{-1} and b) COF-5-10 (SH) and COF-5-10-PEG (SH) in comparison with maleimide-PEG showing the typical CH-stretching vibrations of methyl groups at 2926 cm^{-1} and CH-vibration of polyenes at 974 cm^{-1} .

3.4 Experimental

Thermal gravimetric analysis (TGA)

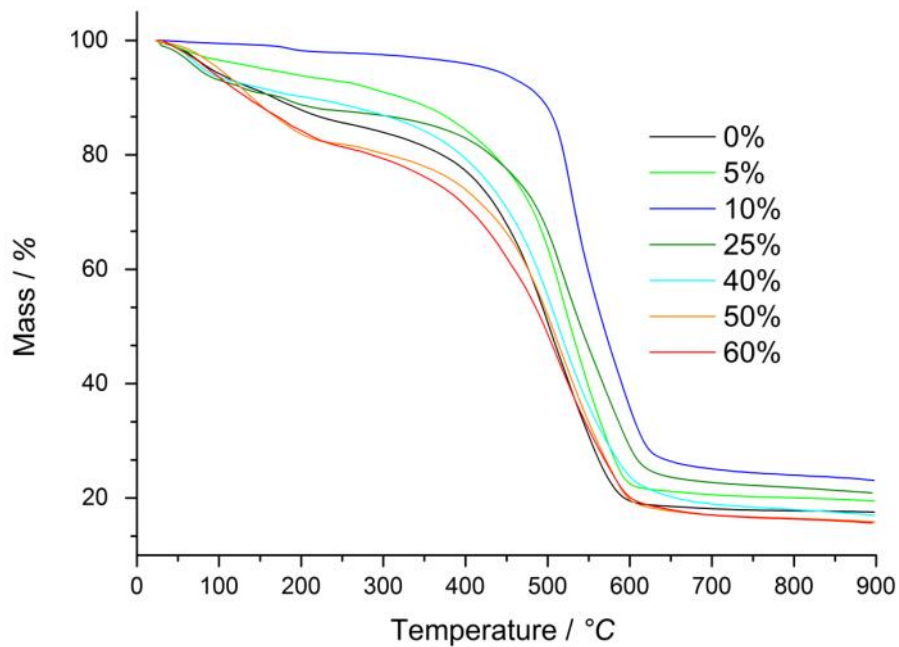


Figure 3.17. Comparison of different COF-5-x (SH) (with x = 0, 10, 25, 50 and 60) samples investigated by TGA. The most crystalline sample (COF-5-10) exhibits the best-defined step at 450-500 °C, indicating a very well-ordered framework without residual starting material or oligomers in the pores.

3.4 Experimental

UV-Vis Spectroscopy

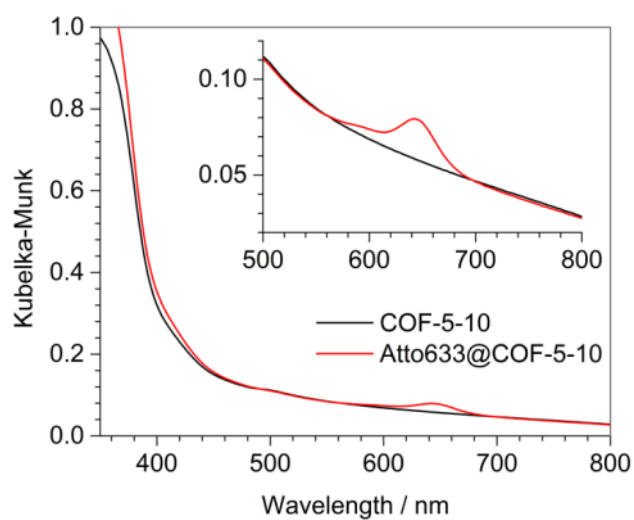


Figure 3.18. Diffuse reflectance spectra of -COOH-functionalized COF-5-10 (black) and the same sample after covalent attachment of the ATTO 633 dye (red). The inset shows a magnified cut-out of the spectrum, highlighting the characteristic absorption of the attached dye.

Fluorescence Spectroscopy

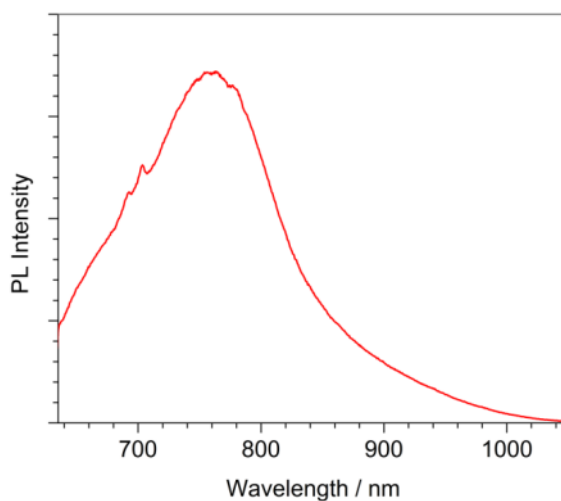


Figure 3.19. Photoluminescence spectrum of the ATTO 633-modified COF-5-10 (COOH) upon excitation with a 632.8 nm laser. The spectral features around 700 nm are artefacts from the setup.

3.4 Experimental

Transmission Electron Microscopy / STEM

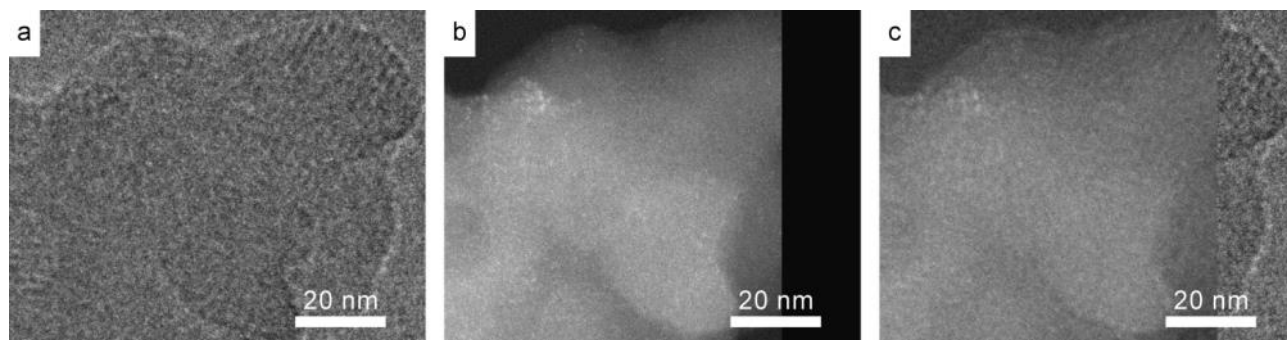


Figure 3.20. (a) TEM micrograph of COF-5-0 stained with iridium. (b) Corresponding scanning transmission electron microscopy (STEM) micrograph of the same sample position. (c) Overlay of TEM and STEM micrographs of COF-5 showing a random distribution of iridium within the COF-5 network.

3.5 References

1. A. P. Côte; A. I. Benin; N. W. Ockwig; M. O’Keeffe; A. J. Matzger; O. M. Yaghi, Porous, Crystalline, Covalent Organic Frameworks. *Science* **2005**, *310*, 1166-1170.
2. F. J. Uribe-Romo; J. R. Hunt; H. Furukawa; C. Klöck; M. O’Keeffe; O. M. Yaghi, A Crystalline Imine-Linked 3-D Porous Covalent Organic Framework. *J. Am. Chem. Soc.* **2009**, *131*, 4570-4571.
3. H. Furukawa; O. M. Yaghi, Storage of Hydrogen, Methane, and Carbon Dioxide in Highly Porous Covalent Organic Frameworks for Clean Energy Applications. *J. Am. Chem. Soc.* **2009**, *131*, 8875-8883.
4. C. J. Doonan; D. J. Tranchemontagne; T. G. Glover; J. R. Hunt; O. M. Yaghi, Exceptional ammonia uptake by a covalent organic framework. *Nat. Chem.* **2010**, *2* (3), 235-238.
5. H. Oh; S. B. Kalidindi; Y. Um; S. Bureekaew; R. Schmid; R. A. Fischer; M. Hirscher, A Cryogenically Flexible Covalent Organic Framework for Efficient Hydrogen Isotope Separation by Quantum Sieving. *Angew. Chem. Int. Ed.* **2013**, *52* (50), 13219-13222.
6. H. Ma; H. Ren; S. Meng; Z. Yan; H. Zhao; F. Sun; G. Zhu, A 3D microporous covalent organic framework with exceedingly high C₃H₈/CH₄ and C₂ hydrocarbon/CH₄ selectivity. *Chem. Commun.* **2013**, *49* (84), 9773-9775.
7. H. Xu; X. Chen; J. Gao; J. Lin; M. Addicoat; S. Irle; D. Jiang, Catalytic covalent organic frameworks via pore surface engineering. *Chem. Commun.* **2014**, *50* (11), 1292-1294.
8. S.-Y. Ding; J. Gao; Q. Wang; Y. Zhang; W.-G. Song; C.-Y. Su; W. Wang, Construction of Covalent Organic Framework for Catalysis: Pd/COF-LZU1 in Suzuki Miyaura Coupling Reaction. *J. Am. Chem. Soc.* **2011**, *133*, 19816-19822.
9. S. Chandra; T. Kundu; S. Kandambeth; R. BabaRao; Y. Marathe; S. M. Kunjir; R. Banerjee, Phosphoric Acid Loaded Azo (-N=N-) Based Covalent Organic Framework for Proton Conduction. *J. Am. Chem. Soc.* **2014**, *136*, 6570-6573.
10. C. R. DeBlase; K. E. Silberstein; T.-T. Truong; H. c. D. Abruña; W. R. Dichtel, β -Ketoenamine-Linked Covalent Organic Frameworks Capable of Pseudocapacitive Energy Storage. *J. Am. Chem. Soc.* **2013**, *135*, 16821-16824.
11. M. Dogru; M. Handloser; F. Auras; T. Kunz; D. Medina; A. Hartschuh; P. Knochel; T. Bein, A Photoconductive Thienothiophene-Based Covalent Organic Framework Showing Charge Transfer Towards Included Fullerene. *Angew. Chem. Int. Ed.* **2013**, *52*, 2920-2924.
12. M. Calik; F. Auras; L. M. Salonen; K. Bader; I. Grill; M. Handloser; D. D. Medina; M. Dogru; F. Löbermann; D. Trauner; A. Hartschuh; T. Bein, Extraction of Photogenerated Electrons and Holes from a Covalent Organic Framework Integrated Heterojunction. *J. Am. Chem. Soc.* **2014**, *136* (51), 17802-17807.
13. X. Feng; Y. Honsho; O. Saengsawang; L. Liu; L. Wang; A. Saeki; S. Irle; S. Seki; Y. Dong; D. Jiang, An Ambipolar Conducting Covalent Organic Framework with Self-Sorted and Periodic Electron Donor-Acceptor Ordering. *Adv. Mater.* **2012**, *24*, 3026-3031.
15. S. Jin; X. Ding; X. Feng; M. Supur; K. Furukawa; S. Takahashi; M. Addicoat; M. E. El-Khouly; T. Nakamura; S. Irle; S. Fukuzumi; A. Nagai; D. Jiang, Charge Dynamics in A Donor-Acceptor Covalent Organic Framework with Periodically Ordered Bicontinuous Heterojunctions. *Angew. Chem. Int. Ed.* **2013**, *52*, 2017-2021.
16. A. P. Côte; H. M. El-Kaderi; H. Furukawa; J. R. Hunt; O. M. Yaghi, Reticular Synthesis of Microporous and Mesoporous 2D Covalent Organic Frameworks. *J. Am. Chem. Soc.* **2007**, *129*, 12914-12915.

3.5 References

17. E. L. Spitler; W. R. Dichtel, Lewis acid-catalysed formation of two-dimensional phthalocyanine covalent organic frameworks. *Nat. Chem.* **2010**, *2*, 672-677.
18. X. Ding; J. Guo; X. Feng; Y. Honsho; J. Guo; S. Seki; P. Maitarad; A. Saeki; S. Nagase; D. Jiang, Synthesis of Metallophthalocyanine Covalent Organic Frameworks That Exhibit High Carrier Mobility and Photoconductivity. *Angew. Chem. Int. Ed.* **2011**, *50*, 1289-1293.
19. J. R. Hunt; C. J. Doonan; J. D. LeVangie; A. P. Côté; O. M. Yaghi, Reticular Synthesis of Covalent Organic Borosilicate Frameworks *J. Am. Chem. Soc.* **2008**, *130* (36), 11872-11873.
20. X. Chen; M. Addicoat; S. Irle; A. Nagai; D. Jiang, Control of Crystallinity and Porosity of Covalent Organic Frameworks by Managing Interlayer Interactions Based on Self-Complementary π -Electronic Force. *J. Am. Chem. Soc.* **2013**, *135*, 546-549.
21. Y.-B. Zhang; J. Su; H. Furukawa; Y. Yun; F. Gándara; A. Duong; X. Zou; O. M. Yaghi, Single-Crystal Structure of a Covalent Organic Framework. *J. Am. Chem. Soc.* **2013**, *135*, 16336-16339.
22. Q. Fang; Z. Zhuang; S. Gu; R. B. Kaspar; J. Zheng; J. Wang; S. Qiu; Y. Yan, Designed synthesis of large-pore crystalline polyimide covalent organic frameworks. *Nat. Comm.* **2014**, *5*.
23. Q. Fang; J. Wang; S. Gu; R. B. Kaspar; Z. Zhuang; J. Zheng; H. Guo; S. Qiu; Y. Yan, 3D Porous Crystalline Polyimide Covalent Organic Frameworks for Drug Delivery. *J. Am. Chem. Soc.* **2015**, *137* (26), 8352-8355.
24. F. J. Uribe-Romo; C. J. Doonan; H. Furukawa; K. Oisaki; O. M. Yaghi, Crystalline covalent organic frameworks with hydrazone linkages *J. Am. Chem. Soc.* **2011**, *133* (30), 11478-11481.
25. S. Dalapati; S. Jin; J. Gao; Y. Xu; A. Nagai; D. Jiang, An Azine-Linked Covalent Organic Framework. *J. Am. Chem. Soc.* **2013**, *135*, 17310-17313.
26. K. T. Jackson; T. E. Reich; H. M. El-Kaderi, Targeted synthesis of a porous borazine-linked covalent organic framework. *Chem. Comm.* **2012**, *48* (70), 8823-8825.
27. W. W. Yu; Y. A. Wang; X. Peng, Formation and Stability of Size-, Shape-, and Structure-Controlled CdTe Nanocrystals: Ligand Effects on Monomers and Nanocrystals. *Chem. Mater.* **2003**, *15* (22), 4300-4308.
28. D. V. Leff; P. C. Ohara; J. R. Heath; W. M. Gelbart, Thermodynamic Control of Gold Nanocrystal Size: Experiment and Theory. *J. Phys. Chem.* **1995**, *99* (18), 7036-7041.
29. A. R. Tao; S. Habas; P. Yang, Shape Control of Colloidal Metal Nanocrystals. *Small* **2008**, *4* (3), 310-325.
30. T. Uemura; S. Kitagawa, Nanocrystals of Coordination Polymers. *Chem. Lett.* **2005**, *34* (2), 132-137.
31. S. Diring; S. Furukawa; Y. Takashima; T. Tsuruoka; S. Kitagawa, Controlled Multiscale Synthesis of Porous Coordination Polymer in Nano/Micro Regimes. *Chem. Mater.* **2010**, *22* (16), 4531-4538.
32. T. Tsuruoka; S. Furukawa; Y. Takashima; K. Yoshida; S. Isoda; S. Kitagawa, Nanoporous Nanorods Fabricated by Coordination Modulation and Oriented Attachment Growth. *Angew. Chem. Int. Ed.* **2009**, *48* (26), 4739-4743.
33. A. Schaate; P. Roy; A. Godt; J. Lippke; F. Waltz; M. Wiebcke; P. Behrens, Modulated Synthesis of Zr-Based Metal-Organic Frameworks: From Nano to Single Crystals. *Chem. Eur. J.* **2011**, *17* (24), 6643-6651.
34. E. Biemmi; A. Darga; N. Stock; T. Bein, Direct growth of $\text{Cu}_3(\text{BTC})_2(\text{H}_2\text{O})_3 \cdot x\text{H}_2\text{O}$ thin films on modified QCM-gold electrodes – Water sorption isotherms. *Microporous Mesoporous Mater.* **2008**, *114* (1-3), 380-386.
35. D. N. Bunck; W. R. Dichtel, Internal Functionalization of Three-Dimensional Covalent Organic Frameworks. *Angew. Chem. Int. Ed.* **2012**, *51*, 1885-1889.

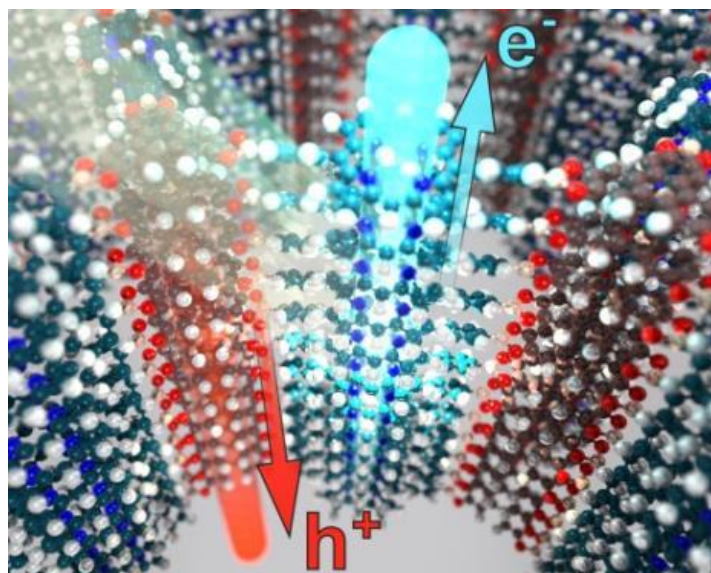
3.5 References

36. D. N. Bunck; W. R. Dichtel, Postsynthetic functionalization of 3D covalent organic frameworks. *Chem. Commun.* **2013**, 49, 2457-2459.
37. S. D. Brucks; D. N. Bunck; W. R. Dichtel, Functionalization of 3D covalent organic frameworks using monofunctional boronic acids. *Polymer* **2014**, 55 (1), 330-334.
38. B. J. Smith; W. R. Dichtel, Mechanistic Studies of Two-Dimensional Covalent Organic Frameworks Rapidly Polymerized from Initially Homogenous Conditions. *J. Am. Chem. Soc.* **2014**, 136, 8783-8789.
39. B. J. Smith; N. Hwang; A. D. Chavez; J. L. Novotney; W. R. Dichtel, Growth rates and water stability of 2D boronate ester covalent organic frameworks. *Chem. Commun.* **2015**, 51, 7532-7535.
40. J. W. Colson; J. A. Mann; C. R. DeBlase; W. R. Dichtel, Patterned Growth of Oriented 2D Covalent Organic Framework Thin Films on Single-Layer Graphene. *J. Polym. Sci. Part A* **2015**, 53, 378-384.
41. K. S. W. Sing; D. H. Everett; R. A. W. Haul; L. Moscou; R. A. Pierotti; J. Rouquérol; T. Siemieniowska, Reporting physisorption data for gassolid systems with special reference to the determination of surface area and porosity (Recommendations 1984). *Pure Appl. Chem.* **1985**, 57 (4), 603-619.
42. M. Thommes; B. Smarsly; M. Groenewolt; P. I. Ravikovitch; A. V. Neimark, Adsorption Hysteresis of Nitrogen and Argon in Pore Networks and Characterization of Novel Micro- and Mesoporous Silicas. *Langmuir* **2006**, 22 (2), 756-764.
43. M. Thommes; K. Cychoz, Physical adsorption characterization of nanoporous materials: progress and challenges. *Adsorption* **2014**, 20 (2-3), 233-250.
44. D. E. Jesson; S. J. Pennycook, Incoherent Imaging of Crystals Using Thermally Scattered Electrons. *Proc. R. Soc. London, Ser. A* **1995**, 449 (1936), 273-293.
45. ATTO 633. http://www.atto-tec.com/fileadmin/user_upload/Katalog_Flyer_Support/ATTO_633.pdf.
46. B. H. Northrop; S. H. Frayne; U. Choudhary, Thiol-maleimide "click" chemistry: evaluating the influence of solvent, initiator, and thiol on the reaction mechanism, kinetics, and selectivity. *Polym. Chem.* **2015**, 6 (18), 3415-3430.

4. Extraction of Photogenerated Electrons and Holes from a COF Integrated Heterojunction

This chapter is based on the following publication:

Calik, M.; Auras, F.; Salonen, L. M.; Bader, K.; Grill, I.; Handloser, M.; Medina, D. D.; Dogru, M.; Löbermann, F.; Trauner, D.; Hartschuh, A.; Bein, T. *J. Am. Chem. Soc.* **2014**, *136*, 17802.



Abstract

Covalent organic frameworks (COFs) offer a strategy to position molecular semiconductors within a rigid network in a highly controlled and predictable manner. The π -stacked columns of layered two-dimensional COFs enable electronic interactions between the COF sheets, thereby providing a path for exciton and charge carrier migration. Frameworks comprising two electronically separated subunits can form highly defined interdigitated donor–acceptor heterojunctions, which can drive the

4.1 Introduction

photogeneration of free charge carriers. Here we report the first example of a photovoltaic device that utilizes exclusively a crystalline organic framework with an inherent type II heterojunction as the active layer. The newly developed triphenylene–porphyrin COF was grown as an oriented thin film with the donor and acceptor units forming one-dimensional stacks that extend along the substrate normal, thus providing an optimal geometry for charge carrier transport. As a result of the degree of morphological precision that can be achieved with COFs and the enormous diversity of functional molecular building blocks that can be used to construct the frameworks, these materials show great potential as model systems for organic heterojunctions and might ultimately provide an alternative to the current disordered bulk heterojunctions.

4.1 Introduction

Organic polymer- and small molecule-based solar cells have reached impressive power conversion efficiencies during the past years.¹⁻⁴ While much of the progress is stimulated by the development of new donor materials, the precise design of their nanoscale morphology within photoactive blends remains a major challenge.⁵⁻⁸ Efficient bulk heterojunction devices require the formation of a bicontinuous network of the donor and acceptor phases with appropriate length scales for charge generation, along with favorable molecular packing and long-range order for efficient charge carrier transport.⁹⁻¹¹ It is, however, extremely difficult to predict and control the packing of functionalized conjugated molecules upon spinodal decomposition of a blend solution, as even minor chemical modifications can induce significant changes in the molecular arrangement. Therefore, the generation of an atomically defined interpenetrated three-dimensional (3D) heterojunction via a deterministic bottom-up approach would be a major breakthrough.

Covalent organic frameworks (COFs) are an emerging class of materials featuring

4.1 Introduction

molecular building blocks that are organized into 2D or 3D porous crystalline structures through covalent bonds.¹²⁻¹⁵ Specifically, the π -stacked aromatic subunits of 2D COFs enable electronic interactions between the COF layers and thus provide a path for exciton and charge carrier transport.¹⁶⁻²⁰ The rigid COF network provides mechanical and thermal stability, while its optoelectronic properties can be tailored to a specific application via the selection of appropriate building blocks.²¹⁻²⁵ Recently, COFs comprising alternating π -stacked columns of two electroactive building blocks have been reported.²⁶⁻²⁷ If the energy levels of these subunits are aligned adequately, an atomically ordered, interdigitated donor–acceptor heterojunction can be formed. Similar to a polymer–fullerene heterojunction, such a material would be expected to promote charge carrier separation upon photoexcitation, thereby presenting an alternative to the present solution-cast disordered photoactive layers. While the photogeneration of charge carriers inside donor–acceptor COFs has been observed in pump–probe experiments,²⁸ the utilization of this effect in a photovoltaic device has remained elusive to date. Recently, two examples of COF-containing photovoltaic devices have been reported by our group²⁹ and others.³⁰ The COFs investigated in those reports, however, did not provide the photoactive junction within their framework but rather served as donor materials when combined with fullerene derivatives as acceptors.

Herein we present for the first time a photovoltaic device that utilizes a vertically oriented thin film of a novel triphenylene–porphyrin (TP-Por) COF as a photoactive donor–acceptor junction. We show that the charge carrier collection yield can be further enhanced under reverse bias, enabling a peak external quantum efficiency of above 30 %.

4.2 Results and Discussion

The new 2D TP-Por COF was formed under solvothermal conditions via co-condensation of 5,15-bis(4-boronophenyl)porphyrin (**1**) and 2,3,6,7,10,11-hexahydroxytriphenylene (HHTP) in a 7:3 mixture of acetonitrile and mesitylene (**Figure 4.1a**, for experimental data see the Supporting Information, SI). The TP-Por COF is a porous hexagonal framework with the trigonal triphenylene units at the corners and the linear porphyrins located at the edges (**Figure 4.1b**).

Powder X-ray diffraction (PXRD) confirms the formation of a periodic structure (Figure 4.2a). The experimental pattern agrees well with the simulated one for an eclipsed (AA stacking) arrangement with $P3$ symmetry (Figure 4.2b), whereas a hypothetical staggered (AB) layer arrangement cannot reproduce the experimental data (Figure 4.2c and Experimental, Figure 4.5). Theoretical calculations carried out for other hexagonal COFs reveal that a slight offset of about 0.1 nm between adjacent layers is energetically favorable.³¹ Due to the non-planar geometry of the porphyrin building block resulting from the large dihedral angle between the porphyrin core and the aryl substituent,³² a similar or even more pronounced offset for the corresponding COF is anticipated. For the large-pore TP-Por COF, however, such deviations from a truly eclipsed structure would be sufficiently small (relative to the lattice parameters) to give rise to a nearly identical experimental PXRD pattern. Consequently, experimental PXRD data cannot provide enough evidence for the actual layer offset. crystal planes. The broad reflection at $2\theta = 24^\circ$ corresponds to the (001) planes, indicating an interlayer distance of 0.38 ± 0.02 nm. The larger interlayer distance of the 2D sheets compared with the

4.2 Results and Discussion

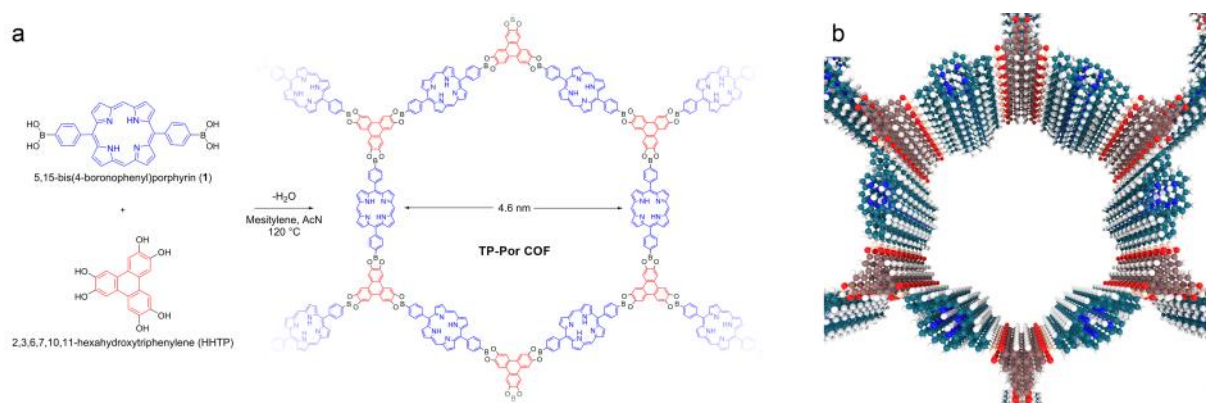


Figure 4.1. (a) Co-condensation of bis(boronophenyl)porphyrin 1 and HHTP leading to the formation of the layered TP-Por COF. The COF features hexagonal pores with a large diameter of 4.6 nm. (b) Illustration of the TP-Por COF highlighting the alternating columns of triphenylene (red) and porphyrin (blue) subunits.

typically observed packing distance of about 0.35 nm¹² can be rationalized as a result of the non-planarity of the porphyrin subunit. Transmission electron microscopy (TEM) images of TP-Por COF powder samples reveal the nanoscale morphology of the framework with crystalline domains of about 50 nm (Figure 4.2d). Straight porous channels that extend through entire crystal domains are visible for a number of crystallites in the lower part of the TEM image. The hexagonal pore arrangement is evident from domains that are oriented along the crystallographic *c*-axis. We observe a pore-to-pore distance of 5.0±0.3 nm, which is in good agreement with the *d*-spacing obtained from the PXRD measurements.

Nitrogen sorption experiments on TP-Por COF bulk material performed at 77 K yielded isotherms with a typical type IV shape, which is characteristic of mesoporous materials (Figure 4.2e). The sorption isotherm exhibits a sharp step from $P/P_0 = 0.42$ to 0.47, indicating a narrow pore size distribution. This was also confirmed by quenched-solid density functional theory (QSDFT) calculations, which showed an average pore diameter of 4.6 nm (Figure 4.2f). The calculated Brunauer–Emmett–Teller (BET) surface area is

4.2 Results and Discussion

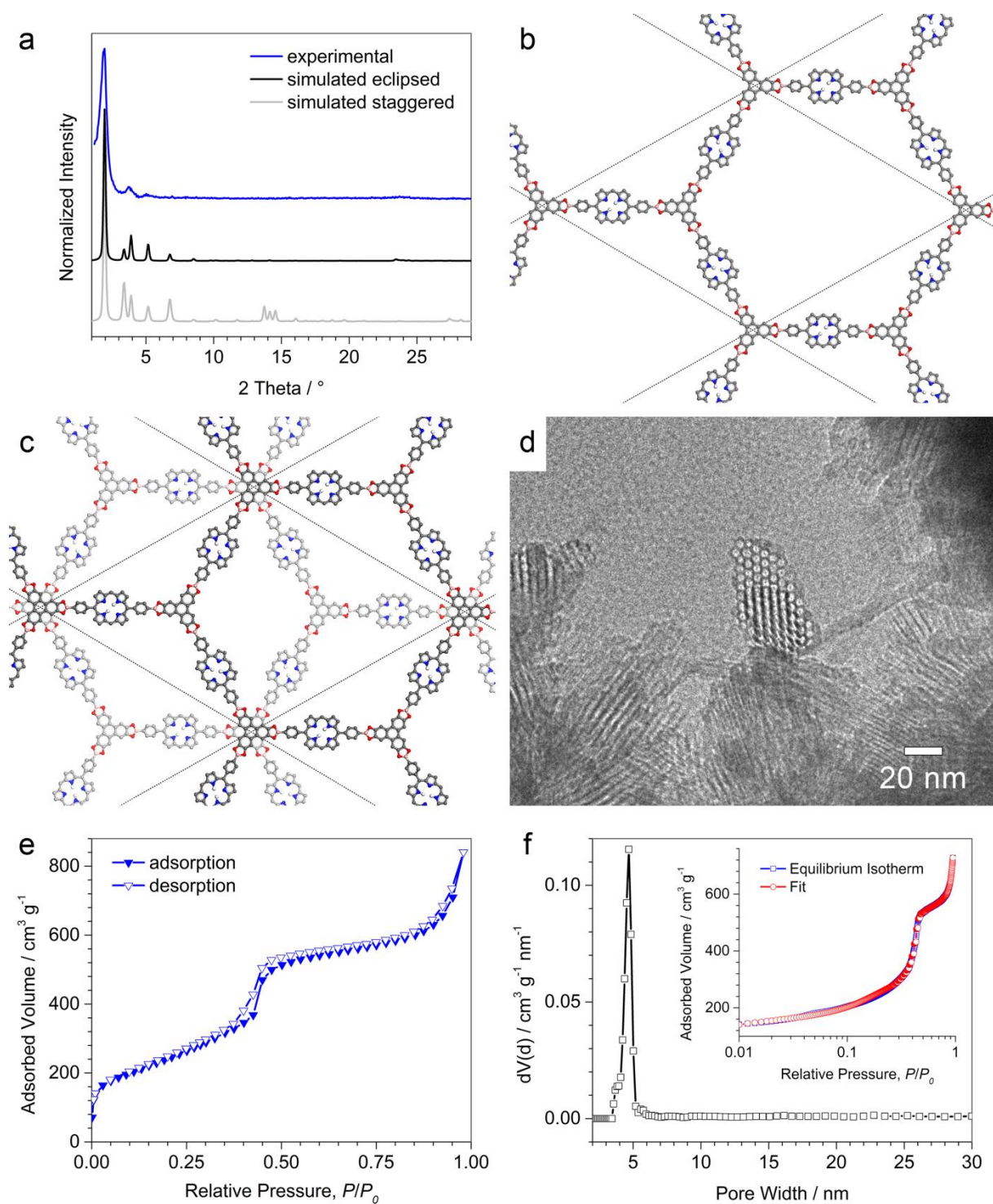


Figure 4.2. (a) Experimental PXRD data (blue) vs simulated patterns (black and gray) for (b) eclipsed and (c) staggered arrangements of the 2D layers. The theoretical patterns were simulated for a crystallite size of 50 nm. (d) Transmission electron micrograph of TP-Por COF bulk material showing the hexagonal pore structure (middle) and straight porous channels (bottom). (e) Nitrogen sorption isotherm of a TP-Por COF powder sample measured at 77 K. (f) Corresponding pore size distribution with an average pore size of 4.6 nm obtained by fitting the experimental data.

4.2 Results and Discussion

The experimental PXRD pattern of the TP-Por COF exhibits an intense reflection at $2\theta = 1.9^\circ$, corresponding to a d spacing of 4.6 ± 0.1 nm that can be assigned to the (100) set of

In order to study the optical properties of the TP-Por COF, thin films were grown on fused silica substrates covered with a 10 nm layer of vacuum-deposited MoO_x . The COF layer was synthesized by immersing the substrates face down into a dilute reaction solution under otherwise identical reaction conditions.³³

The TP-Por COF film exhibits a broad optical absorption covering the entire visible range up to 680 nm with distinct absorption bands that can be ascribed to the triphenylene unit (279 nm) and the porphyrin Soret band (425 nm) and Q-bands (510–640 nm) (Figure 4.3a). Compared with the spectrum of a 2:3 mixture of the reactants, the absorption spectrum of the COF lacks the features of the porphyrin diboronic acid at 300 and 350 nm (Experimental, Figure 4.9). At longer wavelengths the spectra are nearly identical, indicating similar packing schemes in the COF and in spin-coated films of its building blocks. Upon excitation at 405 nm, both the COF and the porphyrin precursor exhibit a bright red-to-infrared photoluminescence (PL) with two sharp main emission bands at 643 and 701 nm. Depending on the molecular packing arrangement, porphyrins are known to possess different allowed and forbidden optical transitions. Red-shifting of the Soret and Q bands compared with those of highly dilute precursor solutions and the existence of sharp PL bands generally indicate the formation of J-aggregates.³⁴⁻³⁵ This can be explained by the large aryl substituent–porphyrin core dihedral angle, which hinders the formation of cofacial aggregates. Moreover, the tilted phenyl groups could even facilitate the formation of regular aggregates featuring a small offset between consecutive layers.

4.2 Results and Discussion

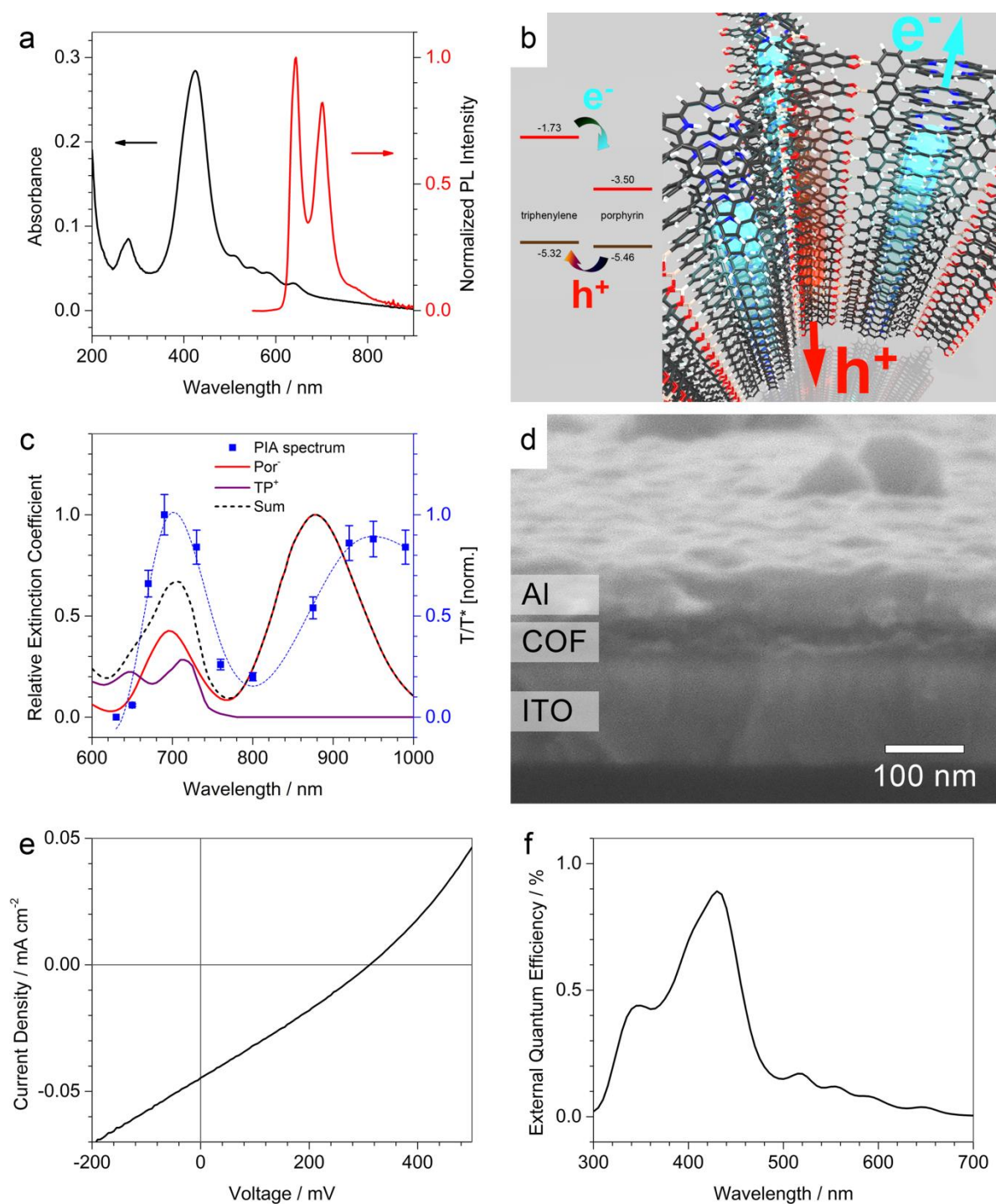


Figure 4.3. (a) Transmission absorption (black) and normalized PL ($\lambda_{exc} = 405\text{ nm}$, red) spectra of a TP-Por COF thin film. (b) Frontier orbital energies of the two COF subunits measured by DPV in solution and a schematic illustration of the photoinduced charge transfer. (c) PIA spectrum of the TP-Por COF film after excitation at 470 nm (blue squares; the blue line serves as a guide to the eye) together with the radical ion absorption spectra of Por^- (red) and TP^+ (purple) and their sum (black) assuming a 1:1 ratio of the two species. After photoexcitation, the TP-Por COF film shows two absorption bands in the range of the free radical ion absorption, indicating electron transfer from the donor to the acceptor moiety within the network (see the text). (d) Cross-sectional scanning electron micrograph of a TP-Por COF-based photovoltaic device showing the COF layer between the ITO and Al electrodes. The MoOx and ZnO contact layers are too thin to be visible in the micrograph. The current-voltage curve (e) and EQE spectrum (f) confirm the successful integration of the donor-acceptor COF as the active layer of the photovoltaic device.

4.2 Results and Discussion

Boronate ester-linked COFs typically comprise two electronically different subunits that are arranged into 1D π -stacked columns. If the building blocks are selected in such a way that the HOMO and LUMO energy levels of one component are higher than the respective energy levels of the other component, the COF will form an interdigitated donor–acceptor structure. Similar to polymer–fullerene bulk heterojunctions, an adequately designed COF would be expected to promote charge separation upon photoexcitation of either of its components (Figure 4.3b). Indeed, the formation of photogenerated charge carriers has been observed on the short time scale of pump–probe experiments in some porphyrin- and phthalocyanine-containing COFs.^{28, 36} However, the yield of free charge carriers was typically low and successful extraction of photogenerated charge carriers from a COF layer has not been demonstrated to date.

Electrochemical methods are widely used tools for analyzing the oxidation and reduction potentials of electroactive species. We employed differential pulse voltammetry (DPV) to determine the positions of the highest occupied molecular orbitals (HOMOs) position of the precursors relative to ferrocene as an internal standard (Experimental, Figure 4.10). Assuming $E(\text{Fc}/\text{Fc}^+) = -4.80$ eV vs. vacuum level³⁷ and calculating the corresponding lowest unoccupied molecular orbital (LUMO) energies as the sum of HOMO energy and the optical band gap, as determined by UV-Vis spectroscopy, we obtain $E_{\text{HOMO}}(\text{TP}) = -5.28$ eV, $E_{\text{LUMO}}(\text{TP}) = -1.69$ eV, $E_{\text{HOMO}}(\text{Por}) = -5.42$ eV, and $E_{\text{LUMO}}(\text{Por}) = -3.46$ eV (Figure 4.3b). Although these data have been obtained from measurements in solution and the absolute values are expected to shift by a few tens of meV upon crystallization of the COF, we expect the type II alignment of the energy levels relative to each other to remain similar. On the basis of these results we expect the TP-Por COF to facilitate photoinduced charge transfer, resulting in the formation of Por^- and TP^+ radical ions that can be traced via photoinduced absorption

4.2 Results and Discussion

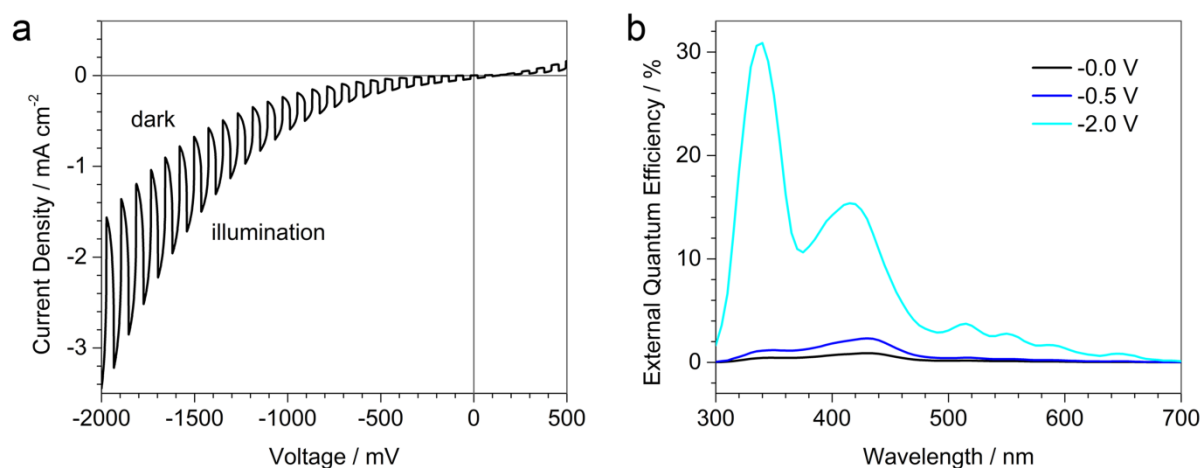


Figure 4.4. (a) Current density–voltage curves for the photovoltaic device under chopped white-light illumination. (b) Bias-dependent EQE spectra illustrating the greatly enhanced charge collection efficiency under reverse-bias conditions.

spectroscopy (PIA). Indeed, the PIA spectrum of a TP-Por COF thin film exhibits two characteristic absorption bands centered at 700 and 960 nm (Figure 4.3c). These signals are very similar to the sum of the absorption spectra of the free radical ions of the electron acceptor (Por⁻)³⁸ and donor (TP⁺)³⁹, indicating efficient electron transfer within the framework. Deviations of our experimental spectrum from those in the literature might stem from the different environment of the radical ion species inside the COF.

Growing the COF as a vertically oriented thin film on a suitable electrode and applying an electronically different top contact should enable us to extract photogenerated charge carriers (Experimental, Figure 4.6 and Figure 4.7). Thus, we constructed a photovoltaic device with the TP-Por COF as the active layer, sandwiched between indium tin oxide (ITO)/MoO_x and ZnO/Al electrodes. Vacuum-deposited, slightly sub-stoichiometric molybdenum trioxide is commonly used as a hole extraction layer in high-efficiency organic solar cells.⁴⁰ Its high work function provides excellent coupling to the HOMO of common donor materials, whereas electron transfer from the LUMO of the acceptor phase is blocked. Zinc oxide has found wide application in organic

4.2 Results and Discussion

photovoltaics as an electron-selective contact because of its low work function and good conductivity.⁴ For the photovoltaic device, the ~50 nm thick TP-Por COF layer was grown (as described above) on patterned ITO substrates coated with a 10 nm MoO_x layer. Subsequently, a 20 nm thick ZnO layer was deposited by spincoating a solution of pre-synthesized ZnO nanoparticles. The COF film remained unchanged upon the addition of the ZnO layer, as confirmed by UV-Vis spectroscopy (Experimental, Figure 4.11). The devices were completed by thermal evaporation of 70 nm Al electrodes (Figure 4.3d).

When illuminating the device with simulated solar light we measured an open-circuit voltage of 312 mV and a short-circuit current density of 44.6 $\mu\text{A cm}^{-2}$ (Figure 4.3e). To the best of our knowledge, this is the first report of a photovoltaic device utilizing the inherent donor–acceptor structure of a COF for photocurrent generation. The importance of the structural precision given by the unique COF geometry is evidenced by a comparison of this device with a reference device based on a randomly intermixed blend of the two building blocks (Experimental, Figure 4.13). At similar thickness and optical absorption of the active layer, the COF-based device is capable of producing a more than 30 times higher short-circuit current and exhibits an about doubled open-circuit voltage.

In order to further characterize the device, we measured the external quantum efficiency (EQE) under short-circuit conditions (Figure 4.3f). The EQE spectrum is in excellent agreement with the absorption spectrum of the COF layer, which further confirms the TP-Por COF to be the origin of the observed photoresponse. When the EQE spectrum is plotted on a logarithmic scale, we observe a distinct feature at around 1.55 eV (Experimental, Figure 4.12). Such sub-bandgap features are commonly observed in organic bulk–heterojunction solar cells and are ascribed to direct photoexcitation of

4.3 Conclusion

the charge-transfer state. Compared to common polymer–fullerene mixtures this feature is remarkably sharp, which could be an indication of a more defined charge–transfer state in our morphologically well-defined COF compared with the disordered nature of bulk heterojunctions that are formed through spinodal decomposition.

Although the photocurrent at 0 V bias is promising, the external quantum efficiency is below 1 %, indicating the presence of strong loss mechanisms. Sweep-out times of mobile charge carriers as well as the generation of free charge carriers from bound polaron pairs can be greatly enhanced upon application of an electric field having the same direction as the built-in field. Indeed, we observed a dramatically enhanced photocurrent (i.e., the difference between the current under illumination and the dark current) under strong reverse bias. This effect is illustrated by the data in Figure 4.4a, which we obtained by using chopped simulated solar illumination to continuously switch between the dark and illuminated current density–voltage curves. At $V_{\text{appl}} = -2 \text{ V}$ we observe a difference of about 2 mA cm^{-2} when the light is switched on, which is orders of magnitude higher than the previously reported photoconductivity values for other COFs.^{19, 36} The EQE under reverse bias can be boosted to more than 30 % at 350 nm and well above 10 % up to 450 nm, which renders this COF-based device concept a promising alternative to small molecule/fullerene–containing devices.

4.3 Conclusion

We have developed a new porphyrin- and triphenylene containing COF featuring ordered columns of donor and acceptor moieties within its framework. The inherent interdigitated heterojunction of this COF was found to promote charge separation upon photoexcitation of either building block. We applied oriented films of this COF in the

4.4 Experimental

construction of the first photovoltaic device in which the COF itself provides the photoactive junction. The structural precision of COF-based heterojunctions presents an opportunity to study charge carrier generation and extraction in well-defined model systems. Quantum efficiency measurements in the presence of an external collection field show the potential of this novel device concept, provided that recombination losses can be minimized. Enhancement of the carrier collection yield that might ultimately lead to competitive device efficiencies is expected from further improvements in the electron and hole transport properties of these materials, a goal we are currently pursuing.

4.4 Experimental

Materials and methods

Unless stated otherwise, all reactions were performed in oven-dried glassware under a positive pressure of Ar. Commercial reagents and solvents were used as received with the exception of pyrrole, which was distilled prior to use using a rotary evaporator. Reactions were stirred magnetically and monitored by NMR spectroscopy or analytical thin-layer chromatography (TLC) using E. Merck 0.25 mm silica gel 60 F254 pre-coated glass plates. TLC plates were visualized by exposure to ultraviolet light (254 nm). Flash column chromatography was performed employing silica gel (60 Å, 40–63 µm, Merck).

Nuclear magnetic resonance (NMR) spectra were recorded on Varian VNMRS 300, VNMRS 400, INOVA 400 or VNMRS 600 spectrometers. Proton chemical shifts are expressed in parts per million (δ scale) and are calibrated using residual undeuterated solvent peak as an internal reference (CDCl_3 : δ 7.26; $\text{THF-}d_8$: δ 1.72, 3.58). Data for ^1H NMR spectra are reported as follows: chemical shift (δ ppm) (multiplicity, coupling constant/Hz, integration). Multiplicities are reported as follows: s = singlet, d = doublet, t

4.4 Experimental

= triplet, q = quartet, m = multiplet, br = broad, or combinations thereof. Carbon chemical shifts are expressed in ppm (δ scale) and are referenced to the carbon resonances of the solvent (CDCl₃: δ 77.16; THF-*d*₈: δ 67.21, 25.31).

Infrared (IR) spectra were recorded on a Perkin Elmer Spectrum BX II FT-IR system and a Thermo Scientific Nicolet™ 6700 FT-IR spectrometer in transmission mode. IR data is reported in frequency of absorption (cm⁻¹).

Mass spectrometry (MS) experiments were performed on a Thermo Finnigan MAT 95 (EI) or on a Thermo Finnigan LTQ FT (ESI) instrument.

The nitrogen sorption isotherm was recorded on a Quantachrome Autosorb 1 at 77.35 K in a pressure range from $p/p^0 = 0.001$ to 0.98. Prior to the measurement of the sorption isotherm the sample was heated for 24 h at 120°C under turbomolecular pump vacuum. For the evaluation of the surface area the BET model was applied between 0.05 and 0.2 p/p^0 . The calculation of the pore size distribution was done using the QSDFT equilibrium model with a carbon kernel for cylindrical pores.

The permanent porosity of COF films was assessed by a krypton sorption measurement of degassed films (24 h at RT *in vacuo*). The isotherm was recorded at 77 K on a Quantachrome autosorb iQ instrument in a pressure range from $p/p^0 = 0.002$ to 0.95 using a vacuum volumetric technique.

X-ray diffraction (XRD) measurements were performed using a Bruker D8 Discover with Ni-filtered Cu K α radiation and a LynxEye position-sensitive detector.

Transmission electron microscopy was performed on an FEI Titan 80-300 equipped with a field emission gun operated at 80 kV. Scanning electron microscopy (SEM) images were recorded with a JEOL 6500F field emission microscope operated at 5 kV using a secondary electron detector.

4.4 Experimental

UV-Vis spectra were recorded using a Perkin-Elmer Lambda 1050 spectrometer equipped with a 150 mm integrating sphere. Absorbance spectra of COF thin films were corrected for the transmission of the substrate and reflection losses.

Photoluminescence (PL) measurements were performed using a home-built setup consisting of a Horiba Jobin Yvon iHR 320 monochromator equipped with a photomultiplier tube and a liquid N₂-cooled InGaAs detector. The samples were illuminated with a pulsed (83 Hz) 405 nm LED at a light intensity of 500 mW cm⁻².

Differential pulse voltammetry (DPV) was measured using 50 μM solutions of **1** and HHTP in acetonitrile or a 3:5 mixture of acetonitrile/1,4-dioxane, respectively, with 0.1 M tetrabutylammonium hexafluorophosphate as electrolyte and 0.1 mM ferrocene as internal reference. Measurements were performed with a Metrohm Autolab PGSTAT302N potentiostat, using Pt wires as the working electrode and counter electrode and a saturated Ag/AgCl reference electrode (Sigma Aldrich, 0.197 V vs. SHE).

Photovoltaic devices were tested under illumination from an AM1.5G solar simulator (Solar Light Model 16S), which was calibrated to 100 mW cm⁻² using a Fraunhofer ISE certified KG5 filtered silicon cell. Current-voltage (*J-V*) curves were recorded with a Keithley 2400 source-measure unit.

External quantum efficiency (EQE) measurements were performed at short circuit unless stated otherwise, and referenced to a Si photodiode with NIST traceable calibration. The device under test was illuminated with chopped (*f* = 7 Hz) monochromatic light. The current response was detected via a lock-in amplifier (Signal Recovery SR7230) with a low-noise pre-amplifier.

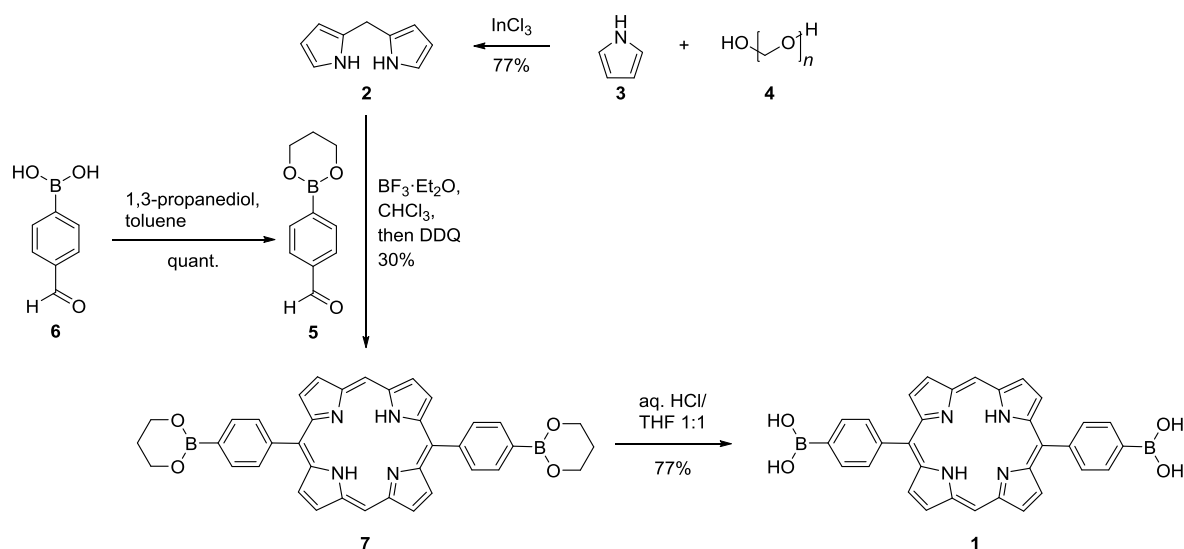
Photoinduced absorption measurements were carried out in transmission geometry using a stabilized continuum white light source in combination with a chopped

4.4 Experimental

excitation laser ($f_{\text{chop}} = 1 \text{ kHz}$, $\lambda_{\text{exc}} = 470 \text{ nm}$). Photoinduced changes in transmission through the thin film were recorded by a photodiode via lock-in detection (SRS 830). Photoinduced absorption spectra in the transparency range of the film were recorded by selecting different detection wavelengths using narrow bandpass filters each having a FWHM of 10 nm.

Synthesis

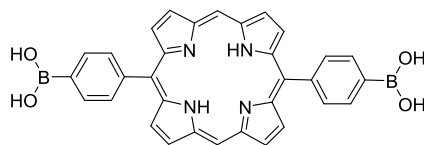
The synthesis of boronic acid porphyrin **1** started with preparation of dipyrromethane **2**⁴² from pyrrole (**3**) and paraformaldehyde (**4**) (Scheme S1). Then, in a procedure adapted from the literature,⁴³ boronic ester-bearing aldehyde **5**, previously obtained by protection of boronic acid **6**, was reacted with dipyrromethane to yield porphyrin **7** in 30 % yield. Finally, acidic deprotection of the boronic ester moieties gave access to porphyrin **1** in 77 % yield.



Scheme 5.1. Synthesis of boronic acid porphyrin **1**.

4.4 Experimental

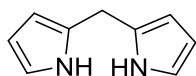
5,15-Bis(4-boronophenyl)porphyrin (**1**)



Porphyrin **7** (1.08 g, 1.71 mmol, 1 equiv.) was stirred in a mixture of THF (450 mL) and aq. HCl solution (450 mL, pH = 1) in the dark at RT for 24 h. Then, CH₂Cl₂ (650 mL) was added, and the precipitated product collected by filtration. The solid was suspended in MeOH, centrifuged, and MeOH was decanted off. The procedure was repeated three times to give **1** (640 mg, 77 %) as purple solid.

Mp > 305 °C (decomp); ¹H NMR (400 MHz, THF-*d*₈+3 drops of D₂O): 8.20 (d, *J* = 8.1 Hz, 4H), 8.30 (d, *J* = 8.1 Hz, 4H), 9.03 (d, *J* = 4.6 Hz, 4H), 9.47 (d, *J* = 4.6 Hz), 10.42 (s, 2H); ¹³C NMR (100 MHz, THF-*d*₈): 106.2, 111.1, 120.1, 131.5, 132.7, 133.9, 134.9, 143.9 (2 signals invisible); IR (ATR): 3282, 1604, 1577, 1471, 1395, 1321, 1236, 1197, 1145, 1103, 1008, 973, 954, 850, 786, 745, 732, 718, 688; HR-ESI-MS: *m/z*: 551.2048 ([*M*+H]⁺, calculated for C₃₂H₂₅B₂N₄O₄⁺: 551.2057).

Di(1*H*-pyrrol-2-yl)methane^[1] (**2**)

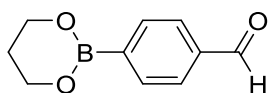


A suspension of paraformaldehyde (**4**) (1.63 g, 54.4 mmol, 1 equiv.) in pyrrole (**3**) (350 mL, 5040 mmol, 93 equiv.) was degassed with Ar for 15 min. The mixture was heated to 55 °C for 10 min before the addition of InCl₃ (1.19 g, 5.38 mmol, 0.1 equiv.). The mixture was stirred at 55 °C for 3 h, cooled down, and treated with powdered NaOH (7.20 g, 180 mmol, 3.3 equiv.). After 1 h at RT, the mixture was filtered over celite, washed with pyrrole, and evaporated to dryness. Purification by CC (SiO₂; packed with isohexane, elution isohexane/EtOAc 9:1) gave **2** (6.15 g, 77 %) as off-white solid.

4.4 Experimental

$R_f = 0.57$ (isohexane/EtOAc 2:1); $^1\text{H NMR}$ (600 MHz, CDCl_3): 3.97 (s, 2H), 6.05 (dddt, $J = 3.3, 2.5, 1.6, 0.8$ Hz, 2H), 6.16 (q, $J = 2.9$ Hz, 2H), 6.64 (td, $J = 2.6, 1.6$ Hz, 2H), 7.78 (br s, 2H); $^{13}\text{C NMR}$ (150 MHz, CDCl_3): 26.5, 106.5, 108.5, 117.4, 129.2; HR-EI-MS: m/z (%): 146.0837 (100, $[M]^+$, calculated for $\text{C}_9\text{H}_{10}\text{N}_2^+$: 146.0844).

4-(1,3,2-Dioxaborinan-2-yl)benzaldehyde⁴⁴ (5)

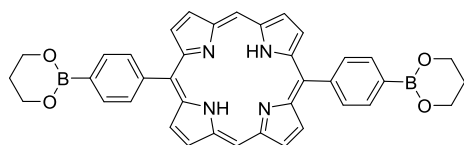


In a flask equipped with a Dean-Stark trap, a suspension of 4-formylphenylboronic acid (6) (10.2 g, 68.0 mmol, 1 equiv.) and 1,3-propanediol (5.20 mL, 72.4 mmol, 1.1 equiv.) in toluene (510 mL) was heated at 135 °C for 5 h. The mixture was evaporated to dryness to give 5 (13 g, quant.) as white solid.

Mp = 60–62 °C; $^1\text{H NMR}$ (300 MHz, CDCl_3): 2.05–2.12 (m, 2H), 4.19 (t, $J = 5.5$ Hz, 4H), 7.84 (d, $J = 8.3$ Hz, 2H), 7.92 (d, $J = 8.1$ Hz, 2H), 10.04 (s, 1H); $^{13}\text{C NMR}$ (75 MHz, CDCl_3): 27.5, 62.3, 128.8, 134.3, 137.9, 193.0 (1 signal invisible); IR (ATR): 2976, 2949, 2897, 2823, 2731, 1695, 1658, 1564, 1505, 1486, 1477, 1429, 1386, 1340, 1308, 1296, 1268, 1207, 1175, 1153, 1126, 1104, 1001, 921, 852, 826, 727, 672; HR-EI-MS: m/z (%): 189.0717 (100, $[M-H]^+$, calculated for $\text{C}_{10}\text{H}_{10}\text{BO}_3^+$: 189.0723).

4.4 Experimental

5,15-Bis(4-(1,3,2-dioxaborinan-2-yl)-phenyl)porphyrin (**7**)



Compounds **2** (1.66 g, 11.4 mmol, 1 equiv.) and **5** (2.14 g, 11.2 mmol, 1 equiv.) were dissolved in anhydrous CHCl_3 (1 L) under Ar, and the mixture was degassed with Ar for 15 min. The reaction mixture was cooled to $0\text{ }^\circ\text{C}$, $\text{BF}_3\cdot\text{OEt}_2$ (320 μL , 2.53 mmol, 0.2 equiv.) was added, and the mixture was stirred for 3 h at RT. Then, DDQ (4.16 g, 18.3 mmol, 1.6 equiv.) was added in one portion, and the mixture was stirred overnight at RT. The mixture was filtered over celite, and poured on to a column of silica (CH_2Cl_2 ; elution $\text{CH}_2\text{Cl}_2/\text{MeOH}$ 100:1). The collected purple solid was recrystallized from CHCl_3 to give **7** (1.08 g, 30 %) as dark purple solid.

$R_f = 0.44$ ($\text{CH}_2\text{Cl}_2/\text{MeOH}$ 95:5); $M_p = 370\text{ }^\circ\text{C}$ (decomp); $^1\text{H NMR}$ (600 MHz, CDCl_3): -3.10 (s, 2H), 2.25 (quintet, $J = 5.5$ Hz, 4H), 4.37 (t, $J = 5.6$ Hz, 8H), 8.21–8.28 (m, 8H), 9.07 (d, $J = 4.5$ Hz, 4H), 9.39 (d, $J = 4.5$ Hz, 4H), 10.31 (s, 2H); $^{13}\text{C NMR}$ (150 MHz, CDCl_3): 27.8, 62.4, 105.4, 119.4, 131.2, 131.7, 132.4, 134.5, 143.7, 145.3, 147.2 (1 signal invisible); IR (ATR): 2935, 2884, 1603, 1579, 1546, 1478, 1417, 1389, 1334, 1302, 1272, 1209, 1150, 1123, 1053, 1005, 992, 986, 972, 955, 864, 855, 795, 751, 735, 718, 693, 664; HR-EI-MS: m/z (%): 630.2613 (100, $[M]^+$, calculated for $\text{C}_{38}\text{H}_{32}\text{B}_2\text{N}_4\text{O}_4^+$: 630.2610).

4.4 Experimental

TP-Por COF

For the synthesis of TP-Por COF 11.5 mg of compound **1** (0.02 mmol, 3 equiv.) and 4.5 mg of HHTP (0.014 mmol, 2 equiv.) were added to a Teflon-lined steel autoclave and dispersed in a solvent mixture of acetonitrile and mesitylene (7:3 v:v, 1 mL). The autoclave was placed in an oven at 120 °C for 72 h. After the time had elapsed, the reaction mixture was allowed to cool down to room temperature and the resulting powder was then collected by filtration through a Hirsch funnel. After washing the product three times with dry toluene it was left under dynamic vacuum to come to complete dryness.

TP-Por COF films

11.5 mg of compound **1** (0.02 mmol, 3 equiv.) and 4.5 mg HHTP (0.014 mmol, 2 eq) were added to a 100 mL Schott flask and dissolved in a solvent mixture of acetonitrile and mesitylene in a 7:3 v:v ratio (30 mL). The substrates (fused silica or ITO-covered glass), covered with a 10 nm layer of vacuum-deposited MoO_x, were placed face down in the reaction solution. The flask was heated in an oven at 120 °C for 18 h. After the reaction mixture had cooled down to room temperature, the films were removed from the flask and washed by a short sonification treatment (2 s) in toluene. The obtained films were dried under a nitrogen flow prior to characterization.

4.4 Experimental

Device fabrication

A stock solution of 5–6 nm ZnO nanocrystals in *n*-BuOH/MeOH/CHCl₃ 88:6:6 v:v:v was prepared following literature procedures.⁴⁵ This solution was sonicated for 15 min prior to use.

The COF-based device was prepared on ITO-coated glass (VisonTec, 12–15 ohms/sq) slides. A 10 nm thick MoO_x electron blocking layer was deposited by thermal evaporation. A COF thin film was subsequently grown on this substrate as described above. An electron-selective contact was applied by spin-coating a dispersion of ZnO nanocrystals, resulting in a layer thickness of about 20 nm. The device was completed by thermal evaporation of 80 nm thick Al contacts in high vacuum through a shadow mask, thus defining an active area of 3×3 mm² for each device.

For the reference device based on a blend of the building blocks, 1.65 mg (3.0 μmol) of compound **1** and 0.65 mg (2.0 μmol) HHTP were dissolved in 200 μL 1,3-dioxolane and 100 μL MeOH. This solution was spin-cast onto a MoO_x-coated ITO substrate, yielding an active layer of ~40 nm thickness. Subsequently, a 10 nm layer of poly[(9,9-bis(2,2'-*N,N'*-dimethylaminopropyl)fluorenyl-2,7-diyl)-*alt-co*-(9,9-dioctylfluorenyl-2,7-diyl)] (PFN), serving as an electron selective contact, was spin-coated from a 2 mg mL⁻¹ methanol solution containing 5 μL acetic acid. The device was completed by thermal evaporation of 120 nm Al contacts.

4.4 Experimental

Simulation of the TP-Por COF crystal structure

To determine the crystal structure of the obtained product, a powder diffraction pattern was calculated based on a simulated crystal structure. The unit cell was constructed using the Materials Studio software and optimized by force field calculations. Due to the non-planar porphyrin building block, the unit cell is limited to a trigonal $P3$ symmetry in the case of an eclipsed stacked structure and $P6_3$ symmetry for a staggered arrangement. The comparison of the calculated pattern with the experimental data identified the obtained structure as AA stacked TP-Por COF.

Table 4.1. Refined crystal data.

Formula	$C_{132} H_{72} B_6 N_{12} O_{12}$
Formula weight	$2082.96 \text{ g mol}^{-1}$
Crystal system	trigonal
Space-group	$P3$
Cell parameters	$a = b = 52.2 \text{ \AA}, c = 3.8 \text{ \AA}$
Cell volume	8977 \AA^3

Table 4.2. Fractional atomic coordinates.

Atom	Wyck.	x	y	z	Atom	Wyck.	x	y	z
C1	3d	0.91955	0.94724	-0.01394	C28	3d	0.38765	0.72147	0.03575
N2	3d	0.69905	0.87622	-0.01391	C29	3d	0.36045	0.6946	0.02411
C3	3d	0.72863	0.88841	0.02061	C30	3d	0.91949	0.97347	-0.03042
C4	3d	0.742	0.91883	0.06597	N31	3d	0.69904	0.82386	0.02666

4.4 Experimental

C5	3d	0.71977	0.92569	0.05331	C32	3d	0.69399	0.79595	0.0092
C6	3d	0.82388	0.9315	-0.21349	C33	3d	0.72858	0.84119	-0.01499
C7	3d	0.793	0.91588	-0.21168	C34	3d	0.74185	0.82408	-0.06292
C8	3d	0.9457	1.00046	-0.03098	C35	3d	0.71962	0.795	-0.04449
C9	3d	0.97289	1.00079	-0.02418	C36	3d	0.82426	0.89354	0.189
C10	3d	0.4139	0.72073	0.03347	C37	3d	0.79337	0.87827	0.19712
N11	3d	0.63444	0.79159	0.03275	O38	3d	0.89131	0.96966	-0.04227
C12	3d	0.63945	0.76894	0.08877	C39	3d	0.94583	0.94658	-0.01434
C13	3d	0.60489	0.77964	0.06862	C40	3d	0.66674	0.89724	-0.03767
C14	3d	0.59155	0.74965	0.15129	C41	3d	0.66672	0.77056	0.05815
C15	3d	0.61379	0.74277	0.16147	C42	3d	0.83951	0.92024	-0.01474
C16	3d	0.50943	0.73532	-0.15931	B43	3d	0.87376	0.9374	-0.01955
C17	3d	0.54032	0.75089	-0.16343	C44	3d	0.5895	0.79531	0.01666
O18	3d	0.44211	0.74513	0.04853	C45	3d	0.49401	0.74759	0.02058
C19	3d	0.38758	0.66751	0.00825	C46	3d	0.55629	0.77871	0.01841
C20	3d	0.36041	0.66725	0.02005	B47	3d	0.45971	0.73047	0.02151
C21	3d	0.41387	0.69447	0.01038	C48	3d	0.69406	0.89911	0
C22	3d	0.63943	0.87159	-0.06308	O49	3d	0.89142	0.9228	0
C23	3d	0.60486	0.82636	-0.03735	N50	3d	0.63444	0.84395	0
C24	3d	0.59148	0.843	-0.11765	O51	3d	0.44205	0.69821	0
C25	3d	0.61372	0.8721	-0.13138	C52	3d	0.744	0.87249	0
C26	3d	0.50951	0.77532	0.19948	C53	3d	0.77723	0.8891	0
C27	3d	0.54041	0.79061	0.20144	C54	3d	0.97284	0.97363	-0.02418

4.4 Experimental

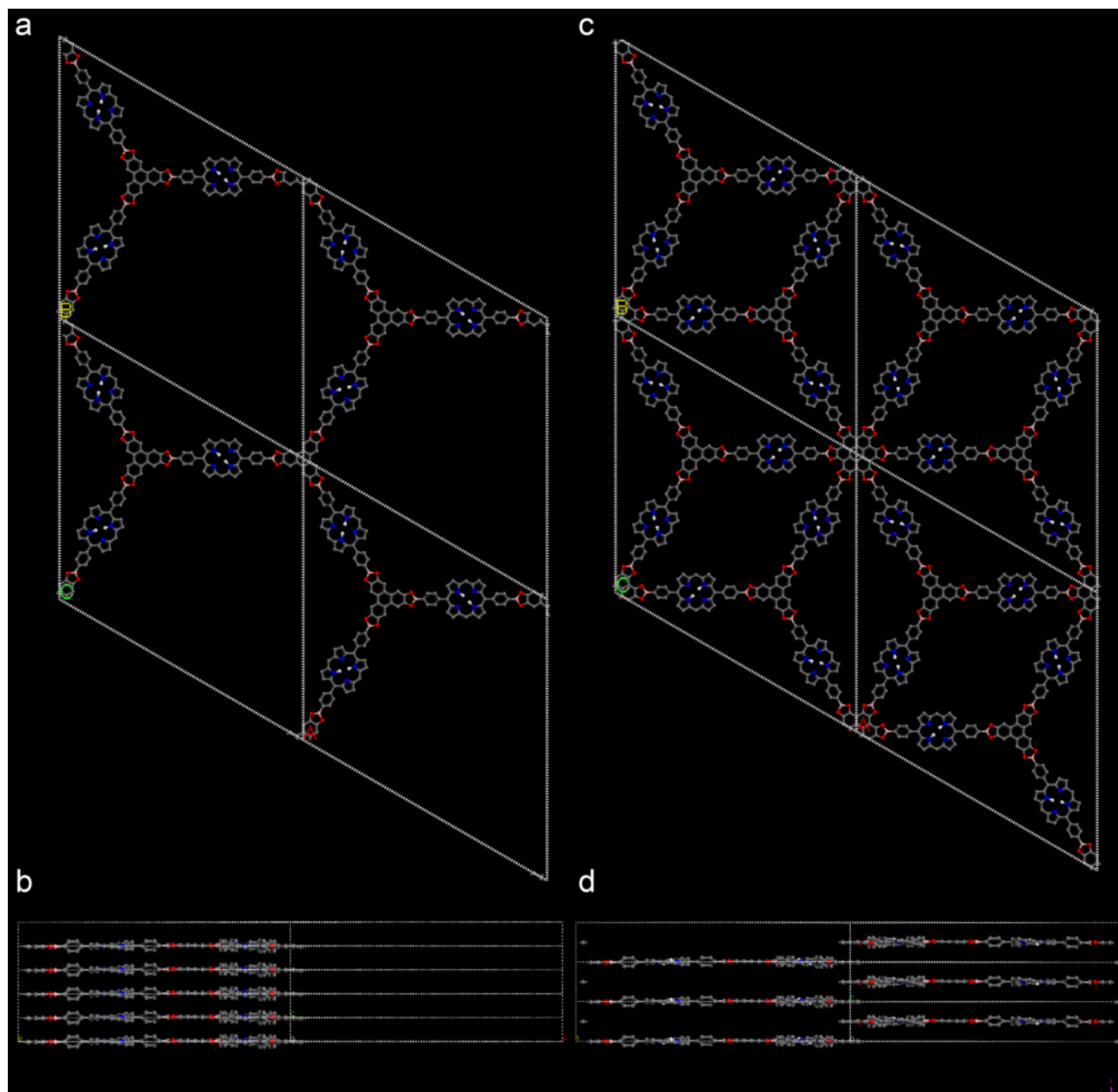


Figure 4.5. Simulation of the crystal lattice of TP-Por COF. a) Top view on the AB plane of 4 unit cells in an eclipsed stacking arrangement with $P3$ symmetry, b) view along the c -axis of this fragment with an interlayer distance of 3.8 Å, c) view on the AB plane of 4 calculated unit cells of the TP-Por COF in a (hypothetical) staggered arrangement with $P6_3$ symmetry, and d) view along the c -axis with an interlayer distance of 6.5 Å.

4.4 Experimental

X-ray diffraction analysis of TP-Por COF thin films

To confirm the successful formation of TP-Por COF films on the conductive substrates they were analyzed by XRD in a detector scan mode. The XRD pattern shows a broad reflection at $24^\circ 2\theta$, indicating oriented film growth with an interlayer distance of 3.8 \AA (Figure 4.6).

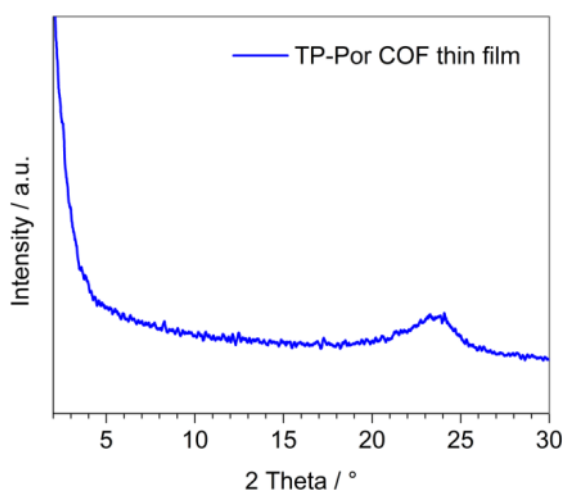


Figure 4.6. X-ray diffraction pattern of a TP-Por COF film measured in detector scan mode.

Krypton sorption on COF thin films

The accessibility of the open pore system of TP-Por COF films was confirmed by krypton sorption measurements. The obtained type IV isotherm, which is characteristic for mesoporous materials, exhibits a sharp jump from 0.33 to 0.47 P/P_0 , indicating a narrow pore size distribution.

4.4 Experimental

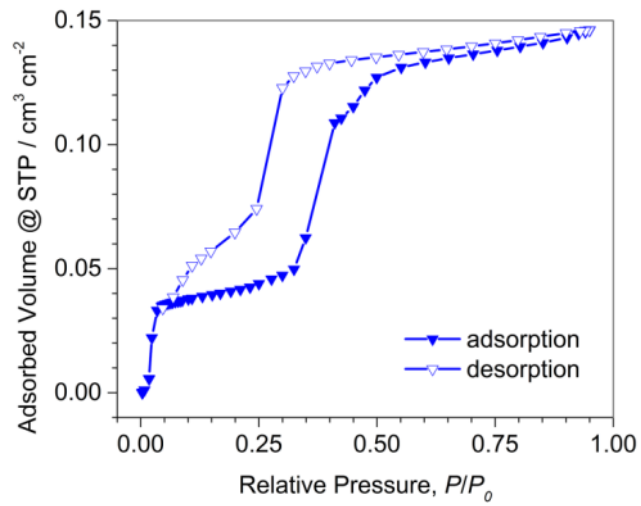


Figure 4.7. Krypton sorption isotherm of a TP-Por COF thin film measured at 77 K.

4.4 Experimental

IR spectroscopy

The successful formation of the boronate ester ring between HHTP and **1** was indicated by Fourier transform infrared (FTIR) spectroscopy through the appearance of the characteristic B–C stretching modes at 1333 cm^{-1} and 1261 cm^{-1} (Figure 4.8).⁴⁶

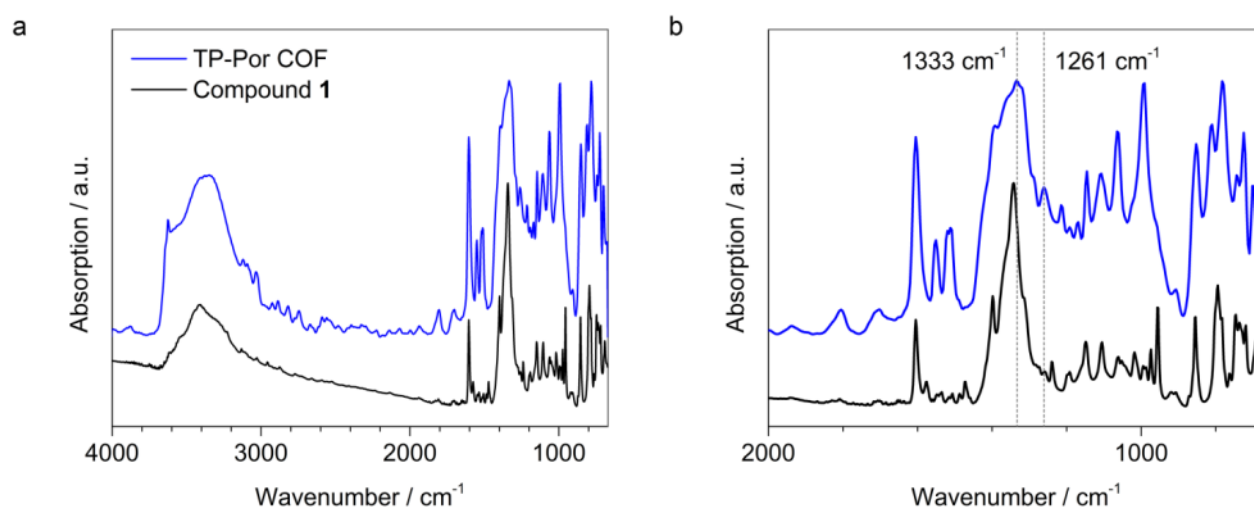


Figure 4.8. IR spectra of a TP-Por COF powder sample and the porphyrin diboronic acid **1**. a) Full range spectrum and b) enlargement of the region below 2000 cm^{-1} showing the characteristic signals of the B–C stretching modes at 1333 cm^{-1} and 1261 cm^{-1} . The spectra were offset for clarity.

Table 4.3. Assignment of the most important IR-bands of TP-Por COF and Compound **1**.

Wavenumber / cm^{-1}	Assignment
1343	asymmetric B–O stretching mode ($-\text{B}(\text{OH})_2$)
1333	“breathing” motion within the $\text{C}_2\text{O}_2\text{B}$ ring
1315	symmetric B–C stretching mode ($-\text{B}(\text{OH})_2$)
1261	coupled B–C and C=C stretching mode
1213	symmetric C–O stretching mode
1062	symmetric B–O stretching mode
972	coupled B–O stretch and O–H in plane bend ($-\text{B}(\text{OH})_2$)
918	symmetric, in plane O–H bending ($-\text{B}(\text{OH})_2$)

4.4 Experimental

UV-Vis spectroscopy

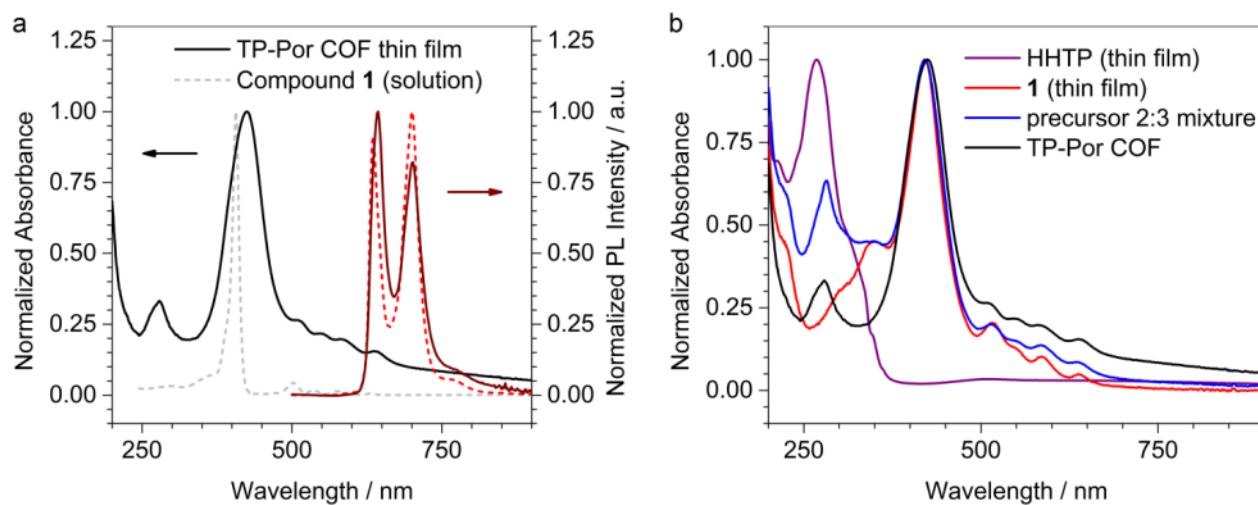


Figure 4.9. a) Absorption (black, gray) and photoluminescence emission spectra (brown, red) of a TP-Por COF thin film (solid line) and a 50 μM 1,4-dioxane solution of the porphyrin diboronic acid **1** (dashed line). b) Comparison of the UV-Vis spectra of the TP-Por COF film (black) with spin-coated thin films of its precursors (purple and red for HHTP and **1**, respectively) and a 2:3 mixture of these precursors (blue).

Differential pulse voltammetry and optical band gap of the COF building blocks

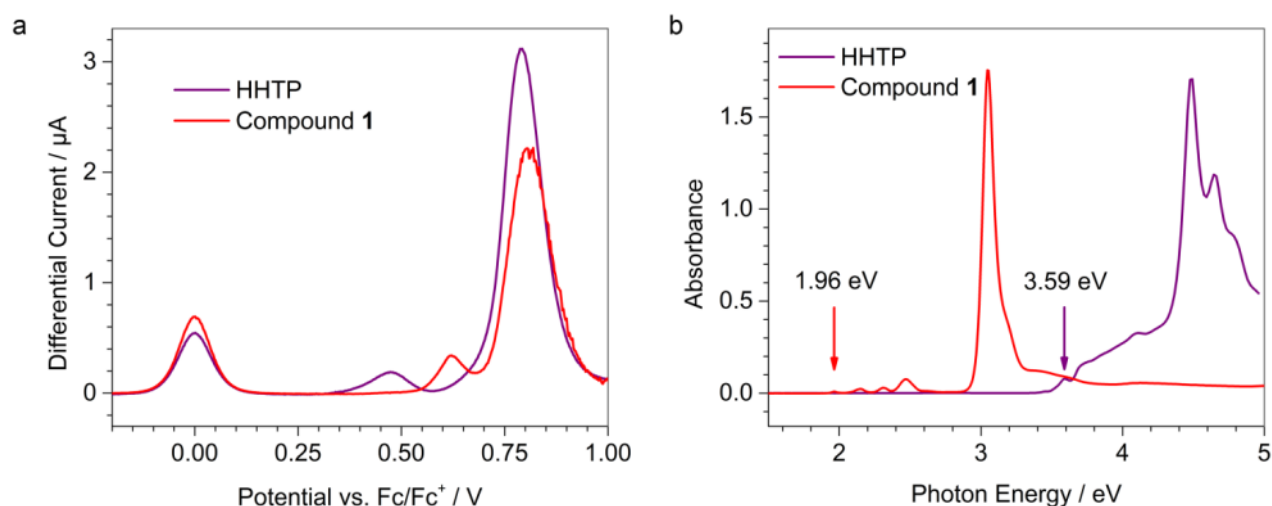


Figure 4.10. a) Differential pulse voltammograms of HHTP (purple) and **1** (red), measured towards more positive potentials (oxidation) and referenced to ferrocene. b) Corresponding UV-Vis spectra of the precursor solutions. The optical band gap is determined from the maximum of the lowest-energy optical transition.

4.4 Experimental

Additional optoelectronic characterization of the photovoltaic devices

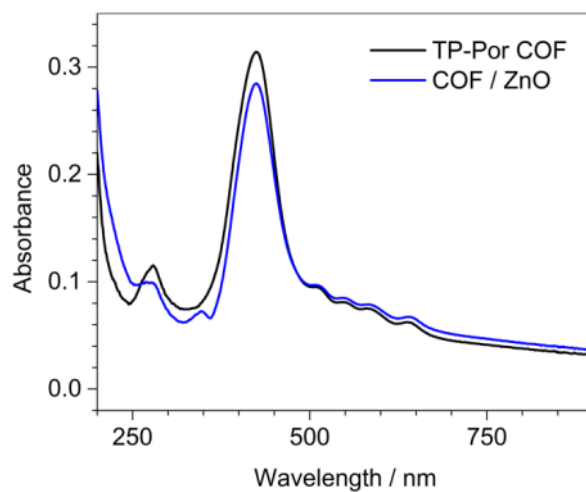


Figure 4.11. Transmission absorption spectra of a TP-Por COF thin film before (black) and after addition of the ZnO electron-selective layer. The additional feature at 347 nm can be ascribed to the ZnO nanocrystals.

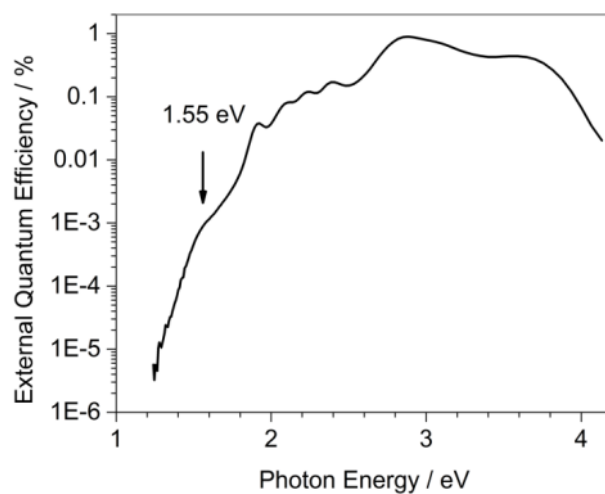


Figure 4.12. External quantum efficiency spectrum of a TP-Por COF-based photovoltaic device in semi-logarithmic representation. The defined feature at 1.55 eV might indicate the formation of a well-defined charge-transfer state inside the donor–acceptor framework.

4.4 Experimental

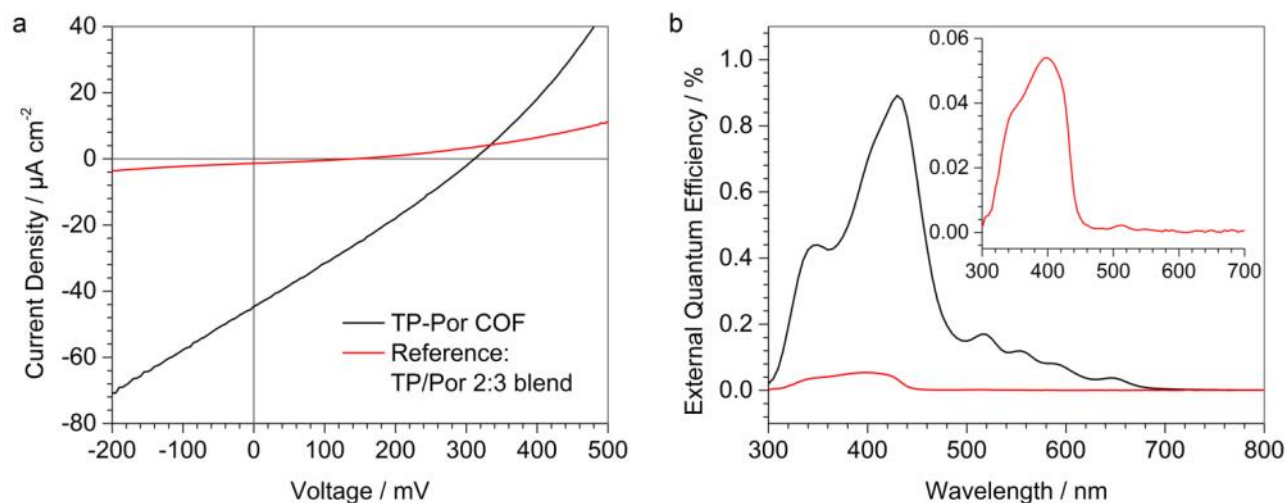


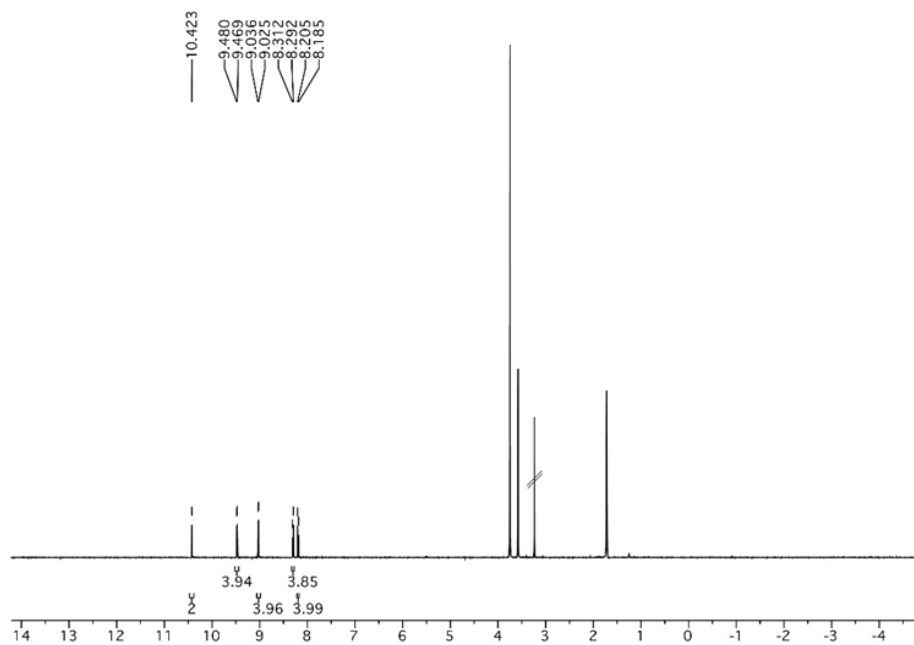
Figure 4.13. Comparison of a) the J - V curves recorded at 100 mW cm^{-2} AM1.5G illumination and b) EQE spectra of the TP-Por COF device (black) and the reference device based on a blend of the COF building blocks (red). The inset shows a magnified representation of the EQE spectrum of the TP/Por blend device.

4.4 Experimental

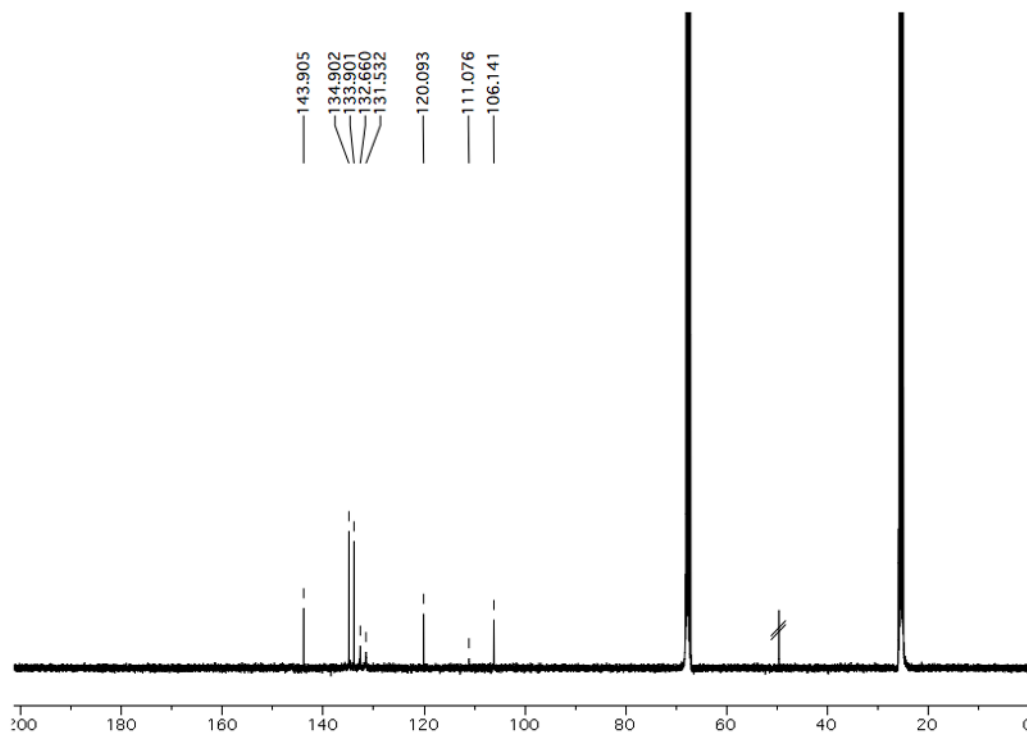
NMR spectra

Compound 1

400 MHz, THF-*d*₈+3 drops of D₂O



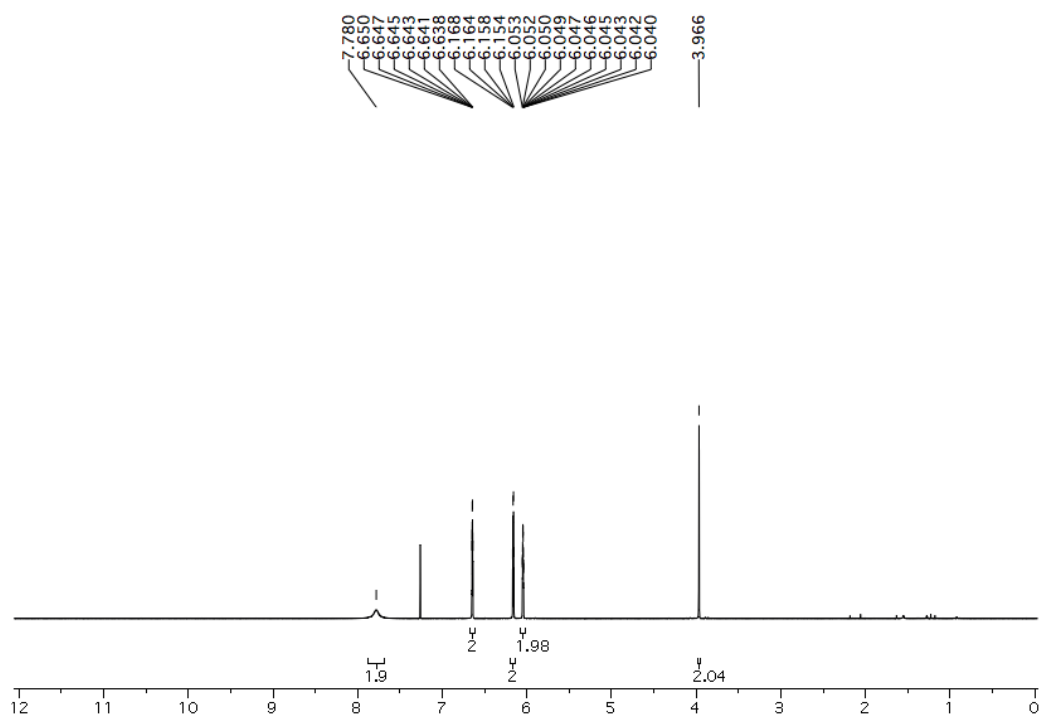
100 MHz, THF-*d*₈+3 drops of D₂O



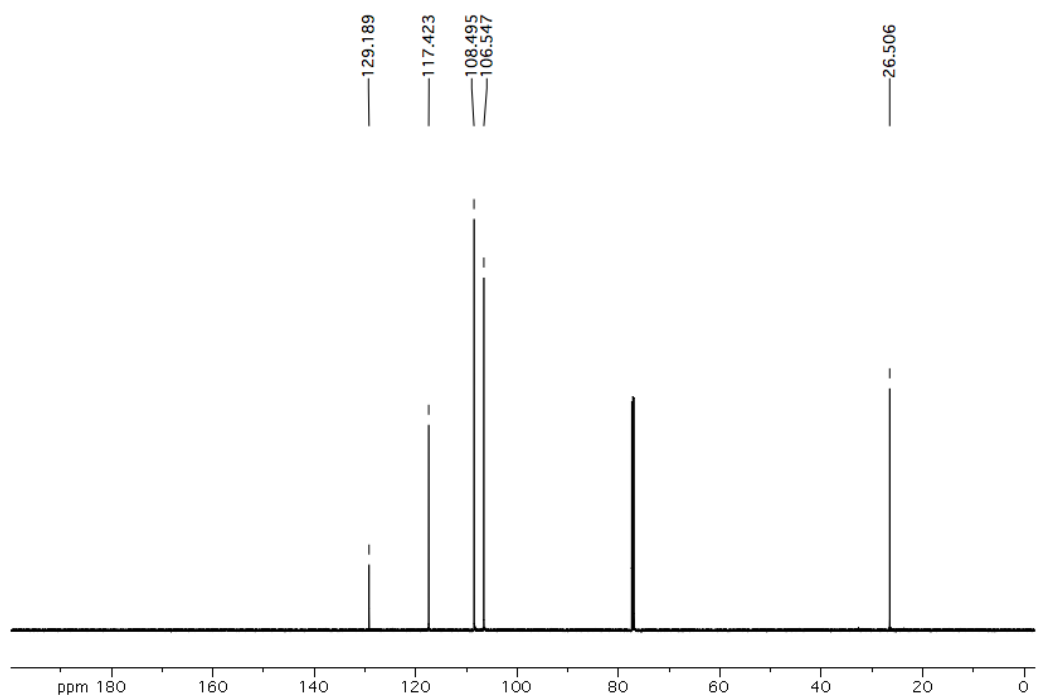
4.4 Experimental

Compound 2

600 MHz, CDCl₃



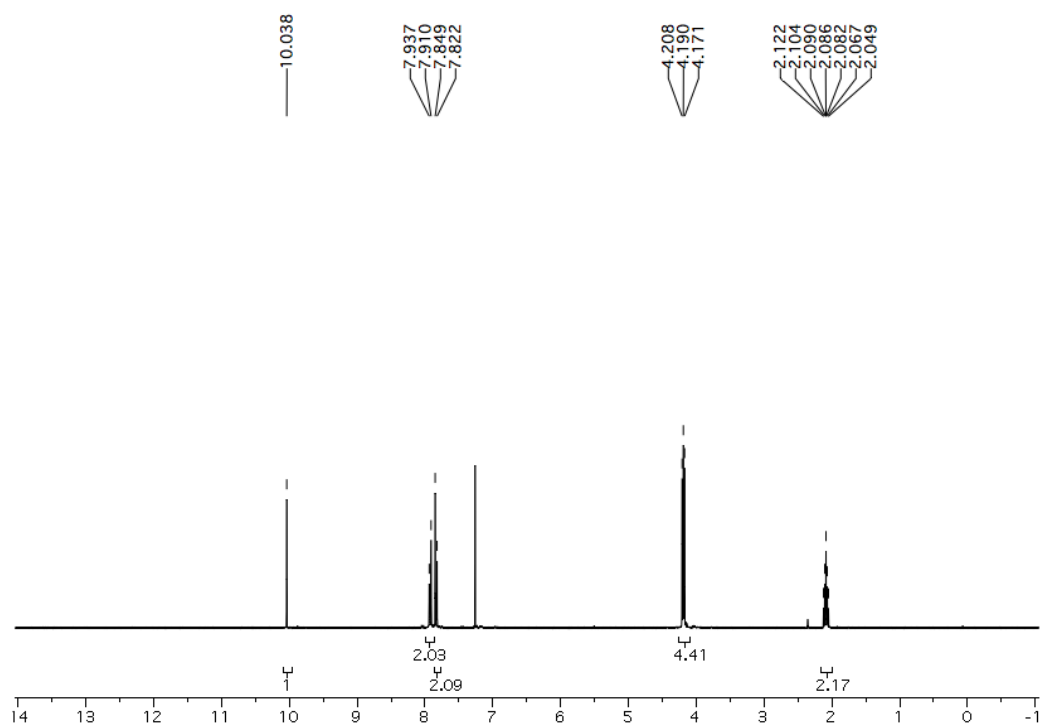
150 MHz, CDCl₃



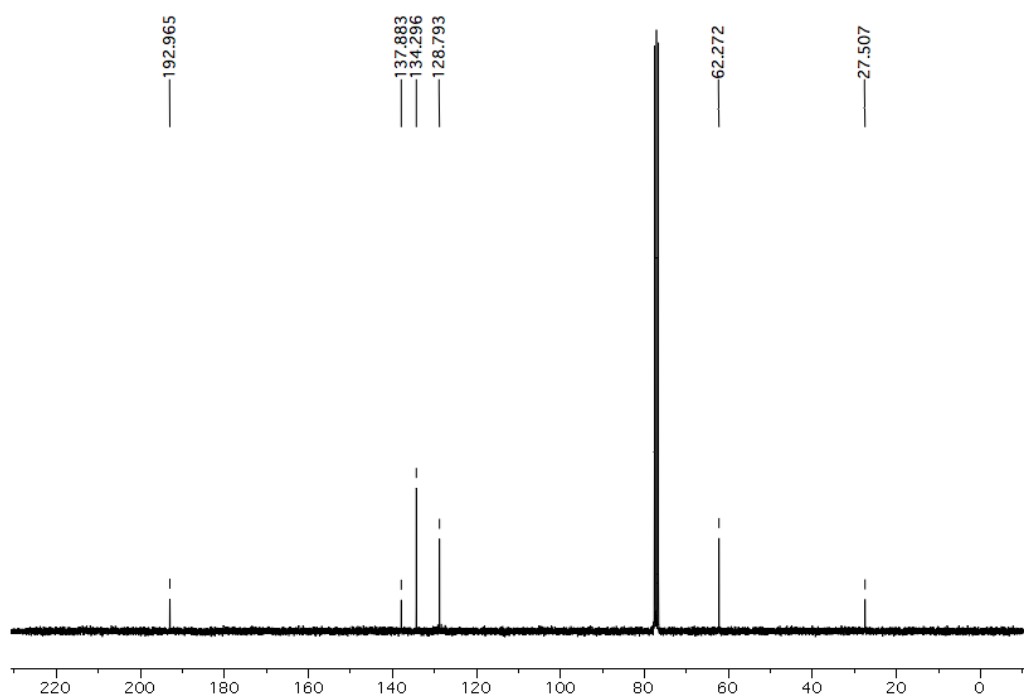
4.4 Experimental

Compound 5

300 MHz, CDCl₃



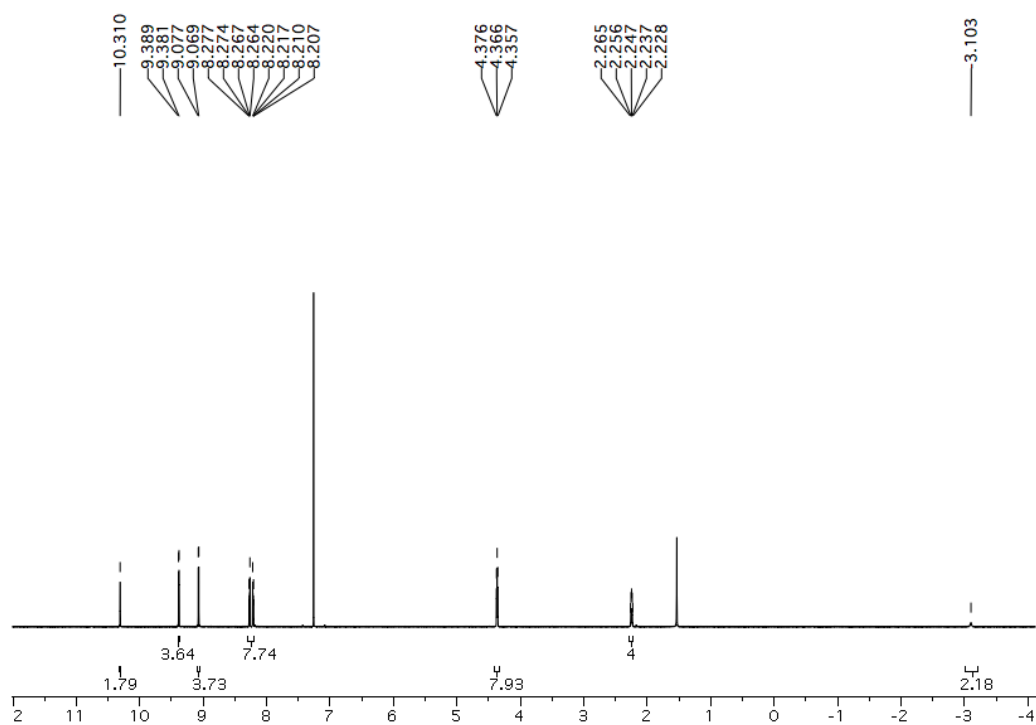
75 MHz, CDCl₃



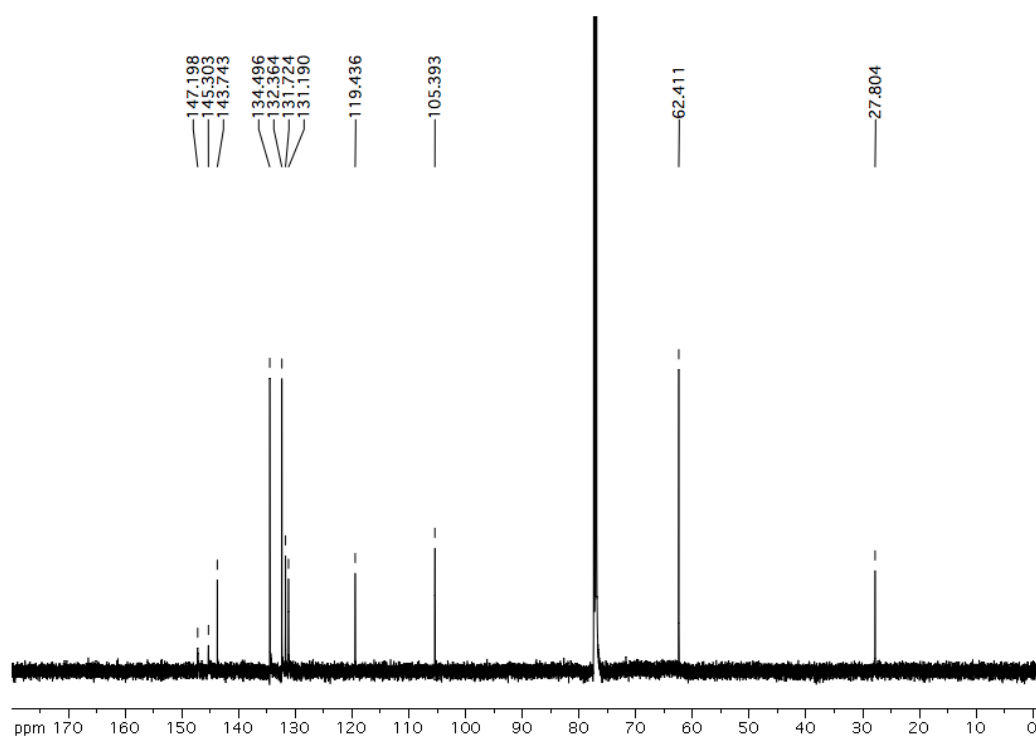
4.4 Experimental

Compound 7

600 MHz, CDCl₃



150 MHz, CDCl₃



4.5 References

1. Z. He; C. Zhong; S. Su; M. Xu; H. Wu; Y. Cao, Enhanced power-conversion efficiency in polymer solar cells using an inverted device structure. *Nat. Photon.* **2012**, *6*, 591-595.
2. E. T. Hoke; K. Vandewal; J. A. Bartelt; W. R. Mateker; J. D. Douglas; R. Noriega; K. R. Graham; J. M. J. Fréchet; A. Salleo; M. D. McGehee, Recombination in Polymer:Fullerene Solar Cells with Open-Circuit Voltages Approaching and Exceeding 1.0 V. *Adv. Energy Mater.* **2013**, *3*, 220-230.
3. S. Chen; C. E. Small; C. M. Amb; J. Subbiah; T.-H. Lai; S.-W. Tsang; J. R. Manders; J. R. Reynolds; F. So, Inverted Polymer Solar Cells with Reduced Interface Recombination. *Adv. Energy Mater.* **2012**, *2*, 1333-1337.
4. A. K. K. Kyaw; D. H. Wang; D. Wynands; J. Zhang; T.-Q. Nguyen; G. C. Bazan; A. J. Heeger, Improved light harvesting and improved efficiency by insertion of an optical spacer (ZnO) in solution-processed small-molecule solar cells. *Nano Lett.* **2013**, *13* (8), 3796-3801.
5. Y. Liang; Z. Xu; J. Xia; S.-T. Tsai; Y. Wu; G. Li; C. Ray; L. Yu, For the Bright Future - Bulk Heterojunction Polymer Solar Cells with Power Conversion Efficiency of 7.4%. *Adv. Mater.* **2010**, *22*, E135-E138.
6. X. Guo; N. Zhou; S. J. Luo; J. Smith; D. B. Tice; J. W. Hennek; R. P. Ortiz; J. T. L. Navarrete; S. Li; J. Strzalka; L. X. Chen; R. P. H. Chang; A. Facchetti; T. J. Marks, Polymer solar cells with enhanced fill factors. *Nat. Photon.* **2013**, *7*, 825-833.
7. Y. Liu; C.-C. Chen; Z. Hong; J. Gao; Y. M. Yang; H. Zhou; L. Dou; G. Li; Y. Yang, Solution-processed small-molecule solar cells: breaking the 10% power conversion efficiency. *Sci. Rep.* **2013**, *3*.
8. H. Qin; L. Li; F. Guo; S. Su; J. Peng; Y. Cao; X. Peng, Solution-processed bulk heterojunction solar cells based on a porphyrin small molecule with 7% power conversion efficiency. *Energy Environ. Sci.* **2014**, *7* (4), 1397-1401.
9. J. Peet; J. Y. Kim; N. E. Coates; W. L. Ma; D. Moses; A. J. Heeger; G. C. Bazan, Efficiency enhancement in low-bandgap polymer solar cells by processing with alkane dithiols. *Nat. Mater.* **2007**, *6*, 497-500.
10. M. A. Ruderer; S. Guo; R. Meier; H.-Y. Chiang; V. Körstgens; J. Wiedersich; J. Perlich; S. V. Roth; P. Müller-Buschbaum, Solvent-Induced Morphology in Polymer-Based Systems for Organic Photovoltaics. *Adv. Funct. Mater.* **2011**, *21*, 3382-3391.
11. P. Westacott; J. R. Tumbleston; S. Shoaee; S. Fearn; J. H. Bannock; J. B. Gilchrist; S. Heutz; J. deMello; M. Heeney; H. Ade; J. Durrant; D. S. McPhail; N. Stingelin, On the role of intermixed phases in organic photovoltaic blends. *Energy Environ. Sci.* **2013**, *6*, 2756-2764.
12. A. P. Côte; A. I. Benin; N. W. Ockwig; M. O'Keeffe; A. J. Matzger; O. M. Yaghi, Porous, Crystalline, Covalent Organic Frameworks. *Science* **2005**, *310*, 1166-1170.
13. J. W. Colson; W. R. Dichtel, Rationally synthesized two-dimensional polymers. *Nat. Chem.* **2013**, *5*, 453-465.
14. A. P. Côte; H. M. El-Kaderi; H. Furukawa; J. R. Hunt; O. M. Yaghi, Reticular Synthesis of Microporous and Mesoporous 2D Covalent Organic Frameworks. *J. Am. Chem. Soc.* **2007**, *129*, 12914-12915.
15. S. Kandambeth; D. B. Shinde; M. K. Panda; B. Lukose; T. Heine; R. Banerjee, Enhancement of Chemical Stability and Crystallinity in Porphyrin-Containing Covalent Organic Frameworks by Intramolecular Hydrogen Bonds. *Angew. Chem. Int. Ed.* **2013**, *52*, 13052-13056.

4.5 References

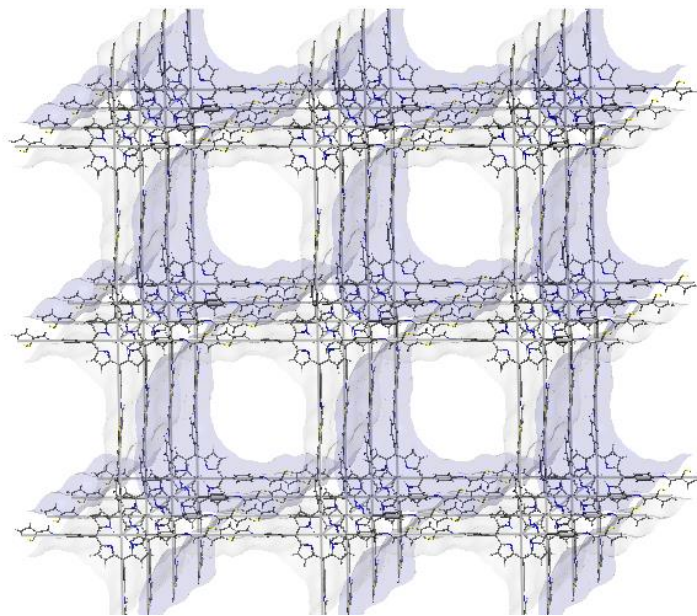
16. E. L. Spitler; W. R. Dichtel, Lewis acid-catalysed formation of two-dimensional phthalocyanine covalent organic frameworks. *Nat. Chem.* **2010**, *2*, 672-677.
17. S. Wan; F. Gándara; A. Asano; H. Furukawa; A. Saeki; S. K. Dey; L. Liao; M. W. Ambrogio; Y. Y. Botros; X. Duan; S. Seki; J. F. Stoddart; O. M. Yaghi, Covalent Organic Frameworks with High Charge Carrier Mobility. *Chem. Mater.* **2011**, *23*, 4094-4097.
18. X. Ding; X. Feng; A. Saeki; S. Seki; A. Nagai; D. Jiang, Conducting metallophthalocyanine 2D covalent organic frameworks: the role of central metals in controlling π -electronic functions. *Chem. Commun.* **2012**, *48*, 8952-8954.
19. X. Ding; L. Chen; Y. Honsho; X. Feng; O. Saengsawang; J. Guo; A. Saeki; S. Seki; S. Irle; S. Nagase; V. Parasuk; D. Jiang, An n-Channel Two-Dimensional Covalent Organic Framework. *J. Am. Chem. Soc.* **2011**, *133*, 14510-14513.
20. S. Patwardhan; A. A. Kocherzhenko; F. C. Grozema; L. D. A. Siebbeles, Delocalization and Mobility of Charge Carriers in Covalent Organic Frameworks. *J. Phys. Chem. C* **2011**, *115*, 11768-11772.
21. M. Dogru; A. Sonnauer; A. Gavryushin; P. Knochel; T. Bein, A Covalent Organic Framework with 4 nm open pores. *Chem. Commun.* **2011**, *47*, 1707-1709.
22. M. Dogru; A. Sonnauer; S. Zimdars; M. Döblinger; P. Knochel; T. Bein, Facile synthesis of a mesoporous benzothiadiazole-COF based on a transesterification process. *CrystEngComm* **2013**, *15*, 1500-1502.
23. S. Wan; J. Guo; J. Kim; H. Ihee; D. Jiang, A Belt-Shaped, Blue Luminescent, and Semiconducting Covalent Organic Framework. *Angew. Chem. Int. Ed.* **2008**, *47*, 8826-8830.
24. G. H. V. Bertrand; V. K. Michaelis; T.-C. Ong; R. G. Griffin; M. Dinca, Thiophene-based covalent organic frameworks. *PNAS* **2013**, *110*, 4923-4928.
25. E. L. Spitler; J. W. Colson; F. J. Uribe-Romo; A. R. Woll; M. R. Giovino; A. Saldivar; W. R. Dichtel, Lattice Expansion of Highly Oriented 2D Phthalocyanine Covalent Organic Framework Films. *Angew. Chem. Int. Ed.* **2012**, *51*, 2623-2627.
26. X. Feng; Y. Honsho; O. Saengsawang; L. Liu; L. Wang; A. Saeki; S. Irle; S. Seki; Y. Dong; D. Jiang, An Ambipolar Conducting Covalent Organic Framework with Self-Sorted and Periodic Electron Donor-Acceptor Ordering. *Adv. Mater.* **2012**, *24*, 3026-3031.
27. S. Jin; K. Furukawa; M. Addicoat; L. Chen; S. Takahashi; S. Irle; T. Nakamura; D. Jiang, Large pore donor-acceptor covalent organic frameworks. *Chem. Sci.* **2013**, *4*, 4505-4511.
28. S. Jin; X. Ding; X. Feng; M. Supur; K. Furukawa; S. Takahashi; M. Addicoat; M. E. El-Khouly; T. Nakamura; S. Irle; S. Fukuzumi; A. Nagai; D. Jiang, Charge Dynamics in A Donor-Acceptor Covalent Organic Framework with Periodically Ordered Bicontinuous Heterojunctions. *Angew. Chem. Int. Ed.* **2013**, *52*, 2017-2021.
29. M. Dogru; M. Handloser; F. Auras; T. Kunz; D. Medina; A. Hartschuh; P. Knochel; T. Bein, A Photoconductive Thienothiophene-Based Covalent Organic Framework Showing Charge Transfer Towards Included Fullerene. *Angew. Chem. Int. Ed.* **2013**, *52*, 2920-2924.
30. J. Guo; Y. Xu; S. Jin; L. Chen; T. Kaji; Y. Honsho; M. A. Addicoat; J. Kim; A. Saeki; H. Ihee, Conjugated organic framework with three-dimensionally ordered stable structure and delocalized π clouds. *Nat. Commun.* **2013**, *4*.
31. E. L. Spitler; B. T. Koo; J. L. Novotney; J. W. Colson; F. J. Uribe-Romo; G. D. Gutierrez; P. Clancy; W. R. Dichtel, A 2D Covalent Organic Framework with 4.7-nm Pores and Insight into Its Interlayer Stacking. *J. Am. Chem. Soc.* **2011**, *133*, 19416-19421.
32. H. L. Anderson, Building molecular wires from the colours of life: conjugated porphyrin oligomers. *Chem. Commun.* **1999**, 2323.

4.5 References

33. M. Calik; F. Auras; L. M. Salonen; K. Bader; I. Grill; M. Handloser; D. D. Medina; M. Dogru; F. Loebermann; D. Trauner; A. Hartschuh; T. Bein, Extraction of Photogenerated Electrons and Holes from a COF Integrated Heterojunction. *J. Am. Chem. Soc.* **2014**.
34. C. Peyratout; L. Daehne, Aggregation of thiocyanine derivatives on polyelectrolytes. *Phys. Chem. Chem. Phys.* **2002**, *4*, 3032-3039.
35. Y. Li; F. Auras; F. Löbermann; M. Döblinger; J. Schuster; L. Peter; D. Trauner; T. Bein, A Photoactive Porphyrin-Based Periodic Mesoporous Organosilica Thin Film. *J. Am. Chem. Soc.* **2013**, *135*, 18513-18519.
36. X. Feng; L. Liu; Y. Honsho; A. Saeki; S. Seki; S. Irle; Y. Dong; A. Nagai; D. Jiang, High-Rate Charge-Carrier Transport in Porphyrin Covalent Organic Frameworks: Switching from Hole to Electron to Ambipolar Conduction. *Angew. Chem. Int. Ed.* **2012**, *51*, 2618-2622.
37. J. M. Frost; M. A. Faist; J. Nelson, Energetic Disorder in Higher Fullerene Adducts: A Quantum Chemical and Voltammetric Study. *Adv. Mater.* **2010**, *22*, 4881-4884.
38. E. A. Alemán; J. M. Rocha; W. Wongwitwichote; L. A. G. Mora-Tovar; D. A. Modarelli, Spectroscopy of Free-Base N-Confused Tetraphenylporphyrin Radical Anion and Radical Cation. *J. Phys. Chem. A* **2011**, *115*, 6456-6471.
39. T. Shida; W. H. Hamill, Molecular Ions in Radiation Chemistry. III. Absorption Spectra of Aromatic-Hydrocarbon Cations and Anions in Organic Glasses. *J. Chem. Phys.* **1966**, *44* (12), 4372-4377.
40. V. Shrotriya; G. Li; Y. Yao; C.-W. Chu; Y. Yang, Transition metal oxides as the buffer layer for polymer photovoltaic cells. *Appl. Phys. Lett.* **2006**, *88*, 073508.

5. Tuning Photoluminescent Lifetimes within Metal-Free Porphyrin Covalent Organic Frameworks

This chapter is based on work in collaboration with Niklas Keller and Florian Auras.



Abstract

Covalent organic frameworks (COFs) have attracted interest for many applications such as gas storage, photo-catalysis and optoelectronics. Their potential for tailoring pore space on a molecular level combined with the robust network and structural order of a crystalline material has caught much attention. Two-dimensional COFs allow for the tuning of their properties by choosing the building units accordingly. The π - π interactions between adjacent layers can thereby facilitate charge carrier migration along the stacking direction. These unique properties motivate new research on COFs as active materials for photovoltaic devices. Herein, we report the successful synthesis of a thienothiophene-porphyrin COF with high stacking order. A slight offset between

5.1 Introduction

successive layers in a preferred direction leads to a reduction in symmetry of the unit cell, causing a splitting of the reflections in the diffraction pattern. Furthermore, the influence of the linear linker molecule within porphyrin COFs on the photo-luminescent decay lifetime was investigated. The lifetime can thereby be increased by electron deficient molecules, allowing for internal charge transfer from the porphyrin unit to the linear linker molecule. We anticipate that the new insights into the TT-Por COF stacking behavior and electronic properties can be transferred to other porphyrin-containing COFs and help to get a better understanding of the occurring electronic processes within these systems.

5.1 Introduction

The first report of covalent organic frameworks (COFs) in 2005 by Coté et al. initiated intense investigations on these unique materials. Two-dimensional (2D) COFs are crystalline porous networks formed by linking organic molecules via covalent bonds to form two-dimensional sheets. These sheets are able to stack in the third dimension by π - π interactions to form porous networks with a defined pore size and shape.¹

COFs have attracted increasing attention as promising materials for gas storage²⁻³, catalysis⁴⁻⁵ and optoelectronic devices⁶⁻⁷. The π -stacking between the adjacent layers can thereby facilitate charge-carrier transport along the columns of the self-assembled COF structure.

This exceptional type of materials allows for tuning its properties by selecting the molecular building blocks accordingly. Porphyrins, with their extended π -electron system and semi- and photo-conducting capabilities, have been in the focus of many investigations.⁸⁻¹² They exhibit very high extinction coefficients in the visible and near

5.1 Introduction

infrared (IR) region where the maximum of the solar flux occurs, which makes them interesting candidates for harvesting light in solar cell devices.¹³

Porphyrins have been integrated into various COF structures. Those COFs were characterized to have an eclipsed structure, meaning that the 2-D sheets are lying on top of each other in an AA-stacking arrangement.¹⁴⁻¹⁹ However, density functional theory calculations performed by different groups suggest that true eclipsed structures are energetically unfavored and that COFs rather adopt structures with slightly offset layers.²⁰⁻²² In principle, the offset can occur with the same probability in all symmetrically equivalent directions. As it is very likely that the layers will stack in a random order, without any preferred direction, the offset is difficult to observe via X-ray powder diffraction. Only a prevalence of distinctive patterns such as serrated, helical or staircase arrangements would be observable via X-ray diffraction, but this has not been observed experimentally thus far.²⁰

In this work we developed a COF consisting of two photoactive units, an electron rich tetragonal amine porphyrin linked to an electron deficient thieno[3,2-b]thiophene-2,5-dicarboxaldehyde (TT) to form a new electroactive material. With the combination of these two molecules, ordered in a COF structure, we were able to extend the fluorescence lifetime by allowing internal charge transfer compared to the molecular building blocks. Furthermore, we observed a reduction in symmetry, which could be caused by a staircase-like stacking behavior of this porphyrin COF, producing a splitting of reflections in the X-ray diffraction pattern.

5.2 Results and Discussion

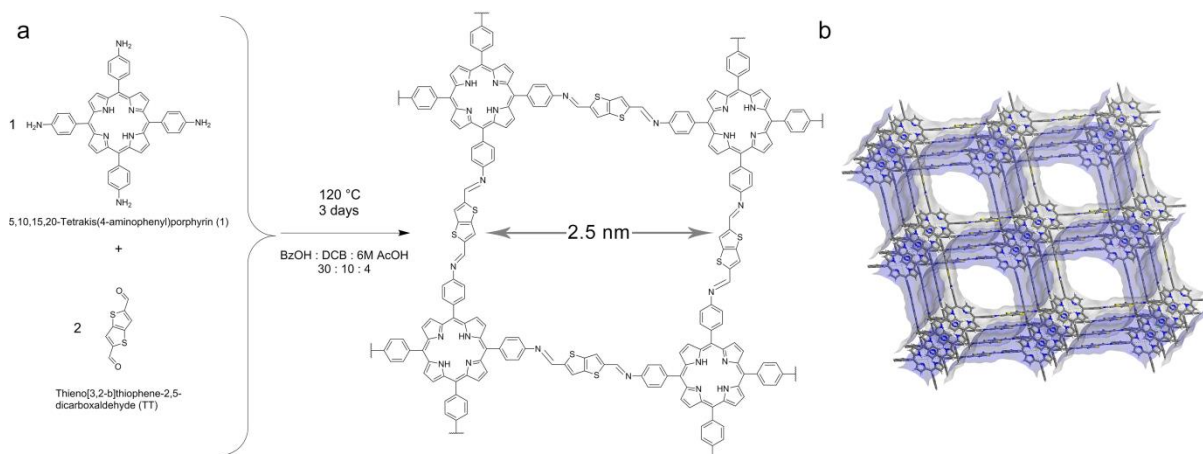


Figure 5.1. (a) Co-condensation reaction of 5,10,15,20-tetrakis(4-aminophenyl)porphyrin (**1**) and thieno[3,2-b]thiophene-2,5-dicarboxaldehyde (TT) in a 1:2 molar ratio to form the TT-Por COF, featuring tetragonal pores with a diameter of 2.5 nm. (b) Illustration of the TT-Por COF, showing the extended, 3 dimensional structure, formed by π - π interacting 2D COF sheets.

5.2 Results and Discussion

The new 2D TT-Por COF was synthesized by combining 5,10,15,20-tetrakis(4-aminophenyl)porphyrin (**1**) with thieno[3,2-b]thiophene-2,5-dicarboxaldehyde (TT) in a 1:2 molar ratio. The solvothermal reaction was carried out in a solvent mixture of benzyl alcohol, dichlorobenzene and 6 molar acetic acid (30:10:4, v:v:v) for 3 days at 120 °C (Figure 5.1a; for experimental data, see the experimental section). The porphyrin units, located at the corners, are linked by the linear TT to form an ordered structure with open channels (Figure 5.1b).

Powder X-ray diffraction (PXRD) measurements of the synthesized bulk material confirmed the formation of a crystalline material. To identify the structure, the calculated pattern of an eclipsed AA-stacking formation was compared to experimental data, but did not match (Figure 5.2a-b). The size of the unit cell, given by the position of the 100 reflection, however, is in good agreement with the measured pattern, suggesting only slight deviations in the unit cell. A shoulder arising on the 100 reflection as well as

5.2 Results and Discussion

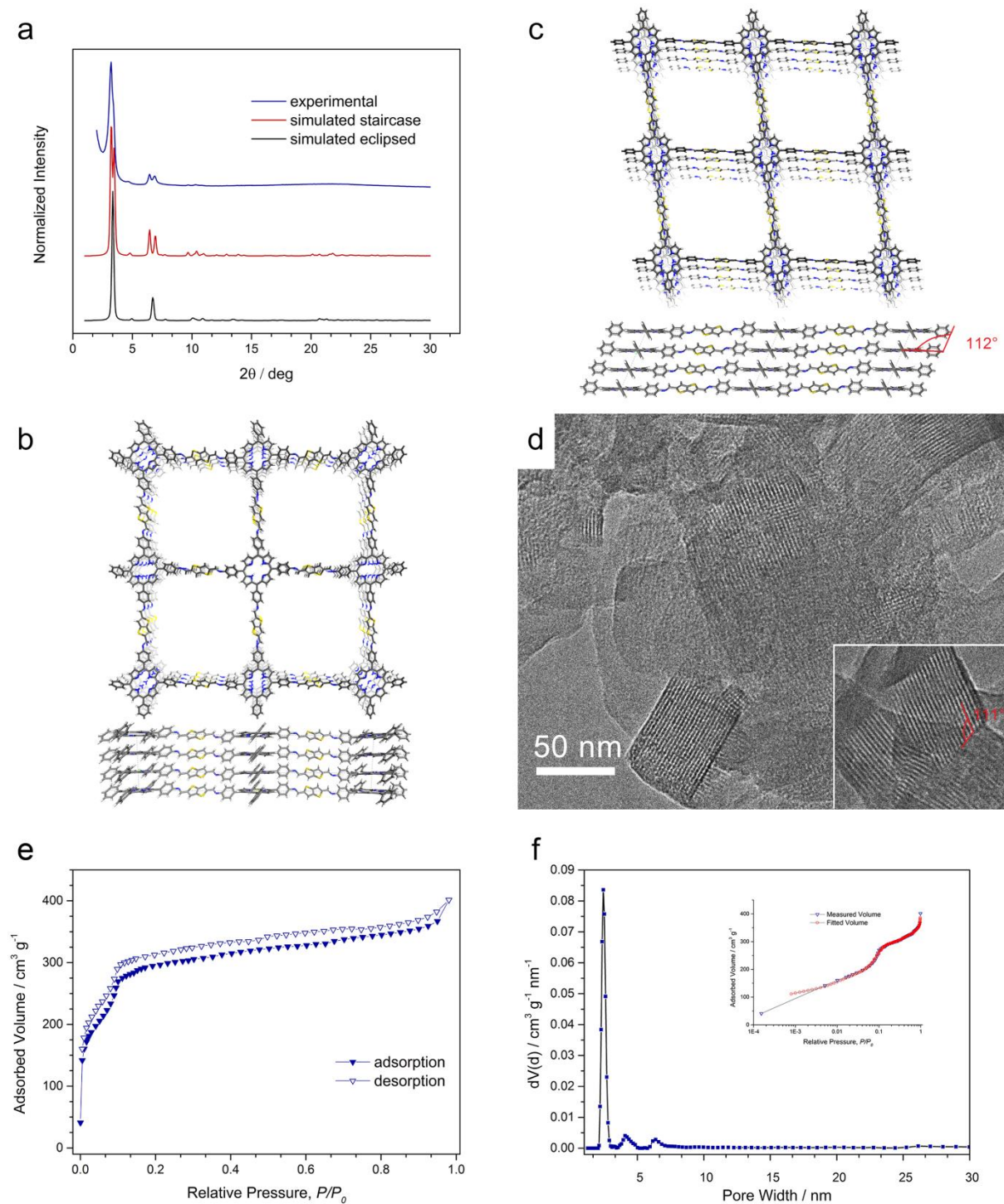


Figure 5.2. (a) Experimental PXRD data (blue) vs. simulated patterns (red and black) for an eclipsed (b) and staircase (c) arrangement of the 2D layers. The theoretical patterns were simulated for a crystallite size of 50 nm. (d) Transmission electron micrograph of TT-Por COF bulk material showing the rectangular pore structure with defined crystal facets (bottom left), straight channels (top right) and the staircase arrangement of the COF with an angle between adjacent layers of 111° (bottom right). (e) Nitrogen sorption isotherm of a TT-Por COF powder sample measured at 77 K. (f) Corresponding pore size distribution with an average pore size of 2.4 nm obtained by fitting the experimental data using a QSDFT adsorption kernel with a fitting error of 0.7 % (inset).

5.2 Results and Discussion

a splitting of the 110 reflection into two new reflections indicates a reduction in symmetry of the unit cell. Performing a geometry optimization using force-field methods by enabling all unit cell parameters to float yielded a simulated pattern that matches the experimental one. In order to produce the experimental pattern without neglecting the symmetry of the starting materials, the unit cell parameter γ has to differ from 90° , resulting in an offset of the adjacent layers (Figure 5.2a and c). This offset results in a staircase-like stacking behavior of this COF, which is so prevalent in one direction that it can be seen in the PXRD pattern. The transmission electron microscopy (TEM) image of the newly synthesized COF confirmed the successful formation of a crystalline and ordered material. Domain sizes of up to 100 nm and the formation of defined rectangular crystal facets could be observed (Figure 5.2d).

Depending on the orientation of the crystallites, the rectangular porous network can be seen from the top, or the porous channels can be observed from the side. Some facets are oriented such that one can see an angle between the sheets (Figure 5.2d, bottom right). The measured angle between the adjacent layers is 111° , which is in excellent agreement with the theoretical angle from the simulated structure (112°). This highly suggests a staircase-like arrangement of the 2D layers (compare Figure 5.2c and d).

Nitrogen sorption measurements revealed the typical shape of a type IV isotherm with a sudden increase in adsorbed volume at $0.09 p/p_0$ (Figure 5.2e) indicative of a uniform pore size. The calculated Brunauer Emmett Teller (BET) surface area is $1000 \text{ m}^2 \text{ g}^{-1}$ with a pore volume of $0.6 \text{ cm}^3 \text{ g}^{-1}$. The pore size, calculated using quenched solid density functional theory (QSDFT) with a carbon kernel for cylindrical pores on the adsorption branch, shows a very narrow distribution with an average pore size of 2.4 nm (Figure 5.2f) with a fitting error of only 0.7 %. This is in good agreement with the theoretical

5.2 Results and Discussion

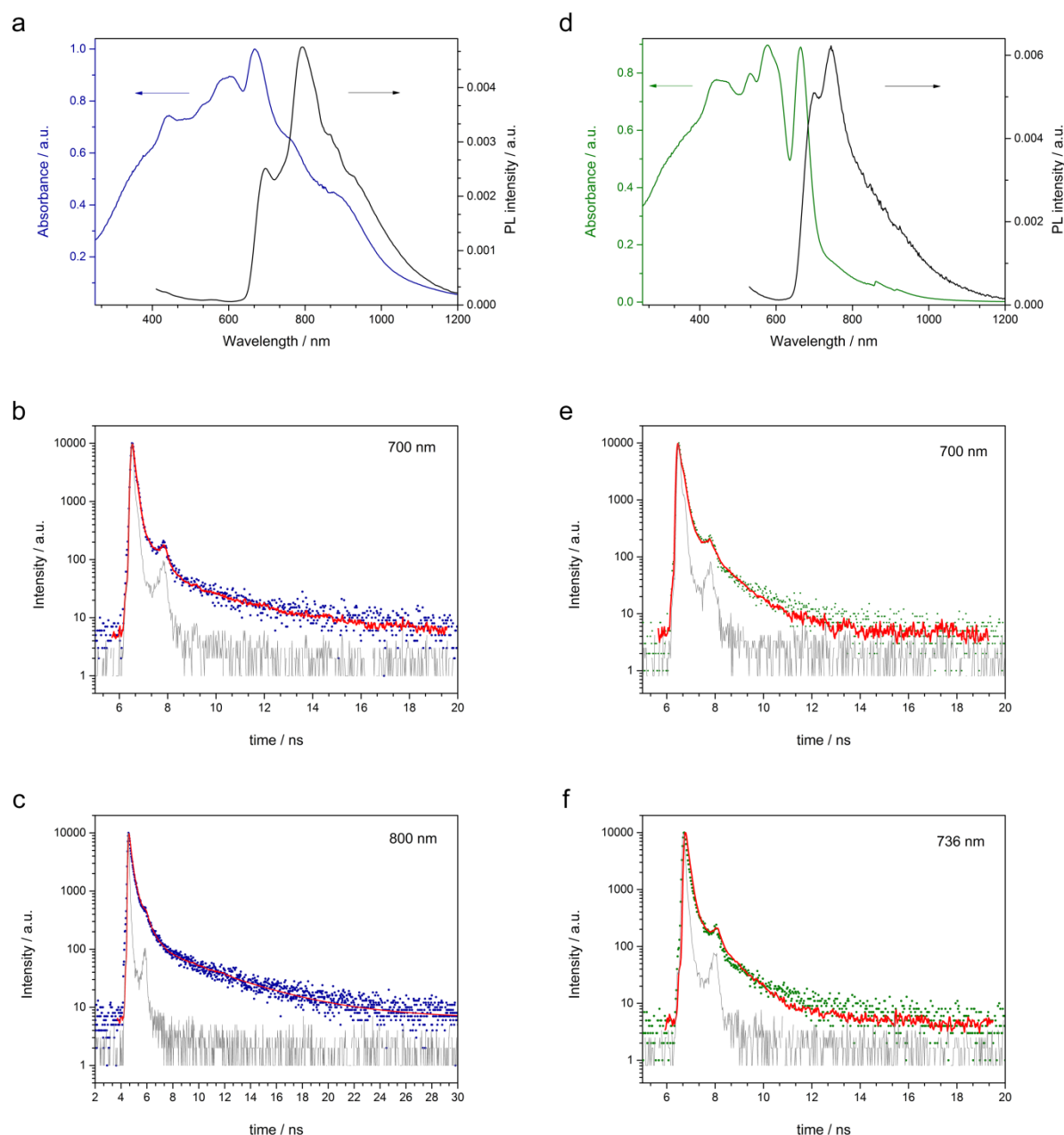


Figure 5.3. (a) Absorption (blue) measured as diffuse reflectance of the solid and converted with the Kubelka Munk equation and PL ($\lambda_{\text{exc}} = 365$ nm, black) spectra of TT-Por COF. (b) Photoluminescence (PL) decay curve for TT-Por COF. The sample was illuminated at 403 nm with a pump fluence of $\sim 0.3 \mu\text{Jcm}^{-2}$; the emission was monitored at the first peak of the PL emission at 700 nm. (c) PL decay curve for TT-Por COF. The sample was illuminated at 403 nm with a pump fluence of $\sim 0.3 \mu\text{Jcm}^{-2}$; the emission was monitored at the maximum of the PL emission at 800 nm. (d) Absorption (green) measured as diffuse reflectance of the solid and converted with the Kubelka Munk equation and PL ($\lambda_{\text{exc}} = 365$ nm, black) spectra of 1P-Por COF. (e) PL decay curve for 1P-Por COF. The sample was illuminated at 403 nm with a pump fluence of $\sim 0.3 \mu\text{Jcm}^{-2}$; the emission was monitored at the first peak of the PL emission at 700 nm. (f) PL decay curve for 1P-Por COF. The sample was illuminated at 403 nm with a pump fluence of $\sim 0.3 \mu\text{Jcm}^{-2}$; the emission was monitored at the maximum of the PL emission at 736 nm.

5.2 Results and Discussion

pore size of 2.5 nm, determined from the simulated structure.

The absorbance spectra of all materials were collected from solid samples in reflection mode and converted by applying the Kubelka Munk equation. The newly synthesized TT-Por COF shows a strong absorbance throughout the UV and visible spectrum, tailing far into the infrared region with distinct features (Figure 5.3a, blue). By comparing the absorption spectra of the starting materials with the one of the COF structure all features can be attributed to the integrated components (Figure 5.6a). When excited with 365 nm light, pronounced photoluminescence occurs with two distinct signals at 700 and 800 nm (Figure 5.3a, black).

Recent work has shown that photoluminescence (PL) dynamics carry important information about diffusion lengths of photo excited species in photovoltaic devices. Here, the lifetime is related to the charge diffusion length of free charge carriers.²³⁻²⁴ To determine the photoluminescence dynamics, TT-Por COF was excited with 405 nm radiation and the photoluminescence decay was measured over time at the two PL signals. The resulting histograms were exponentially fitted, revealing 3 different lifetimes. At 700 nm, the fit of the PL decay reveals that 79 % of the excited species has a very fast decay lifetime of 0.08 ns, followed by a second species with a decay lifetime of 0.51 ns (12 %), and a long living species with lifetimes of 3.17 ns (8.3 %) (Figure 5.3b). When measuring the PL decay lifetime at 800 nm, where the maximum of PL occurs, lifetimes of 0.15 ns (80.6 %), 0.55 ns (18.5 %), and 4.90 ns (16.4 %) for the excited species were found (Figure 5.3c). These results signify an increase in lifetimes of the excited species compared to the neat starting materials TT with 2.3 ns (9.7 %) and 0.42 ns (90.3 %) and **1** with 1.00 ns (100 %) at 700 nm and 0.37 ns (52 %) and 1.01 ns (48 %) at 800 nm, respectively (Figure 5.8, see below).

To investigate the influence of the TT building block on the decay lifetimes, a porphyrin

5.3 Conclusion

COF was synthesized build from compound **1** and terephthal aldehyde forming 1P-Por COF (for more details see experimental section and Figure 5.4 and Figure 5.6b). The absorbance of 1P-Por COF occurs in the region from 250 – 720 nm with a tail reaching to 1000 nm (Figure 5.3d, green). When excited with 365 nm light, PL occurs at 700 and 736 nm (Figure 5.3d, black). The PL decay was measured at 700 nm and bi-exponentially fitted to reveal two different photoluminescent species with lifetimes of 0.13 ns (80.3 %) and 1.04 ns (19.64 %) (Figure 5.3e). Measuring the PL decay at the PL maximum at 736 nm reveals lifetimes of 0.11 ns (80.5 %) and 0.92 ns (19.5 %) for 1P-Por COF (Figure 5.3f). These values are very similar to those of the neat starting materials, suggesting analogical occurring processes leading to the decay of the excited species without any beneficial effects from the order of the COF structure. The electron rich porphyrin unit, coupled to the electron rich phenyl group does not allow for internal charge transfer and delocalization of the electrons, resulting in fast decays of the excited species. In contrast, when conjugated to electron deficient TT building blocks, electrons are enabled to delocalize from the porphyrin units throughout the COF structure. This internal charge transfer allows for a stabilization of generated electrons leading to prolonged lifetimes of the excited species.

5.3 Conclusion

Herein, we have developed a new imine-linked COF, comprising two photoactive sub-units, an electron rich tetragonal porphyrin and electron deficient linear thienothiophene linker. The symmetry of the new material was found to not match a simulated eclipsed structure, but to rather adopt a staircase-like stacking arrangement. PXRD data confirmed a splitting of reflections, caused by a reduction in symmetry. For the first time it was able to observe this prevalence of patterns in a preferred direction

5.3 Conclusion

of the adjacent layers to form this staircase like structure.

Furthermore, the new TT-Por COF was found to stabilize photoluminescent dynamics, resulting in prolonged lifetimes compared to the starting materials or 1P-Por COF. The combination of electron rich and deficient sub-units to construct a COF framework facilitates internal charge transfer, which leads to a delocalization of electrons throughout the framework and thus a stabilization of the excited species.

The high structural order of COFs enables a unique chance to investigate the occurring processes upon excitation on the nanoscale. We believe that the insights gained from these well-defined model systems can be transferred to the currently used organic photovoltaic devices, and help to understand and optimize these systems.

5.4 Experimental

5.4 Experimental

Materials and methods

Unless stated otherwise, all reactions were performed in oven-dried glassware under a positive pressure of Ar. Commercial reagents and solvents were used as received. Thieno[3,2-*b*]thiophene-2,5-dicarboxaldehyde and the 5,10,15,20-(tetra-4-aminophenyl) porphyrin were acquired from Sigma Aldrich and PorphyChem. The solvents were purchased from Sigma-Aldrich in the common purities. All materials were used without further purification.

Infrared (IR) spectra were recorded on a Perkin Elmer Spectrum BX II FT-IR system and a Thermo Scientific Nicolet™ 6700 FT-IR spectrometer in transmission mode. IR data are reported in wavenumbers (cm^{-1}).

The nitrogen sorption isotherm was recorded on a Quantachrome Autosorb 1 at 77.35 K in a pressure range from $p/p^0 = 0.001$ to 0.98. Prior to the measurement of the sorption isotherm, the sample was heated for 24 h at 120°C under turbomolecular pump vacuum. For the evaluation of the surface area, the BET model was applied between 0.05 and 0.2 p/p^0 . The calculation of the pore size distribution was done using the QSDFT equilibrium model with a carbon kernel for cylindrical pores.

X-ray diffraction (XRD) measurements were performed using a Bruker D8 Discover with Ni-filtered Cu K_{α} radiation and a LynxEye position-sensitive detector.

Transmission electron microscopy was performed on an FEI Titan 80-300 equipped with a field emission gun operated at 80 kV. Scanning electron microscopy (SEM) images were recorded with a JEOL 6500F field emission microscope operated at 5 kV using a secondary electron detector.

5.4 Experimental

UV-Vis spectra were recorded using a Perkin-Elmer Lambda 1050 spectrometer equipped with a 150 mm integrating sphere.

Photoluminescence (PL) measurements were performed using a home-built setup consisting of a Horiba Jobin Yvon iHR 320 monochromator equipped with a photomultiplier tube and a liquid N₂-cooled InGaAs detector. The samples were illuminated with a pulsed (83 Hz) 405 nm LED at a light intensity of 500 mW cm⁻².

Time-resolved PL measurements were acquired using a time correlated single photon counting (TCSPC) setup (FluoTime 300, PicoQuant GmbH). The samples were photo-excited using a 507 nm laser head (LDH-P-C-510, PicoQuant GmbH) pulsed at 500 kHz, with a pulse duration of 117 ps and fluence of ~300 nJcm⁻²/pulse. The samples were exposed to the pulsed light source set at 3 μJcm⁻²/pulse fluence for ~10 minutes prior to measurement to ensure stable sample emission. The PL was collected using a high-resolution monochromator and hybrid photomultiplier detector assembly (PMA Hybrid 40, PicoQuant GmbH).

5.4 Experimental

Synthesis

TT-Por COF

For the synthesis of TT-Por COF 13.5 mg of compound **1** (0.02 mmol, 1 equiv.) and 7.9 mg of TT (0.04 mmol, 2 equiv.) were added to a 10 mL *Schott* culture tube with screw cap and dispersed in a solvent mixture of benzyl alcohol, o-dichlorobenzene and 6M acetic acid (30:10:4 v:v:v, 550 μ L). The tube was placed in an oven at 120 °C for 72 h. After the time had elapsed, the reaction mixture was allowed to cool down to room temperature and the resulting powder was then collected by filtration through a Hirsch funnel. After washing the product three times with dry 1,2-dioxane it was left under dynamic vacuum to come to complete dryness.

1P-Por COF

13.5 mg compound **1** (0.02 mmol, 1 equiv.) and 5.36 mg of terephthal aldehyde (0.04 mmol, 2 equiv.) were dispersed in a solvent mixture of benzyl alcohol, mesitylene and 6M acetic acid (10:20:3 v:v:v, 550 μ L) in a 10 mL *Schott* culture tube with screw cap. The tube was heated in an oven to 120 °C for 72 h. After cooling down, the product was isolated by filtration, followed by three washing cycles with 1,4-dioxane. The dark purple product was brought to complete dryness under reduced pressure.

5.4 Experimental

Simulation of the TT-Por COF crystal structure

To determine the crystal structure of the obtained product, a powder diffraction pattern was calculated based on a simulated crystal structure. The unit cell was constructed using the Materials Studio software and optimized by force field calculations. Due to the non-planar porphyrin building block, the unit cell is limited to a triclinic *P1* symmetry in the case of a stacked staircase structure and to *P4* symmetry for an eclipsed arrangement. The comparison of the calculated pattern with the experimental data identified the obtained structure as staircase stacked TT-Por COF.

Table 5.1. Refined crystal data.

Formula	$C_{60} H_{42} N_8 S_4$
Formula weight	$2082.96 \text{ g mol}^{-1}$
Crystal system	triclinic
Space-group	<i>P1</i>
Cell parameters	$a = 27.96 \text{ \AA}$ $b = 27.92 \text{ \AA}$, $c = 4.51 \text{ \AA}$ $\alpha = 113.8$ $\beta = 80.0$ $\gamma = 96.0$

5.4 Experimental

XRD spectroscopy

1P-Por COF was analyzed via PXRD revealing a crystalline network.

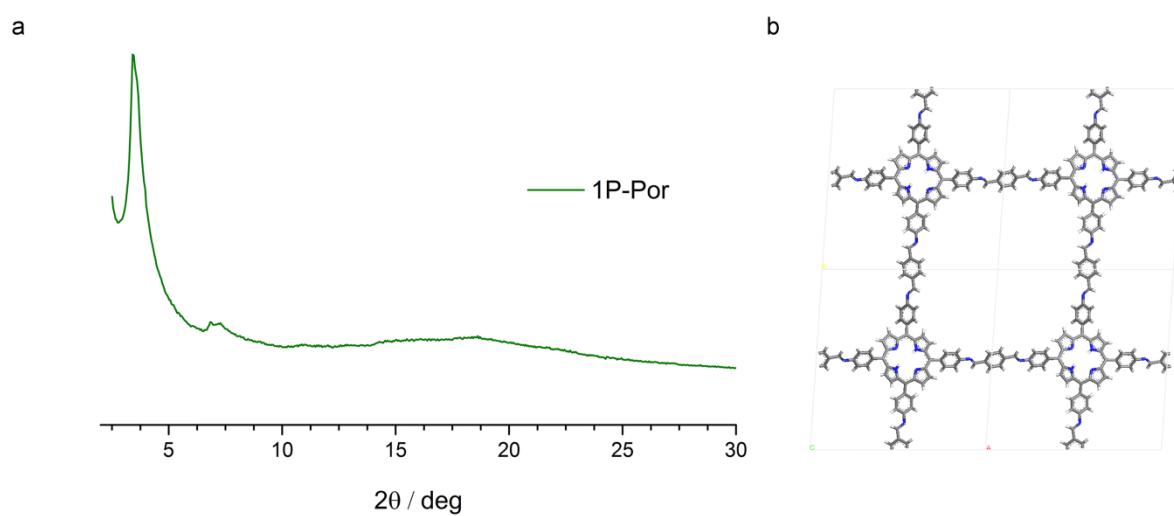


Figure 5.4. (a) PXRD pattern of 1P-Por COF. (b) Simulated crystal structure of 1P-Por COF.

5.4 Experimental

IR spectroscopy

The successful formation of the imine-linked TT-Por COF was confirmed by Fourier transform infrared (FTIR) spectroscopy. Consistent with previously reported COFs, the appearance of the characteristic C=N stretching mode at 1585 cm^{-1} indicates the coupling of the monomers via an imine bond (Figure 6.4). The lack of the aldehyde Fermi double resonance at 2841 and 2755 cm^{-1} as well as the aldehyde C=O stretching vibration at 1700 cm^{-1} suggests the complete consumption of the starting material TT-dialdehyde. Furthermore, the attenuation of the characteristic C-N stretching mode at 1284 cm^{-1} indicates the absence of the second starting material porphyrin-tetra-phenylamine.²⁵⁻²⁶

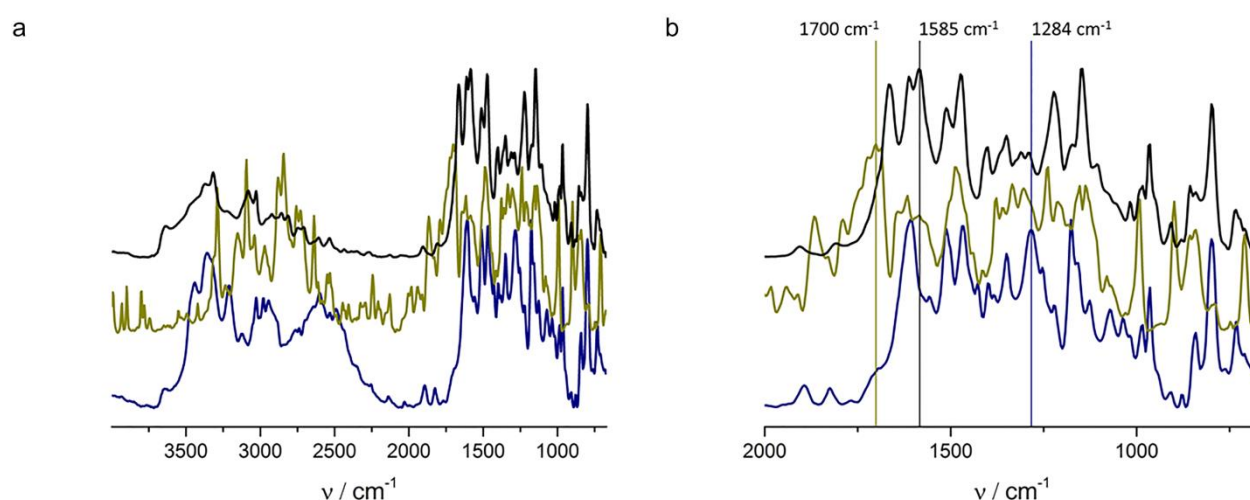


Figure 5.5. (a) IR spectra of TT-Por COF (black), thienothiophene monomer (dark yellow) and porphyrin monomer (blue), measured as powder. (b) Enlargement of the region of interest.

5.4 Experimental

UV-Vis / photoluminescence spectroscopy

Absorption spectra of the starting materials, TT-Por COF, and 1P-Por COF were collected from solid samples in diffuse reflection mode and transferred into absorption spectra by applying the Kubelka Munk equation:

$$\frac{K}{S} = \frac{(1 - R_{\infty})^2}{2R_{\infty}}$$

with K = Absorption Coefficient, S = the Scattering Coefficient, R_{∞} = reflectance of sample with infinite thickness.²⁷

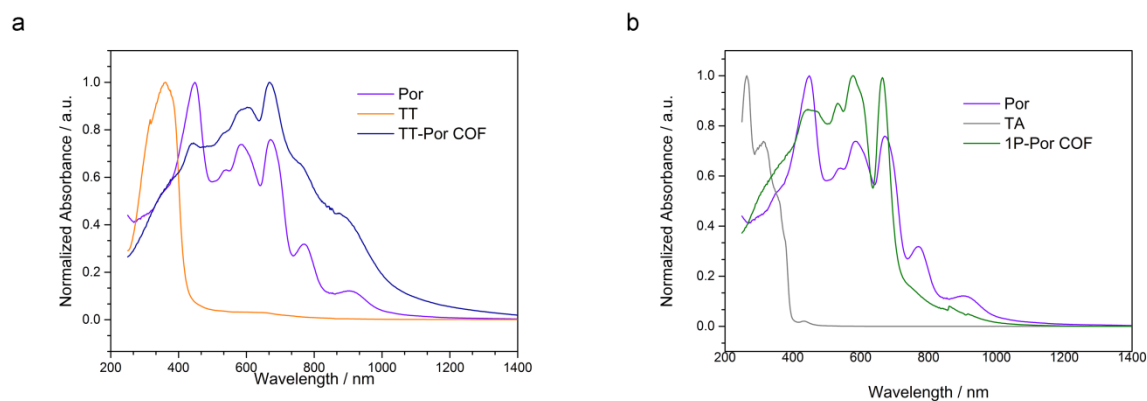


Figure 5.6. (a) UV-Vis spectra of TT-Por COF (blue) and the corresponding starting materials compound **1** (Por, purple) and thienothiophene (TT, orange). (b) UV-Vis spectra of 1P-Por COF (green) and the corresponding starting materials compound **1** (Por, purple) and terephthal aldehyde (TA, gray).

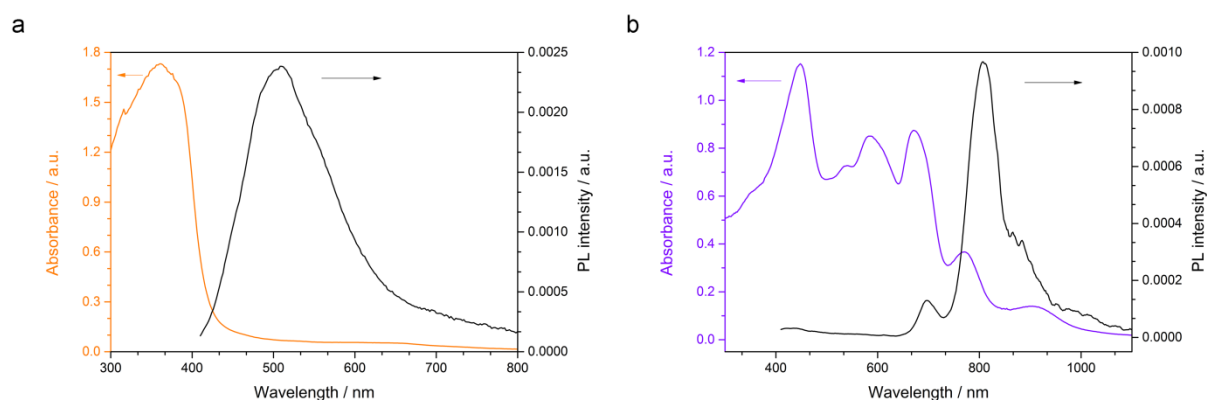


Figure 5.7. (a) Absorption (orange) and PL ($\lambda_{\text{exc}} = 365$ nm, black) spectra of the TT starting material. (b) Absorption (purple) and PL ($\lambda_{\text{exc}} = 365$ nm, black) spectra of the compound **1**.

5.4 Experimental

Time Correlated Single Photon Counting

The PL lifetime was measured of the two starting materials TT and (**1**) by illumination at 405 nm with a pump fluence of $\sim 0.3 \mu\text{Jcm}^{-2}$; the emission was monitored at the maximum of the PL emission at 510 nm for TT and at 700 nm and 800 nm for (**1**).

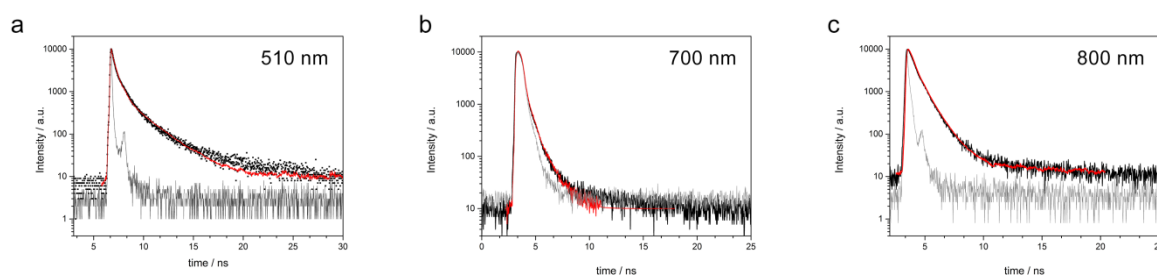


Figure 5.8. (a) PL decay of TT linker (black dots), bi-exponential fit of the decay (red) and instrument response function (gray) excited with 405 nm and measured at the PL maximum at 510 nm. (b) PL decay of compound (**1**) (black dots) measured at the first PL maximum at 700 nm, bi-exponential fit of the decay (red) and instrument response function (gray). (c) PL decay of compound (**1**) (black dots) measured at the second PL maximum at 800 nm, bi-exponential fit of the decay (red) and instrument response function (gray).

5.5 References

1. A. P. Côte; A. I. Benin; N. W. Ockwig; M. O'Keeffe; A. J. Matzger; O. M. Yaghi, Porous, Crystalline, Covalent Organic Frameworks. *Science* **2005**, *310*, 1166-1170.
2. C. J. Doonan; D. J. Tranchemontagne; T. G. Glover; J. R. Hunt; O. M. Yaghi, Exceptional ammonia uptake by a covalent organic framework. *Nat. Chem.* **2010**, *2* (3), 235-238.
3. M. G. Rabbani; A. K. Sekizkardes; Z. Kahveci; T. E. Reich; R. Ding; H. M. El-Kaderi, A 2D Mesoporous Imine-Linked Covalent Organic Framework for High Pressure Gas Storage Applications. *Chem. Eur. J.* **2013**, *19* (10), 3324-3328.
4. S.-Y. Ding; J. Gao; Q. Wang; Y. Zhang; W.-G. Song; C.-Y. Su; W. Wang, Construction of Covalent Organic Framework for Catalysis: Pd/COF-LZU1 in Suzuki–Miyaura Coupling Reaction. *J. Am. Chem. Soc.* **2011**, *133* (49), 19816-19822.
5. S. Lin; C. S. Diercks; Y.-B. Zhang; N. Kornienko; E. M. Nichols; Y. Zhao; A. R. Paris; D. Kim; P. Yang; O. M. Yaghi; C. J. Chang, Covalent organic frameworks comprising cobalt porphyrins for catalytic CO₂ reduction in water. *Science* **2015**, *349* (6253), 1208-1213.
6. M. Calik; F. Auras; L. M. Salonen; K. Bader; I. Grill; M. Handloser; D. D. Medina; M. Dogru; F. Löbermann; D. Trauner; A. Hartschuh; T. Bein, Extraction of Photogenerated Electrons and Holes from a Covalent Organic Framework Integrated Heterojunction. *J. Am. Chem. Soc.* **2014**, *136* (51), 17802-17807.
7. M. Dogru; M. Handloser; F. Auras; T. Kunz; D. Medina; A. Hartschuh; P. Knochel; T. Bein, A Photoconductive Thienothiophene-Based Covalent Organic Framework Showing Charge Transfer Towards Included Fullerene. *Angew. Chem. Int. Ed.* **2013**, *52*, 2920-2924.
8. H. L. Anderson, Building molecular wires from the colours of life: conjugated porphyrin oligomers. *Chem. Commun.* **1999**, (23), 2323-2330.
9. L. Li; Y. Huang; J. Peng; Y. Cao; X. Peng, Highly responsive organic near-infrared photodetectors based on a porphyrin small molecule. *J. Mater. Chem. C* **2014**, *xx*, xxxx.
10. Y. Li; F. Auras; F. Löbermann; M. Döblinger; J. Schuster; L. Peter; D. Trauner; T. Bein, A Photoactive Porphyrin-Based Periodic Mesoporous Organosilica Thin Film. *J. Am. Chem. Soc.* **2013**, *135*, 18513-18519.
11. L. Luo; C.-J. Lin; C.-S. Hung; C.-F. Lo; C.-Y. Lin; E. W.-G. Diau, Effects of potential shift and efficiency of charge collection on nanotube-based porphyrin-sensitized solar cells with conjugated links of varied length. *Phys. Chem. Chem. Phys.* **2010**, *12*, 12973-12977.
12. N. C. Maiti; S. Mazumdar; N. Periasamy, J- and H-Aggregates of Porphyrin-Surfactant Complexes: Time-Resolved Fluorescence and Other Spectroscopic Studies. *J. Phys. Chem. B* **1998**, *102*, 1528-1538.
13. M. V. Martínez-Díaz; G. de la Torre; T. Torres, Lighting porphyrins and phthalocyanines for molecular photovoltaics. *Chem. Commun.* **2010**, *46*, 7090-7108.
14. X. Feng; L. Chen; Y. Dong; D. Jiang, Porphyrin-based two-dimensional covalent organic frameworks: synchronized synthetic control of macroscopic structures and pore parameters. *Chem. Commun.* **2011**, *47*, 1979-1981.
15. X. Feng; L. Liu; Y. Honsho; A. Saeki; S. Seki; S. Irle; Y. Dong; A. Nagai; D. Jiang, High-Rate Charge-Carrier Transport in Porphyrin Covalent Organic Frameworks: Switching from Hole to Electron to Ambipolar Conduction. *Angew. Chem. Int. Ed.* **2012**, *51*, 2618-2622.
16. S. Jin; X. Ding; X. Feng; M. Supur; K. Furukawa; S. Takahashi; M. Addicoat; M. E. El-Khouly; T. Nakamura; S. Irle; S. Fukuzumi; A. Nagai; D. Jiang, Charge Dynamics in A

5.5 References

Donor-Acceptor Covalent Organic Framework with Periodically Ordered Bicontinuous Heterojunctions. *Angew. Chem. Int. Ed.* **2013**, *52*, 2017-2021.

17. S. Jin; K. Furukawa; M. Addicoat; L. Chen; S. Takahashi; S. Irle; T. Nakamura; D. Jiang, Large pore donor-acceptor covalent organic frameworks. *Chem. Sci.* **2013**, *4*, 4505-4511.

18. S. Kandambeth; D. B. Shinde; M. K. Panda; B. Lukose; T. Heine; R. Banerjee, Enhancement of Chemical Stability and Crystallinity in Porphyrin-Containing Covalent Organic Frameworks by Intramolecular Hydrogen Bonds. *Angew. Chem. Int. Ed.* **2013**, *52*, 13052-13056.

19. V. S. P. K. Neti; X. Wu; S. Deng; L. Echegoyen, Synthesis of a phthalocyanine and porphyrin 2D covalent organic framework. *CrystEngComm* **2013**, *15*, 6892-6895.

20. E. L. Spitler; B. T. Koo; J. L. Novotney; J. W. Colson; F. J. Uribe-Romo; G. D. Gutierrez; P. Clancy; W. R. Dichtel, A 2D Covalent Organic Framework with 4.7-nm Pores and Insight into Its Interlayer Stacking. *J. Am. Chem. Soc.* **2011**, *133*, 19416-19421.

21. W. Zhou; H. Wu; T. Yildirim, Structural stability and elastic properties of prototypical covalent organic frameworks. *Chem. Phys. Lett.* **2010**, *499* (1-3), 103-107.

22. L. Ascherl; T. Sick; J. T. Margraf; S. H. Lapidus; M. Calik; C. Hettstedt; K. Karaghiosoff; M. Döblinger; T. Clark; K. W. Chapman; F. Auras; T. Bein, Molecular docking sites designed for the generation of highly crystalline covalent organic frameworks. *Nat. Chem.* **2016**, *advance online publication*.

23. S. D. Stranks; G. E. Eperon; G. Grancini; C. Menelaou; M. J. Alcocer; T. Leijtens; L. M. Herz; A. Petrozza; H. J. Snaith, Electron-hole diffusion lengths exceeding 1 micrometer in an organometal trihalide perovskite absorber. *Science* **2013**, *342* (6156), 341-344.

24. G. Xing; N. Mathews; S. Sun; S. S. Lim; Y. M. Lam; M. Grätzel; S. Mhaisalkar; T. C. Sum, Long-range balanced electron-and hole-transport lengths in organic-inorganic CH₃NH₃PbI₃. *Science* **2013**, *342* (6156), 344-347.

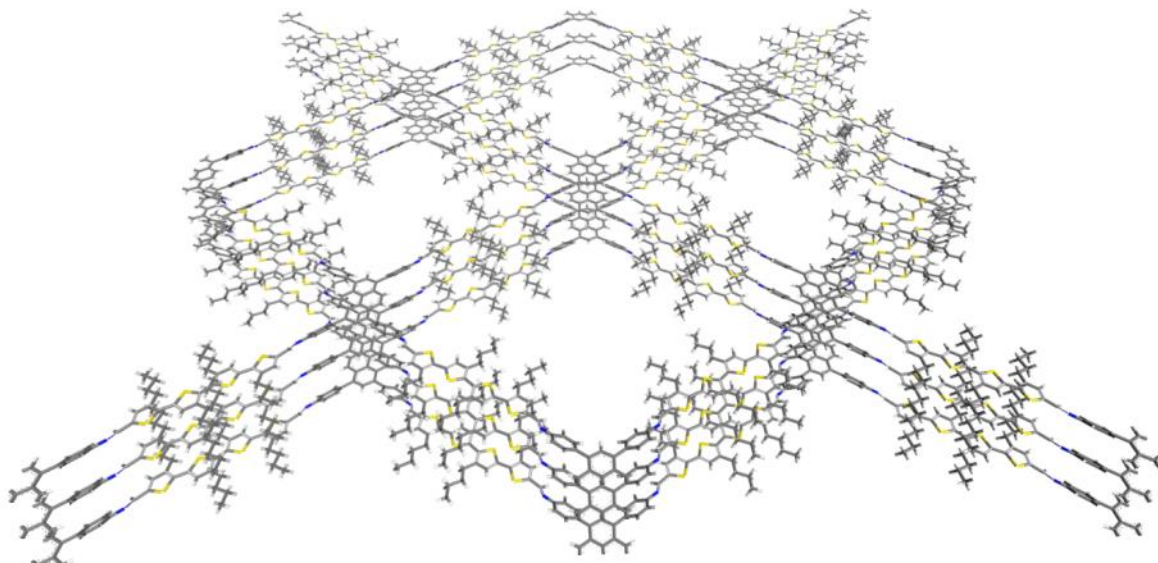
25. F. J. Uribe-Romo; J. R. Hunt; H. Furukawa; C. Klöck; M. O'Keeffe; O. M. Yaghi, A crystalline imine-linked 3-D porous covalent organic framework. *J. Am. Chem. Soc.* **2009**, *131* (13), 4570-4571.

26. L. Stegbauer; K. Schwinghammer; B. V. Lotsch, A hydrazone-based covalent organic framework for photocatalytic hydrogen production. *Chemical Science* **2014**, *5* (7), 2789-2793.

27. P. Kubelka; F. Munk, An article on optics of paint layers. *Z. Tech. Phys* **1931**, *12* (593-601).

6. Development of an Asymmetric Linker as Key for the Construction of Extended Covalent Organic Frameworks

This chapter is based on the work in collaboration with Niklas Keller and Florian Auras.



Abstract

Covalent organic frameworks (COFs) have evoked much interest as they offer the possibility to fine-tune the properties of periodic porous systems on the nanoscale. Their pore geometry, pore size and shape are determined by the constituent organic building blocks. In two-dimensional (2D) COFs, the two dimensional sheets stack through π - π interactions to form 3D materials that can enable charge transport along the stacked columns.

In order to achieve a better understanding of the influence of the chosen molecular building blocks on the properties of the resulting frameworks, a variety of possible building units and the corresponding COFs need to be developed and investigated.

5.5 References

Herein, we report the synthesis of an asymmetric molecule as building block for the COF synthesis and the successful formation of a new COF. The resulting pyrene-tetrathioephene (Pyr-4T) COF is based on imine-linked tetrathioephene and pyrene linker molecules, and adopts a layered structure with tetragonal pores that are decorated with butyl chains. This Pyr-4T COF exhibits crystallinity with a high degree of order. Initial measurements of its photoluminescence (PL) and the lifetime of the photoluminescent species reveal its high potential as photoactive material. We anticipate that the introduction of asymmetric solubilizing chains offers great potential to synthesize new extended functional linkers and thus is the key to create functional COFs constructed from extended linker molecules.

6.1 Introduction

6.1 Introduction

Since the development of covalent organic frameworks in 2005, many efforts have been made to understand and enhance the properties of these unique materials.¹⁻⁶ One focus of research lies on the development of highly functional building blocks. COFs are light-weight materials assembled through strong covalent bonds between organic linker molecules. In 2D COFs, the emerging 2-dimensional layers stack via π - π -interactions to form an extended porous framework. The geometry and size of the pore system strongly depend on the length and shape of the building units, as well as their connectivity. Moreover, the properties of the resulting materials can be influenced by integrating photoactive and/or photoluminescent units.⁷⁻⁹

Oligo- and polythiophenes can feature electrical conductivity and have attracted much attention as photoconductive materials.¹⁰⁻¹¹ For example, so-called double cable polymers with polythiophene as backbone component have been reported in 1996 by Benincori *et al.*¹² Their outstanding conductivity led to the development of highly efficient bulk heterojunctions based on poly(3-hexylthiophene) (P3HT) and fullerene derivatives such as P3HT:PCBM.¹³ Moreover, integrated into a COF structure, thiophenes were found to enable and conduct light-induced charges to be collected within the first COF:PCBM solar cell device.⁸

In contrast to kinetically controlled polymer synthesis based on irreversible covalent bond formation, the synthesis of crystalline COFs requires slight reversibility of the polymerization reaction.¹⁴ The reversibility of the bond formation allows the system to form, break and re-form covalent bonds, which provides a “self-healing” feedback mechanism. The difficulty in synthesizing a new COF lies in the adjustment of the building block reactivity and of the solvent mixtures to find the optimum ratio between

6.2 Results and Discussion

condensation and dissociation of the starting materials. Moreover, the solubility of the building blocks in the solvent mixture should enable sufficient polymerization rates.

In this work a new linker molecule was developed by coupling multiple thiophene units to extend the π -system and thus the optical absorption in the visible. To tune its solubility, alkyl groups were installed in an asymmetric fashion. We anticipate that the asymmetric nature of the building block leads to an enhancement in crystallinity of the resulting network, as a possible alternating stacking of those units can reduce steric repulsion during stacking.

6.2 Results and Discussion

The new Pyr-4T COF was synthesized by combining 4,4',4'',4'''-(1,8-dihydropyrene-1,3,6,8-tetrayl) tetraaniline (pyrene) and 3,3''-dibutyl-[2,2':5',2'':5'',2'''-quaterthiophene]-5,5'''-dicarbaldehyde (4T) in a 2 : 1 molar ratio in a solvent mixture of benzyl alcohol and 6M acetic acid (10 : 1, v : v) (Figure 6.1a; for experimental data, see the experimental section). The synthesis strategy for the 4T units is described in the experimental section. The resulting anticipated framework exhibits an average theoretical pore size of 3.7 nm (Figure 6.1a and b).

The successful formation of a crystalline material was confirmed by powder X-ray (PXRD) diffraction, revealing a highly ordered system with even high angle reflections visible (Figure 6.2a). To identify the structure of the newly synthesized material, the crystal structure was simulated using the Materials Studio software. As the 4T building units exhibit substantial asymmetry, a precise determination of the location of the alkyl groups was not possible. Therefore, the structure was simulated assuming all thiophenes bearing a butyl chain, each with an occupancy of 50 %. The experimental

6.2 Results and Discussion

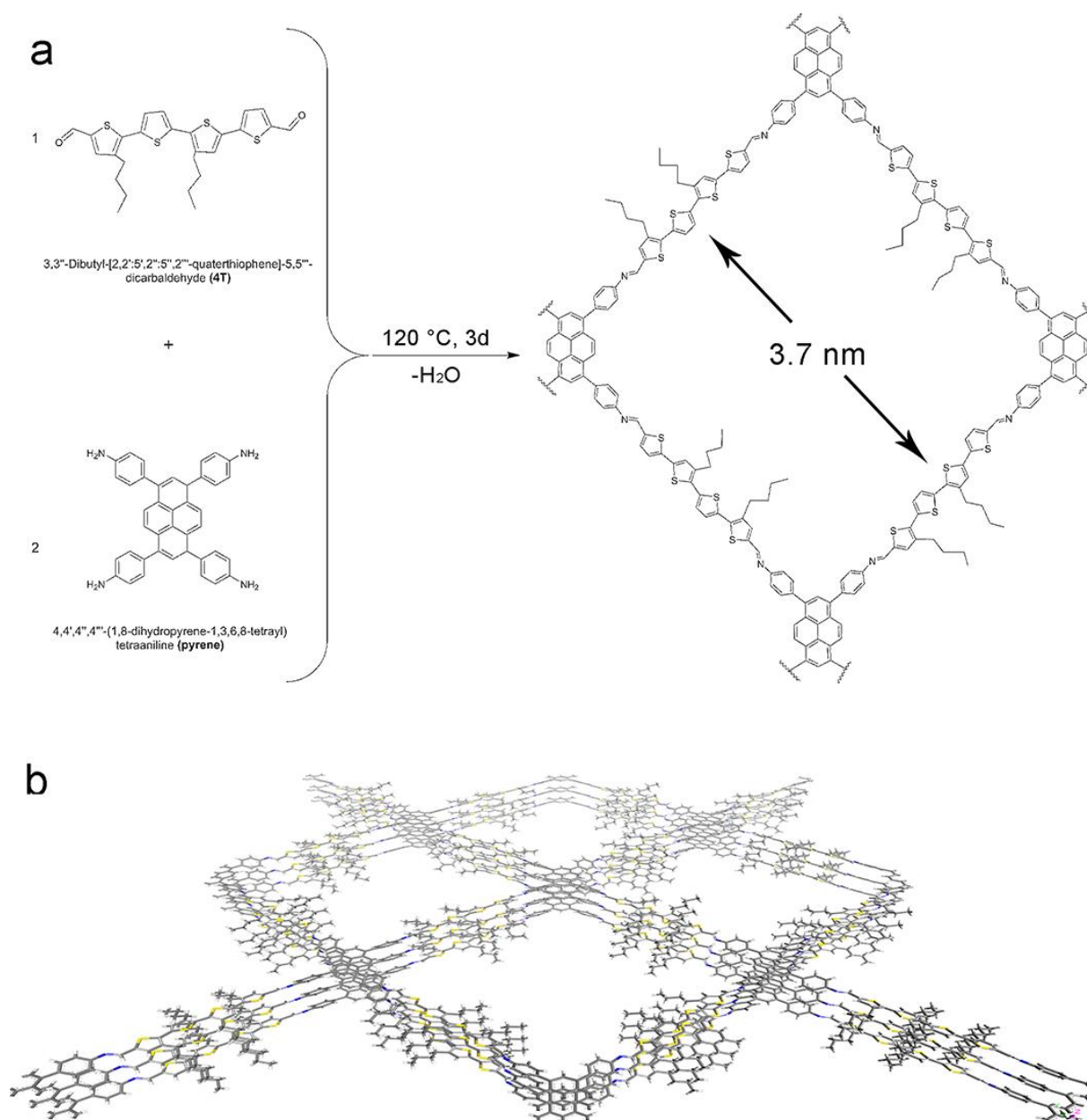


Figure 6.1. (a) Co-condensation reaction of 4T and pyrene in a 1:2 molar ratio to form the Pyr-4T COF, featuring tetragonal pores with a diameter of 3.7 nm. (b) Illustration of the Pyr-4T COF, showing the extended, 3 dimensional structure of a 2x2 unit cell, formed by π - π interacting 2D COF sheets.

6.2 Results and Discussion

data agree very well with the simulated pattern for a tetragonal unit cell with an eclipsed stacking arrangement (Figure 6.2a and b). At higher angles the typical 001 reflection is observed. The position of this reflection indicates the distance between adjacent layers. The maximum of the 001 reflection arises at $23.7\ 2\theta$, thus the interlayer distance can be calculated to be $3.75\ \text{\AA}$ by applying the *Scherrer* equation.

Pyr-4T COF was further characterized by electron microscopy. Transmission electron microscopy (TEM) images show the porous channels of the extended COF structure in side view, with crystal domains sized up to about $100\ \text{nm}$ (Figure 6.2c). The scanning electron micrograph (SEM) reveals a cauliflower-like macrostructure with intergrown spherical particles ranging from $100 - 250\ \text{nm}$ in size (Figure 6.2d).

The successful formation of the imine-linkage between the pyrene and 4T units within the Pyr-4T COF was confirmed by Fourier transform infrared (FTIR) spectroscopy (experimental section, Figure 6.4). The missing vibrational modes for the characteristic aldehyde C=O stretching vibration at $1676\ \text{cm}^{-1}$ as well as the C-N stretching mode at $1270\ \text{cm}^{-1}$ and the N-H wagging vibration at $766\ \text{cm}^{-1}$, typical for primary amines, are indicative for the absence of all starting materials. The appearance of the characteristic C=N stretching mode at $1575\ \text{cm}^{-1}$ suggests the successful formation of the Pyr-4T COF through the formation of imine bonds.¹⁵

Pyr-4T COF exhibits a maximum in the optical absorbance at $465\ \text{nm}$ with a shoulder reaching far into the visible and near IR region of the spectrum (Figure 6.2e). When excited with $455\ \text{nm}$ light, the COF shows a distinct photoluminescence (PL), red-shifted to the absorbance by $161\ \text{nm}$ with a maximum at $626\ \text{nm}$ (Figure 6.2e). The absorbance and PL spectra are broadened and red shifted compared to the corresponding spectra of the 4T monomer (experimental section, Figure 6.5). This can be attributed to the larger

6.2 Results and Discussion

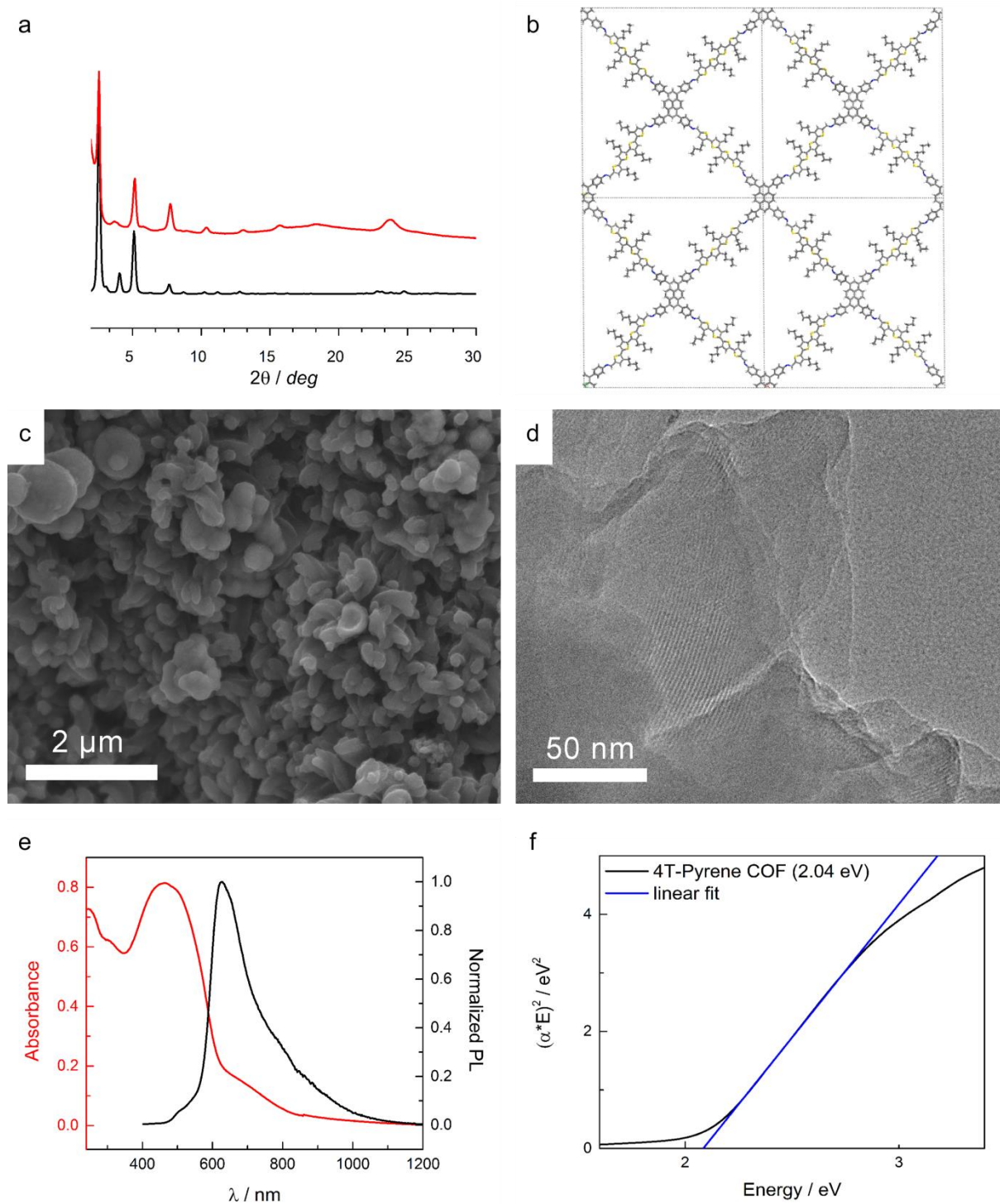


Figure 6.2. (a) Experimental PXRD data (red) vs. simulated patterns (black) for an eclipsed (b) arrangement of the 2D layers. The theoretical patterns were simulated for a crystallite size of 50 nm. (c) Transmission electron micrograph of Pyr-4T COF bulk material showing the straight porous channels in side view. (d) Scanning electron micrograph of a Pyr-4T COF powder sample revealing the intergrowth of smaller COF domains. (e) Transmission absorption (blue) and normalized PL ($\lambda_{\text{exc}} = 455 \text{ nm}$, black) spectra of Pyr-4T COF. (f) Tauc plot of the absorption spectrum with a linear fit to estimate the optical band gap, resulting in 2.04 eV.

6.2 Results and Discussion

conjugated system of pyrene moieties coupled to the 4T within the COF. The experimental data of the absorbance were used for bandgap calculations by applying the Tauc plot assuming a direct bandgap.

The steep increase in absorbance which can be seen in Figure 6.2e signifies the bandgap for the Pyr-4T COF where photons with energy corresponding to the bandgap are absorbed. The distinct linear section in the Tauc plot indicates this onset of absorption and by extrapolating this section to the abscissa with a linear fit the energy of the optical bandgap of Pyr-4T COF can be estimated to be 2.04 eV (Figure 6.2). The enlargement of the molecular crystal to a 2D COF network with an extended electronic system leads to a significant decrease in energy compared to the 4T monomer with a HOMO-LUMO energy difference of 2.63 eV (experimental section, Figure 6.5b). The conjugation of the two monomers pyrene and 4T within the Pyr-4T COF enables internal charge transfer, resulting in a beneficial shifting of the absorption spectrum in the visible region.

Furthermore, the photoluminescent lifetime of the excited species was measured using time correlated single photon counting (TCSPC). In order to ensure that the observed signals in the PL spectrum belong to the same species and do not implicate the presence of another species or impurities, the measurements were performed for both the global (626 nm) and local maxima (660 nm). The results show that the measured lifetimes coincide and thus no impurities are the source of the PL signal but both maxima correspond to one system, the Pyr-4T covalent organic framework (experimental section, Figure 6.6a). Applying a bi-exponential decay fit revealed the photoluminescent lifetimes for the Pyr-4T COF to be 1.07 ns and 0.05 ns. The PL lifetime of the 4T monomer exhibits a lifetime of only 0.58 ns (experimental section, Figure 6.6b)

6.3 Conclusion

6.3 Conclusion

In this work we successfully synthesized a new linker molecule composed of 4 thiophene units with 2 alkyl chains, installed in an asymmetric fashion. These asymmetrically arranged alkyl chains not only tune the solubility such that a successful synthesis of the COF can be achieved but also offer the possibility of alternating their position and thus reducing steric repulsion between adjacent layers.

The newly formed Pyr-4T COF exhibits high crystallinity, indicated by the diffraction pattern showing even high angle reflections with narrow peak widths.

The incorporation of the 4T monomer within an ordered COF structure broadened and extended the absorption and photoluminescent spectra to lower energy compared to those of the monomers. This corresponds to a decrease in the optical bandgap energy of about 20 %.

The introduction of alkyl chains in an asymmetric fashion enables the construction of linkers with extended π -systems while retaining their solubility to construct COFs. The asymmetry of the solubilizing groups thereby does not hinder the crystallization as the linker molecules can reduce steric strain by alternating within the crystalline framework. We anticipate that this approach for the design of large linker molecules will offer new opportunities for the construction of novel COF structures comprising large and complex building blocks.

6.4 Experimental

6.4 Experimental

Unless stated otherwise, all reactions were performed in oven-dried glassware under a positive pressure of Ar. Commercial reagents and solvents were used as received. Reactions were stirred magnetically and monitored by NMR spectroscopy or analytical thin-layer chromatography (TLC) using E. Merck 0.25 mm silica gel 60 F254 pre-coated glass plates. TLC plates were visualized by exposure to ultraviolet light (254 nm). Flash column chromatography was performed employing silica gel (60 Å, 40–63 µm, Merck).

Nuclear magnetic resonance (NMR) spectra were recorded on Varian VNMRS 300, VNMRS 400, INOVA 400 or VNMRS 600 spectrometers. Proton chemical shifts are expressed in parts per million (δ scale) and are calibrated using residual undeuterated solvent peak as an internal reference (CDCl_3 : δ 7.26; $\text{THF-}d_8$: δ 1.72, 3.58). Data for ^1H NMR spectra are reported as follows: chemical shift (δ ppm) (multiplicity, coupling constant/Hz, integration). Multiplicities are reported as follows: s = singlet, d = doublet, t = triplet, q = quartet, m = multiplet, br = broad, or combinations thereof.

Infrared (IR) spectra were recorded on a Perkin Elmer Spectrum BX II FT-IR system and a Thermo Scientific Nicolet™ 6700 FT-IR spectrometer in transmission mode. IR data is reported in frequency of absorption (cm^{-1}).

Mass spectrometry (MS) experiments were performed on a Thermo Finnigan MAT 95 (EI) or on a Thermo Finnigan LTQ FT (ESI) instrument.

X-ray diffraction (XRD) measurements were performed using a Bruker D8 Discover with Ni-filtered $\text{Cu K}\alpha$ radiation and a LynxEye position-sensitive detector.

Transmission electron microscopy was performed on an FEI Titan 80-300 equipped with a field emission gun operated at 80 kV. Scanning electron microscopy (SEM) images were recorded with a JEOL 6500F field emission microscope operated at 5 kV using a

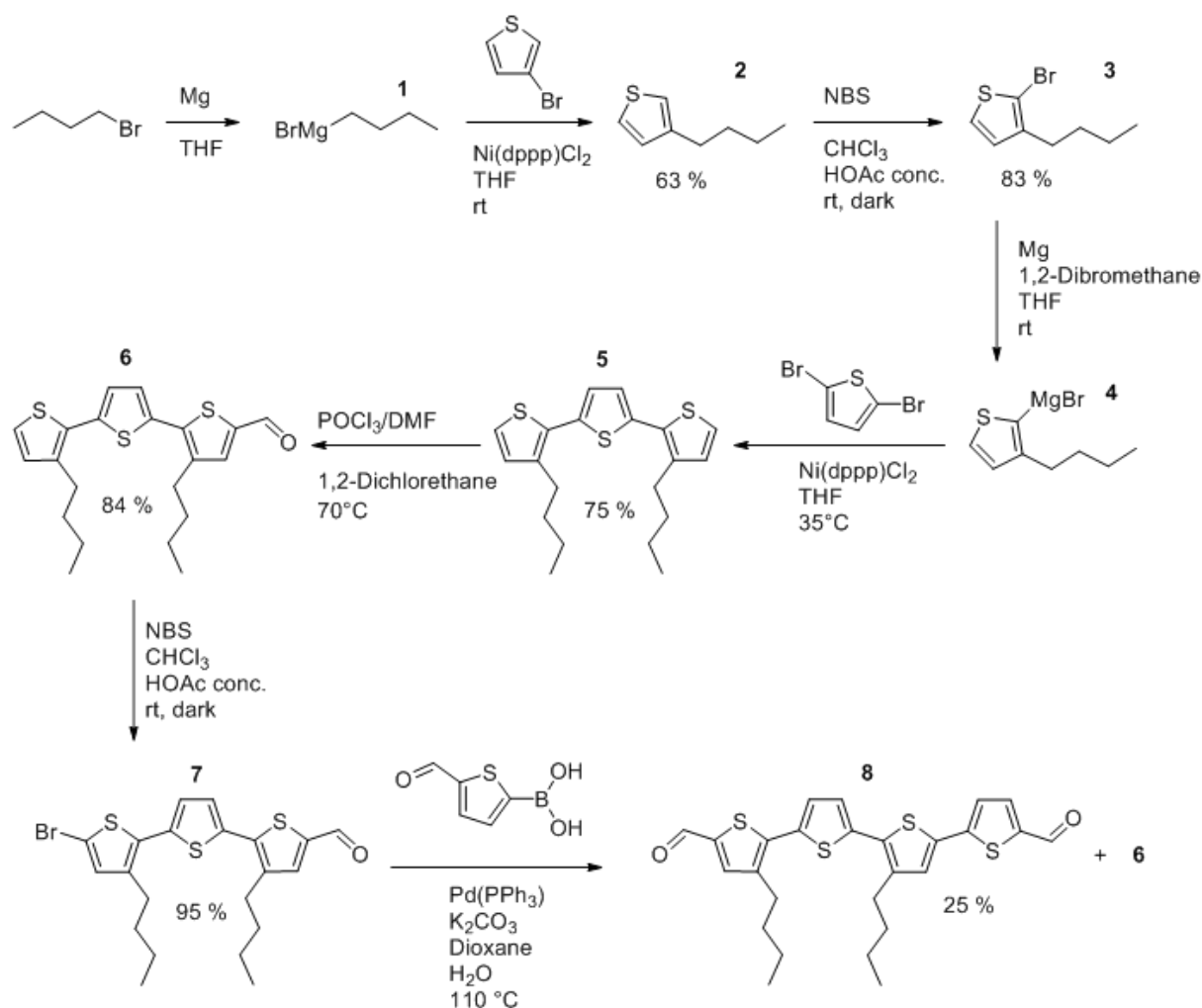
6.4 Experimental

secondary electron detector.

UV-Vis spectra were recorded using a Perkin-Elmer Lambda 1050 spectrometer equipped with a 150 mm integrating sphere. Absorbance spectra of COF thin films were corrected for the transmission of the substrate and reflection losses.

Photoluminescence (PL) measurements were performed using a home-built setup consisting of a Horiba Jobin Yvon iHR 320 monochromator equipped with a photomultiplier tube and a liquid N₂-cooled InGaAs detector. The samples were illuminated with a pulsed (83 Hz) 405 nm LED at a light intensity of 500 mW cm⁻².

The substituted tetrathiophene synthesized in this work will be referred to as 4T in the following sections due to its four thiophene groups.

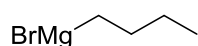


6.4 Experimental

Figure 6.3: Successful synthesis route of 4T (**8**) with by-product 6 that was reintroduced into the synthesis cycle.

The synthesis of the 4T-linker was started by activating 1-bromobutane with magnesium in THF, followed by a Grignard-reaction of butylmagnesium bromide (**1**) with 3-bromothiophene to obtain 3-butylthiophene(**2**)¹⁶ in fair yields. (**2**) was then easily brominated with NBS in a mixture of CHCl₃ 1:1 conc. AcOH to provide (**3**) in very good yields.¹⁷ After activating (**3**) with magnesium in a solvent mixture of THF and 1,2-dibromoethane to furnish (3-butylthiophen-2-yl)magnesium bromide (**4**), 2,5-dibromothiophene was added in a Ni-catalyzed Grignard-reaction to obtain terthiophene (**5**).¹⁸ The aldehyde (**6**) was formed by formylating (**5**) with one equivalent of the Vilsmeier reagent and was brominated following the same procedure as described above, furnishing (**7**) in excellent yields. The Pd-catalyzed coupling of (**7**) with 5-bromo-2-thienylboronic acid in water-spiked 1,4-dioxane was accomplished with yielding the desired product (**8**).¹⁹ As a by-product compound **6** was obtained, which was then recycled through bromination to achieve total yields of up to 60 %.

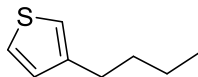
Butylmagnesium bromide (**1**)



A dispersion of magnesium (1.97 g, 81.0 mmol, 1.35 eq.) in 100 mL anhydrous THF was prepared in a 250 mL three-necked round bottom flask, equipped with a magnetic stirring bar. A mixture of 1-Brombutane (8.6 mL, 80.4 mmol, 1.34 eq) and 40 mL anhydrous THF were added dropwise under Ar. The mixture was kept at ambient temperature by a water bath until the magnesium was dissolved. The solution containing compound **1** was used without further purification.

6.4 Experimental

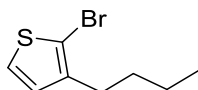
3-Butylthiophene (2)



Ni(dppp)Cl₂ (650.4 mg, 1.2 mmol, 0.02 eq.) was added to the solution containing **1** in a three necked 250 mL round bottom flask, and 3-bromothiophene (5.6 mL, 60 mmol, 1 eq.) was added slowly while the reaction was cooled with a water/ice mixture under Ar. The reaction was allowed to warm to ambient temperature and stirred for 16 h. 1 mL 1 M HCl was added to quench the reaction and the aqueous mixture was extracted with Et₂O (50 mL) three times. The combined organic layers were washed with H₂O (50 mL) for three times and dried over MgSO₄ (3 g) filtered and concentrated *in vacuo*. The crude product was purified by distillation to provide **2** (5.264 g, 63 %) as colorless oil.¹⁶

¹H NMR (400 MHz, Chloroform-*d*) δ : 7.24 (dd, *J* = 4.9, 2.9 Hz, 1H), 6.97 – 6.89 (m, 2H), 2.63 (t, *J* = 7.5 Hz, 2H), 1.66 – 1.56 (m, 2H), 1.42 – 1.31 (m, 2H), 0.93 (t, *J* = 7.3 Hz, 3H).

2-Bromo-3-butylthiophene (3)



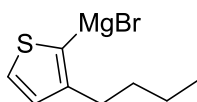
Compound **2** (5.264 g, 37.5 mmol, 1 eq.) was dissolved in 38 mL CHCl₃ and 38 ml conc. acetic acid under Ar in a 250 mL three-necked round bottom flask, equipped with a magnetic stir bar. N-Bromosuccinimide (7.015 g, 39.4 mmol, 1.05 eq.) was added to the solution in the dark and the solution was stirred for 17 h. The reaction was quenched by adding 130 mL H₂O, and the aqueous mixture was extracted with CHCl₃. (50 mL) three times. The combined organic layers were washed with saturated NaHCO₃-solution

6.4 Experimental

(50 mL) for three times and H₂O (50 mL) for three times before they were dried over MgSO₄ (3 g) filtered and concentrated *in vacuo*. Purification of the crude product by distillation furnished the desired compound **3** (6.806 g, 83 %) as colorless oil.¹⁷

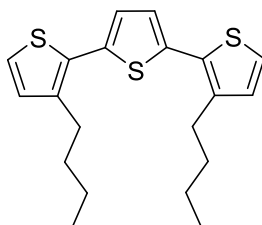
¹H NMR (400 MHz, Chloroform-*d*) δ : 7.18 (d, *J* = 5.6 Hz, 1H), 6.80 (d, *J* = 5.6 Hz, 1H), 2.57 (t, *J* = 7.6 Hz, 2H), 1.61 – 1.52 (m, 2H), 1.42 – 1.31 (m, 2H), 0.94 (t, *J* = 7.3 Hz, 3H).

(3-Butylthiophen-2-yl)magnesium bromide (**4**)



Compound **3** (3.92 g, 17.8 mmol, 3 eq.) and 1,2-dibromoethane (1.534 mL, 17.8 mmol, 3 eq.) were placed to a 50 mL round bottom flask. 18 mL anhydrous THF were added dropwise over a time range of 1.5 h (1/3 per 30 min) to magnesium (865 mg, 35.6 mmol, 6 eq.) in 60 mL THF under sonication under ambient temperature. After further sonication until the magnesium did not react anymore, the solution was used for the next step without further purification.

3,3''-Dibutyl-2,2':5',2''-terthiophene (**5**)



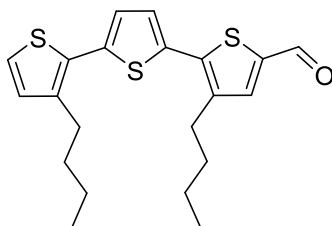
Solution (**4**) was transferred into a mixture of 2,5-dibromothiophene (0.667 mL, 5.9 mmol, 1 eq.) and Ni(dppp)Cl₂ (320 mg, 0.59 mmol, 0.1 eq.) in 60 mL anhydrous THF, prepared in a 250 mL three-necked round bottom flask. The reaction mixture was

6.4 Experimental

stirred with a magnetic stir bar at 35 °C for four days (forming a greenish mixture) and then quenched by adding 100 mL HCl (1 M) and 100 g ice. The aqueous mixture was extracted with Et₂O (70 mL) three times, dried over MgSO₄ (3 g) filtered and concentrated *in vacuo*. The crude product was purified by flash chromatography (SiO₂, 60 Å, 40–63 μm, Merck, heptane) to obtain **5** (1.59 g, 75 %) as orange oil.¹⁸

¹H NMR (400 MHz, Chloroform-*d*) δ: 7.18 (d, *J* = 5.2 Hz, 1H), 7.06 (s, 1H), 6.94 (d, *J* = 5.2 Hz, 1H), 2.79 (t, *J* = 7.8 Hz, 2H), 1.69 – 1.59 (m, 2H), 1.46 – 1.35 (m, 2H), 0.94 (t, *J* = 7.3 Hz, 3H).

3,3''-Dibutyl-[2,2':5',2''-terthiophene]-5-carbaldehyde (**6**)



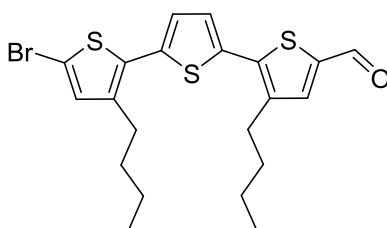
Compound **5** (1.59 g, 4.4 mmol, 1 eq.) was dissolved in 1,2-dichloroethane under Ar in a 250 mL three-necked round bottom flask, equipped with a stir bar. The Vilsmeier reagent was prepared by adding POCl₃ (0.602 mL, 6.6 mmol, 1.5 eq.) into 4.172 mL anhydrous DMF, measured with an eppendorf pipette. After a few minutes the reagent turned red and was then added to the solution containing **5**. The reaction mixture was stirred at 70 °C for 17 h, quenched by adding 100 mL H₂O, and 10 mL 1 M NaOH was added to increase the pH-value to 9-11. The aqueous mixture was extracted with DCM (40 mL) three times, dried over MgSO₄ (3 g) filtered and concentrated *in vacuo*.

Purification of the crude product by flash chromatography (SiO₂, 60 Å, 40–63 μm, Merck, EtOAc 1:5 heptane) furnished compound **6** (1.431 g, 84 %) as orange oil.

6.4 Experimental

¹H NMR (400 MHz, Chloroform-*d*) δ : 9.83 (s, 1H), 7.60 (s, 1H), 7.24 (d, $J = 3.8$ Hz, 1H), 7.22 (d, $J = 5.2$ Hz, 1H), 7.11 (d, $J = 3.8$ Hz, 1H), 6.96 (d, $J = 5.2$ Hz, 1H), 2.84 (t, $J = 7.7$ Hz, 2H), 2.79 (t, $J = 7.8$ Hz, 2H), 1.74 – 1.60 (m, 4H), 1.49 – 1.36 (m, 4H), 0.96 (t, $J = 7.3$ Hz, 4H), 0.93 (t, $J = 7.4$ Hz, 2H).

5''-Bromo-3,3''-dibutyl-[2,2':5',2''-terthiophene]-5-carbaldehyde (**7**)

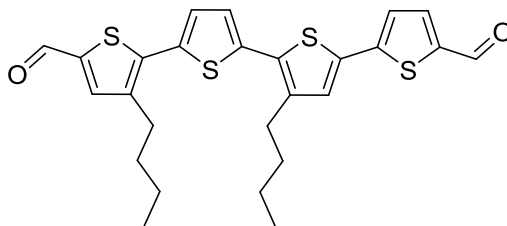


Compound **6** (978.3 mg, 2.51 mmol, 1 eq.) was dissolved in 24 mL CHCl₃ and 24 mL concentrated acetic acid under Ar in a 250 mL three-necked round bottom flask. The solution was then cooled to 0 °C, and N-bromosuccinimide (492.9 mg, 2.77 mmol, 1.1 eq.) was added in the dark. After the reaction mixture stirred at ambient temperature for two days, 125 mL H₂O was added and the aqueous mixture was extracted with DCM (50 mL) three times. The combined organic layers were dried over MgSO₄ (3 g), filtered and concentrated *in vacuo*. The crude product was purified by flash chromatography (SiO₂, 60 Å, 40–63 μm, Merck, n-hexane 1:3 DCM) yielding compound **7** (1119.1 mg, 95 %) as orange oil which crystallized as orange solid.¹⁷

¹H NMR (400 MHz, Chloroform-*d*) δ : 9.83 (s, 1H), 7.60 (s, 1H), 7.22 (d, $J = 3.8$ Hz, 1H), 7.05 (d, $J = 3.8$ Hz, 1H), 6.92 (s, 1H), 2.82 (t, $J = 7.8$ Hz, 2H), 2.73 (t, $J = 7.7$ Hz, 2H), 1.72 – 1.56 (m, 5H), 1.49 – 1.34 (m, 5H), 0.97 (t, $J = 7.3$ Hz, 3H), 0.93 (t, $J = 7.4$ Hz, 3H).

6.4 Experimental

3,3''-Dibutyl-[2,2':5',2'':5'',2''''-quaterthiophene]-5,5''''-dicarbaldehyde (**8**)



Compound **7**, (837.4 mg, 1.79 mmol, 1 eq.), 5-formyl-2-thienylboronic acid (307.3 mg, 1.97 mmol, 1.1 eq.), Pd(PPh₃)₄ (207.0 mg, 0.18 mmol, 0.1 eq.) and K₂CO₃ (495.1 mg, 3.58 mmol, 2 eq.) were placed in a 100 mL three-necked round bottom flask, equipped with a magnetic stir bar. After adding 9 mL 1,4-dioxane and 2.5 mL H₂O (under Ar) the mixture was stirred at 110 °C for 2 d. After two days the mixture was quenched by adding 50 mL H₂O and extracted with DCM (20 mL) for three times. The combined organic layers were dried over MgSO₄ (3 g), filtered and concentrated *in vacuo*. The crude product was purified by flash chromatography (SiO₂, 60 Å, 40–63 μm, Merck, DCM) to provide compound **8** (224.2 mg, 25 %) as red solid.¹⁹

¹H NMR (400 MHz, Chloroform-*d*) δ: 9.87 (s, 1H), 9.84 (s, 1H), 7.68 (d, *J* = 4.0 Hz, 1H), 7.61 (s, 1H), 7.27 (s, 1H), 7.25 (d, *J* = 4.0 Hz, 1H), 7.21 (s, 1H), 7.17 (d, *J* = 3.9 Hz, 1H), 2.84 (t, *J* = 8.1 Hz, 2H), 2.80 (t, *J* = 7.9 Hz, 3H), 1.76 – 1.62 (m, 4H), 1.45 (h, *J* = 7.4 Hz, 5H), 0.97 (td, *J* = 7.3, 1.7 Hz, 7H).

¹³C NMR (101 MHz, Chloroform-*d*) δ: 182.68, 182.57, 146.73, 141.94, 141.60, 140.78, 140.70, 140.65, 139.14, 137.47, 137.38, 135.46, 134.28, 131.95, 129.29, 128.05, 126.94, 124.38, 32.77, 32.60, 29.42, 29.35, 22.81, 22.75, 14.08, 14.06.

HR-EI-MS: *m/z* (%): 498.0811 (100, [M]⁺, calculated for C₂₆H₂₆O₂S₄⁺: 498.0810).

6.4 Experimental

4T-Pyrene-COF

Compound **8** was then used as a building block in the synthesis of a covalent organic framework with the second building block 4,4',4'',4'''-(pyrene-1,3,6,8-tetrayl)tetraaniline synthesized following the procedure described in literature.²⁰ The solvents were purchased from Sigma-Aldrich and used without further purification.

For the preparation of the reaction 5.66 mg 4,4',4'',4'''-(pyrene-1,3,6,8-tetrayl)tetraaniline (0.01 mmol, 1 eq.) and 9.96 mg 4T (0.02 mmol, 2 eq.) were added to 500 μ L benzyl alcohol and 50 μ L 6 M acetic acid in a small *Schott* tube (culture tube with screw cap, air-tight sealing under Ar, 5 mL). The reaction mixture was heated at 120 °C for three days, cooled down to ambient temperature and filtered. The obtained reddish dark precipitate was characterized by powder diffraction.

6.4 Experimental

IR Spectroscopy

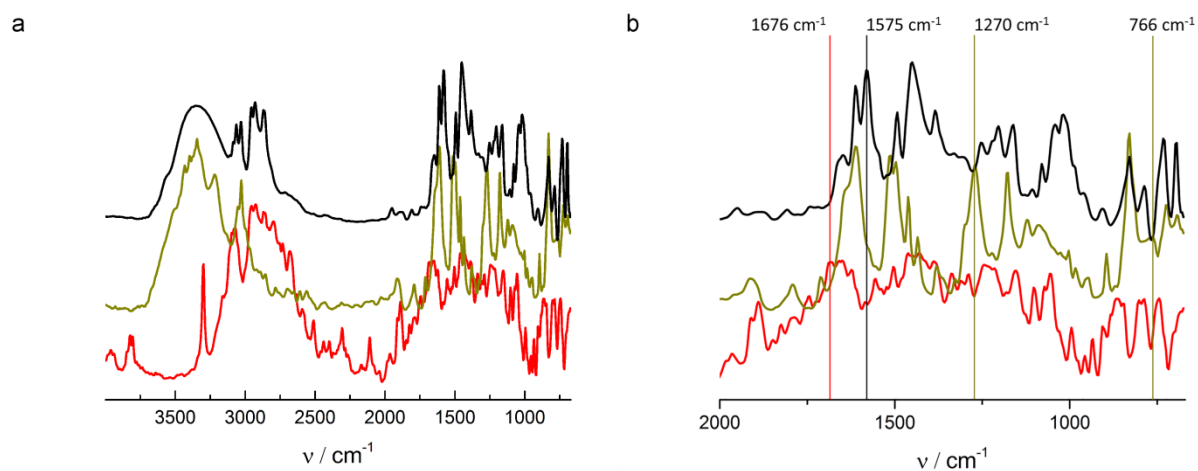


Figure 6.4 (a) IR spectra of Pyr-4T COF (black), pyrene monomer (dark yellow), and 4T monomer (red) measured as solids. (b): Enlargement of IR spectra of Pyr-4T COF (black), pyrene monomer (dark yellow), and 4T monomer (red) measured as solids.

UV-Vis/Photoluminescence

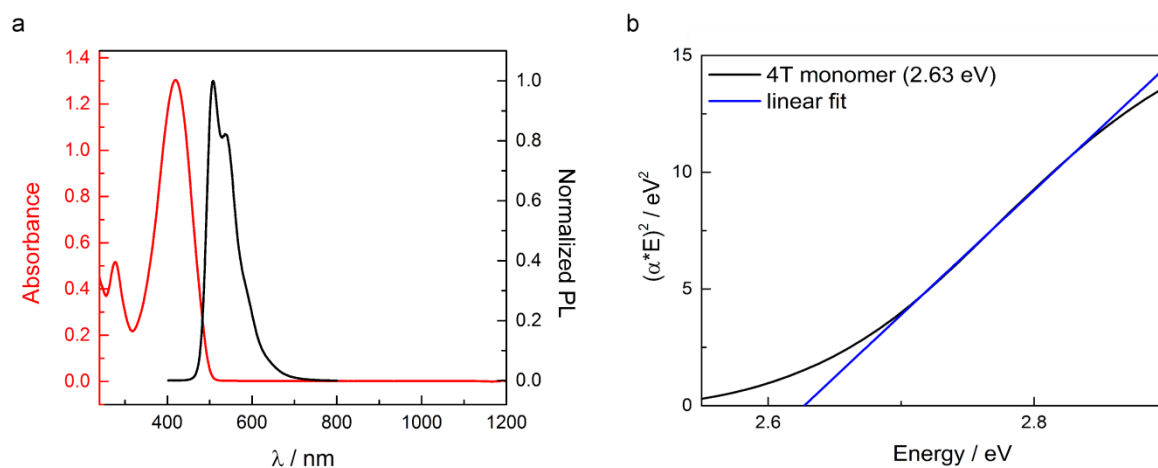


Figure 6.5.(a) The photoluminescence spectrum (black) compared with the absorption spectrum (red) of the 4T monomer **8** measured as a 50 μM solution in 1,4-dioxane. (b) Tauc plot for the 4T monomer **8** (black) absorption spectrum and the linear fit (blue).

6.4 Experimental

Time correlated single photon counting

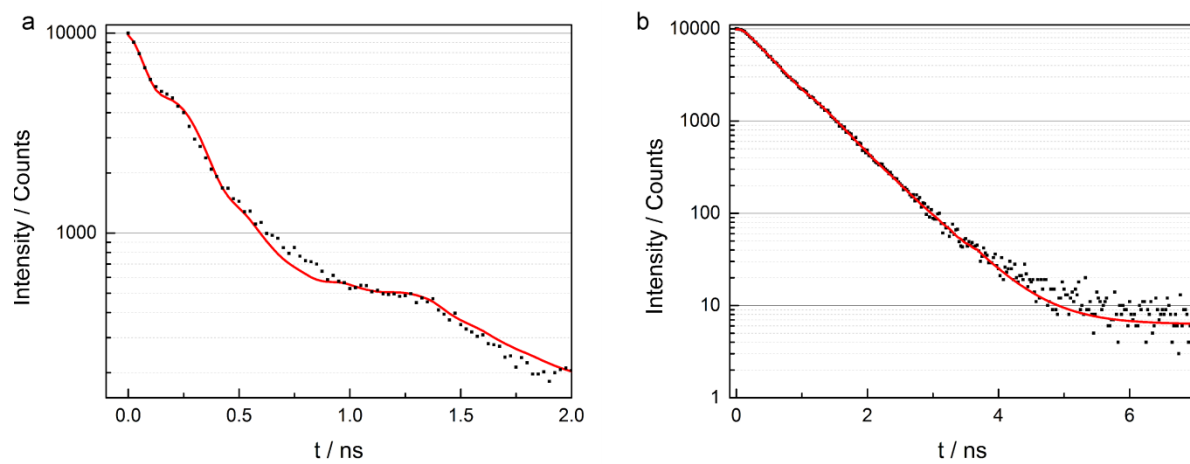


Figure 6.6. (a) TCSPC histograms of fluorescence (black) and exponential decay fit (red) in log scale for the Pyr-4T COF (with $\tau_1 = 1.07$ ns and $\tau_2 = 0.05$ ns) and (b) for the 4T monomer **8** ($\tau = 0.57853$ ns).

6.5 References

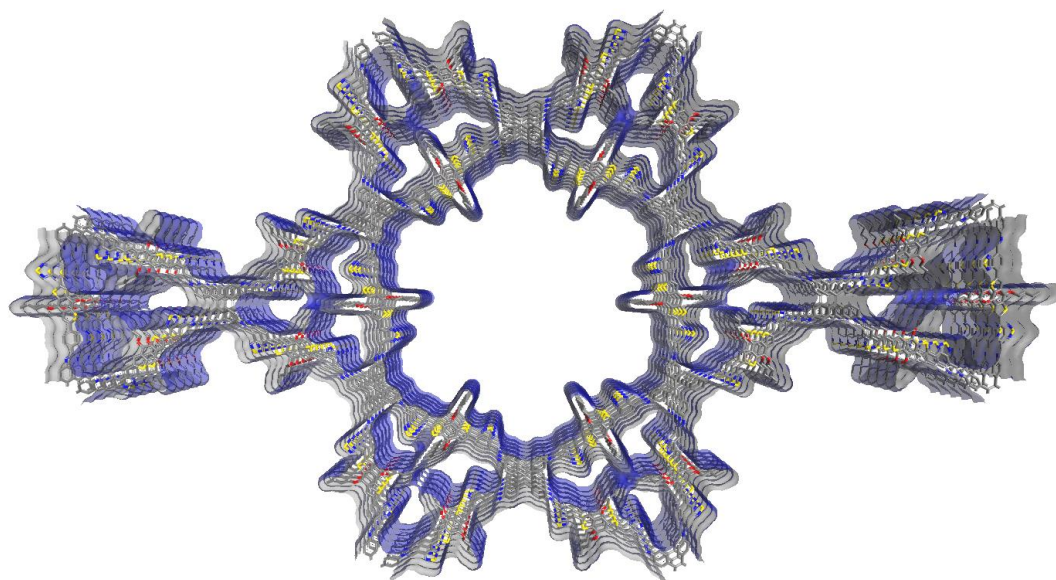
1. A. P. Côte; A. I. Benin; N. W. Ockwig; M. O’Keeffe; A. J. Matzger; O. M. Yaghi, Porous, Crystalline, Covalent Organic Frameworks. *Science* **2005**, *310*, 1166-1170.
2. S. Wan; F. Gándara; A. Asano; H. Furukawa; A. Saeki; S. K. Dey; L. Liao; M. W. Ambrogio; Y. Y. Botros; X. Duan; S. Seki; J. F. Stoddart; O. M. Yaghi, Covalent Organic Frameworks with High Charge Carrier Mobility. *Chem. Mater.* **2011**, *23*, 4094-4097.
3. L. Ascherl; T. Sick; J. T. Margraf; S. H. Lapidus; M. Calik; C. Hettstedt; K. Karaghiosoff; M. Döblinger; T. Clark; K. W. Chapman; F. Auras; T. Bein, Molecular docking sites designed for the generation of highly crystalline covalent organic frameworks. *Nat Chem* **2016**, *advance online publication*.
4. A. A. Bakulin; A. Rao; V. G. Pavelyev; P. H. M. Loosdrecht; M. S. Pshenichnikov; D. Niedzialek; J. Cornil; D. Beljonne; R. H. Friend, The Role of Driving Energy and Delocalized States for Charge Separation in Organic Semiconductors. *Science* **2012**, *335*, 1340-1344.
5. E. L. Spitler; B. T. Koo; J. L. Novotney; J. W. Colson; F. J. Uribe-Romo; G. D. Gutierrez; P. Clancy; W. R. Dichtel, A 2D covalent organic framework with 4.7-nm pores and insight into its interlayer stacking. *J. Am. Chem. Soc.* **2011**, *133* (48), 19416-19421.
6. M. Calik; T. Sick; M. Dogru; M. Döblinger; S. Datz; H. Budde; A. Hartschuh; F. Auras; T. Bein, From Highly Crystalline to Outer Surface-Functionalized Covalent Organic Frameworks—A Modulation Approach *J. Am. Chem. Soc.* **2016**, *138* (4), 1234-1239.
7. S. Wan; J. Guo; J. Kim; H. Ihee; D. Jiang, A Belt-Shaped, Blue Luminescent, and Semiconducting Covalent Organic Framework. *Angew. Chem. Int. Ed.* **2008**, *47*, 8826-8830.
8. M. Dogru; M. Handloser; F. Auras; T. Kunz; D. Medina; A. Hartschuh; P. Knochel; T. Bein, A Photoconductive Thienothiophene-Based Covalent Organic Framework Showing Charge Transfer Towards Included Fullerene. *Angew. Chem. Int. Ed.* **2013**, *52*, 2920-2924.
9. M. Calik; F. Auras; L. M. Salonen; K. Bader; I. Grill; M. Handloser; D. D. Medina; M. Dogru; F. Loebermann; D. Trauner; A. Hartschuh; T. Bein, Extraction of Photogenerated Electrons and Holes from a COF Integrated Heterojunction. *J. Am. Chem. Soc.* **2014**.
10. J. Hou; Z. a. Tan; Y. Yan; Y. He; C. Yang; Y. Li, Synthesis and photovoltaic properties of two-dimensional conjugated polythiophenes with bi (thienylenevinylene) side chains. *J. Am. Chem. Soc.* **2006**, *128* (14), 4911-4916.
11. J. Cremer; P. Bäuerle, Star-shaped perylene-oligothiophene-triphenylamine hybrid systems for photovoltaic applications. *J. Mater. Chem.* **2006**, *16* (9), 874-884.
12. T. Benincori; E. Brenna; F. Sannicolò; L. Trimarco; P. Sozzani; G. Zotti, The first “charm bracelet” conjugated polymer: an electroconducting polythiophene with covalently bound fullerene moieties. *Angew. Chem. Int. Ed.* **1996**, *35* (6), 648-651.
13. P. Schilinsky; C. Waldauf; C. J. Brabec, Recombination and loss analysis in polythiophene based bulk heterojunction photodetectors. *Appl. Phys. Lett.* **2002**, *81* (20), 3885-3887.
14. S. J. Rowan; S. J. Cantrill; G. R. Cousins; J. K. Sanders; J. F. Stoddart, Dynamic covalent chemistry. *Angew. Chem. Int. Ed.* **2002**, *41* (6), 898-952.
15. F. J. Uribe-Romo; J. R. Hunt; H. Furukawa; C. Klöck; M. O’Keeffe; O. M. Yaghi, A crystalline imine-linked 3-D porous covalent organic framework. *J. Am. Chem. Soc.* **2009**, *131* (13), 4570-4571.

6.5 References

16. J. Zhou; S. Xie; E. F. Amond; M. L. Becker, Tuning Energy Levels of Low Bandgap Semi-Random Two Acceptor Copolymers. *Macromolecules* **2013**, *46* (9), 3391-3394.
17. L. Biniak; C. L. Chochos; N. Leclerc; G. Hadziioannou; J. K. Kallitsis; R. Bechara; P. Leveque; T. Heiser, A [3,2-b]thienothiophene-alt-benzothiadiazole copolymer for photovoltaic applications: design, synthesis, material characterization and device performances *J. Mater. Chem.* **2009**, *19* (28), 4946-4951.
18. P. T. Henderson; D. M. Collard, Thiophene:alkylthiophene copolymers from substituted dialkyloligothiophenes. *Chem. Mater.* **1995**, *7* (10), 1879-1889.
19. S. Fuse; S. Sugiyama; M. M. Maitani; Y. Wada; Y. Ogomi; S. Hayase; R. Katoh; T. Kaiho; T. Takahashi, Elucidating the Structure–Property Relationships of Donor– π -Acceptor Dyes for Dye-Sensitized Solar Cells (DSSCs) through Rapid Library Synthesis by a One-Pot Procedure. *Chem. Eur. J.* **2014**, *20* (34), 10685-10694.
20. X. Chen; N. Huang; J. Gao; H. Xu; F. Xu; D. Jiang, Towards covalent organic frameworks with predesignable and aligned open docking sites. *Chem. Commun.* **2014**, *50* (46), 6161-6163.

7. Hand-Tailoring the Properties of a Covalent Organic Framework by the Integration of a Push-Pull Building Block

This chapter is based on work in collaboration with: Florian Auras, Simon Herbert, Laura Ascherl, and Markus Döblinger.



Abstract

Organic polymer- and small molecule-based solar cells have reached impressive power conversion efficiencies during the past years; however, the precise design and control of the nanoscale morphology of the photoactive material remains a major challenge. Covalent organic frameworks (COFs) offer a strategy to integrate functional groups within a crystalline network to precisely control the position of the moieties on a nanoscale level. π - π Interactions between the layers of two dimensional (2D) COFs

7.1 Introduction

enable the formation of aligned columns, which can facilitate charge carrier transport along the stacking direction. The properties of COFs can be tuned by integrating appropriate linker molecules. Here, we report the development of a new push-pull linker that comprises electron-rich and -deficient moieties within its structure. This design promotes internal charge transfer, resulting in the reduction of the band gap energy. Integrated within a COF structure, the push-pull linker was found to increase the absorption spectrum such that light can be harvested efficiently throughout almost the complete visible region. The energy levels of the push-pull linker are thereby finely tuned to align with those of a fullerene acceptor and to eventually function as donor material in a COF-based ordered bulk heterojunction solar cell device.

7.1 Introduction

Coté *et al.* have initiated intensive investigations on covalent organic frameworks (COFs) after they introduced this new class of materials in 2005.¹ 2D COFs are light-weight materials consisting of organic linker molecules linked by covalent bonds to form two dimensional (2D) sheets, which are able to stack and form an extended 3D network by π - π interlayer interactions. This unique class of materials offers the possibility to tune its properties by integrating appropriate linker molecules with desired functionality. The shape and size of the resulting porous channels strongly depend on the linker geometry and length, and by integrating functional moieties the optical and electrochemical properties can be tuned. With appropriate linkers and stacking interactions, charge transport along the stacked columns becomes possible, making COFs promising candidates to serve as active materials in solar cell devices.²⁻¹¹

In this context, the focus of research lies on the development of new electroactive linker

7.1 Introduction

molecules to form the corresponding electroactive COFs and to take advantage of these crystalline materials to construct ordered bulk heterojunctions (BHJ).¹²⁻¹³ For example, the COF framework can act as electron donor material that can be infiltrated with an electron acceptor such as a fullerene derivative, to construct a highly ordered and defined BHJ.¹²

In order for a COF to efficiently function within such device, besides close contact between the electron donor and acceptor phase, the energy levels of these phases have to be aligned to promote electron transfer from the donor to the acceptor phase. An established strategy for polymer solar cell devices is the use of “push-pull” structures to modulate the energy level of the highest occupied molecular orbital (HOMO) and lowest unoccupied molecular orbital (LUMO) in such a way to properly match the energy levels of the fullerene derivative [6,6]-phenyl C₆₁-butyric acid methyl ester (PCBM), which is commonly used in BHJ devices.¹⁴⁻¹⁹

These “push-pull” systems consist of π -conjugated linkers that exhibit electron rich and electron deficient areas within their structure. The difference in electronegativity causes intramolecular charge transfer which reduces the band gap energy and thus results in a broadening of the optical absorption spectrum towards lower energy.¹⁸

In this work we developed a new push-pull linker composed of an electron rich benzodithiophene (BDT) unit coupled to two electron deficient benzothiadiazoles(BT). We anticipate that the integration of this linker will form a COF with strong absorption throughout the visible spectrum that could ultimately function as photoactive material within a solar cell device.

7.2 Results and Discussion

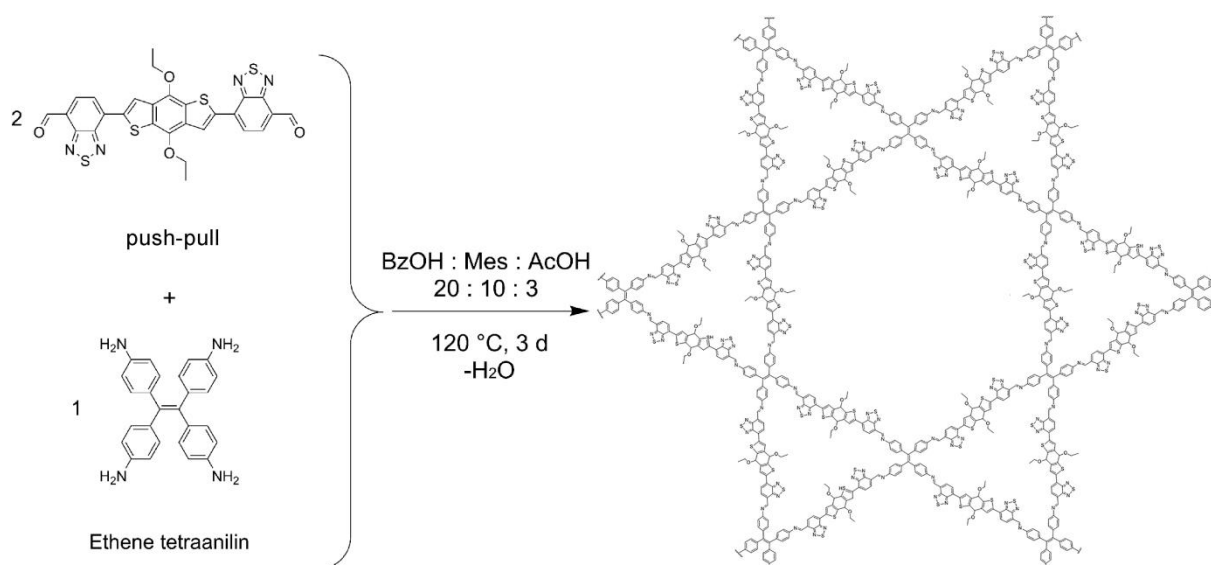


Figure 7.1. Co-condensation reaction of 7,7'-(4,8-diethoxybenzo[1,2-b:4,5-b']dithiophene-2,6-diyl)bis(benzo[c][1,2,5]thiadiazole-4-carbaldehyde) (PP) and 1,1,2,2-tetrakis(4-aminophenyl)ethene (ETTA) in a 2:1 molar ratio to form the PP-ETTA COF, featuring hexagonal pores with a diameter of 4.9 nm and trigonal pores with 1.95 nm.

7.2 Results and Discussion

The newly synthesized push-pull linker 7,7'-(4,8-diethoxybenzo[1,2-b:4,5-b']dithiophene-2,6-diyl)bis(benzo[c][1,2,5]thiadiazole-4-carbaldehyde) (PP) was integrated within a COF structure via a co-condensation reaction with 1,1,2,2-tetrakis(4-aminophenyl)ethene (ETTA) in a 2 : 1 molar ratio to form PP-ETTA COF (Figure 7.1). To ensure the reversibility of the bond formation, catalytic amounts of 6 molar acetic acid were added to a solvent mixture of benzyl alcohol and mesitylene (BzOH : Mes : AcOH, v : v : v, 20 : 10 : 3) (for further experimental data see the experimental section).

The crystallinity of the PP-ETTA COF was confirmed by powder X-ray (PXRD) diffraction (Figure 7.2a). In order to determine the structure of PP-ETTA COF, two different crystalline arrangements were simulated using the Materials Studio software and

7.2 Results and Discussion

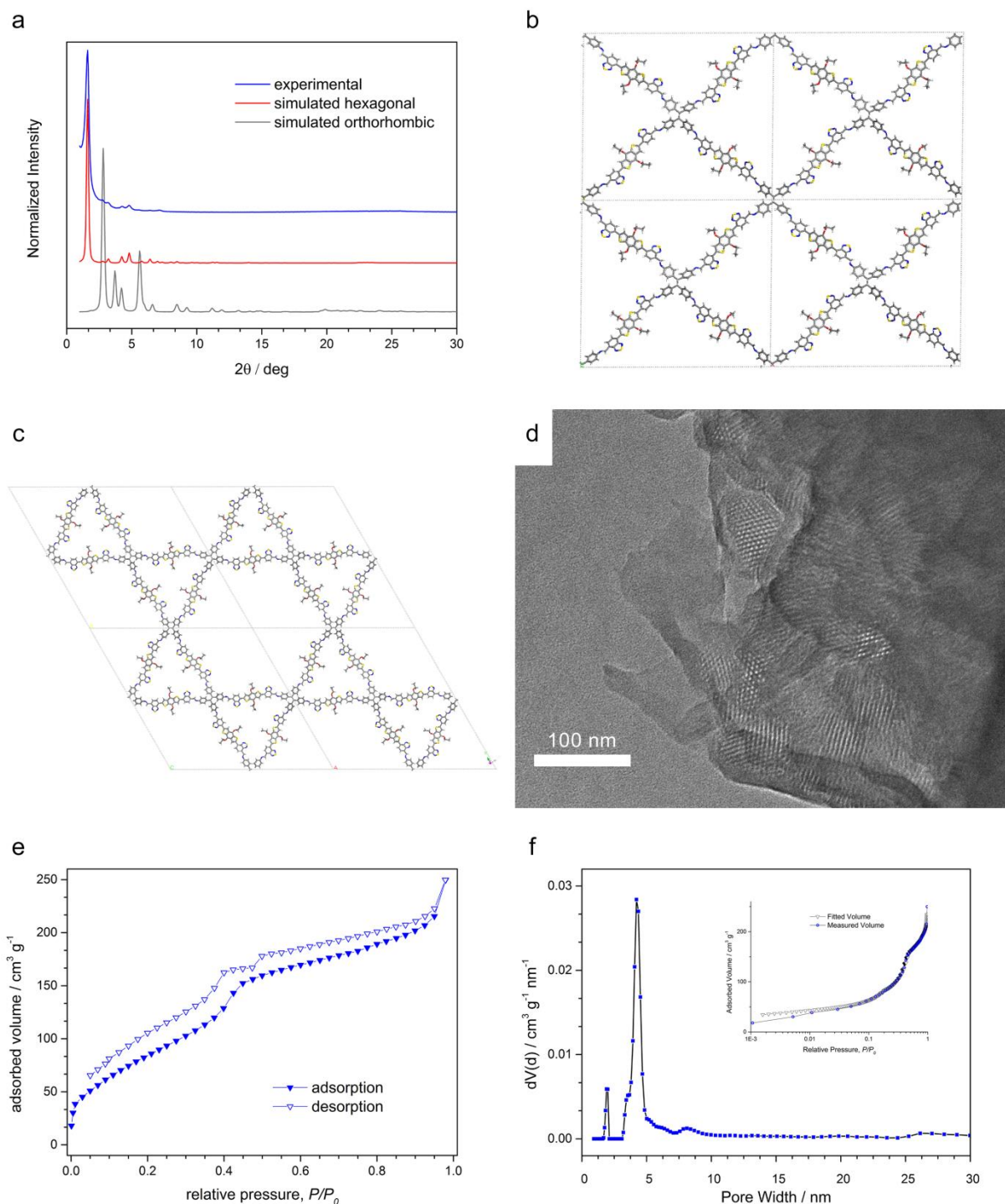


Figure 7.2. (a) Experimental PXRD data (blue) vs. simulated patterns (red and gray) for an orthorhombic (b) and hexagonal (c) arrangement of the linker molecules. The theoretical patterns were simulated for a crystallite size of 50 nm. (d) Transmission electron micrograph of PP-ETTA COF bulk material showing the hexagonal pore structure in top view and straight porous channels in side view. (e) Nitrogen sorption isotherm of a PP-ETTA COF powder sample measured at 77 K. (f) Corresponding pore size distribution with two different pore sizes of 1.9 nm and 4.2 nm, obtained by fitting the experimental data using a QSDFT adsorption kernel with a fitting error of 1.3 % (inset).

7.2 Results and Discussion

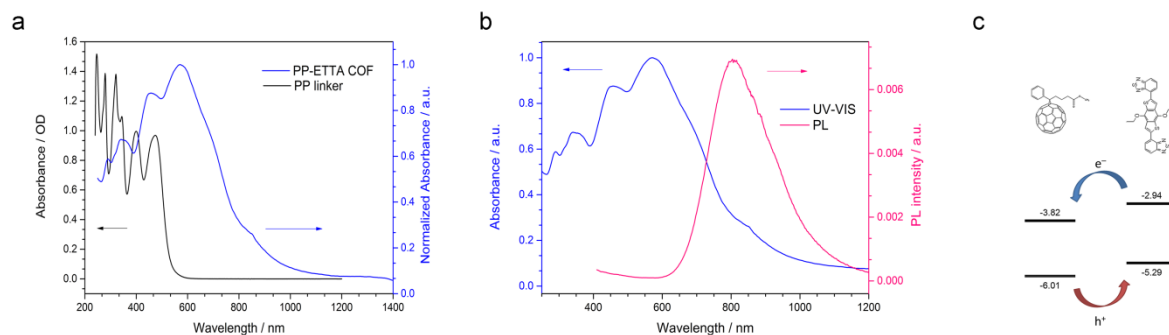


Figure 7.3. Transmission absorption spectrum of the PP linker (black) measured in a 1 cm quartz cuvette as a 50 μM solution in 1,4-dioxane and PP-ETTA COF (blue), measured as diffuse reflectance of the solid and converted with the Kubelka Munk equation. (b) Absorbance (blue) and PL ($\lambda_{\text{exc}} = 455 \text{ nm}$, magenta) spectra of PP-ETTA COF. (c) Energy levels of PCBM and the naked PP linker (without aldehyde groups) obtained with DPV.

compared to the experimental data. The diffraction pattern of a possible orthorhombic arrangement of the linker molecules does not match the experimental data (Figure 7.2a and b). However, when compared to the pattern of a simulated hexagonal structure the reflection positions and intensities agree very well with the experimentally obtained data (Figure 7.2a and c).

The successful formation of the PP-ETTA COF was further confirmed by transmission electron microscopy (TEM). The micrograph of the bulk material reveals the hexagonal, honeycomb-like structure of the COF, which can be seen in top view (Figure 7.2d). The expected channels are also visible, with crystalline domains sized up to about 100 nm.

The permanent porosity of the PP-ETTA COF was elucidated via nitrogen sorption measurements. The isotherm adopts a type IV shape, typical for mesoporous materials. Additionally, an increased uptake can be observed in the microporous region (Figure 7.2e). The Brunauer Emmett Teller (BET) surface area was calculated to be 400 $\text{m}^2 \text{g}^{-1}$. This rather modest surface area could be attributed to the large number of ethoxy groups decorating the internal pore surface. The pore size distribution was obtained by

7.2 Results and Discussion

applying a kernel for carbon materials using quenched solid density functional theory (QSDFT) for cylindrical pores on the adsorption branch of the isotherm; it reveals two different pore sizes with a fitting error of only 1.3 % (Figure 7.2f). The first pore size, attributed to the trigonal pores within the COF structure, has an average size of 1.9 nm, which is in excellent agreement with the theoretical pore size of 1.95 nm. The second pore was calculated to have an average size of 4.2 nm, which is smaller than the expected pore size of 4.9 nm. The decreased surface area as well as the smaller average pore size of the hexagonal pores is tentatively attributed to the presence of the ethoxy groups at the pore walls.

The PP linker was found to have a strong absorption spectrum reaching into the visible region with distinct absorption features (Figure 7.3a, black). When integrated within the COF structure, the spectrum retains all optical features, while the signals broaden and red-shift, covering now almost the whole visible absorption spectrum by reaching from 400 to 700 nm. When the COF is excited with laser light at 455 nm, a distinct photoluminescence occurs with a maximum intensity at 800 nm (Figure 7.3b).

The HOMO-LUMO energy levels of the naked PP linker were determined by differential pulse voltammetry (DPV) and compared to those of PCBM (Figure 7.3c). The PP LUMO level thereby has an energy of -2.94 eV, which offers a sufficient driving force for excited electrons to be transferred to the PCBM LUMO level with its smaller energy of -3.82 eV. Also, photo-generated holes have a preferred direction to travel from the PCBM HOMO (-6.01 eV) to the PP HOMO (-5.29 eV).

7.3 Conclusion

7.3 Conclusion

In this study we have developed a push-pull linker molecule for the construction of novel covalent organic frameworks, consisting of an electron rich BDT moiety linked to two electron-deficient BT units. This push-pull linker was successfully integrated within a COF structure by coupling to ETTA molecules through imine formation. The new PP-ETTA COF was found to adopt a hexagonal symmetry creating a star shaped, dual pore system. The crystalline structure could be confirmed via TEM, showing the hexagonal arrangement of the mesoporous channels.

The integration of the PP linker within the PP-ETTA COF through conjugation with the ETTA building block shifted its absorbance deep into the visible such that it spreads throughout the ultra-violet and almost the complete visible region. This renders the new COF a promising candidate as active material in a solar cell device as it efficiently harvests light in the region where most of the solar flux occurs. Furthermore, the energy levels of the HOMO and LUMO are well-aligned to enable electron transport to the commonly used PCBM acceptor phase.

We anticipate that the development of finely tuned push-pull linkers such as the one described here will allow for the construction of covalent organic frameworks with the appropriate properties to be used as active materials in ordered BHJ solar cell devices.

7.4 Experimental

7.4 Experimental

Methods

Unless stated otherwise, all reactions were performed in oven-dried glassware under a positive pressure of Ar. Commercial reagents and solvents were used as received. Reactions were stirred magnetically and monitored by NMR spectroscopy or analytical thin-layer chromatography (TLC) using E. Merck 0.25 mm silica gel 60 F254 pre-coated glass plates. TLC plates were visualized by exposure to ultraviolet light (254 nm). Flash column chromatography was performed employing silica gel (60 Å, 40–63 µm, Merck).

The nitrogen sorption isotherms were recorded on a Quantachrome Autosorb 1 at 77.35 K in a pressure range from $p/p^0 = 0.001$ to 0.98. Prior to the measurement of the sorption isotherm the sample was heated for 24 h at 120°C under turbomolecular pump vacuum. For the evaluation of the surface area the BET model was applied between 0.05 and 0.2 p/p^0 . The calculation of the pore size distribution was done using the QSDFT adsorption model with a carbon kernel for cylindrical pores.

X-ray diffraction (XRD) measurements were performed using a Bruker D8 Discover with Ni-filtered Cu $K\alpha$ radiation and a LynxEye position-sensitive detector.

Transmission electron microscopy was performed on an FEI Titan 80-300 equipped with a field emission gun operated at 300 kV. Scanning electron microscopy (SEM) images were recorded with a JEOL 6500F field emission microscope operated at 5 kV using a secondary electron detector.

UV-Vis spectra were recorded using a Perkin-Elmer Lambda 1050 spectrometer equipped with a 150 mm integrating sphere. Absorbance spectra of COF thin films were corrected for the transmission of the substrate and reflection losses.

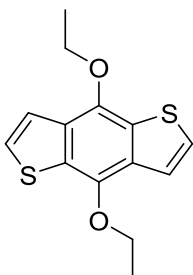
7.4 Experimental

Photoluminescence (PL) measurements were performed using a home-built setup consisting of a Horiba Jobin Yvon iHR 320 monochromator equipped with a photomultiplier tube and a liquid N₂-cooled InGaAs detector. The samples were illuminated with a pulsed (83 Hz) 405 nm LED at a light intensity of 500 mW cm⁻².

Differential pulse voltammetry (DPV) was measured using 50 μM solutions of **PP** in acetonitrile or a 3:5 mixture of acetonitrile/1,4-dioxane, respectively, with 0.1 M tetrabutylammonium hexafluorophosphate as electrolyte and 0.1 mM ferrocene as internal reference. Measurements were performed with a Metrohm Autolab PGSTAT302N potentiostat, using Pt wires as the working electrode and counter electrode and a saturated Ag/AgCl reference electrode (Sigma Aldrich, 0.197 V vs. SHE).

7.4 Experimental

Synthesis

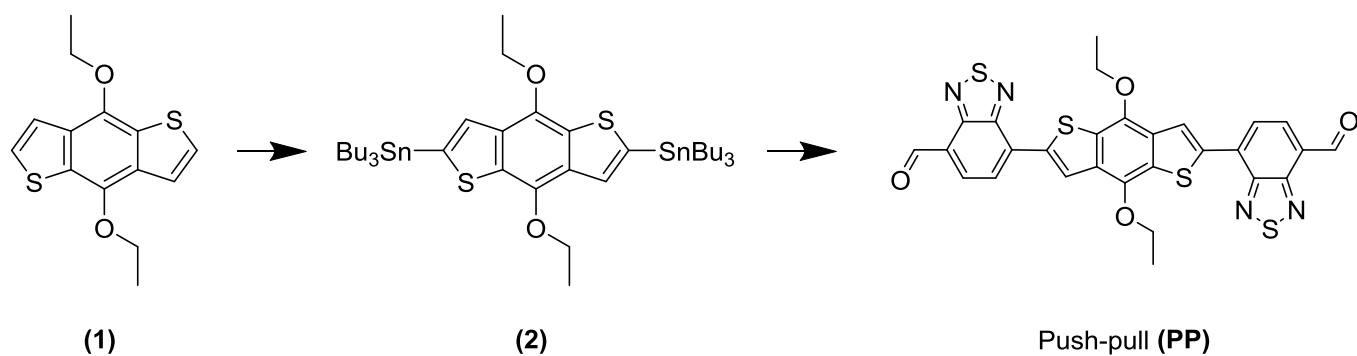


(1)

4,8-Diethoxybenzo[1,2-b:4,5-b']dithiophene (1)

A mixture of benzo[1,2-b:4,5-b']dithiophene-4,8-dione (2.0 g, 4.55 mmol) and Zn dust (660 mg, 1.01 mmol) were placed in a 500 mL round bottom flask equipped with a magnetic stir bar. EtOH (2 mL) and an aqueous solution of NaOH (20 %, 15 mL) were added and the mixture was heated to reflux at 100 °C for 1 h. Ethyl-p-toluenesulfonate (3.41 g, 4.00 mL, 17.0 mmol) was added dropwise over 12 min and the reaction mixture was stirred at 100 °C for an additional 1 h. After cooling to RT the brown precipitate was filtrated and washed with a saturated boiling aqueous solution of Na₂S₂O₅. The residual yellow material was dissolved in 50 mL diethyl ether (Et₂O), filtrated and the separated organic phase was dried over anhydrous MgSO₄ (3 g). After filtration, the solvent was removed by rotary evaporation and the crude product was purified by column chromatography on silica gel with isohexane / ethyl acetate (98:2) to yield **(1)** as colorless crystalline solid (1.05 g, 83 %). M.p.:95-96 °C; IR(ATR) ν [cm⁻¹] = 3101, 2911, 2873, 1515, 1476, 1436, 1373, 1349, 1200, 1106, 1084, 1031, 979, 874, 811, 7366, 695; ¹H-NMR (CDCl₃, 300.06 MHz) δ = 1.49 (t, ³J_{HH} = 7.1 Hz, 6H); 4.38 (m, 4H); 7.37 (d, ³J_{HH} = 5.6 Hz, 2H); 7.48 (d, ³J_{HH} = 5.6 Hz, 2H).

7.4 Experimental

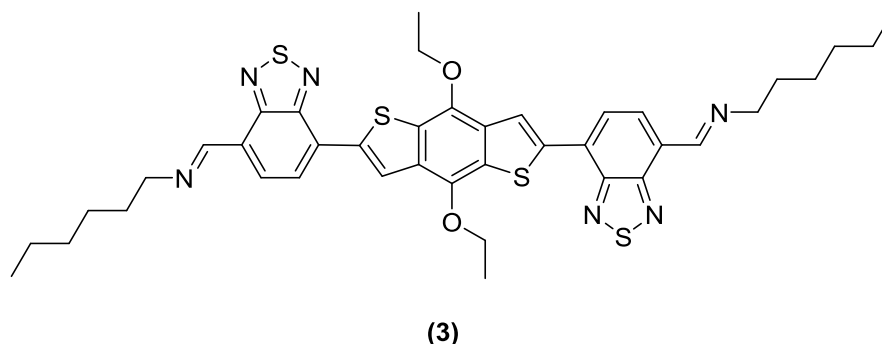


7,7'-(4,8-dipropoxybenzo[1,2-b:4,5-b']dithiophene-2,6-diyl)bis(benzo[c][1,2,5]thiadiazole-4-carbaldehyde) (PP)

A solution of pre-dried compound **(1)** (100 mg, 0.3 mmol) in anhydrous tetrahydrofuran (THF) (5 mL) was stirred and cooled to -78°C (dry ice, acetone) under an argon atmosphere. A solution of n-butyllithium in hexane (2.5 M, 0.24 mL, 0.61 mmol) was added slowly over 5 min. The reaction mixture was allowed to warm up to room temperature and continuously stirred for an additional 1 h. Bu_3SnCl (283 mg, 0.87 mmol) was added to yield [4,8-diethoxybenzo[1,2-b:4,5-b']dithiophene-2,6-diyl]bis(tributylstannane) **(2)**. 660 mg (0.72 mmol) of compound **(2)** and 370 mg (1.5 mmol) 7-bromo-2,1,3-benzothiadiazole-4-carboxaldehyde were added to a 500 mL round bottom flask, equipped with a magnetic stir bar. The reagents were dissolved in 30 mL dry toluene, 20 mg (0.035 mmol) bis(dibenzylideneacetone)palladium(0) and 20 mg (0.08 mmol) tri(2-furyl)phosphine were added before heating the reaction mixture at 80°C for 12 h. After the time had elapsed, the mixture was allowed to cool down to room temperature. The product was isolated by filtration and purified by 3 washing steps with 20 mL Et_2O to yield 300 mg (0.45 mmol, 0.63 %) **(PP)**. M.p. $121\text{--}127^{\circ}\text{C}$; IR (ATR) ν [cm^{-1}] = 2972, 2928, 2861, 1686, 1535, 1519, 1440, 1374, 1349, 1261, 1165, 1084, 1043, 1012, 838, 802; HRMS (DEI⁺) m/z: [M]⁺ Calc. for $\text{C}_{28}\text{H}_{18}\text{N}_4\text{O}_4\text{S}_4$ 602.0216, found 602.0216.

7.4 Experimental

For detailed characterization purpose the corresponding dime of **PP**.



(1E,1'E)-1,1'-((4,8-diethoxybenzo[1,2-b:4,5-b']dithiophene-2,6-diyl)bis(benzo[c][1,2,5]thiadiazole-7,4-diyl))bis(N-hexylmethanimine) (3)

PP (10 mg, 0.02 mmol) and excess of hexylamine (28 mg, 0.28 mmol) were placed in a 50 mL round bottom flask and sonicated and stirred in anhydrous THF (1.5 mL) under argon atmosphere for 1 h. CDCl_3 (0.3 mL) was added and the reaction mixture was heated to reflux at 80 °C for 5 h. The stirring was continued overnight and the solvent was removed *in vacuo* to afford **(3)** as beige solid. IR (ATR) ν [cm^{-1}] = 295, 2925, 2856, 1632, 1540, 1526, 1491, 1449, 1376, 1351, 1309, 1264, 1170, 1051, 900, 841, 829; $^1\text{H-NMR}$ (CDCl_3 , 598.97 MHz) δ = 0.91 (m), 1.35 (m), 1.42 (m), 1.61 (t, $^3J_{\text{HH}} = 7.0$ Hz), 1.78 (quin, $^3J_{\text{HH}} = 7.2$ Hz), 3.76 (t, $^3J_{\text{HH}} = 7.2$ Hz), 4.52 (q, $^3J_{\text{HH}} = 7.0$ Hz), 7.96 (d, $^3J_{\text{HH}} = 7.2$ Hz), 8.21 (d, $^3J_{\text{HH}} = 7.2$ Hz), 8.73 (s), 9.05 (s);

PP-ETTA COF

For the synthesis of PP-ETTA COF, 6.59 mg of compound **PP** (0.01 mmol, 2 equiv.) and 1.96 mg of 1,1,2,2-tetrakis(4-aminophenyl)ethene (ETTA) (0.005 mmol, 1 equiv.) were added to a *Schott* tube with pressure-sealing screw cap and dispersed in a solvent mixture of benzyl alcohol, mesitylene, and 6 molar acetic acid (10 : 20 : 3, $v : v : v$, 1.1 mL). The tube was placed in an oven at 120 °C for 72 h. After the time had elapsed,

7.4 Experimental

the reaction mixture was allowed to cool down to room temperature and the resulting powder was then collected by filtration through a Hirsch funnel. After washing the product three times with 20 mL dry toluene it was left under dynamic vacuum to come to complete dryness.

7.4 Experimental

UV-Vis spectroscopy

Absorption spectrum of PP-ETTA COF was collected from a solid sample in diffuse reflectance mode and transferred into absorption spectra by applying the Kubelka Munk equation:

$$\frac{K}{S} = \frac{(1 - R_{\infty})^2}{2R_{\infty}}$$

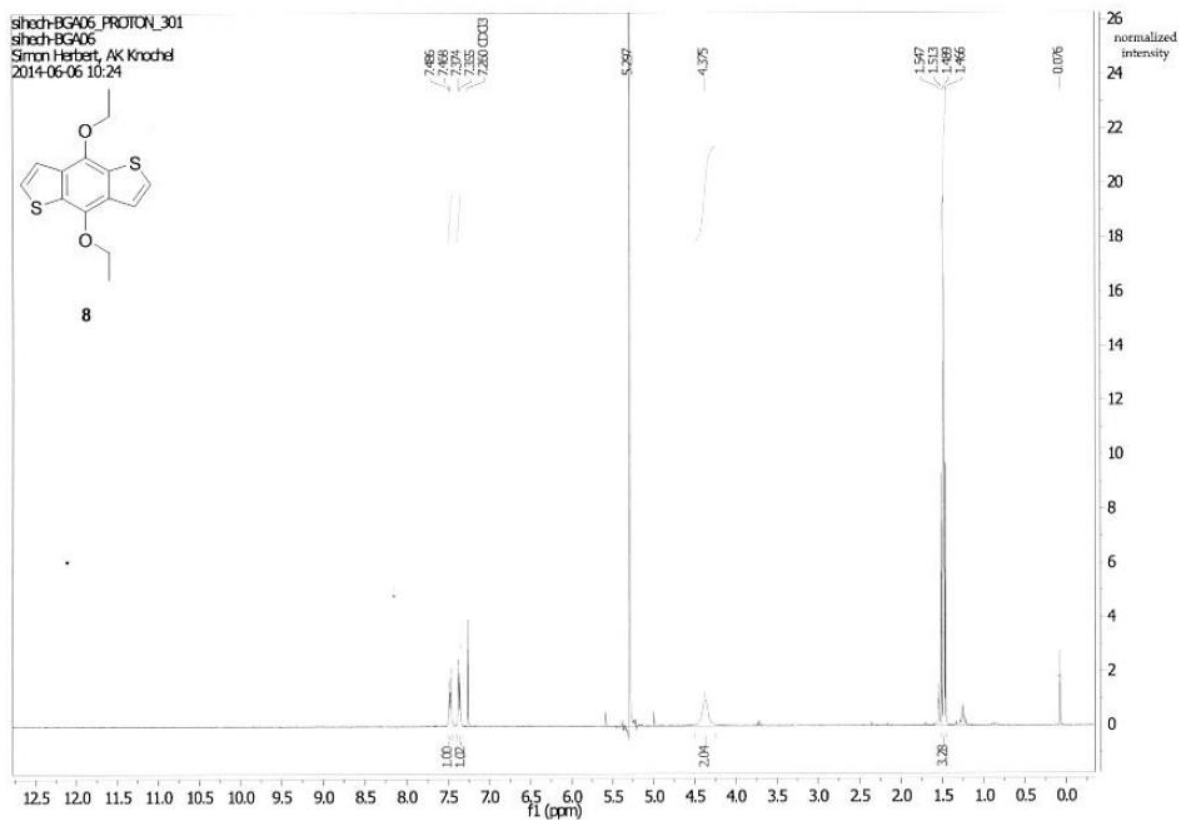
with K = Absorption Coefficient, S = the Scattering Coefficient, R_{∞} = reflectance of sample with infinite thickness.²⁰

7.4 Experimental

NMR spectra

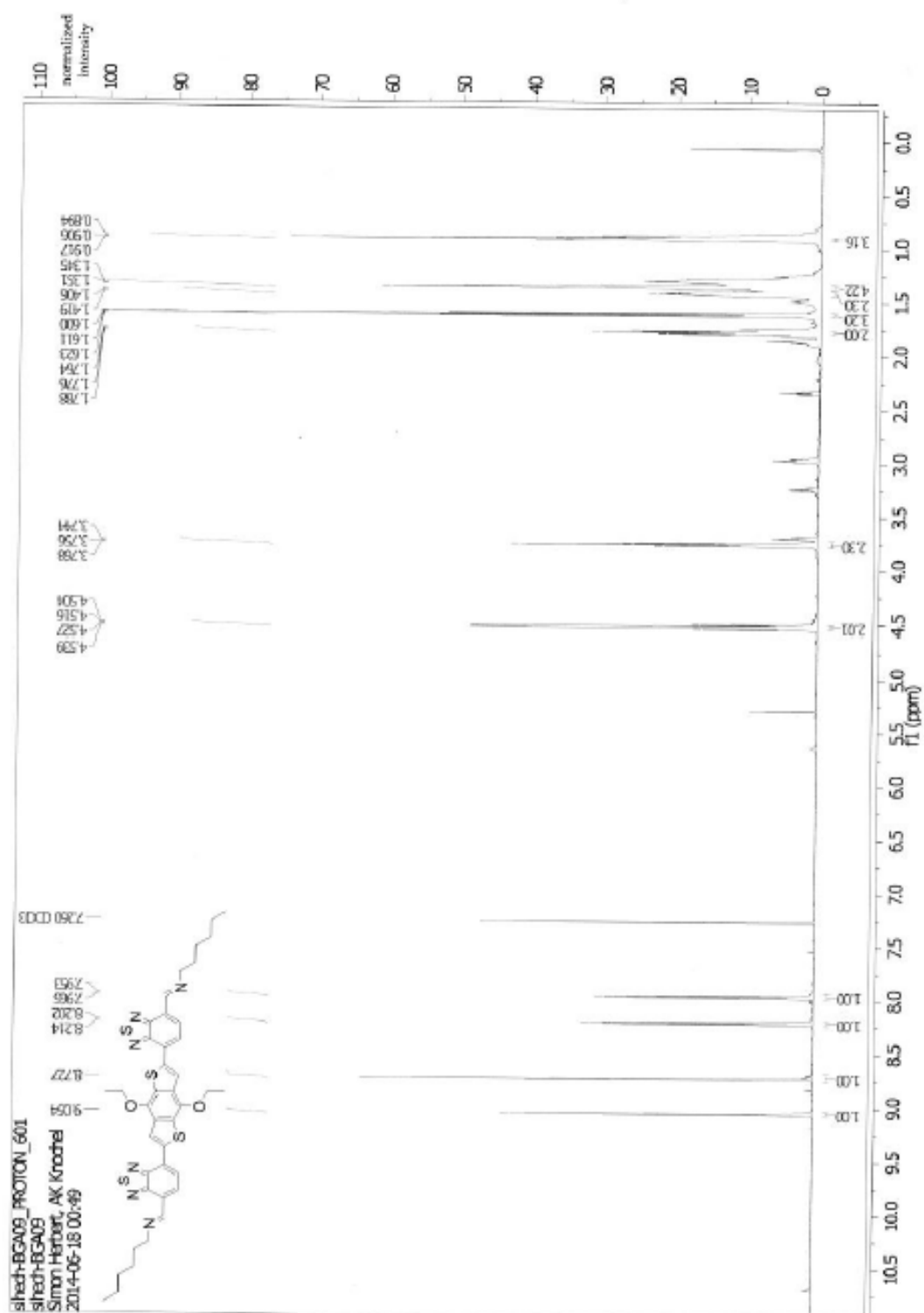
4,8-Diethoxybenzo[1,2-b:4,5-b']dithiophene (DET)

$^1\text{H-NMR}$ (CDCl_3 , 300.06 MHz)



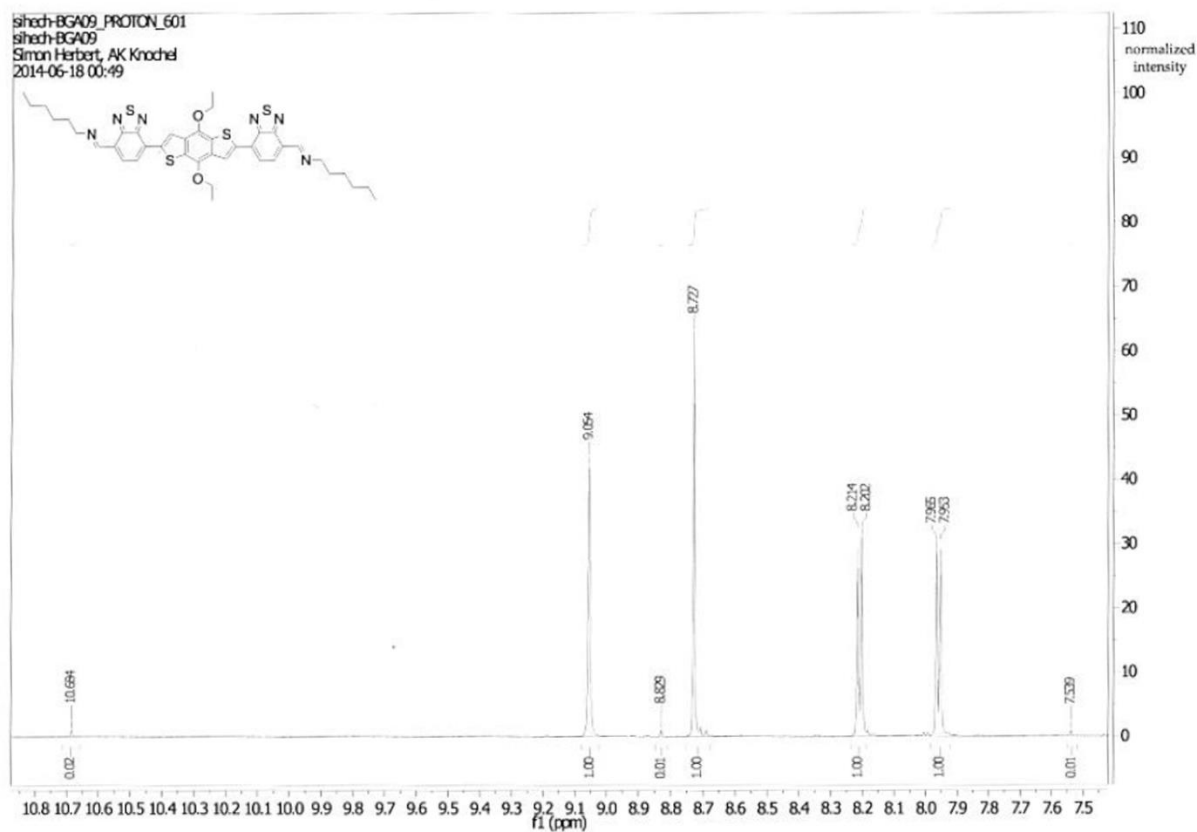
7.4 Experimental

(1E,1'E)-1,1'-((4,8-diethoxybenzo[1,2-b:4,5-b']dithiophene-2,6-diyl)bis(benzo[1,2,5]thiadiazole-7,4-diyl))bis(N-hexylmethanimine)
¹H-NMR (CDCl₃, 598.97 MHz)

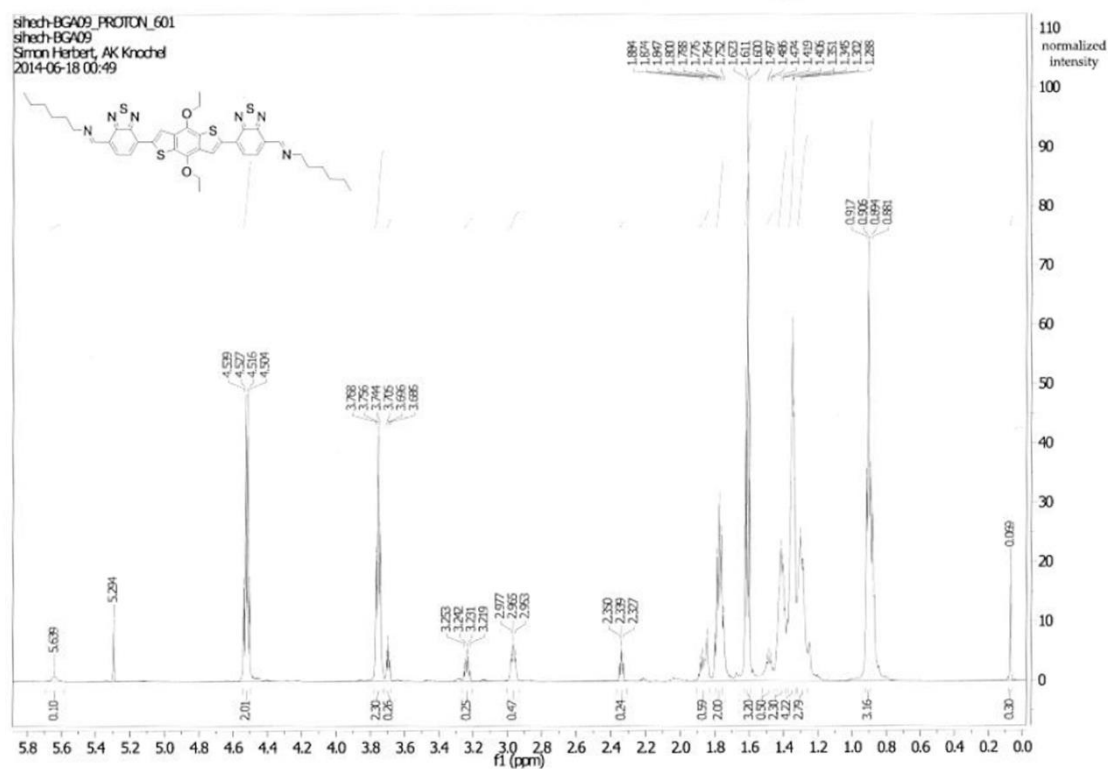


7.4 Experimental

$^1\text{H-NMR}$ (CDCl_3 , 598.97 MHz): 10.8–7.5 ppm



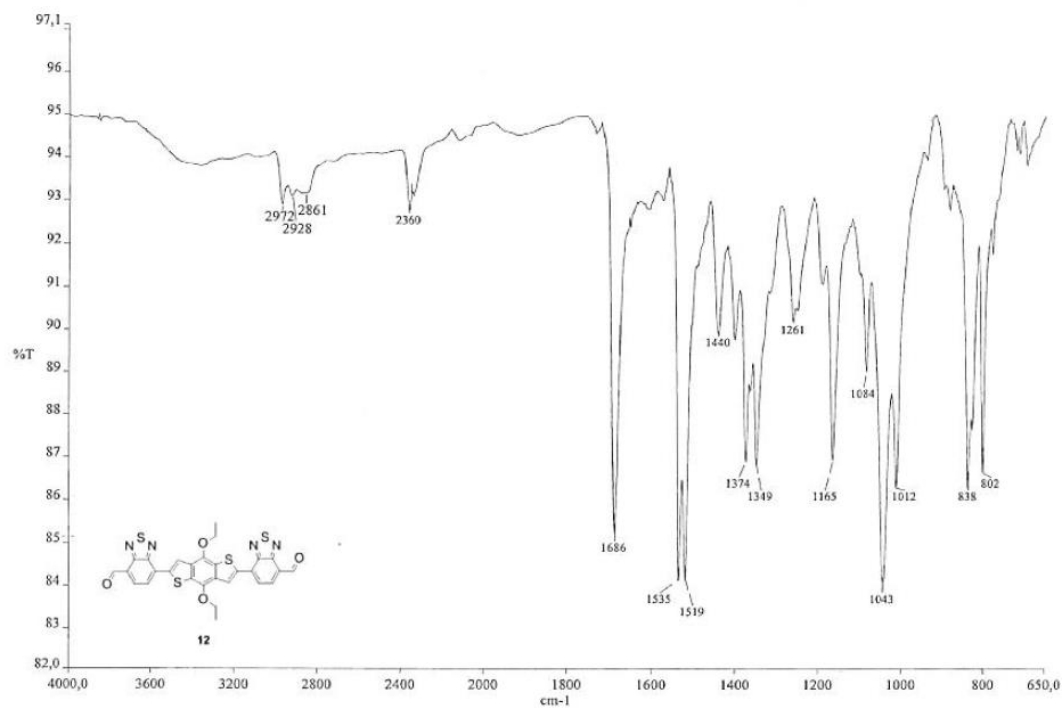
$^1\text{H-NMR}$ (CDCl_3 , 598.97 MHz): 5.8–0.0 ppm



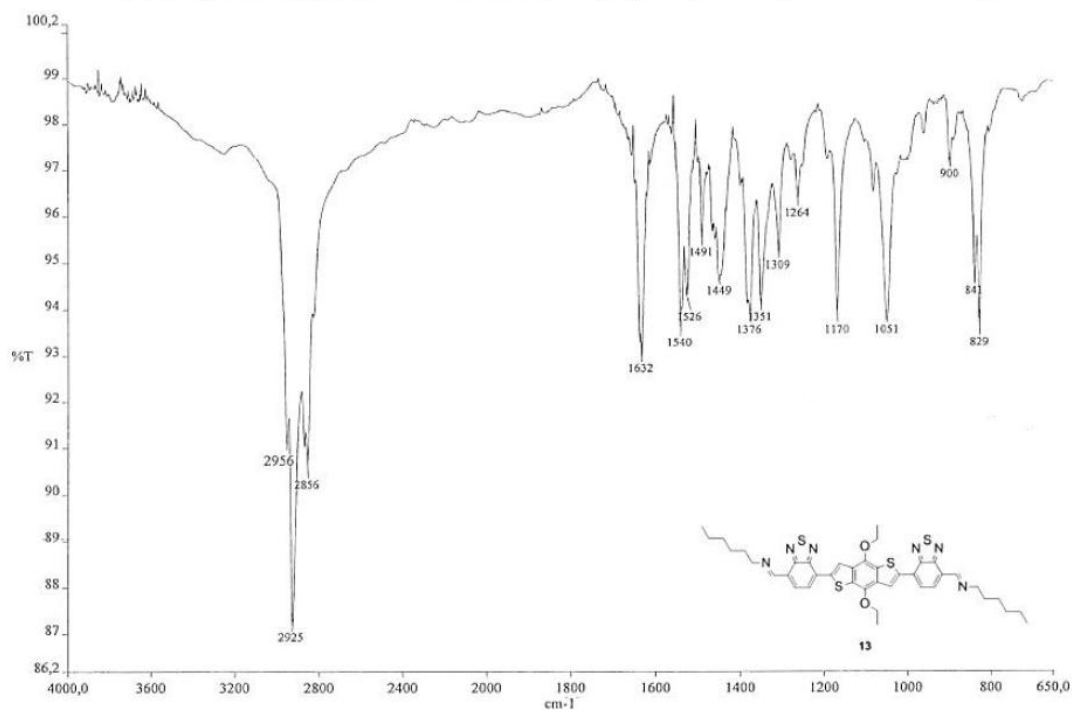
7.4 Experimental

IR Spectra

7,7'-(4,8-Diethoxybenzo[1,2-b:4,5-b']-dithiophene-2,6-diyl)bis(benzo[1,2,5]thiadiazole-4-carbaldehyde)



(1E,1'E)-1,1'-((4,8-diethoxybenzo[1,2-b:4,5-b']dithiophene-2,6-diyl)bis(benzo[1,2,5]thiadiazole-7,4-diyl))bis(N-hexylmethanimine)



7.5 References

1. A. P. Côte; A. I. Benin; N. W. Ockwig; M. O'Keeffe; A. J. Matzger; O. M. Yaghi, Porous, Crystalline, Covalent Organic Frameworks. *Science* **2005**, *310*, 1166-1170.
2. S. Patwardhan; A. A. Kocherzhenko; F. C. Grozema; L. D. A. Siebbeles, Delocalization and Mobility of Charge Carriers in Covalent Organic Frameworks. *J. Phys. Chem. C* **2011**, *115* (23), 11768-11772.
3. S. Wan; J. Guo; J. Kim; H. Ihee; D. Jiang, A Belt-Shaped, Blue Luminescent, and Semiconducting Covalent Organic Framework. *Angew. Chem. Int. Ed.* **2008**, *47*, 8826-8830.
4. X. Feng; L. Liu; Y. Honsho; A. Saeki; S. Seki; S. Irle; Y. Dong; A. Nagai; D. Jiang, High-Rate Charge-Carrier Transport in Porphyrin Covalent Organic Frameworks: Switching from Hole to Electron to Ambipolar Conduction. *Angew. Chem. Int. Ed.* **2012**, *51*, 2618-2622.
5. S. Jin; X. Ding; X. Feng; M. Supur; K. Furukawa; S. Takahashi; M. Addicoat; M. E. El-Khouly; T. Nakamura; S. Irle, Charge dynamics in a donor-acceptor covalent organic framework with periodically ordered bicontinuous heterojunctions. *Angew. Chem. Int. Ed.* **2013**, *52* (7), 2017-2021.
6. S. Wan; F. Gándara; A. Asano; H. Furukawa; A. Saeki; S. K. Dey; L. Liao; M. W. Ambrogio; Y. Y. Botros; X. Duan; S. Seki; J. F. Stoddart; O. M. Yaghi, Covalent Organic Frameworks with High Charge Carrier Mobility. *Chem. Mater.* **2011**, *23*, 4094-4097.
7. X. Feng; L. Chen; Y. Dong; D. Jiang, Porphyrin-based two-dimensional covalent organic frameworks: synchronized synthetic control of macroscopic structures and pore parameters. *Chem. Commun.* **2011**, *47*, 1979-1981.
8. S. Jin; X. Ding; X. Feng; M. Supur; K. Furukawa; S. Takahashi; M. Addicoat; M. E. El-Khouly; T. Nakamura; S. Irle; S. Fukuzumi; A. Nagai; D. Jiang, Charge Dynamics in A Donor-Acceptor Covalent Organic Framework with Periodically Ordered Bicontinuous Heterojunctions. *Angew. Chem. Int. Ed.* **2013**, *52*, 2017-2021.
9. S. Jin; K. Furukawa; M. Addicoat; L. Chen; S. Takahashi; S. Irle; T. Nakamura; D. Jiang, Large pore donor-acceptor covalent organic frameworks. *Chem. Sci.* **2013**, *4*, 4505-4511.
10. S. Kandambeth; D. B. Shinde; M. K. Panda; B. Lukose; T. Heine; R. Banerjee, Enhancement of Chemical Stability and Crystallinity in Porphyrin-Containing Covalent Organic Frameworks by Intramolecular Hydrogen Bonds. *Angew. Chem. Int. Ed.* **2013**, *52*, 13052-13056.
11. V. S. P. K. Neti; X. Wu; S. Deng; L. Echegoyen, Synthesis of a phthalocyanine and porphyrin 2D covalent organic framework. *CrystEngComm* **2013**, *15*, 6892-6895.
12. M. Dogru; M. Handloser; F. Auras; T. Kunz; D. Medina; A. Hartschuh; P. Knochel; T. Bein, A Photoconductive Thienothiophene-Based Covalent Organic Framework Showing Charge Transfer Towards Included Fullerene. *Angew. Chem. Int. Ed.* **2013**, *52*, 2920-2924.
13. M. Calik; F. Auras; L. M. Salonen; K. Bader; I. Grill; M. Handloser; D. D. Medina; M. Dogru; F. Loebermann; D. Trauner; A. Hartschuh; T. Bein, Extraction of Photogenerated Electrons and Holes from a COF Integrated Heterojunction. *J. Am. Chem. Soc.* **2014**.
14. B. Pépin-Donat; C. Ottone; C. Morell; C. Lombard; A. Lefrançois; P. Reiss; M. Leclerc; S. Sadki, Electron Paramagnetic Resonance Tracing of Electronic Transfers in Push-Pull Copolymers/PCBM or Nanocrystal Composites. *J. Phys. Chem. C* **2014**, *118* (35), 20647-20660.

7.5 References

15. J. Y. Kim; Y. Qin; D. M. Stevens; V. Kalihari; M. A. Hillmyer; C. D. Frisbie, High open-circuit voltage photovoltaic cells with a low bandgap copolymer of Isothianaphthene, Thiophene, and Benzothiadiazole units. *J. Phys. Chem. C* **2009**, *113* (52), 21928-21936.
16. V. Malytskyi; J.-J. Simon; L. Patrone; J.-M. Raimundo, Thiophene-based push-pull chromophores for small molecule organic solar cells (SMOSCs). *RSC Advances* **2015**, *5* (1), 354-397.
17. N. Cai; Y. Wang; M. Xu; Y. Fan; R. Li; M. Zhang; P. Wang, Engineering of Push-Pull Thiophene Dyes to Enhance Light Absorption and Modulate Charge Recombination in Mesoscopic Solar Cells. *Adv. Funct. Mater.* **2013**, *23* (14), 1846-1854.
18. J. Y. Lee; K. S. Kim; B. J. Mhin, Intramolecular charge transfer of π -conjugated push-pull systems in terms of polarizability and electronegativity. *The Journal of Chemical Physics* **2001**, *115* (20), 9484-9489.
19. A. Slama-Schwok; M. Blanchard-Desce; J. Lehn, Intramolecular charge transfer in donor-acceptor molecules. *J. Phys. Chem.* **1990**, *94* (10), 3894-3902.
20. P. Kubelka; F. Munk, An article on optics of paint layers. *Z. Tech. Phys* **1931**, *12* (593-601).

8. Conclusion

In this work, a modulation strategy was developed for the growth of highly crystalline COFs with large domains and very high porosity. The competition between the bridging COF building block and the terminating modulation agent was found to influence the dynamic equilibrium during framework formation, slowing down the COF growth and supporting the self-healing of crystal defects. Under optimized conditions, the crystal domains of the boronate ester-linked COF-5 reached several hundreds of nanometers. The pores of the framework were found to be open and fully accessible even without any activation procedure, which is reflected by a surface area close to the theoretical maximum and a very narrow pore size distribution.

Compositional analysis via NMR revealed that the COF-5 structure forms over a wide range of molecular compositions, from highly diboronic acid-deficient frameworks to networks comprising an excess of the linear building block.

The use of functionalized modulating agents furthermore provides a new strategy for functionalizing the outer surface of COF crystallites. These functional groups were found to be accessible for the subsequent covalent attachment of molecules or polymers, allowing for further modification of the chemical, physical, or electronic properties of the COF.

The combination of an enhanced degree of crystallinity and the option for an outer surface post-modification of COF domains might prove beneficial for a range of applications, such as gas separation, catalysis, super resolution imaging, and optoelectronics.

In a second project, a new porphyrin- and triphenylene containing COF was developed featuring ordered columns of donor and acceptor moieties within its framework. The

8 Conclusion

inherent interdigitated heterojunction of this COF was found to promote charge separation upon photoexcitation of either building block. Oriented films of this COF were applied in the construction of the first photovoltaic device in which the COF itself provides the photoactive junction. The structural precision of COF-based heterojunctions presents an opportunity to study charge carrier generation and extraction in well-defined model systems. Quantum efficiency measurements in the presence of an external collection field show the potential of this novel device concept, provided that recombination losses can be minimized. Enhancement of the carrier collection yield that might ultimately lead to competitive device efficiencies is expected from further improvements in the electron and hole transport properties of these materials.

The development of a novel thienothiophene-porphyrin (TT-Por) COF suggested evidence for a preferred stacking behavior of porphyrin-containing COFs. The symmetry of the new material was found to not match a simulated eclipsed, but to rather adopt a staircase-like stacking arrangement. PXRD data confirmed a splitting of reflections, caused by the reduction of symmetry. The new TT-Por COF was found to stabilize photoluminescent dynamics, resulting in prolonged lifetimes compared to the starting materials or 1P-Por COF. The use of the electron rich porphyrin coupled to the electron deficient TT to construct a COF framework facilitates internal charge transfer, which allows for a delocalization of electrons throughout the framework and thus a stabilization of the excited species. The high structural order of COFs thereby enables a unique chance to investigate the occurring processes upon excitation on the nanoscale.

Additionally, a new strategy was developed to integrate large, light-harvesting linker molecules within COF structures. The newly developed linker molecule composed of 4 thiophenes with an asymmetric attachment of alkyl chains was successfully integrated

8 Conclusion

within a COF structure. These alkyl chains not only tune the solubility such that COF formation can be achieved but also offer the possibility of alternating within the COF structure and thereby reducing steric repulsion between adjacent layers.

The new Pyr-4T COF exhibits exceptionally high crystallinity, indicated by the diffraction pattern showing sharp high angle reflections with good intensity. The incorporation of the 4T monomer within an ordered COF structure broadened the absorption and photoluminescence spectra compared to those of the monomer, suggesting conjugation between the building blocks. This corresponds to a decrease in the optical bandgap energy of 20 %.

Another strategy to enhance the optical properties of linker molecules and therefore of the resulting COF is the use of “push-pull” systems. A new linker molecule was developed, consisting of an electron-rich benzodithiophene (BDT) unit linked to two electron deficient benzothiadiazole (BT) units. This push-pull (PP) linker was successfully integrated within a COF structure by coupling to 1,1,2,2-tetrakis(4-aminophenyl)ethene (ETTA) molecules. The new PP-ETTA COF was found to adopt a hexagonal symmetry creating a dual pore system.

The integration of the PP linker within the PP-ETTA COF caused a significant shift in the optical absorbance, such that it spreads throughout the ultra-violet and almost the complete visible region. This renders the new COF an attractive candidate as active material in a solar cell device, as it efficiently harvests light in the region where most of the solar flux occurs. Furthermore, the energy levels of the HOMO and LUMO of the linker molecule are well-aligned to enable electron transport to the commonly used PCBM acceptor phase. We believe that the development of finely tuned push-pull linker molecules allows for the construction of covalent organic frameworks with favorable properties to be used as active material in ordered BHJ solar cell devices.